STRUCTURES AND FRAGMENTATION REACTIONS OF PROTONATED NEONICOTINOID INSECTICIDES BY INFRARED MULTIPHOTON DISSOCIATION SPECTROSCOPY AND COMPUTATIONAL METHODS

by © Kelsey Jane Menard

A dissertation submitted to the School of Graduate Studies in partial fulfillment of the requirement for the degree of Master of Science

Department of Chemistry

Memorial University of Newfoundland

St. John's, Newfoundland and Labrador, Canada

December 2020

ABSTRACT

Imidacloprid and thiamethoxam belong to the nitroguanidine subclass of neonicotinoid insecticides. Nitroguanidine neonicotinoids induce higher acute and chronic toxicity in bees, therefore, analytical methods have been developed to evaluate the biological and ecological effects of neonicotinoids. The structures and unimolecular chemistries of protonated imidacloprid and protonated thiamethoxam have been studied in the gas phase by infrared multiphoton dissociation (IRMPD) spectroscopy and computational methods. Electronic structure calculations employing density functional theory (DFT) were conducted to determine thermodynamic results, relative enthalpies and Gibbs energies, and to compute the infrared frequencies of stretching and bending vibrations. Comparison of the experimental IRMPD and computed IR spectra was done to identify the vibrational features of the protonated neonicotinoids, imidacloprid and thiamethoxam.

The lowest energy isomer of protonated imidacloprid, protonated at the pyridine nitrogen, generates an IR spectrum that is most consistent with the IRMPD spectrum. The spectroscopic IRMPD data for protonated imidacloprid urea (loss of N_2O), protonated desnitroimidacloprid (loss of $NO_2^{\bullet}$), protonated desnitrosoimidacloprid (loss of $NO^{\bullet}$), and the loss $NO^{\bullet}$ and $^{\bullet}OH$ from protonated imidacloprid are also presented. A DFT calculated potential energy diagram of protonated desnitroimidacloprid reveals the energetic barriers for intramolecular proton transfer versus bond dissociation of $NO_2^{\bullet}$. A possible mechanism for the loss of $NO^{\bullet}$ and $^{\bullet}OH$ from protonated imidacloprid describes isomerization of the $NO^{\bullet}$ loss product ion and tautomerization of the $^{\bullet}OH$ product ion.

The structures, energetics, and infrared spectra of protonated thiamethoxam were computed using the B3LYP and M06-2X methods. There is a discrepancy in the computed energies for the lowest energy isomers of protonated thiamethoxam, therefore, a comparison of the calculated IR spectra and the IRMPD spectrum reveals that the oxygen protonated isomer is the best match. IRMPD spectroscopy experiments in conjunction with DFT computations are also performed for protonated desnitro-thiamethoxam (loss of $NO_2^{\bullet}$), and protonated dechlorinated desnitro-thiamethoxam (loss of $NO_2^{\bullet}$ and $Cl^{\bullet}$).

ACKNOWLEDGEMENTS

There are numerous people who have motivated me to pursue a graduate degree, and without their help the research presented in this thesis would not have been accomplished. First, I would like to express my sincere gratitude toward my supervisor, Dr. Travis Fridgen, for his patience and guidance throughout my academic development. Dr. Fridgen's impartialness has created an excellent work environment for his students. He has given me the opportunity to present my research at multiple conferences pertaining to mass spectrometry and for that I am grateful.

I would like to state my great appreciation to Dr. Fridgen's group members, both past and present, for offering their feedback and criticism on my research. I thank them for generously giving up their time to collaborate on ideas about complicated experimental results. Thank you, Ruodi, Mahsa, Yanyang, Sam, Barry, Willow, and Kianna, for making this degree a truly enjoyable experience.

I would like to give recognition to my supervisory committee, Dr. Heather Reader and Dr. Yuming Zhao, for reviewing my thesis and providing insightful comments on my work. I am also thankful for the wonderful staff in the chemistry department general office for their help and support during my masters' program.

I gratefully acknowledge the support of the FELIX laboratory and Jonathan Martens for his assistance with conducting experiments.

Finally, I would like to convey my appreciation to my parents, Paula and Marc, for inspiring me to have a passion for learning and teaching me the value of hard work. I would like to thank my brother, Lucas, and my mom for inspecting my thesis for

grammatical errors and spelling mistakes. I owe a special thanks to my boyfriend, Matthew, for his continuous support and encouragement throughout these past few years.

TABLE OF CONTENTS

LIST OF FIGURES

Figure 2.5. A schematic representation of a free electron laser. A beam of electrons is produced by the electron accelerator and then is directed through the alternating magnetic field of the undulator. Coherent and intense radiation is amplified within the optical cavity by mirrors placed at either end of the undulator. Figure taken from the FELIX website.

Figure 2.6. The electrospray ionization process. Charged droplets of analyte solution are produced at the capillary tip, solvent evaporation and Coulombic explosion split larger charged droplets into smaller highly charged droplets, and gas phase ions are formed by the CRM or IEM. Figure reproduced from reference 36 with permission.

Figure 3.1. IRMPD mass spectra for protonated imidacloprid and its fragmentation products (*m/z* 256 → *m/z* 226, *m/z* 256 → *m/z* 212, *m/z* 256 → *m/z* 210, *m/z* 256 → *m/z* 209) at their maximum ion dissociation.

Figure 3.2. Comparison of the experimental IRMPD spectra (black trace) and the computed IR spectra (grey trace) for the lowest energy structures of protonated imidacloprid. Protonation at the nitrogen atom of the pyridine ring (N5 position) is calculated to be favoured over the other basic sites. All relative thermochemistries are 298 K values and are in kJ mol^{-1}.

Figure 3.3. Comparison of the experimental IRMPD spectra (black trace) and the computed IR spectra (grey trace) for the lowest energy structures of protonated desnitrosoimidacloprid (loss of NO$^{\bullet}$). All relative thermochemistries are 298 K values and are in kJ mol^{-1}.

Figure 3.4. Comparison of the experimental IRMPD spectra (black trace) and the computed IR spectra (grey trace) for the lowest energy isomers of protonated imidacloprid urea (loss of N_2O). All relative thermochemistries are 298 K values and are in kJ mol^{-1}.

Figure 3.5. Comparison of the experimental IRMPD spectra (black trace) and the computed IR spectra (grey trace) for the lowest energy isomers of protonated desnitroimidacloprid (loss of $NO_2^{\bullet}$). All relative thermochemistries are 298 K values and are in kJ mol^{-1}.

Figure 3.6. Comparison of the experimental IRMPD spectra (black trace) and the computed IR spectra (grey trace) for the loss of NO$^{\bullet}$ and $^{\bullet}$OH from protonated imidacloprid, singlet state isomers. All relative thermochemistries are 298 K values and are in kJ mol^{-1}.

Figure 3.7. Potential mechanism for the formation of the *m/z* 209 ion resulting from the dissociation of NO$^{\bullet}$ and $^{\bullet}$OH from protonated imidacloprid.

Figure 4.10. The IRMPD spectrum for the *m/z* 181 fragment ion depicting the reaction mechanism for the loss of $NH^{2\bullet}$ and $CH_3^{\bullet}$ and the reaction mechanism for the loss of CH_2O from protonated dechlorinated desnitro-thiamethoxam.

Figure S3.1. Comparison of the experimental IRMPD spectra (black trace) and the computed IR spectra (grey trace) for the lowest energy isomer of protonated imidacloprid, the N1-N5 conformers. All relative thermochemistries are 298 K values and are in kJ mol^{-1}.

Figure S3.2. Comparison of the experimental IRMPD spectra (black trace) and the computed IR spectra (grey trace) for higher energy tautomers of protonated imidacloprid. All relative thermochemistries are 298 K values and are in kJ mol^{-1}.

Figure S3.3. Comparison of the experimental IRMPD spectra (black trace) and the computed IR spectra (grey trace) for higher energy tautomers of protonated imidacloprid. All relative thermochemistries are 298 K values and are in kJ mol^{-1}.

Figure S3.4. Comparison of the experimental IRMPD spectra (black trace) and the computed IR spectra (grey trace) for higher energy tautomers of protonated desnitrosoimidacloprid (loss of $NO^{\bullet}$). All relative thermochemistries are 298 K values and are in kJ mol^{-1}.

Figure S3.5. Potential energy diagram for protonated desnitrosoimidacloprid to show the enthalpy and Gibbs energy barrier for proton transfer following the loss of $NO^{\bullet}$.

Figure S3.6. Comparison of the experimental IRMPD spectra (black trace) and the computed IR spectra (grey trace) for the lowest energy isomer of protonated imidacloprid urea (loss of N_2O), the N1-N5 conformers. All relative thermochemistries are 298 K values and are in kJ mol^{-1}.

Figure S3.7. Comparison of the experimental IRMPD spectra (black trace) and the computed IR spectra (grey trace) for higher energy tautomers of protonated imidacloprid urea (loss of N_2O). All relative thermochemistries are 298 K values and are in kJ mol^{-1}.

Figure S3.8. Potential energy diagram for protonated desnitroimidacloprid to show the enthalpy and Gibbs energy barriers for proton transfer preceding the loss of $NO_2^{\bullet}$.

Figure S3.9. Potential energy diagram for protonated desnitroimidacloprid to show the enthalpy and Gibbs energy barriers for proton transfer following the loss of $NO_2^{\bullet}$.

Figure S3.10. Potential energy diagram for protonated desnitroimidacloprid to show the enthalpy and Gibbs energy barriers for tautomerization following the loss of $NO_2^{\bullet}$.

Figure S3.11. Comparison of the experimental IRMPD spectra (black trace) and the computed IR spectra (grey trace) for higher energy tautomers of protonated

desnitroimidacloprid (loss of $NO_2^{\bullet}$). All relative thermochemistries are 298 K values and are in kJ mol^{-1}.

Figure S3.12. Comparison of the experimental IRMPD spectra (black trace) and the computed IR spectra (grey trace) for the loss of $NO^{\bullet}$ and $^{\bullet}OH$ from protonated imidacloprid, singlet state isomers. All relative thermochemistries are 298 K values and are in kJ mol^{-1}.

Figure S3.13. Comparison of the experimental IRMPD spectra (black trace) and the computed IR spectra (grey trace) for the loss of $NO^{\bullet}$ and $^{\bullet}OH$ from protonated imidacloprid, triplet state isomers. All relative thermochemistries are 298 K values and are in kJ mol^{-1}.

Figure S3.14. Comparison of the experimental IRMPD spectra (black trace) and the computed IR spectra (grey trace) for the loss of $NO_2^{\bullet}$ and $H^{\bullet}$ from the C2 position of protonated imidacloprid, triplet state isomers. All relative thermochemistries are 298 K values and are in kJ mol^{-1}.

Figure S3.15. Comparison of the experimental IRMPD spectra (black trace) and the computed IR spectra (grey trace) for the loss of $NO_2^{\bullet}$ and $H^{\bullet}$ from the C2 position of protonated imidacloprid, triplet state isomers. All relative thermochemistries are 298 K values and are in kJ mol^{-1}.

Figure S3.16. Comparison of the experimental IRMPD spectra (black trace) and the computed IR spectra (grey trace) for the loss of $NO_2^{\bullet}$ and $H^{\bullet}$ from the C3 position of protonated imidacloprid, triplet state isomers. All relative thermochemistries are 298 K values and are in kJ mol^{-1}.

Figure S3.17. Comparison of the experimental IRMPD spectra (black trace) and the computed IR spectra (grey trace) for the loss of $NO_2^{\bullet}$ and $H^{\bullet}$ from the C3 position of protonated imidacloprid, triplet state isomers. All relative thermochemistries are 298 K values and are in kJ mol^{-1}.

Figure S3.18. Comparison of the experimental IRMPD spectra (black trace) and the computed IR spectra (grey trace) for the loss of $NO_2^{\bullet}$ and $H^{\bullet}$ from the C4 position of protonated imidacloprid, triplet state isomers. All relative thermochemistries are 298 K values and are in kJ mol^{-1}.

Figure S3.19. Comparison of the experimental IRMPD spectra (black trace) and the computed IR spectra (grey trace) for the loss of $NO_2^{\bullet}$ and $H^{\bullet}$ from the C4 position of protonated imidacloprid, triplet state isomers. All relative thermochemistries are 298 K values and are in kJ mol^{-1}.

Figure S3.20. Energetics for the formation of pIMI-NOOH_N2-N2a from pDIMI-H_N2.

Figure S3.21. Comparison of the experimental IRMPD spectra (black trace) and the computed IR spectra (grey trace) for protonated dechlorinated desnitroimidacloprid (loss of $Cl^{\bullet}$), triplet state isomers. All relative thermochemistries are 298 K values and are in kJ mol^{-1}.

Figure S3.22. Comparison of the experimental IRMPD spectra (black trace) and the computed IR spectra (grey trace) for protonated dechlorinated desnitroimidacloprid (loss of $Cl^{\bullet}$), singlet state isomers involving N2-C5 bond formation. All relative thermochemistries are 298 K values and are in kJ mol^{-1}.

Figure S3.23. Comparison of the experimental IRMPD spectra (black trace) and the computed IR spectra (grey trace) for protonated dechlorinated desnitroimidacloprid (loss of $Cl^{\bullet}$), singlet state isomers involving N2-C5 bond formation. All relative thermochemistries are 298 K values and are in kJ mol^{-1}.

Figure S3.24. Comparison of the experimental IRMPD spectra (black trace) and the computed IR spectra (grey trace) for protonated dechlorinated desnitroimidacloprid (loss of $Cl^{\bullet}$), singlet state isomers involving N2-C6 bond formation. All relative thermochemistries are 298 K values and are in kJ mol^{-1}.

Figure S3.25. Comparison of the experimental IRMPD spectra (black trace) and the computed IR spectra (grey trace) for protonated dechlorinated desnitroimidacloprid (loss of $Cl^{\bullet}$), singlet state isomers involving N2-C9 bond formation. All relative thermochemistries are 298 K values and are in kJ mol^{-1}.

Figure S3.26. Comparison of the experimental IRMPD spectra (black trace) and the computed IR spectra (grey trace) for protonated dechlorinated desnitroimidacloprid (loss of $Cl^{\bullet}$), singlet state isomers involving N2-C9 bond formation and a hydrogen shift from C9 to N2. All relative thermochemistries are 298 K values and are in kJ mol^{-1}.

Figure S3.27. Comparison of the experimental IRMPD spectra (black trace) and the computed IR spectra (grey trace) for protonated dechlorinated desnitroimidacloprid (loss of $Cl^{\bullet}$), singlet state isomers involving N2-C8 bond formation. All relative thermochemistries are 298 K values and are in kJ mol^{-1}.

Figure S3.28. Comparison of the experimental IRMPD spectra (black trace) and the computed IR spectra (grey trace) for protonated dechlorinated desnitroimidacloprid (loss of $Cl^{\bullet}$), singlet state isomers involving N2-C8 bond formation. All relative thermochemistries are 298 K values and are in kJ mol^{-1}.

Figure S4.1. Half chair enantiomer of the oxadiazinane ring for the lower energy isomers of protonated thiamethoxam.

Figure S4.2. Half chair enantiomer of the oxadiazinane ring for the higher energy isomers of protonated thiamethoxam.

Figure S4.3. The experimental IRMPD spectrum (black trace) and the computed IR spectra (grey trace) for the isomers of protonated desnitro-thiamethoxam where the radical is localized on C7 (pDTMX_N2-C6-S1).

Figure S4.4. The experimental IRMPD spectrum (black trace) and the computed IR spectra (grey trace) for the isomers of protonated desnitro-thiamethoxam where the radical is localized on C7 (pDTMX_N2-C6-C7).

Figure S4.5. The experimental IRMPD spectrum (black trace) and the computed IR spectra (grey trace) for the isomers of protonated desnitro-thiamethoxam where the radical is localized on S1 (pDTMX_S1d-C5).

Figure S4.6. The experimental IRMPD spectrum (black trace) and the computed IR spectra (grey trace) for the isomers of protonated desnitro-thiamethoxam where the radical is localized on S1 (pDTMX_S1d-N2).

Figure S4.7. The experimental IRMPD spectrum (black trace) and the computed IR spectra (grey trace) for the isomers of protonated desnitro-thiamethoxam where the radical is localized on C5 (pDTMX_S1d-C5H).

Figure S4.8. The experimental IRMPD spectrum (black trace) and the computed IR spectra (grey trace) for isomers of protonated dechlorinated desnitro-thiamethoxam where the radicals reside on N2 and C8 (pDTMX-Cl).

Figure S4.9. The experimental IRMPD spectrum (black trace) and the computed IR spectra (grey trace) for isomers of protonated dechlorinated desnitro-thiamethoxam where the N2-C6 bond is formed and the radicals reside on C7 and C8 (pDTMX-Cl_N2-C6-S1_T).

Figure S4.10. The experimental IRMPD spectrum (black trace) and the computed IR spectra (grey trace) for isomers of protonated dechlorinated desnitro-thiamethoxam where the N2-C6 bond is formed and the radicals reside on C7 and C8 (pDTMX-Cl_N2-C6-C7_T).

Figure S4.11. The experimental IRMPD spectrum (black trace) and the computed IR spectra (grey trace) for isomers of protonated dechlorinated desnitro-thiamethoxam where the N2-C6 bond is formed and the radicals reside on C8 (pDTMX-Cl_N2-C6-S1_S).

Figure S4.12. The experimental IRMPD spectrum (black trace) and the computed IR spectra (grey trace) for isomers of protonated dechlorinated desnitro-thiamethoxam where the N2-C6 bond is formed and the radicals reside on C8 (pDTMX-Cl_N2-C6-C7_S).

Figure S4.13. The experimental IRMPD spectrum (black trace) and the computed IR spectra (grey trace) for isomers of protonated dechlorinated desnitro-thiamethoxam where the N2-C6 bond is formed and the C6-S1 bond is cleaved (pDTMX-Cl_S1d-C5).

Figure S4.14. The experimental IRMPD spectrum (black trace) and the computed IR spectra (grey trace) for isomers of protonated dechlorinated desnitro-thiamethoxam where a hydrogen is transferred from C5 to S1 and the radicals reside on C5 and C8 (pDTMX-Cl_S1d-C5H).

Figure S4.15. The experimental IRMPD spectrum (black trace) and the computed IR spectra (grey trace) for isomers of protonated dechlorinated desnitro-thiamethoxam where the N2-C7 bond is formed and the radicals reside on C6 and C8 (pDTMX-Cl_N2-C7).

Figure S4.16. The experimental IRMPD spectrum (black trace) and the computed IR spectra (grey trace) for isomers of protonated dechlorinated desnitro-thiamethoxam where the N2-S1 bond is formed and the C8-S1 bond is cleaved (pDTMX-Cl_N2-S1).

Figure S4.17. The experimental IRMPD spectrum (black trace) and the computed IR spectra (grey trace) for isomers of protonated dechlorinated desnitro-thiamethoxam where formation of the N2-C8 bond results in cleavage of the N3-C5 bond (pDTMX-Cl_N2-C8-N5).

LIST OF TABLES

LIST OF SCHEMES

LIST OF ABBREVIATIONS AND SYMBOLS

$\Delta_{rel}G$	Relative Gibbs energy
$\Delta_{rel}H$	Relative enthalpy
3D	Three-dimensional
APCI	Atmospheric pressure chemical ionization
B3LYP	Becke 3-parameter, Lee–Yang–Parr (exchange-correlation functional)
BIRD	Blackbody infrared radiative dissociation
CCD	Colony collapse disorder
CCDC	Cambridge Crystallographic Data Centre
CID	Collision-induced dissociation
cm^{-1}	Wavenumbers
CRM	Charge residue model
DC	Direct current
D_0	Dissociation threshold
DFT	Density functional theory
ECD	Electron capture dissociation
EID	Electron-induced dissociation
ESI	Electrospray ionization
ESI-CID	Electrospray ionization collision-induced dissociation
ESI-MS	Electrospray ionization-mass spectrometry
EU	European Union

FEL	Free electron laser
FELIX	Free Electron Laser for Infrared eXperiments
FTICR	Fourier transform ion cyclotron resonance
FT-IR	Fourier transform infrared spectroscopy
FT-Raman	Fourier transform-Raman spectroscopy
GTO	Gaussian-type orbital
HCD	Higher-energy collision dissociation
ICR	Ion cyclotron resonance
IEM	Ion evaporation model
IMI	Imidacloprid
IR	Infrared
IRMPD	Infrared multiphoton dissociation
IVR	Intramolecular vibrational energy redistribution
K	Temperature; Kelvin
kJ mol^{-1}	Kilojoules per mole
LD_{50}	Median lethal dose
LC-MS	Liquid chromatography-mass spectrometry
LC-MS/MS	Liquid chromatography-tandem mass spectrometry
LC/TOF-MS	Liquid chromatography/time-of-flight mass spectrometry
µg/bee	Microgram per bee
M06-2X	A functional of the 06 family of the Minnesota suite of density functionals

m/z	Mass-to-charge ratio
mJ/pulse	Energy; millijoule per pulse
mM or mmol L^{-1}	Millimoles per liter
MP2	Møller-Plesset second order perturbation theory
MS	Mass spectrometry
MS/MS or MS^n	Tandem mass spectrometry
nAChRs	Nicotinic acetylcholine receptors
PCM	Polarization continuum model
pDIMI	Protonated desnitro-imidacloprid
pIMI	Protonated imidacloprid
pIMI-NO	Protonoated desnitroso-imidacloprid
pIMIU	Protonated imidacloprid urea
pDTMX	Protonated desnitro-thiamethoxam
pDTMX-Cl	Protonated dechlorinated desnitro-thiamethoxam
pTMX	Protonated thiamethoxam
PMRA	Health Canada's Pest Management Regulatory Agency
QIT	Quadrupole ion trap
RF	Radio frequency
RHF	Relativistic Hartree-Fock
SORI-CID	Sustained off-resonance irradiation collision-induced dissociation
SID	Surface-induced dissociation

STO	Slater-type orbital
TMX	Thiamethoxam
TMX-dm	Desmethyl derivative of thiamethoxam
TMX-NH	Desnitroguanidine
TMX-NNH_2	Aminoguanidine
TMX-NNO	Nitrosoguanidine
TMX-Urea	Urea derivative of thiamethoxam
UPLC-MS/MS	Ultra-performance liquid chromatography-tandem mass spectrometry
UVPD	Ultraviolet photodissociation
VAC	Vacuum

LIST OF APPENDICES

Chapter 1 – Introduction

1.1 A Brief History of Neonicotinoid Insecticides

Currently, there are seven neonicotinoids commercially available on the global market. Since the introduction of the first neonicotinoid insecticide, imidacloprid, neonicotinoids have become the fastest growing class of chemical insecticides. Neonicotinoids are categorized based on their molecular features and divided into sub-classes: *N*-nitroguanidines (imidacloprid, thiamethoxam, clothianidin, and dinotefuran), nitromethylenes (nitenpyram), and *N*-cyanoamidines (acetamiprid and thiacloprid).[1,2] The chemical structures of the identified neonicotinoids are depicted in Figure 1.1.

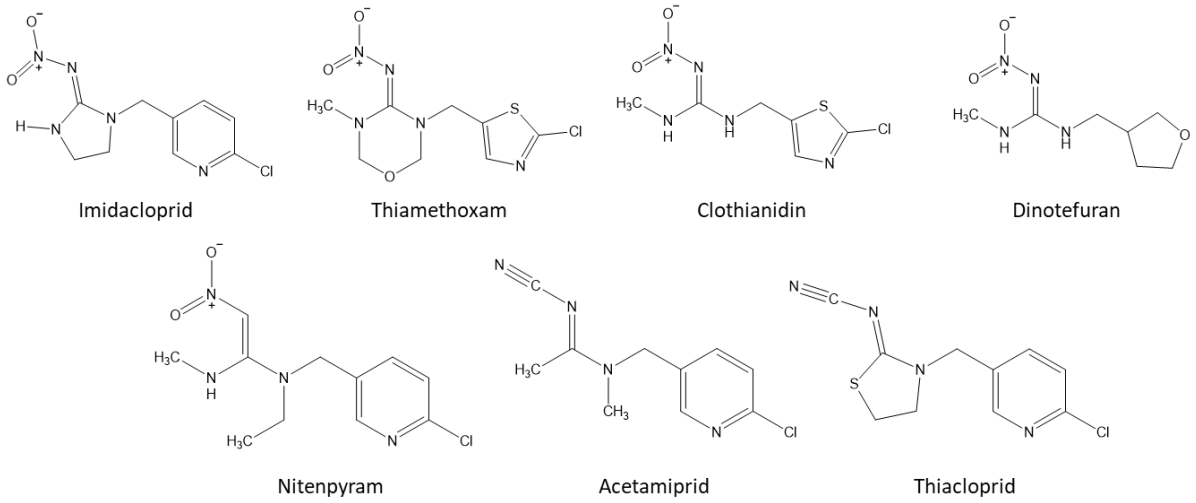

Figure 1.1. Chemical structures of the neonicotinoid insecticides.

Nicotinic acetylcholine receptors (nAChRs) are major excitatory neurotransmitter receptors found in vertebrates and invertebrates that play a key role in neuronal signal transduction.[3–6] nAChRs are molecular targets for compounds that exhibit toxic effects in

insect pests.[3–5] Potent agonists of insect nAChRs disrupt neurotransmission causing abnormal behaviour, immobility, and death of target insect organisms.[6,7] Nithiazine, a nitromethylene heterocyclic compound developed by Shell in the 1970s, demonstrated moderate insecticidal activity and was found to be active on insect nAChRs. Nithiazine was never used as a commercialized product due to the poor photostability but was used in the synthesis of the first neonicotinoid.[3,8–11] Substitution of the nitroguanidine group, in place of the nitromethylene group and addition of the chloropyridine ring, resulted in the development of imidacloprid. Imidacloprid was introduced to the agrochemical market in 1991 by Bayer CropScience, and since the discovery of imidacloprid several other neonicotinoids have been commercialized. Nitenpyram was launched in 1995 by Sumitomo Chemical Takedo Agro Company, acetamiprid in 1996 by Nippon Soda, thiamethoxam in 1998 by Syngenta, thiacloprid in 2000 by Bayer CropScience, clothianidin in 2002 by Takedo and Bayer, and dinotefuran in 2002 by Mitsui Chemicals.[2,3,11,12]

Neonicotinoids show good activity against pests that are resistant to other classes of insecticides such as organophosphates, carbamates, pyrethroids, and chlorinated hydrocarbons.[13–16] Neonicotinoids were developed to replace synthetic organic insecticides in an attempt to integrate a higher specificity for insect pests and to lower vertebrate toxic effects that impair cognitive functions, behaviour, and physiological functions.[16]

1.2 Motivation for Studying Neonicotinoid Insecticides

A computational study describing the structural and electronic properties of imidacloprid was conducted by Moreira *et al.*[17] to gain information about the charge distribution and the binding interaction of imidacloprid with nAChRs. Hirschfeld Population Analysis and Natural Population Analysis were performed on imidacloprid structural conformers to predict the electronic charges. The electronic charge distribution examination revealed a pronounced negative charge in the nitroguanidine moiety due to the electronegative oxygen atoms in the nitro group as well as the negatively charged imine nitrogen. The delocalized negative charge that is present in the tip of the molecule enhances the interaction between imidacloprid and the positively charged amino acid residues on the active sites of nAChRs. In addition, the electronegative nitrogen in the chloropyridine ring facilitates the binding interaction by acting as a hydrogen bond acceptor.[17] Investigation of the electronic parameters of imidacloprid has proven to be useful in understanding the mechanism of molecular recognition of imidacloprid and its receptors.

Neonicotinoids act as agonists at the nAChRs of insects. The selective toxicity of neonicotinoids toward insects over mammals is due to the stronger binding specificity of target sites in insects.[18–22] Neonicotinoid insecticides are neurotoxins that can cause receptor blockage, paralysis, and death in target organisms.[23] The systemic uptake of these insecticides in plants makes them effective against a broad spectrum of insect pests.[24,25] The widespread use and persistence of neonicotinoids in soil and water environments can have biological and ecological implications on non-target terrestrial and aquatic invertebrates.[26,27] When honeybees (*Apis mellifera*) and bumblebees (*Bombus*

terrestris) are exposed to environmental concentrations of neonicotinoids, these pesticides present adverse effects such as impairing the following: bee flight ability, foraging activity, long-term memory formation, olfactory learning, and immune system response thus increasing susceptibility to diseases.[28–33] Honeybees are essential for the pollination of agricultural crops and wilds plants; therefore, bee pollinators are important for food security and the maintenance of biodiversity.[6,33]

Neonicotinoids possessing the nitroguanidine moiety induce higher acute and chronic toxicity in bees (Acute contact toxicity LD_{50}: imidacloprid 0.081 µg/bee, thiamethoxam 0.024 µg/bee. Acute oral toxicity LD_{50}: imidacloprid 0.0037 µg/bee, thiamethoxam 0.005 µg/bee. Chronic oral toxicity LD_{50}: imidacloprid >0.00282 µg/bee).[34–36] Consequently, the European Food Safety Authority (EFSA) implemented a moratorium on the use of neonicotinoids in flowering crops in 2013 to further assess the implications of clothianidin, imidacloprid, and thiamethoxam on non-target organisms, specifically, honeybees and bumblebees.[37] Similarly, Health Canada's Pest Management Regulatory Agency (PMRA) conducted a pollinator risk assessment to re-evaluate imidacloprid and its associated products. Risk mitigation measures have been put in place to reduce pollinator exposure and to monitor the effects on honeybee and bumble bee colonies, as well as solitary bee species.[38] These mitigation measures include, but are not limited to, the removal of certain pesticides containing imidacloprid and restrictions on application times for crops that are attractive to bees.

The lethal and sublethal effects on pollinator species caused by exposure to field realistic doses of neonicotinoids has prompted the development of analytical methods for the determination of neonicotinoids and their metabolites in agricultural products

(cucumbers, spinach, apple, pomelo, chestnut, shallot, ginger, tea, cabbage, potato, rice, tomato, lettuce, pepper, etc.),[39–44] bee products (honeybees, honey, pollen, beeswax),[14,45–49] and in the environment (soil, water)[39,50–53]. The detection and quantification of neonicotinoid insecticide residues in biological matrices is accomplished using liquid chromatography coupled with mass spectrometry; these mass spectrometric techniques include LC-MS, LC-MS/MS, and UPLC-MS/MS. Studying the structures, energetics, and reactions of gas phase ions will allow us to better understand the ion-molecule chemistry of these insecticides in a mass spectrometer. Research on the physical chemistry of gas phase protonated neonicotinoid complexes studied by tandem mass spectrometry will help environmental chemists to improve analytical techniques that are used to detect and identify neonicotinoids currently in use. Structural information obtained from gas phase studies will aid in the development of alternative pest management methods; replacing former neonicotinoids with chemical insecticides that display greater efficacy for controlling target pests.

1.3 Vibrational and Computational Studies of Imidacloprid

Theoretical infrared and Raman spectra generated from quantum chemistry calculations were used to identify vibrational signatures of imidacloprid in vacuum and solvated models. The spectral features were assigned using the global minimum energy conformers obtained using the M06-2X and B3LYP exchange-correlation functionals with the basis set 6-311++G(d,p).[54] For the purpose of this summary only the vibrational modes identified by infrared (IR) spectroscopy are discussed here. The IR spectrum for imidacloprid in the 1200-2000 cm^{-1} region and the minimum energy conformers obtained

from the geometry optimizations are portrayed in Figure 1.2. In the experimental IR spectrum of imidacloprid, the absorption bands observed at 1585, 1570, and 1551 cm^{-1} correspond to C-H in plane bending, N-C-N and N-C(=N)-N stretching in the imidazolidine ring, and N-O and O-N-O stretching in the nitro moiety. The vibrational modes observed at 1456 and 1447 cm^{-1} can be attributed to C=C stretching and CH_2 bending, respectively. The IR bands at 1295 and 1279 cm^{-1} are due to C-N-H and CH_2 bending and C-C-N stretching in the imidazolidine ring, as well as N-O stretching in the nitro group. The absorption band at 1233 cm^{-1} in the IR spectrum corresponds to N-N-O and C=N-N stretching in the nitroguanidine group, N-C=N and C-N-C stretching in the imidazolidine ring, and C-C-N stretching in the methylene bridge.[54] Moreira *et al.*[54] used M06-2X and B3LYP functionals to calculate IR spectra in the solution phase using the polarization continuum model (PCM) and in vacuum (VAC). The computational results predicted the structural features and vibrational frequencies of imidacloprid. The B3LYP functional was found to outperform the M06-2X functional in identifying experimental absorption bands, producing the smallest deviation when comparing theoretical frequencies to experimental values. In the current thesis, structural characteristics of protonated imidacloprid were determined using IRMPD spectroscopy, and experimental absorption bands were assigned based on the computed vibrational frequencies obtained from DFT calculations.

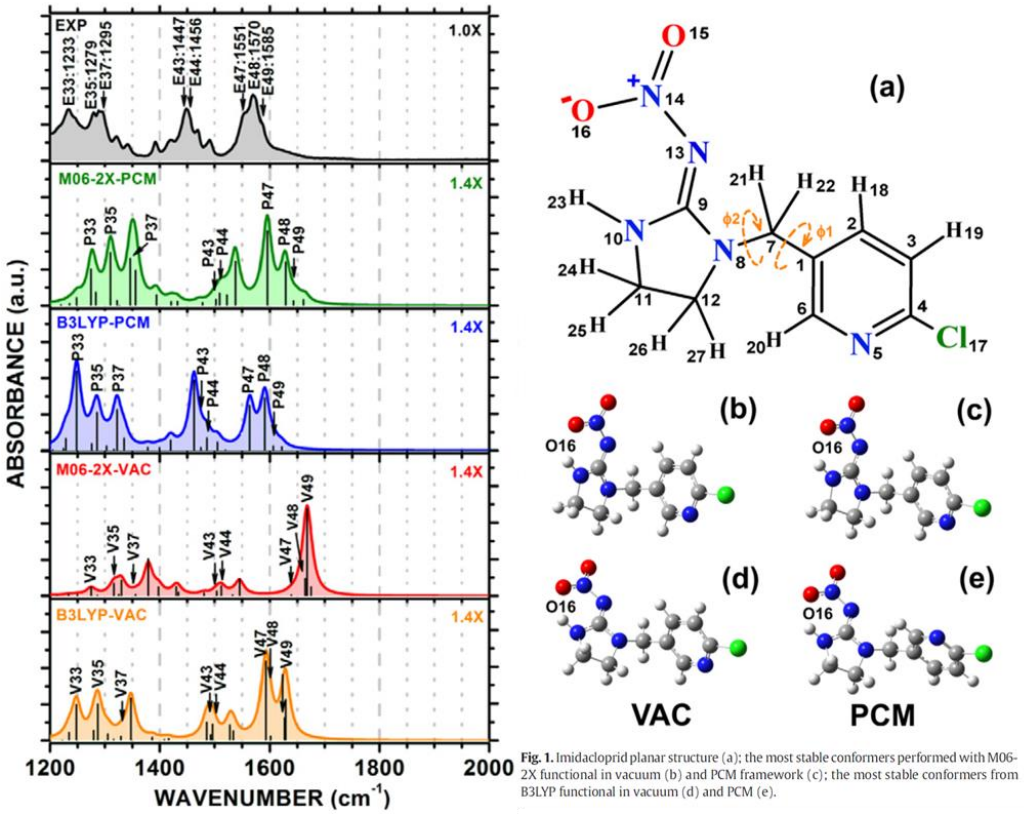

Fig. 1. Imidacloprid planar structure (a); the most stable conformers performed with M06-2X functional in vacuum (b) and PCM framework (c); the most stable conformers from B3LYP functional in vacuum (d) and PCM (e).

Figure 1.2. The IR spectrum for imidacloprid in the region of 1200 to 2000 cm^{-1}; the experimental results are depicted in the top of the figure followed by the theoretical results computed using the M06-2X and B3LYP functionals. Figure adapted from reference 54 with permission.

Gas phase imidacloprid structures and reactivities have been studied in the protonated form. The proton affinities of imidacloprid were calculated using density functional theory (DFT) at the B3LYP/6-311++G(d,p) level of theory.[55] The calculated proton affinities for each possible protonation site of imidacloprid, desnitroimidacloprid, and desnitrosoimidacloprid are presented in Figure 1.3. It has been determined by Donald *et al.*[55] that the most favourable site of protonation is the pyridine nitrogen of the chloropyridine ring. The next lowest energy site of protonation is the imine nitrogen of the nitroguanidine group which is calculated to be 24.2 kJ mol^{-1} higher in energy than the

pyridine basic site. Furthermore, when protonated imidacloprid loses a fragment of $NO_2^{\bullet}$, the imine nitrogen of the guanidine group is computed to be the lowest energy site of protonation and is calculated to be 32.7 kJ mol^{-1} lower in energy than the pyridine nitrogen. Similarly, when protonated imidacloprid loses $NO^{\bullet}$, the imine nitrogen of the group is computed to be the lowest energy site of protonation and is calculated to be 20.7 kJ mol^{-1} lower in energy than the pyridine nitrogen.[55] Vibrational spectroscopy experiments are needed to confirm if the fragmentation of the nitroguanidine group results in a proton transfer between the pyridine nitrogen and the imine nitrogen or if the dissociation of $NO_2^{\bullet}$ and $NO^{\bullet}$ causes the proton to be maintained at the pyridine nitrogen basic site. Moreover, it is important to know whether the IRMPD absorption bands of desnitroimidacloprid and desnitrosoimidacloprid are more consistent with the calculated IR bands of the protonated pyridine nitrogen product ions or the protonated imine nitrogen product ions.

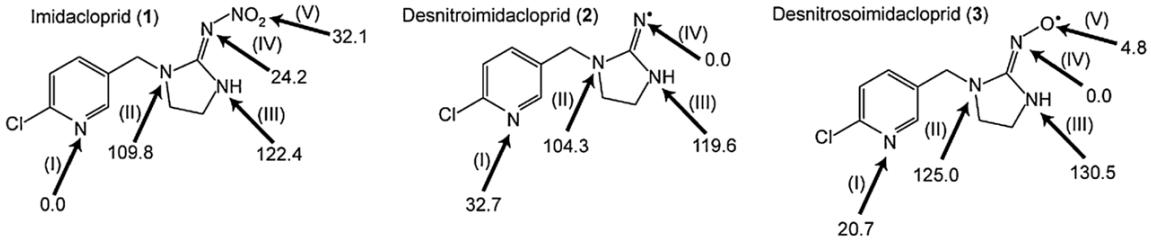

Figure 1.3. Calculated proton affinities (in kJ mol^{-1}) for each basic site of (1) imidacloprid, (2) desnitroimidacloprid, and (3) desnitrosoimidacloprid. Figure adapted from reference 55 with permission.

Tandem mass spectrometry experiments and DFT calculations were conducted by Fusetto *et al.*[56] to compare the structures and dissociation of olefin-imidacloprid to imidacloprid. Isomeric structures of the olefin metabolite were explored by placing the

proton on all heteroatoms (N and O) and computing the relative proton affinities for each protonation site. The B3LYP/6-311G++(d,p) calculated proton affinities and the optimized geometries of protonated olefin-imidacloprid are shown in Figure 1.4. Protonation at the N5 pyridine nitrogen ($\mathbf{2H_a^+}$) was found to be the thermodynamically favoured site of protonation. The succeeding favoured sites of protonation are the O2 oxygen atom of the nitro group ($\mathbf{2H_b^+}$), the N2 imine nitrogen of the nitroguanidine group ($\mathbf{2H_c^+}$), the O1 oxygen atom of the nitro group ($\mathbf{2H_d^+}$), and the N1 nitrogen of the imidazole ring ($\mathbf{2H_e^+}$). The results of the DFT calculations reveal that the ionizing proton is positioned on N5 in both imidacloprid[55] and olefin-imidacloprid[56]. Moreover, the O2 position shows a significant difference in proton affinities, where the relative proton affinity obtained for imidacloprid is 32.1 kJ mol^{-1} and for olefin-imidacloprid is 9 kJ mol^{-1}. The greatest difference in proton affinities is attained from the proton residing on the N1 position, the relative proton affinities were computed to be 122.4 kJ mol^{-1} for imidacloprid and 193 kJ mol^{-1} for olefin-imidacloprid.[55,56] X-ray crystallographic analysis of imidacloprid and olefin-imidacloprid showed that extensive delocalization of the electron density in the nitroguanidine moiety led to the structure adopting two resonance forms, A1 and A2. The resonance forms deriving from tautomer A are displayed in Figure 1.5. The structural parameters obtained from the Cambridge Crystallographic Data Centre (CCDC) suggest that there is a greater contribution by resonance form A2 for olefin-imidacloprid based on the N-N and C-N bond distances, and that resonance form A1 predominates in imidacloprid. Resonance form A2 explains why O2 is more basic and N1 is less basic for olefin-imidacloprid in comparison to imidacloprid.[56]

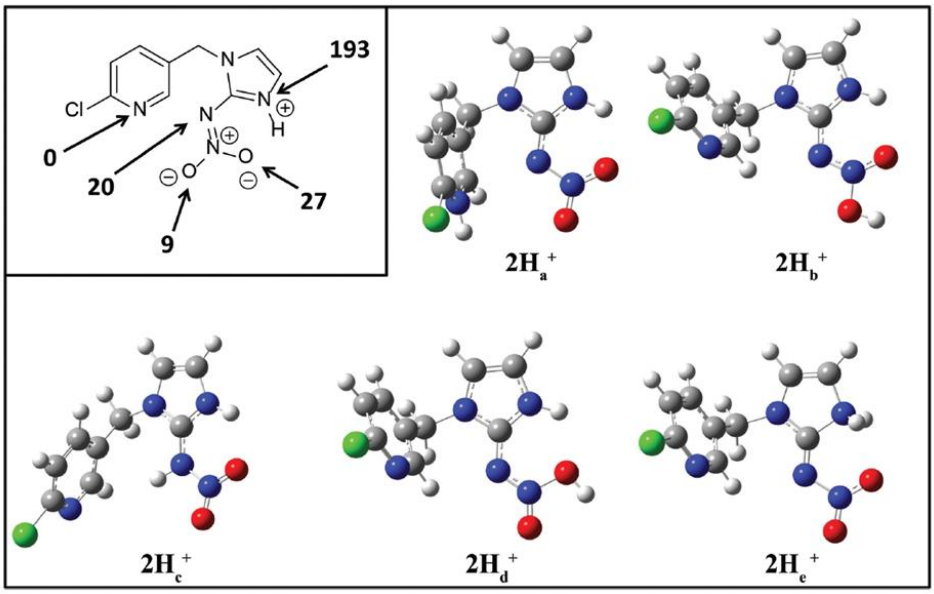

Figure 1.4. Optimized geometries of the various protonation sites of olefin-imidacloprid. The DFT calculated proton affinities (in kJ mol^{-1}) are relative to the most favourable site of protonation **2H$_a^+$** and are designated as **2H$_b^+$**, **2H$_c^+$**, **2H$_d^+$**, and **2H$_e^+$**. Figure reproduced from reference 56 with permission.

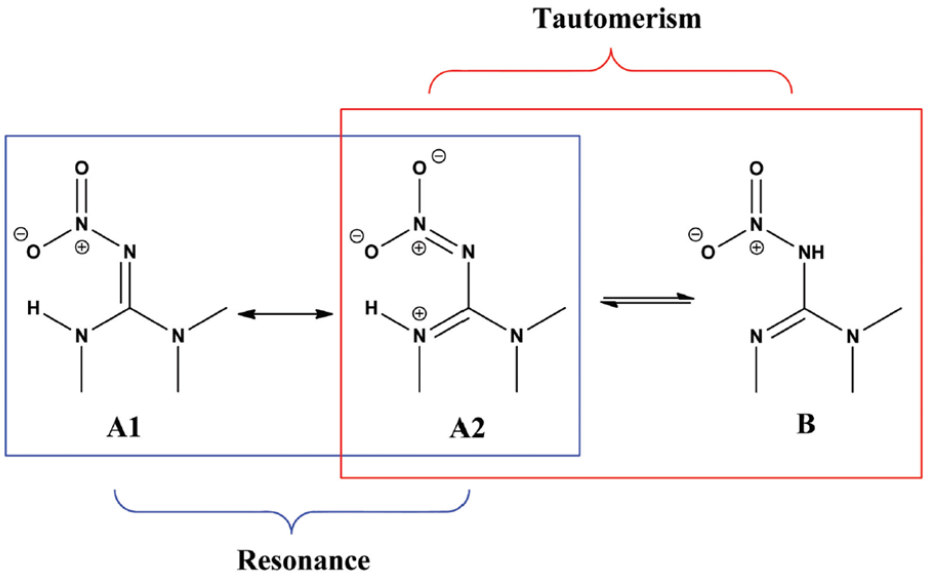

Figure 1.5. Structures containing a nitroguanidine group can exist as two tautomers. Tautomer A can be represented by two resonance forms, A1 and A2. Figure adapted from reference 56 with permission.

Theoretical calculations are often used to support and complement experimental results, hence furthering our knowledge about the structures and thermochemical properties of molecules. Previous studies investigating the ionization reactions of protonated nitroimidazoles have been conducted to show that the position of the proton has a role in determining the unimolecular chemistry of 2-nitroimidazole, 4-nitroimidazole, and 5-nitroimidazole.[57,58] The proton affinities of all possible protonation sites were assessed by DFT calculations, employing B3LYP/6-31++G(d,p)[57] and M06-2X/6-311+G(d,p)[58] levels of theory. The results of the proton affinity calculations indicate that protonation on the nitrogen of the imidazole ring is favoured in contrast to the oxygens of the nitro group, thus providing insight into the chemical reactivity.[57,58] In another study, electronic energies, zero-point energies, and proton affinities for alkyl- and nitro- substituted imidazoles were computed using B3LYP and MP2 methods.[59] This study showed that the electron-donating alkyl groups increase the basicity of the imidazole ring; therefore, the proton affinity increases as the chain length of the alkyl group increases. The electron-withdrawing nitro groups, on the other hand, decrease the basicity of the imidazole, resulting in increased charge delocalization and decreased proton affinity.[59]

Computational chemistry has been used to determine the preferential sites of protonation on structurally related compounds of imidacloprid, specifically heteroaromatic molecules.[60–62] In a computational study, the calculated proton affinities of 23 five-membered heteroaromatic molecules were obtained from the total energies computed using the Gaussian-3 (G3) composite method and geometry optimizations performed using the MP2 method.[60] The G3 proton affinities reveal that the primary site

of protonation is the carbon atom adjacent to the heteroatom in molecules with a single nitrogen, oxygen, or sulfur atom (furans, pyrroles, and thiophenes). Furthermore, the G3 proton affinity results show that protonation on the pyridine-type nitrogen occurs in heteroaromatics that consist of more than one heteroatom (oxazoles, thiazoles, diazoles, triazoles, pyrazoles, and imidazoles). The calculated proton affinities of the most basic sites are in excellent agreement with the experimental values reported in the literature.[60] In a similar study, the proton affinities of 24 heterocyclic amines were calculated using the B3LYP/6-31G(d) and B3LYP/6-31++G(d,p) levels of theory, as well as the G3B3 method, a variant of G3 theory in which structures are optimized and zero point vibrational energies are calculated using the B3LYP functional.[61] The computational results demonstrate that the proton tends to interact with the electron lone pair on the ring nitrogen. The theoretical proton affinities obtained from B3LYP/6-31++G(d,p) and G3B3 calculations were in exceptionally good agreement with the experimental values obtained from Hunter and Lias.[61]

IRMPD spectroscopy in combination with electronic structure calculations can be used as a powerful tool to probe structural characteristics and thermochemical properties of protonated imidacloprid and its decomposition products.

1.4 Vibrational and Computational Study of Thiamethoxam

Thiamethoxam was characterized by FT-IR, FT-Raman, and UV-vis spectra to provide insights on the vibrational and electronic properties of thiamethoxam.[63] The vibrational and electronic absorption spectra for thiamethoxam are shown in Figure 1.6. Harmonic frequencies and geometry optimizations were computed using DFT methods; B3LYP,

CAMB3LYP, M06, and PBE1PBE, and relativistic Hartree-Fock (RHF) methods with the basis set 6-311++G(d,p). Spectral features were assigned based on the comparison between the experimental and computational results. In the chlorothiazole ring, the IR band observed at 1413 cm^{-1} corresponds to C=N stretching coupled with C=C and C-Cl stretching. The absorption band observed at 1111 cm^{-1} is attributed to the C-H bending mode coupled with the C-N stretching mode. Furthermore, the vibrations observed at 693 and 631 cm^{-1} correspond to C-S stretching modes in the IR experimental spectra. In the nitroimino-oxadiazinane ring, the vibrational modes observed at 1520 and 1527 cm^{-1} correspond to C-N stretching, C-N-H bending, and CH_2 bending. The N-O stretching modes of the nitro group are observed at 1520 cm^{-1} in the IR spectrum. The C-O-H bending modes are observed at 1433 cm^{-1} coupled with H-C-N-C wagging out-of-plane vibrational modes. C-H bending modes are observed at 1389, 1326, 1269, and 1177 cm^{-1} in the IR spectrum. Moreover, the IR band at 902 cm^{-1} is assigned predominantly to C-O stretching as well as C-N stretching in the oxadiazinane ring, and N-N stretching in the nitroguanidine group. The RHF and DFT methods were found to overestimate the vibrational frequencies in comparison with the experimental frequencies; however, the best results are obtained using the B3LYP functional with the smallest margin of error.[63] In the current thesis, the B3LYP and M06-2X functionals were employed for structural optimization and calculating the harmonic vibrational frequencies of protonated thiamethoxam, as well as computing the IR spectra to compare with the IRMPD spectroscopic data.

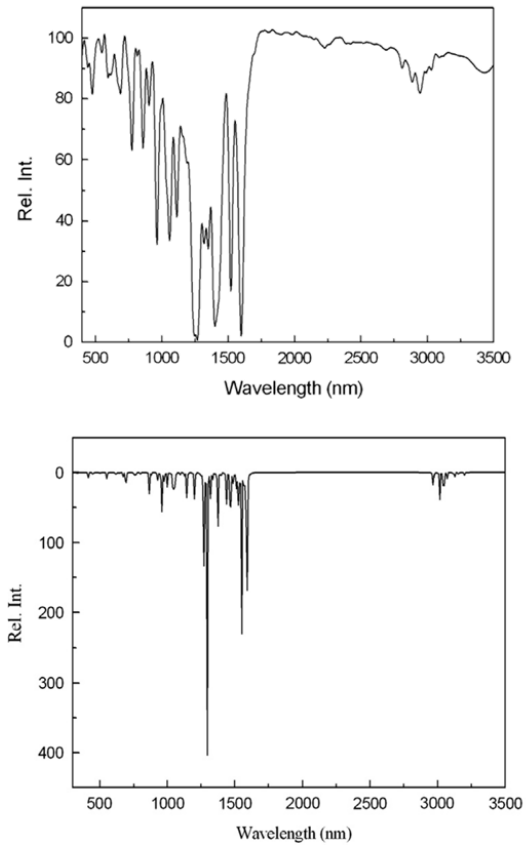

Figure 1.6. The experimental and calculated IR spectra for thiamethoxam. Figure adapted from reference 63 with permission.

1.5 Fragmentation Chemistry of Protonated Neonicotinoid Complexes

The fragmentation pathways of neonicotinoid insecticides undergoing collision-induced dissociation (CID) have been reported in previous work. IRMPD activation (photon-mediated) produces fragmentation patterns that are similar to CID activation (collision-mediated) where dissociations occur through the lowest energy pathways for both ion activation techniques.[64,65] The current work examines the IRMPD mass spectra of protonated neonicotinoid complexes to determine if the IRMPD fragments observed complement the CID fragments described in the literature. The fragmentation pathway

proposed by Xiao *et al.*[66] is shown in Figure 1.7, portraying tentative structures for the main fragment ions of seven neonicotinoids. The unimolecular chemistry of the nitroguanidine sub-class of insecticides is initiated by fragmentation of the nitroimine functional group. The CID reaction of protonated imidacloprid (*m/z* 256) mainly involves the concurrent loss of $H^{\bullet}$ and $NO_2^{\bullet}$ (*m/z* 209) and the simultaneous loss of $NO_2^{\bullet}$ and $Cl^{\bullet}$ (*m/z* 175).[43–45,66] The decomposition of imidacloprid by ozonation gives rise to the dissociation products mentioned above, and the loss of N_2O (*m/z* 212) and loss of $NO^{\bullet}$ (*m/z* 226).[67] The loss of $NO_2^{\bullet}$ and $Cl^{\bullet}$ (*m/z* 211) is reported for the decomposition reaction of protonated thiamethoxam (*m/z* 292). Likewise, the primary dissociation pathway for protonated clothianidin (*m/z* 250) proceeds via the loss of $NO_2^{\bullet}$ and $Cl^{\bullet}$ (*m/z* 169).[43–45,66] The fragmentation mechanisms for protonated thiamethoxam and protonated clothianidin present conflicting chemical structures for the product ion at *m/z* 132. The chemical structure for the decomposition product of thiamethoxam is proposed to be either dimethyl-nitroguanidine[44] or chloro-methyl-thiazole[45,66]. Similarly, the chemical structure for the decomposition product of clothianidin is depicted as chloro-methyl-thiazole[43,66] or dimethyl-nitroguanidine[44,45]. CID of protonated dinotefuran (*m/z* 203) results in the loss of $NO_2^{\bullet}$ (*m/z* 157),[44,45] and the simultaneous loss of CH_2 and NNO_2 (*m/z* 129).[43–45,66] Tandem mass spectrometry studies were undertaken to analyze pesticide residues and propose fragmentation structures for the product ions observed in the mass spectra of neonicotinoids. The fragmentation mechanisms reported in the literature for imidacloprid and thiamethoxam will be discussed further in Chapters 3 and 4, respectively.

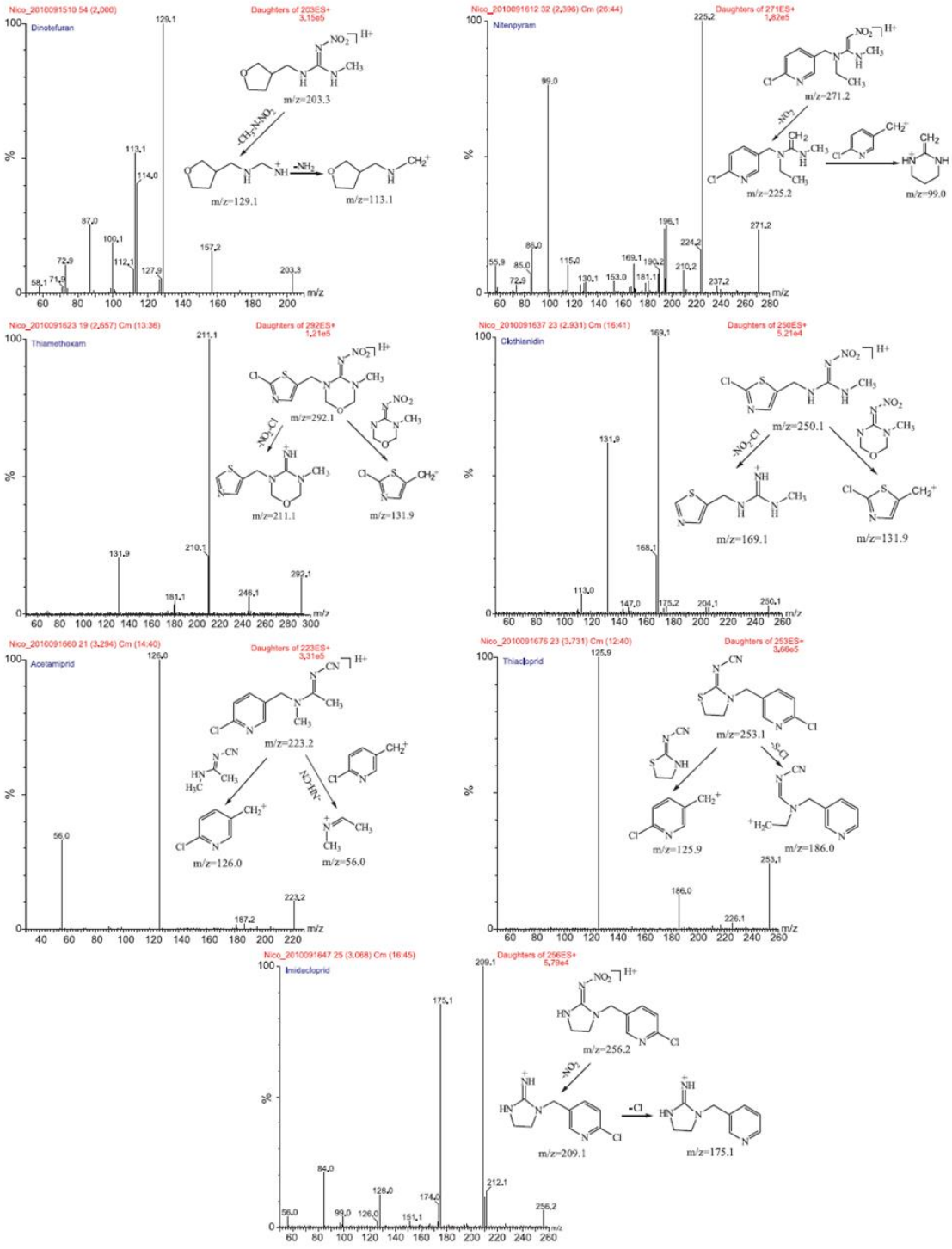

Figure 1.7. Proposed fragmentation pattern and MS/MS product scan spectra of seven neonicotinoids. Figure reproduced from reference 66 with permission.

The dissociation of the nitromethylene sub-class of insecticides is initiated by the fragmentation of the nitromethylene group. The CID reaction of protonated nitenpyram (*m/z* 271) primarily proceeds via the loss of $NO_2^{\bullet}$ (*m/z* 225).[44,45,66,68] Fragment ions observed at *m/z* 189, and *m/z* 99 are related to the losses of $H^{\bullet}$ and $Cl^{\bullet}$,[44] and chloromethylpyridinyl,[45,66,68] respectively. A competing fragmentation pathway involves the consecutive losses of $^{\bullet}OH$ (*m/z* 254 and *m/z* 237).[68] The unimolecular fragmentation of the cyanoamidine sub-class of neonicotinoids is not initiated by cleavage of the cyanoimine functional group. The dissociation products of protonated acetamiprid (*m/z* 223) are observed at *m/z* 126 corresponding to chloro-methyl-pyridine,[43,45,66] and *m/z* 56 corresponding to methyl-ethanimine.[43–45,66] In addition, the dissociation products of protonated thiacloprid (*m/z* 253) are observed at *m/z* 186 ascribed to the loss of S and $Cl^{\bullet}$,[44,45,66] and *m/z* 126 attributed to chloro-methyl-pyridine.[43,45,66]

1.6 Contents of this Thesis

In Chapter 2 of this thesis, structural characterization achieved using Infrared Multiphoton Dissociation (IRMPD) spectroscopy in combination with ion trapping mass spectrometry, specifically Quadrupole Ion Traps (QIT) and Fourier-Transform Ion Cyclotron Resonance (FT-ICR) mass spectrometers, are discussed in detail. Electronic structure calculations performed using density functional theory with different basis sets will also be described. Chapter 3 examines the tautomerization and fragmentation pathway of protonated imidacloprid. The structures of protonated imidacloprid and its fragment ions are investigated using IRMPD spectroscopy in the 500-1900 cm^{-1} region. Geometry optimization and harmonic frequency calculations are performed to obtain

relative enthalpies ($\Delta_{rel}H$) and Gibbs energies ($\Delta_{rel}G$). Chapter 4 provides structural insight into protonated thiamethoxam and its fragment ions using the same experimental and computational methods. In Chapters 3 and 4, the experimental IRMPD spectra and the computed IR spectra are compared to determine the most probable structures and assign the vibrational signatures of these complexes.

1.7 References

1. Jeschke, P.; Nauen, R. Neonicotinoids – from Zero to Hero in Insecticide Chemistry. *Pest Manag. Sci.* **2008**, *64* (11), 1084–1098.
2. Jeschke, P.; Nauen, R.; Schindler, M.; Elbert, A. Overview of the Status and Global Strategy for Neonicotinoids. *J. Agric. Food Chem.* **2011**, *59* (7), 2897–2908.
3. Millar, N. S.; Denholm, I. Nicotinic Acetylcholine Receptors: Targets for Commercially Important Insecticides. *Invertebr. Neurosci.* **2007**, *7* (1), 53–66.
4. Thany, S. H.; Lenaers, G.; Raymond-Delpech, V.; Sattelle, D. B.; Lapied, B. Exploring the Pharmacological Properties of Insect Nicotinic Acetylcholine Receptors. *Trends Pharmacol. Sci.* **2007**, *28* (1), 14–22.
5. Taillebois, E.; Cartereau, A.; Jones, A. K.; Thany, S. H. Neonicotinoid Insecticides Mode of Action on Insect Nicotinic Acetylcholine Receptors Using Binding Studies. *Pestic. Biochem. Physiol.* **2018**, *151* (April), 59–66.
6. Brandt, A.; Gorenflo, A.; Siede, R.; Meixner, M.; Büchler, R. The Neonicotinoids Thiacloprid, Imidacloprid, and Clothianidin Affect the Immunocompetence of Honey Bees (Apis Mellifera L.). *J. Insect Physiol.* **2016**, *86*, 40–47.
7. Fossen, M. Environmental Fate of Imidacloprid. *Regulation* **2006**, 1–16.

8. Casida, J. E. Neonicotinoids and Other Insect Nicotinic Receptor Competitive Modulators: Progress and Prospects. *Annu. Rev. Entomol.* **2018**, *63* (1), 125–144.
9. Matsuda, K.; Ihara, M.; Sattelle, D. B. Neonicotinoid Insecticides: Molecular Targets, Resistance, and Toxicity. *Annu. Rev. Pharmacol. Toxicol.* **2020**, *60* (1), 241–255.
10. Ihara, M.; Buckingham, S. D.; Matsuda, K.; Sattelle, D. B. Modes of Action, Resistance and Toxicity of Insecticides Targeting Nicotinic Acetylcholine Receptors. *Curr. Med. Chem.* **2017**, *24* (27), 1–8.
11. Maienfisch, P.; Angst, M.; Brandl, F.; Fischer, W.; Hofer, D.; Kayser, H.; Kobel, W.; Rindlisbacher, A.; Senn, R.; Steinemann, A.; et al. Chemistry and Biology of Thiamethoxam: A Second Generation Neonicotinoid. *Pest Manag. Sci.* **2001**, *57* (10), 906–913.
12. Bass, C.; Denholm, I.; Williamson, M. S.; Nauen, R. The Global Status of Insect Resistance to Neonicotinoid Insecticides. *Pestic. Biochem. Physiol.* **2015**, *121*, 78–87.
13. Seccia, S.; Fidente, P.; Barbini, D. A.; Morrica, P. Multiresidue Determination of Nicotinoid Insecticide Residues in Drinking Water by Liquid Chromatography with Electrospray Ionization Mass Spectrometry. *Anal. Chim. Acta* **2005**, *553* (1–2), 21–26.
14. Kamel, A. Refined Methodology for the Determination of Neonicotinoid Pesticides and Their Metabolites in Honey Bees and Bee Products by Liquid Chromatography-Tandem Mass Spectrometry (LC-MS/MS). *J. Agric. Food Chem.* **2010**, *58* (10), 5926–5931.

15. Tomizawa, M.; Casida, J. E. Selective Toxicity of Neonicotinoids Attributable To Specificity of Insect and Mammalian Nicotinic Receptors. *Annu. Rev. Entomol.* **2003**, *48* (1), 339–364.
16. Le Goff, G.; Giraudo, M. Effects of Pesticides on the Environment and Insecticide Resistance. In *Olfactory Concepts of Insect Control - Alternative to insecticides*; Picimbon, J.-F., Ed.; Springer Nature Switzerland AG, 2019; pp 51–78.
17. Moreira, A. A. G.; De Lima-Neto, P.; Caetano, E. W. S.; Barroso-Neto, I. L.; Freire, V. N. Computational Electronic Structure of the Bee Killer Insecticide Imidacloprid. *New J. Chem.* **2016**, *40* (12), 10353–10362.
18. Elbert, A.; Haas, M.; Springer, B.; Thielert, W.; Nauen, R. Applied Aspects of Neonicotinoid Uses in Crop Protection. *Pest Manag. Sci.* **2008**, *64* (11), 1099–1105.
19. Matsuda, K.; Buckingham, S. D.; Kleier, D.; Rauh, J. J.; Grauso, M.; Sattelle, D. B. Neonicotinoids: Insecticides Acting on Insect Nicotinic Acetylcholine Receptors. *Trends Pharmacol. Sci.* **2001**, *22* (11), 573–580.
20. Tomizawa, M.; Casida, J. E. NEONICOTINOID INSECTICIDE TOXICOLOGY: Mechanisms of Selective Action. *Annu. Rev. Pharmacol. Toxicol.* **2005**, *45* (1), 247–268.
21. Tomizawa, M.; Casida, J. E. Molecular Recognition of Neonicotinoid Insecticides: The Determinants of Life or Death. *Acc. Chem. Res.* **2009**, *42* (2), 260–269.
22. Tomizawa, M.; Casida, J. E. Unique Neonicotinoid Binding Conformations Conferring Selective Receptor Interactions. *J. Agric. Food Chem.* **2011**, *59* (7), 2825–2828.

23. Goulson, D. An Overview of the Environmental Risks Posed by Neonicotinoid Insecticides. *J. Appl. Ecol.* **2013**, *50* (4), 977–987.
24. Simon-Delso, N.; Amaral-Rogers, V.; Belzunces, L. P.; Bonmatin, J. M.; Chagnon, M.; Downs, C.; Furlan, L.; Gibbons, D. W.; Giorio, C.; Girolami, V.; et al. Systemic Insecticides (Neonicotinoids and Fipronil): Trends, Uses, Mode of Action and Metabolites. *Environ. Sci. Pollut. Res.* **2015**, *22* (1), 5–34.
25. Decourtye, A.; Devillers, J. Ecotoxicity of Neonicotinoid Insecticides to Bees. In *Insect Nicotinic Acetylcholine Receptors*; Thany, S. H., Ed.; Landes Bioscience and Springer Science+Business Media, 2010; Vol. 683, pp 85–95.
26. Pisa, L. W.; Amaral-Rogers, V.; Belzunces, L. P.; Bonmatin, J. M.; Downs, C. A.; Goulson, D.; Kreutzweiser, D. P.; Krupke, C.; Liess, M.; Mcfield, M.; et al. Effects of Neonicotinoids and Fipronil on Non-Target Invertebrates. *Environ. Sci. Pollut. Res.* **2014**, *22* (1), 68–102.
27. Morrissey, C. A.; Mineau, P.; Devries, J. H.; Sanchez-Bayo, F.; Liess, M.; Cavallaro, M. C.; Liber, K. Neonicotinoid Contamination of Global Surface Waters and Associated Risk to Aquatic Invertebrates: A Review. *Environ. Int.* **2015**, *74*, 291–303.
28. Christen, V.; Mittner, F.; Fent, K. Molecular Effects of Neonicotinoids in Honey Bees (Apis Mellifera). *Environ. Sci. Technol.* **2016**, *50* (7), 4071–4081.
29. Li, Z.; Yu, T.; Chen, Y.; Heerman, M.; He, J.; Huang, J.; Nie, H.; Su, S. Brain Transcriptome of Honey Bees (Apis Mellifera) Exhibiting Impaired Olfactory Learning Induced by a Sublethal Dose of Imidacloprid. *Pestic. Biochem. Physiol.* **2019**, *156* (February), 36–43.

30. Schneider, C. W.; Tautz, J.; Grünewald, B.; Fuchs, S. RFID Tracking of Sublethal Effects of Two Neonicotinoid Insecticides on the Foraging Behavior of Apis Mellifera. *PLoS One* **2012**, *7* (1), 1–10.
31. Van der Sluijs, J. P.; Simon-Delso, N.; Goulson, D.; Maxim, L.; Bonmatin, J. M.; Belzunces, L. P. Neonicotinoids, Bee Disorders and the Sustainability of Pollinator Services. *Curr. Opin. Environ. Sustain.* **2013**, *5* (3–4), 293–305.
32. Belzunces, L. P.; Tchamitchian, S.; Brunet, J. L. Neural Effects of Insecticides in the Honey Bee. *Apidologie* **2012**, *43* (3), 348–370.
33. Tosi, S.; Burgio, G.; Nieh, J. C. A Common Neonicotinoid Pesticide, Thiamethoxam, Impairs Honey Bee Flight Ability. *Sci. Rep.* **2017**, *7* (1), 1–8.
34. Jiang, J.; Ma, D.; Zou, N.; Yu, X.; Zhang, Z.; Liu, F.; Mu, W. Concentrations of Imidacloprid and Thiamethoxam in Pollen, Nectar and Leaves from Seed-Dressed Cotton Crops and Their Potential Risk to Honeybees (Apis Mellifera L.). *Chemosphere* **2018**, *201*, 159–167.
35. European Food Safety Authority. Conclusion on the Peer Review of the Pesticide Risk Assessment for Bees for the Active Substance Imidacloprid Considering All Uses Other than Seed Treatments and Granules. *EFSA J.* **2015**, *13* (8), 1–82.
36. European Food Safety Authority. Conclusion on the Peer Review of the Pesticide Risk Assessment for Bees for the Active Substance Thiamethoxam Considering All Uses Other than Seed Treatments and Granules. *EFSA J.* **2015**, *13* (8), 1–70.
37. Gross, M. EU Ban Puts Spotlight on Complex Effects of Neonicotinoids. *Curr. Biol.* **2013**, *23* (11), R462–R464.

38. Health Canada. Re-evaluation Decision RVD2019-06, Imidacloprid and Its Associated End-use Products: Pollinator Re-evaluation https://www.canada.ca/en/health-canada/services/consumer-product-safety/reports-publications/pesticides-pest-management/decisions-updates/reevaluation-decision/2019/imidacloprid.html (accessed Jul 23, 2020).
39. Abdel-Ghany, M. F.; Hussein, L. A.; El Azab, N. F.; El-Khatib, A. H.; Linscheid, M. W. Simultaneous Determination of Eight Neonicotinoid Insecticide Residues and Two Primary Metabolites in Cucumbers and Soil by Liquid Chromatography–Tandem Mass Spectrometry Coupled with QuEChERS. *J. Chromatogr. B Anal. Technol. Biomed. Life Sci.* **2016**, *1031*, 15–28.
40. Zhang, Y.; Xu, J.; Dong, F.; Liu, X.; Li, X.; Li, Y.; Wu, X.; Liang, X.; Zheng, Y. Simultaneous Determination of Four Neonicotinoid Insecticides Residues in Cereals, Vegetables and Fruits Using Ultra-Performance Liquid Chromatography/Tandem Mass Spectrometry. *Anal. Methods* **2013**, *5* (6), 1449–1455.
41. Obana, H.; Okihashi, M.; Akutsu, K.; Kitagawa, Y.; Hori, S. Determination of Neonicotinoid Pesticide Residues in Vegetables and Fruits with Solid Phase Extraction and Liquid Chromatography Mass Spectrometry. *J. Agric. Food Chem.* **2003**, *51* (9), 2501–2505.
42. Ferrer, I.; Thurman, E. M.; Fernández-Alba, A. R. Quantitation and Accurate Mass Analysis of Pesticides in Vegetables by LC/TOF-MS. *Anal. Chem.* **2005**, *77* (9), 2818–2825.
43. Xie, W.; Han, C.; Qian, Y.; Ding, H.; Chen, X.; Xi, J. Determination of Neonicotinoid Pesticides Residues in Agricultural Samples by Solid-Phase Extraction Combined

with Liquid Chromatography-Tandem Mass Spectrometry. *J. Chromatogr. A* **2011**, *1218* (28), 4426–4433.

44. Liu, S.; Zheng, Z.; Wei, F.; Ren, Y.; Gui, W.; Wu, H.; Zhu, G. Simultaneous Determination of Seven Neonicotinoid Pesticide Residues in Food by Ultraperformance Liquid Chromatography Tandem Mass Spectrometry. *J. Agric. Food Chem.* **2010**, *58* (6), 3271–3278.
45. Hou, J.; Xie, W.; Hong, D.; Zhang, W.; Li, F.; Qian, Y.; Han, C. Simultaneous Determination of Ten Neonicotinoid Insecticides and Two Metabolites in Honey and Royal-Jelly by Solid−phase Extraction and Liquid Chromatography−tandem Mass Spectrometry. *Food Chem.* **2019**, *270* (January 2018), 204–213.
46. Gbylik-Sikorska, M.; Sniegocki, T.; Posyniak, A. Determination of Neonicotinoid Insecticides and Their Metabolites in Honey Bee and Honey by Liquid Chromatography Tandem Mass Spectrometry. *J. Chromatogr. B Anal. Technol. Biomed. Life Sci.* **2015**, *990*, 132–140.
47. Tanner, G.; Czerwenka, C. LC-MS/MS Analysis of Neonicotinoid Insecticides in Honey: Methodology and Residue Findings in Austrian Honeys. *J. Agric. Food Chem.* **2011**, *59* (23), 12271–12277.
48. Jovanov, P.; Guzsvány, V.; Franko, M.; Lazić, S.; Sakač, M.; Šarić, B.; Banjaca, V. Multi-Residue Method for Determination of Selected Neonicotinoid Insecticides in Honey Using Optimized Dispersive Liquid-Liquid Microextraction Combined with Liquid Chromatography-Tandem Mass Spectrometry. *Talanta* **2013**, *111*, 125–133.
49. Yáñez, K. P.; Bernal, J. L.; Nozal, M. J.; Martín, M. T.; Bernal, J. Determination of Seven Neonicotinoid Insecticides in Beeswax by Liquid Chromatography Coupled to

Electrospray-Mass Spectrometry Using a Fused-Core Column. *J. Chromatogr. A* **2013**, *1285*, 110–117.

50. Zhou, Y.; Lu, X.; Fu, X.; Yu, B.; Wang, D.; Zhao, C.; Zhang, Q.; Tan, Y.; Wang, X. Development of a Fast and Sensitive Method for Measuring Multiple Neonicotinoid Insecticide Residues in Soil and the Application in Parks and Residential Areas. *Anal. Chim. Acta* **2018**, *1016*, 19–28.
51. Dankyi, E.; Gordon, C.; Carboo, D.; Fomsgaard, I. S. Quantification of Neonicotinoid Insecticide Residues in Soils from Cocoa Plantations Using a QuEChERS Extraction Procedure and LC-MS/MS. *Sci. Total Environ.* **2014**, *499* (1), 276–283.
52. Hao, C.; Morse, D.; Zhao, X.; Sui, L. Liquid Chromatography/Tandem Mass Spectrometry Analysis of Neonicotinoids in Environmental Water. *Rapid Commun. Mass Spectrom.* **2015**, *29* (23), 2225–2232.
53. Hao, C.; Noestheden, M. R.; Zhao, X.; Morse, D. Liquid Chromatography-Tandem Mass Spectrometry Analysis of Neonicotinoid Pesticides and 6-Chloronicotinic Acid in Environmental Water with Direct Aqueous Injection. *Anal. Chim. Acta* **2016**, *925*, 43–50.
54. Moreira, A. A. G.; De Lima-Neto, P.; Caetano, E. W. S.; Barroso-Neto, I. L.; Freire, V. N. The Vibrational Properties of the Bee-Killer Imidacloprid Insecticide: A Molecular Description. *Spectrochim. Acta - Part A Mol. Biomol. Spectrosc.* **2017**, *185*, 245–255.
55. Donald, W. A.; Leeming, M. G.; O'Hair, R. A. J. Gas-Phase Ion Chemistry of the Pesticide Imidacloprid: Proton Driven Radical Fragmentation of the Nitro-Guanidine Functional Group. *Int. J. Mass Spectrom.* **2012**, *316–318*, 91–99.

56. Fusetto, R.; White, J. M.; Hutton, C. A.; O'Hair, R. A. J. Structure of Olefin–Imidacloprid and Gas-Phase Fragmentation Chemistry of Its Protonated Form. *Org. Biomol. Chem.* **2016**, *14* (5), 1715–1726.
57. Flammang, R.; Elguero, J.; Le, H. T.; Gerbaux, P.; Nguyen, M. T. Collisionally Induced Loss of NO2 Radical from Protonated Nitroimidazoles and Nitropyrazoles. *Chem. Phys. Lett.* **2002**, *356* (3–4), 259–266.
58. Feketeová, L.; Postler, J.; Zavras, A.; Scheier, P.; Denifl, S.; O'Hair, R. A. J. Decomposition of Nitroimidazole Ions: Experiment and Theory. *Phys. Chem. Chem. Phys.* **2015**, *17* (19), 12598–12607.
59. Singh, H. J.; Mukherjee, U. Computational Study of Proton and Methyl Cation Affinities of Imidazole-Based Highly Energetic Ionic Liquids. *J. Mol. Model.* **2011**, *17* (10), 2687–2692.
60. Kabli, S.; Van Beelen, E. S. E.; Ingemann, S.; Henriksen, L.; Hammerum, S. The Proton Affinities of Saturated and Unsaturated Heterocyclic Molecules. *Int. J. Mass Spectrom.* **2006**, *249–250*, 370–378.
61. Rao, J. S.; Sastry, G. N. Proton Affinity of Five-Membered Heterocyclic Amines: Assessment of Computational Procedures. *Int. J. Quantum Chem.* **2006**, *106* (5), 1217–1224.
62. Hwang, S.; Jang, Y. H.; Chung, D. S. Gas Phase Proton Affinity, Basicity, and PKa Values for Nitrogen Containing Heterocyclic Aromatic Compounds. *Bull. Korean Chem. Soc.* **2005**, *26* (4), 585–588.

63. Zhang, F.; Zhang, Y.; Ni, H.; Ma, K.; Li, R. Experimental and DFT Studies on the Vibrational, Electronic Spectra and NBO Analysis of Thiamethoxam. *Spectrochim. Acta - Part A Mol. Biomol. Spectrosc.* **2014**, *118*, 162–171.
64. Bayat, P.; Lesage, D.; Cole, R. B. Tutorial: Ion Activation in Tandem Mass Spectrometry Using Ultra-High Resolution Instrumentation. *Mass Spectrom. Rev.* **2020**, No. February, 1–23.
65. Brodbelt, J. S.; Wilson, J. J. Infrared Multiphoton Dissociation in Quadrupole Ion Traps. *Mass Spectrom. Rev.* **2009**, *28*, 390–424.
66. Xiao, Z.; Yang, Y.; Li, Y.; Fan, X.; Ding, S. Determination of Neonicotinoid Insecticides Residues in Eels Using Subcritical Water Extraction and Ultra-Performance Liquid Chromatography-Tandem Mass Spectrometry. *Anal. Chim. Acta* **2013**, *777*, 32–40.
67. Bourgin, M.; Violleau, F.; Debrauwer, L.; Albet, J. Ozonation of Imidacloprid in Aqueous Solutions: Reaction Monitoring and Identification of Degradation Products. *J. Hazard. Mater.* **2011**, *190* (1–3), 60–68.
68. Chandran, J.; Aravind, U. K.; Rajalakshmi, C.; Thomas, V. I.; Nguyen, P. T.; Aravindakumar, C. T. Solvent Dependent ESI-Collisionally Induced Dissociation of Protonated Nitenpyram. *Int. J. Mass Spectrom.* **2019**, *445*, 116207.

Chapter 2 - Methods

2.1 Experimental Methods

2.1.1 Quadrupole Ion Trap (QIT) Mass Spectrometry

The three-dimensional (3D) quadrupole ion trap (QIT) operates as both a storage device to confine gaseous ions and a mass spectrometer so that the mass-to-charge ratio, *m/z*, of the trapped ions can be measured.[1] The 3D quadrupole ion trap consists of three electrodes: two end-cap electrodes and one ring electrode which is aligned symmetrically between the two end-cap electrodes.[1–3] There are holes located in the end-cap electrodes for the transmission of ions into and out of the ion trap.[3] Figure 2.1 depicts the hyperbolic electrodes of a quadrupole ion trap.

Ions of a specified *m/z* are confined in the ion trap provided that the trajectories are stable in both the radial and axial directions. Ions of lower *m/z* have unstable trajectories in the radial direction while ions of higher *m/z* have unstable trajectories in the axial direction.[4] Ion confinement is achieved by varying the magnitude of the direct current (DC) and radio frequency (RF) voltage imposed by the electrodes, establishing the quadrupole trapping field. The oscillatory motion of the ions is characterized by the secular frequencies of the axial and radial directions.[5] Resonant excitation is carried out for ion isolation, excitation, dissociation, and ejection. A supplemental RF potential oscillating at the axial secular frequency is applied to the electrodes to increase the kinetic energy of the ions so that the ions experience a greater trapping field.

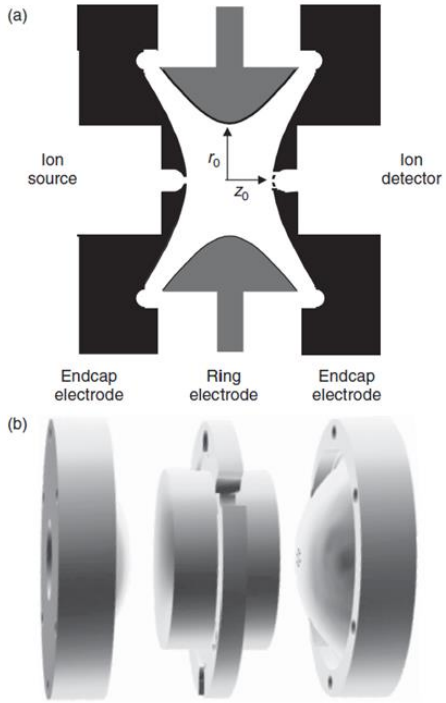

Figure 2.1. (a) Schematic diagram of a quadrupole ion trap displaying the r_0 and z_0 dimensions. (b) A model of the end-cap electrodes and the central ring electrode. Figure reproduced from reference 3 with permission.

The motion of ions in a quadrupole field are described mathematically.[5,6] Ions within a quadrupole field experience restoring forces that focus ions near the center of the ion trap. The quadrupolar potential, ϕ, at any point within the electric field is shown in Equation 2.1,

$$\phi = \frac{\phi_0}{r_0^2}(\lambda x^2 + \sigma y^2 + \gamma z^2) \tag{2.1}$$

where ϕ_0 is the applied electric potential, λ, σ, and γ are weighing constants for *x*, *y*, and *z*, respectively, and r_0 is a constant defined based on the device. The applied potential is a combination of the DC potential, U, and the RF potential, $V\cos\Omega t$.

$$\phi_0 = U + V\cos\Omega t \tag{2.2}$$

Equation 2.1 must satisfy the Laplace condition, $\nabla^2\phi = 0$, such that

$$\lambda + \sigma + \gamma = 0 \tag{2.3}$$

The simplest case for the quadrupole ion trap fulfilling the Laplace condition is $\lambda = 1$, $\sigma = 1$, and $\gamma = -2$. Substituting the values of λ, σ, and γ into Equation 2.1 yields Equation 2.4.

$$\phi_{x,y,z} = \frac{\phi_0}{r_0^2}(x^2 + y^2 - 2z^2) \tag{2.4}$$

The forces in the *x*, *y*, and *z* coordinate directions can be determined independently because the quadrupolar field is uncoupled. As an example, the force acting on an ion in the *x*-direction is demonstrated by Equation 2.5,

$$F_x = ma = m\left(\frac{d^2x}{dt^2}\right) = -e\frac{\partial\phi}{\partial x} \tag{2.5}$$

where *m* corresponds to the mass, *a* corresponds to the acceleration, and *e* corresponds to the charge of the ion. Substituting Equation 2.2 for applied potential into Equation 2.1 for quadrupolar potential and obtaining the partial differentials with respect to *x*, *y*, and *z* gives the potential gradients, represented by Equations 2.6 – 2.8.

$$\frac{\partial\phi}{\partial x} = \frac{2\lambda x}{r_0^2}(U + V\cos\Omega t) \tag{2.6}$$

$$\frac{\partial\phi}{\partial y} = \frac{2\sigma y}{r_0^2}(U + V\cos\Omega t) \tag{2.7}$$

$$\frac{\partial\phi}{\partial z} = \frac{2\gamma z}{r_0^2}(U + V\cos\Omega t) \tag{2.8}$$

Substitution of the potential gradients in the *x*-, *y*-, and *z*-directions into the equations for the force components acting on the ion in each cartesian direction leads to the equations of motion, presented by Equations 2.9 – 2.11.

$$\frac{d^2x}{dt^2} + \left(\frac{2e\lambda}{mr_0^2}\right)(U + V\cos\Omega t)x = 0 \tag{2.9}$$

$$\frac{d^2y}{dt^2} + \left(\frac{2e\sigma}{mr_0^2}\right)(U + V\cos\Omega t)y = 0 \tag{2.10}$$

$$\frac{d^2z}{dt^2} + \left(\frac{2e\gamma}{mr_0^2}\right)(U + V\cos\Omega t)z = 0 \tag{2.11}$$

The motion of the ions in the trap can be expressed in terms of solutions to the Mathieu equation, a second-order linear differential equation,

$$\frac{d^2u}{d\xi^2} + (a_u - 2q_u\cos 2\xi)u = 0 \tag{2.12}$$

where u represents the coordinate axes *x*, *y*, and *z*, ξ is a dimensionless variable relating to frequency and time, and a_u and q_u are dimensionless trapping parameters. Using the chain rule and the relationship $\xi = \frac{\Omega t}{2}$, Equation 2.13 can be obtained.

$$\frac{d^2u}{dt^2} = \frac{d\xi}{dt}\frac{du}{d\xi}\left\{\frac{du}{dt}\right\} = \frac{\Omega^2}{4}\frac{d^2u}{d\xi^2} \tag{2.13}$$

Comparing Equations 2.9 – 2.11 to the Mathieu equation and applying the operator notation defined above, the trapping parameters, a_u and q_u, can be determined where u constitutes the cartesian coordinate axes or cylindrical coordinate axes.

The quadrupole ion trap has cylindrical symmetry; thus, it is essential to convert the cartesian coordinates of $\phi_{x,y,z}$ into cylindrical polar coordinates in order to acquire an equation for $\phi_{r,z}$. This is accomplished by employing the functions $x = r\cos\theta$, $y = r\sin\theta$, and $z = z$ and applying the trigonometric identity $sin^2\theta + cos^2\theta = 1$.

$$\phi_{r,z} = \frac{\phi_0}{r_0^2}(r^2 - 2z^2) \tag{2.14}$$

The trapping parameters with regards to the radial (r) and axial (z) directions of the QIT can be obtained in a similar manner to the derivation presented above.

$$a_r = \frac{4eU}{mr_0^2\Omega^2}; q_r = -\frac{2eV}{mr_0^2\Omega^2} \tag{2.15}$$

$$a_z = -\frac{8eU}{mr_0^2\Omega^2}; q_z = \frac{4eV}{mr_0^2\Omega^2} \tag{2.16}$$

The trapping parameters, a_u and q_u, provide solutions to the Mathieu equation which govern the stability and instability of the ion trajectories within the quadrupole ion trap. Stable trajectories are delineated as the ion displacement periodically passing back through the origin of the device, and unstable trajectories are described as the ion displacement increasing to infinity.[6] The Mathieu stability diagram in Figure 2.2 portrays the stability regions in the *r*- and *z*-directions. The limits of the stable trajectories are bounded by the β_r and β_z lines. The trajectories of the ions are determined by altering the potential applied to the electrodes. When an RF potential is applied to the ring electrode and no DC potential is applied between the ring and end-cap electrodes, all ions possess a_z values of zero. The locus of all possible mass-to-charge ratios are mapped directly onto the q_z axis. By increasing the amplitude of the RF potential, ions of successively increasing *m/z* will adopt unstable trajectories.[1,3,6] Ion species will be ejected axially through perforations in the end-cap electrodes and detected by an electron multiplier, and is known as mass-selective instability.

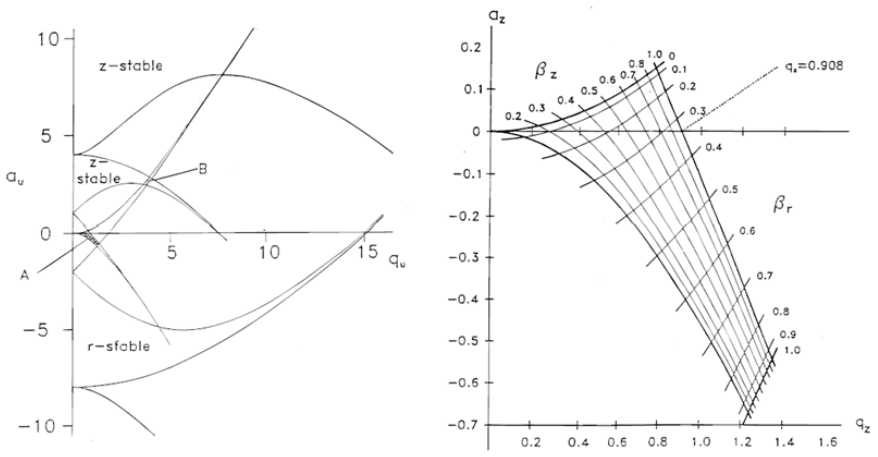

Figure 2.2. The Mathieu stability diagram in $a_u - q_u$ space for the quadrupole ion trap. The intersection of the *r*-stable and *z*-stable regions, labelled A and B, coincide with ion trajectories whose radial and axial components are stable. Figure adapted from reference 5 with permission.

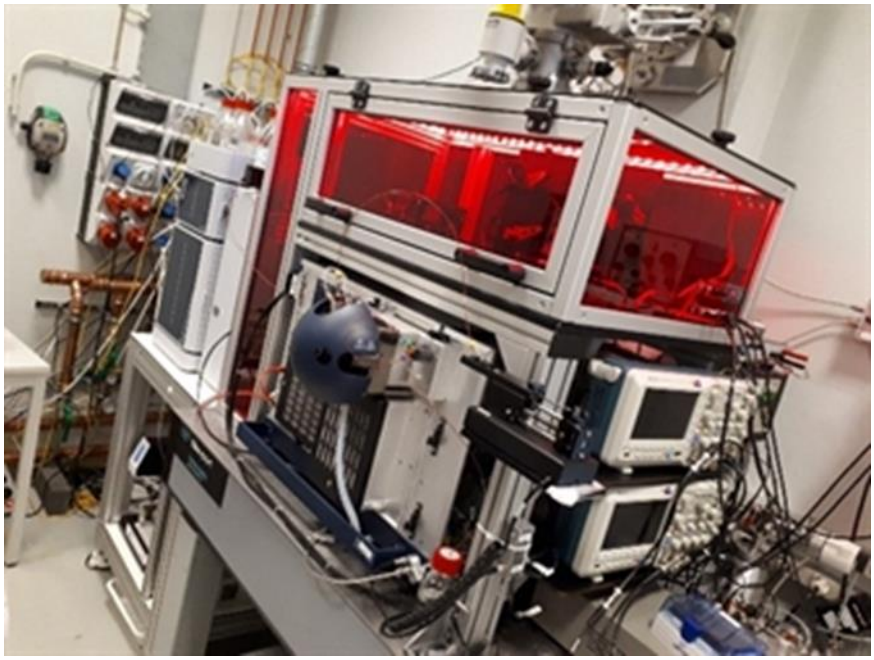

Figure 2.3. The Bruker amaZon Speed ETD ion trap mass spectrometer at the FELIX laboratory. Figure taken from the FELIX website.[7]

The Free Electron Lasers for Infrared eXperiments (FELIX) facility in the Netherlands is equipped with a modified 3D quadrupole ion trap mass spectrometer [Bruker amaZon Speed ETD].[8] A photograph of the QIT mass spectrometer is shown in Figure 2.3. The instrument has been modified to permit optical access to the ion population for conducting infrared ion spectroscopy experiments. The ring electrode contains two 3 mm holes to create an optical path for the free electron laser. In addition, IR transparent windows have been installed in the MS vacuum housing and two gold coated mirrors have been placed below the ion trap so that the laser beam can pass through the ion trap.

2.1.2 Fourier Transform Ion Cyclotron Resonance (FTICR) Mass Spectrometry

Mass spectrometry is an analytical technique that accurately measures the mass-to-charge ratio, *m/z*, of ions. A Fourier Transform Ion Cyclotron Resonance (FTICR) mass spectrometer provides ultra-high mass resolving power, mass resolution, and mass accuracy.[9] In an FTICR mass spectrometer, ions of a particular *m/z* are detected according to their cyclotron frequency, and trapping mass-selective ions for sufficiently long periods allows for the cyclotron frequency to be determined with high precision. The high-resolution capabilities of the FTICR can be used to examine the ion-molecule reactions of biological molecules by performing multistage tandem mass spectrometric measurements.

Ions moving in the ion cyclotron resonance (ICR) cell experience an oscillating electric field that is perpendicular to the magnetic field causing ions to undergo circular orbits. In the presence of a spatially uniform magnetic field, an ion will rotate at a frequency characteristic of its mass-to-charge ratio.[9–13] The cyclotron motion effectively

traps ions in the ICR cell, where excitation and detection also take place. Equation 2.17 demonstrates the relationship between the angular velocity, ν_c, and the cyclotron frequency, ω_c.

$$\nu_c = \frac{\omega_c}{2\pi} \tag{2.17}$$

Equation 2.18 shows that the cyclotron frequency can be expressed in terms of the magnetic field strength, *B*, the mass of the ion, *m*, and the charge of the ion, *q*.

$$\omega_c = \frac{qB}{m} \tag{2.18}$$

Equations 2.17 and 2.18 are combined and rearranged to yield Equation 2.19, an expression for the mass-to-charge ratio, *m/q*.

$$\frac{m}{q} = \frac{B}{\omega_c} \tag{2.19}$$

Ion cyclotron motion must be spatially coherent in order to be detectable, therefore, an oscillating electric field applied to the trapped ions within the ICR cell is done to excite ions to larger detectable cyclotron radii. The coherent orbiting ion packet induces an image charge on the opposed detector electrodes when the ions' orbital is near a detection plate. The image charge is detected as a sinusoidal image current which is measured as a function of time. A Fourier transformation of the time-domain transient gives the frequency-domain spectrum, which is then converted to a mass spectrum. A Bruker Apex-Qe 7.0 FTICR mass spectrometer at Memorial University is used to perform SORI-CID experiments. A brief overview of FTICR mass spectrometry is presented in this section, and ion activation and fragmentation by SORI-CID is outlined in the following section.

2.1.3 Collision-Induced Dissociation (CID)

Tandem mass spectrometry (MS/MS) is a powerful tool used for the structural elucidation of biomolecules. MS/MS involves the mass selection of a precursor ion of interest and subjecting it to energetic excitation through activation techniques, resulting in the subsequent unimolecular dissociation of the precursor ion.[14,15] Herein, we describe the ion activation techniques of collision-induced dissociation (CID) and sustained off-resonance irradiation collision-induced dissociation (SORI-CID). In CID and SORI-CID experiments, many successive inelastic collisions with a nonreactive target gas (N_2, Ar, or He) at low pressures of ~10^{-6} Torr are necessary to activate the precursor ion and produce fragmentation.[16] The collision process converts a portion of the ion's translational energy into internal energy thus depositing sufficient energy in the precursor ion for dissociation.[17] Low-energy CID experiments, in the range of 1-100 eV, are typically performed using tandem quadrupole and trapping devices such as quadrupole ion traps and Fourier-transform ion cyclotron resonance instruments, which are discussed above. In contrast, high-energy CID experiments, in the range of a few keV, are conducted using sector and time-of-flight instruments.[17]

SORI-CID experiments are typically conducted in FTICR mass spectrometers. The confined ions are irradiated by a radio-frequency pulse that is off-resonance with the ion's natural cyclotron frequency. As a result of the offset excitation frequency, ions undergo numerous acceleration and deceleration cycles that lead to increasing and decreasing the orbital radius during SORI excitation.[16–18] Consequently, many more collisions occur between the excited ions and target gas, and deposit less kinetic energy per collision

causing the internal energy of the ions to increase slowly.[18] This slow activation of molecules causes dissociation to occur through the lowest energy pathway.[16] SORI-CID experiments are performed in the Laboratory for the Study of Energetics, Structures, and Reactions of Gaseous Ions at Memorial University, however, SORI-CID mass spectra are omitted from this thesis due to the indistinguishable fragmentation patterns observed between SORI-CID and IRMPD mass spectra. It has been shown previously that the fragmentation products in the MS/MS of IRMPD are typically similar to fragments observed in the MS/MS of CID.[19,20]

Additional ion dissociation techniques constituting collision-mediated activation in mass spectrometry include surface-induced dissociation (SID) and higher-energy collision dissociation (HCD). Photon-mediated ion activation and dissociation methods utilized in mass spectrometry include infrared multiphoton dissociation (IRMPD), blackbody infrared radiative dissociation (BIRD), and ultraviolet photodissociation (UVPD). Further, electron-mediated ion activation and dissociation techniques encompass electron capture dissociation (ECD), electron transfer dissociation (ETD), electron detachment dissociation (EDD), and electron-induced dissociation (EID).[15,16] IRMPD is the experimental technique of choice for the research conducted on protonated neonicotinoid complexes, therefore, IRMPD spectroscopy will be described in the next section.

2.1.4 Infrared Multiphoton Dissociation (IRMPD)

Infrared multiphoton dissociation (IRMPD) is a fragmentation technique used for the characterization of molecular structure in ion spectroscopy. An ion of interest is selected based on its mass and irradiated with tunable infrared radiation from the laser. For the

process of IRMPD to occur there must be a vibrational mode in resonance with the laser frequency, permitting infrared photons to be absorbed ($v = 0 \rightarrow v = 1$ transition).[21] The energy absorbed by a normal mode of the ion is rapidly redistributed to other vibrational degrees of freedom in the molecule by a process known as intramolecular vibrational energy redistribution (IVR). IVR disperses the initial absorbing photons energy to other vibrational modes so that subsequent absorptions can occur. The sequential absorption of photons preceding IVR slowly causes an increase in the internal energy of the ions until the dissociation threshold, D_0, is reached and exceeded, resulting in dissociation of the precursor ion.[15,21,22] Figure 2.4 gives a detailed description of the IRMPD mechanism, depicting the process of infrared photon absorption followed by IVR. Absorption of one or multiple infrared photons is detected by a loss in precursor ion signal and a change in the mass-to-charge ratio, *m/z*, is observed, which is indicative of the emergence of fragment ions.[21,23] Monitoring fragmentation of the ion as a function of the infrared laser wavelength, a vibrational IRMPD spectrum can be obtained.[22] The IRMPD efficiency, given by Equation 2.20, is defined as the negative logarithm of the precursor ion intensity divided by the sum of the precursor and fragment ion intensities.

$$\text{IRMPD Efficiency} = -\log\left(\frac{I_{precursor}}{I_{precursor} + \sum_i I_{fragment(i)}}\right) \qquad (2.20)$$

IRMPD spectroscopy is referred to as a "consequence" spectroscopy technique because it is the consequence of infrared photon absorption that is detected and measured.[24]

To the best of our knowledge the application of IRMPD spectroscopy has not been used to study neonicotinoids. The application of IRMPD to probe the structures and unimolecular reactivity of protonated imidacloprid and protonated thiamethoxam will be

discussed in Chapters 3 and 4, respectively. The IRMPD spectra were collected at the FELIX laboratory in Nijmegen, the Netherlands.[25] The free electron laser produces tunable radiation in the form of infrared pulses (energies up to 150 mJ/pulse) in the 500-1900 cm^{-1} spectral region.

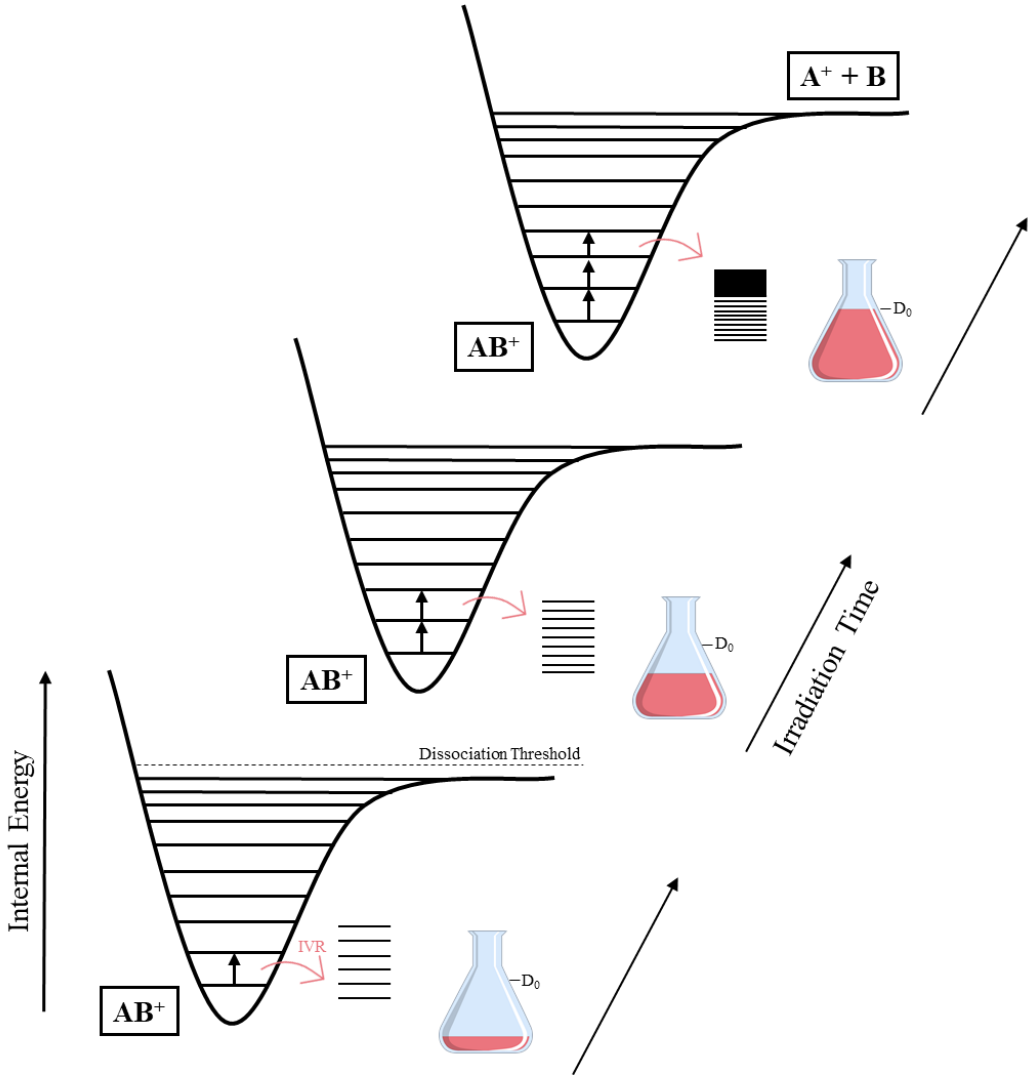

Figure 2.4. Schematic representation of the IRMPD mechanism. Absorption of infrared photons occurs, and the energy absorbed is redistributed to other vibrational modes. This raises the internal energy of the ion, and thus, the density of vibrational states. The process of absorption followed by IVR continues until the internal energy of the ion surpasses the dissociation threshold, resulting in fragmentation of the ion.

2.1.5 Free Electron Laser (FEL)

A free electron laser (FEL) operates as a source of continuously tunable, high power radiation for wavelengths ranging from the microwave to the X-ray of the electromagnetic spectrum.[26] Free electrons, unbound to atomic nuclei, are ejected from an electron gun and accelerated to relativistic speeds by a radio-frequency linear accelerator (rf Linacs). The electron beam passes through a periodic magnetic field, an undulator, which is generated by an array of magnets. Due to the Lorentz force, the electrons propagating through the alternating magnetic field are subjected to a wiggling motion.[26–28] The transverse oscillations of the electrons result in the emission of incoherent radiation at each change in direction. In order to give rise to stimulated emission, it is necessary for the electrons to form coherent bunches.[26,29] The electrons propagate at a speed less than light, therefore to achieve coherence, the radiation advances by an integer value of the wavelength per undulator period, $n\lambda$, in relation to the electron bunch. A diagram of an FEL is illustrated in Figure 2.5.[30] The wavelength of the radiation emitted can be tuned by altering the energy of the electron beam, or the magnetic field of the undulator.[31]

The IRMPD experiments in the present work are conducted at the FELIX user facility at Radboud University in the Netherlands. Vibrational spectra in the 500-2000 cm^{-1} region are collected using a quadrupole ion trap mass spectrometer interfaced to the electron beamline of FELIX.[29,32] FELIX produces infrared radiation as macropulses, 5-10 μs duration, consisting of a train of micropulses, 0.1-10 ps duration. The average output

power of a macropulse is of the order of 10 kW and the peak power of a micropulse is in the range of MW.

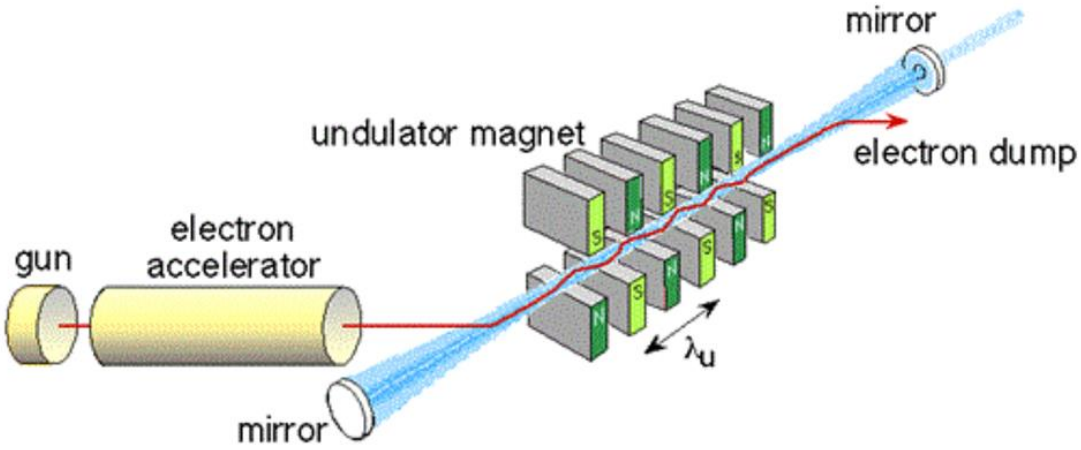

Figure 2.5. A schematic representation of a free electron laser. A beam of electrons is produced by the electron accelerator and then is directed through the alternating magnetic field of the undulator. Coherent and intense radiation is amplified within the optical cavity by mirrors placed at either end of the undulator. Figure taken from the FELIX website.

2.1.6 Electrospray Ionization (ESI)

Electrospray ionization (ESI) is a method used in mass spectrometry that allows for the sensitive analysis of non-volatile and thermally labile compounds.[33] ESI is a soft ionization technique that requires the formation of gaseous ions from solution.[34,35] The mechanistic description of the ESI process is provided here. A high voltage (2-5 kV) is applied to the metal capillary through which the solution containing the analyte of interest is expelled.[33,36–39] The electric field gradient, created by the applied voltage, gives rise to the separation of charged ions in solution. The repulsion of the ions caused by the accumulation of charge on the surface and the pull of the electric field results in the

distortion of the meniscus at the capillary tip; consequently, the solution emerges in the form of a Taylor cone. Evaporation of the solvent is aided by a heated drying gas that flows in the opposite direction of the ions. Removal of the neutral solvent decreases the size of the charged droplets, which increases the charge density of the droplets. When the Coulombic repulsion of the surface charge overcomes the cohesive force of the surface tension, a point called the Rayleigh limit is reached. As a result, the charged droplets undergo Coulombic explosion, namely droplet fission, to produce smaller charged droplets. Figure 2.6 illustrates the process of electrospray ionization for the formation of gas phase ions from highly charged droplets of solution.

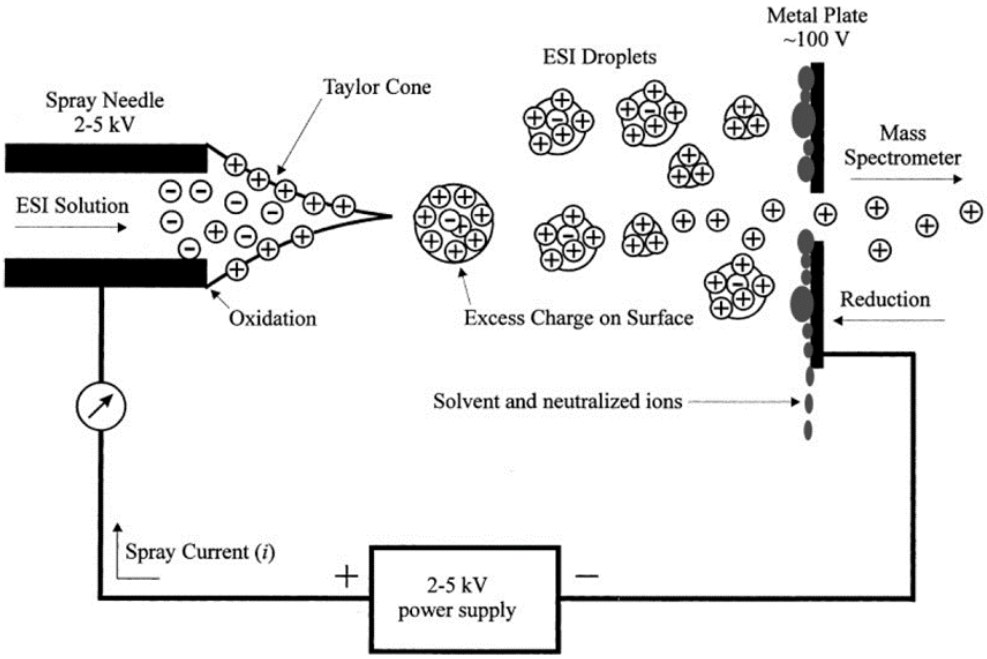

Figure 2.6. The electrospray ionization process. Charged droplets of analyte solution are produced at the capillary tip, solvent evaporation and Coulombic explosion split larger charged droplets into smaller highly charged droplets, and gas phase ions are formed by the CRM or IEM. Figure reproduced from reference 36 with permission.

There are two principal theories that explain the formation of gas phase ions: the charge residue model (CRM) and the ion evaporation model (IEM). The CRM suggests that solvent evaporation and Coulombic fission at the Rayleigh limit continue until only the charged analyte ion remains.[40] The IEM suggests that when solvent evaporation and Coulombic explosion have reduced the size of the charged droplets to a radius of 10-20 nm, an analyte ion is desorbed, released from the droplet surface, into the gas phase, thereby diminishing the Coulombic repulsion within the charged droplet.[41]

2.2 Computational Methods

2.2.1 Density Functional Theory (DFT)

Density functional theory (DFT) is used in quantum chemistry to calculate the electronic structure of atoms and molecules. This computational theory is based on the electron density, $\rho(r)$, rather than the many-electron wave function, $\psi(r_1,r_2,\ldots,r_N)$. DFT methods originate from the Hohenberg-Kohn[42] theorem, which states that the ground state electronic properties of a many-electron system can be determined from the ground state density, the electron density depending only on three spatial variables.[43] The external potential is a unique functional of the density, and the external potential is part of the Hamiltonian which provides solutions to the Schrödinger equation. As a result, the electronic wave function can be defined by the electron density. Density functional theory is further developed by the Kohn-Sham[44] equations, which introduce a set of imaginary orbitals for individual electrons used to describe a many-electron system.[45] Exchange and correlation effects are considered in the Kohn-Sham scheme, providing a better

representation of the kinetic energies of the interacting and non-interacting electron systems.

Theoretical methods, B3LYP and M06-2X density functionals, are used exclusively in this thesis to calculate electronic structures, 298 K relative enthalpies and Gibbs energies, and theoretical vibrational spectroscopy (IR band positions and intensities). The B3LYP hybrid functional integrates the Becke 3-parameter exchange functional and the Lee-Yang-Parr correlation functional.[46,47] M06-2X is a Minnesota functional that is established from meta-generalized gradient approximations, exploiting kinetic energy density and exchange-correlation functionals.[48]

2.2.2 Basis Sets

A basis set in theoretical and computational chemistry is a linear combination of atomic orbitals used to construct molecular orbitals. A basis set is made up of a finite number of mathematical functions.[49] Slater-type orbital (STO) functions and Gaussian-type orbital (GTO) functions are the most commonly used basis functions in molecular calculations for representing the electronic wave function.[49,50] In the current research, the atomic orbitals are expanded in terms of Gaussian functions to approximate the electron distribution of neonicotinoid molecules. A Gaussian function is defined in Equation 2.21.

$$\chi_{GTO} = Nx^l y^m z^n e^{-\zeta r^2} \tag{2.21}$$

In this equation, N is a normalization constant, x, y, and z are the position coordinates measured from the nucleus, the sum of l, m, and n determines the angular momentum ($l + m + n = 0$, $l + m + n = 1$, and $l + m + n = 2$ correspond to s, p, and d orbitals, respectively), and ζ is an orbital exponent.[51,52]

A minimal basis set, a single zeta basis set, gives the simplest representation of the occupied orbitals for an atom and requires only a single basis function to describe each orbital.[50,53] Minimal basis sets give an insufficient explanation of the spherical symmetry and the process of bond formation in molecules. Split-valance basis sets provide an improved description of the relative energies and molecular geometries. The core and the valance atomic orbitals of split-valance basis sets are defined independently, in which one or more basis functions are assigned.[54] In this thesis, the enthalpies and Gibbs free energies of protonated imidacloprid and protonated thiamethoxam are computed using the split-valance double zeta basis set 6-31+G(d,p). The core orbitals of the 6-31+G(d,p) basis set are represented by one basis function, consisting of six Gaussian functions. The valance orbitals are represented by two basis functions, the inner shell composed of three Gaussian functions and the outer shell composed of one Gaussian function. Single point energies are calculated using the split-valance triple zeta basis set 6-311+G(3df,2pd).

Polarization functions, higher angular momentum functions, allow for displacement of electron distribution away from the nuclei.[55] Polarization functions are introduced to basis sets to permit more flexibility and account for the distortion of the atomic symmetry. The inclusion of (d,p) or ** to the basis set means that *d*-type polarizations functions are added to main group elements (carbons, nitrogens, oxygens, and sulfur atoms) and *p*-type polarization functions are added to hydrogen atoms. Moreover, diffuse functions are necessary to account for electrons held at larger distances from the nuclei than core or bonding electrons.[49] The addition of + to the basis set denotes the

incorporation of diffuse functions, functions with small values of $e^{-\zeta r^2}$, *s*-type and *p*-type diffuse functions are added to non-hydrogen atoms.

2.3 References

1. Stafford, G. C.; Kelley, P. E.; Syka, J. E. P.; Reynolds, W. E.; Todd, J. F. J. Recent Improvements in and Analytical Applications of Advanced Ion Trap Technology. *Int. J. Mass Spectrom. Ion Process.* **1984**, *60* (1), 85–98.
2. Cooks, R. G.; Kaiser, R. E. Quadrupole Ion Trap Mass Spectrometry. *Acc. Chem. Res.* **1990**, *23* (7), 213–219.
3. Ridgeway, M. E.; Glish, G. L. Triple Quadrupole and Quadrupole Ion Trap Mass Spectrometers. In *Encyclopedia of Drug Metabolism and Interactions*; Lyubimov, A. V., Ed.; John Wiley & Sons, Inc.: Chapel Hill, NC, 2012; pp 1–25.
4. Dawson, P. H. Principles of Operation. In *Quadrupole Mass Spectrometry and its Applications*; Elsevier Scientific Publishing Company, 1976; pp 9–64.
5. March, R. E. An Introduction to Quadrupole Ion Trap Mass Spectrometry. *J. Mass Spectrom.* **1997**, *32* (4), 351–369.
6. March, R. E. Quadrupole Ion Traps. *Mass Spectrom. Rev.* **2009**, *28*, 961–989.
7. User station 9: Quadrupole ion trap MS for IR ion spectroscopy https://www.ru.nl/felix/facility-0/measurement-station/user-station-9-quadrupole-ion-trap-ms-ir-ion/.
8. Martens, J.; Berden, G.; Gebhardt, C. R.; Oomens, J. Infrared Ion Spectroscopy in a Modified Quadrupole Ion Trap Mass Spectrometer at the FELIX Free Electron Laser Laboratory. *Rev. Sci. Instrum.* **2016**, *87* (10).

9. Marshall, A. G.; Hendrickson, C. L. Fourier Transform Ion Cyclotron Resonance Detection: Principles and Experimental Configurations. *Int. J. Mass Spectrom.* **2002**, *215* (1–3), 59–75.
10. Marshall, A. G.; Hendrickson, C. L.; Jackson, G. S. Fourier Transform Ion Cyclotron Resonance Mass Spectrometry: A Primer. *Mass Spectrom. Rev.* **1998**, *17* (1), 1–35.
11. Marshall, A. G.; Chen, T. 40 Years of Fourier Transform Ion Cyclotron Resonance Mass Spectrometry. *Int. J. Mass Spectrom.* **2015**, *377* (1), 410–420.
12. Guan, S.; Marshall, A. G. Ion Traps for Fourier Transform Ion Cyclotron Resonance Mass Spectrometry: Principles and Design of Geometric and Electric Configurations. *Int. J. Mass Spectrom. Ion Process.* **1995**, *147*, 261–296.
13. Amster, I. J. Fourier Transform Mass Spectrometry. *J. Mass Spectrom.* **1996**, *31*, 1325–1337.
14. Laskin, J.; Futrell, J. H. Collisional Activation of Peptide Ions in FT-ICR Mass Spectrometry. *Mass Spectrom. Rev.* **2003**, *22* (3), 158–181.
15. Bayat, P.; Lesage, D.; Cole, R. B. Tutorial: Ion Activation in Tandem Mass Spectrometry Using Ultra-High Resolution Intrumentation. *Mass Spectrom. Rev.* **2020**, *00*, 1–23.
16. Herrmann, K. A.; Somogyi, Á.; Wysocki, V. H.; Drahos, L.; Vékey, K. Combination of Sustained Off-Resonance Irradiation and on-Resonance Excitation in FT-ICR. *Anal. Chem.* **2005**, *77* (23), 7626–7638.
17. Sleno, L.; Volmer, D. A. Ion Activation Methods for Tandem Mass Spectrometry. *J. Mass Spectrom.* **2004**, *39* (10), 1091–1112.

18. Heeren, R. M. A.; Kleinnijenhuis, A. J.; McDonnell, L. A.; Mize, T. H. A Mini-Review of Mass Spectrometry Using High-Performance FTICR-MS Methods. *Anal. Bioanal. Chem.* **2004**, *378* (4), 1048–1058.
19. Brodbelt, J. S.; Wilson, J. J. Infrared Multiphoton Dissociation in Quadrupole Ion Traps. *Mass Spectrom. Rev.* **2009**, *28*, 390–424.
20. Laskin, J.; Futrell, J. H. Activation of Large Ions in FT-ICR Mass Spectrometry. *Mass Spectrom. Rev.* **2005**, *24* (2), 135–167.
21. Polfer, N. C. Infrared Multiple Photon Dissociation Spectroscopy of Trapped Ions. *Chem. Soc. Rev.* **2011**, *40* (5), 2211–2221.
22. Eyler, J. R. Infrared Multiple Photon Dissociation Spectroscopy of Ions in Penning Traps. *Mass Spectrom. Rev.* **2009**, *28*, 448–467.
23. Fridgen, T. D.; McMahon, T. B. IRMPD. *The Encyclopedia of Mass Spectrometry*. 2005, 327–337.
24. Fridgen, T. D. Infrared Consequence Spectroscopy of Gaseous Protonated and Metal Ion Cationized Complexes. *Mass Spectrom. Rev.* **2009**, *28*, 586–607.
25. Martens, J.; van Outersterp, R. E.; Vreeken, R. J.; Cuyckens, F.; Coene, K. L. M.; Engelke, U. F.; Kluijtmans, L. A. J.; Wevers, R. A.; Buydens, L. M. C.; Redlich, B.; et al. Infrared Ion Spectroscopy: New Opportunities for Small-Molecule Identification in Mass Spectrometry - A Tutorial Perspective. *Anal. Chim. Acta* **2020**, *1093*, 1–15.
26. Freund, H. P.; Antonsen, T. M., Jr. *Principles of Free Electron Lasers*; Cham: Springer International AG, 2018.
27. Socol, Y. High-Power Free-Electron Lasers-Technology and Future Applications. *Opt. Laser Technol.* **2013**, *46* (1), 111–126.

28. Renk, K. F. Free-Electron Laser. In *Basics of Laser Physics*; Springer Berlin Heidelberg, 2012; pp 333–367.
29. Oomens, J.; Sartakov, B. G.; Meijer, G.; von Helden, G. Gas-Phase Infrared Multiple Photon Dissociation Spectroscopy of Mass-Selected Molecular Ions. *Int. J. Mass Spectrom.* **2006**, *254* (1–2), 1–19.
30. Kim, K.-J.; Sessler, A. Free-Electron Lasers: Present Status and Future Prospects. *Science (80-.).* **1990**, *250*, 88–93.
31. Oepts, D.; van der Meer, A. F. G.; van Amersfoort, P. W. The Free-Electron-Laser User Facility FELIX. *Infrared Phys. Technol.* **1995**, *36* (1), 297–308.
32. FEL operating principle https://www.ru.nl/felix/about-felix/about-felix/fel-operating-principle/.
33. Smith, R. D.; Loo, J. A.; Edmonds, C. G.; Barinaga, C. J.; Udseth, H. R. New Developments in Biochemical Mass Spectrometry: Electrospray Ionization. *Anal. Chem.* **1990**, *62* (9), 882–899.
34. Konermann, L.; Ahadi, E.; Rodriguez, A. D.; Vahidi, S. Unraveling the Mechanism of Electrospray Ionization. *Anal. Chem.* **2013**, *85* (1), 2–9.
35. Fenn, J. B.; Mann, M.; Meng, C. K.; Wong, S. F.; Whitehouse, C. M. Electrospray Ionization for Mass Spectrometry of Large Biomolecules. *Science (80-.).* **1989**, *246* (4926), 64–71.
36. Cech, N. B.; Enke, C. G. Practical Implications of Some Recent Studies in Electrospray Ionization Fundamentals. *Mass Spectrom. Rev.* **2001**, *20* (6), 362–387.
37. Cole, R. B. Some Tenets Pertaining to Electrospray Ionization Mass Spectrometry. *J. Mass Spectrom.* **2000**, *35* (7), 763–772.

38. Kebarle, P. A Brief Overview of the Present Status of the Mechanisms Involved in Electrospray Mass Spectrometry. *J. Mass Spectrom.* **2000**, *35* (7), 804–817.
39. Kebarle, P.; Verkcerk, U. H. Electrospray: From Ions in Solution to Ions in the Gas Phase, What We Know Now. *Mass Spectrom. Rev.* **2009**, *28* (6), 898–917.
40. Dole, M.; Mack, L. L.; Hines, R. L.; Mobley, C. R.; Ferguson, L. D.; Alice, M. B. Molecular Beams of Macroions. *J. Chem. Phys.* **1968**, *49* (5), 2240–2249.
41. Iribarne, J. V.; Thomson, B. A. On the Evaporation of Small Ions from Charged Droplets. *J. Chem. Phys.* **1976**, *64* (6), 2287–2294.
42. Hohenberg, P.; Kohn, W. Inhomogeneous Electron Gas. *Phys. Rev.* **1964**, *136* (3B), B864–B871.
43. Koch, W.; Holthausen, M. C. *A Chemist's Guide to Density Functional Theory*, 2nd ed.; Wiley-VCH: Weinheim, Germany, 2001.
44. Kohn, W.; Sham, L. J. Self-Consistent Equations Including Exchange and Correlation Effects. *Phys. Rev.* **1965**, *140* (4A), A1133–A1138.
45. Parr, R. G.; Yang, W. Density-Functional Theory. In *Density-Functional Theory of Atoms and Molecules*; Oxford University Press: New York, 1989.
46. Becke, A. D. Density-Functional Exchange-Energy Approximation with Correct Asymptotic Behavior. *Phys. Rev. A* **1988**, *38* (6), 3098–3100.
47. Lee, C.; Yang, W.; Parr, R. G. Development of the Colle-Salvetti Correlation-Energy Formula into a Functional of the Electron Density. *Phys. Rev. B* **1988**, *37* (2), 785–789.
48. Zhao, Y.; Truhlar, D. G. The M06 Suite of Density Functionals for Main Group Thermochemistry, Thermochemical Kinetics, Noncovalent Interactions, Excited

States, and Transition Elements: Two New Functionals and Systematic Testing of Four M06-Class Functionals and 12 Other Function. *Theor. Chem. Acc.* **2008**, *120* (1–3), 215–241.

49. Lewars, E. G. *Ab Initio* Calculations. In *Computational Chemistry: Introduction to the Theory and Applications of Molecular and Quantum Mechanics*; Springer International Publishing AG, 2016; pp 159–337.
50. Jensen, F. Basis Sets. In *Introduction to Computational Chemistry*; John Wiley & Sons, Incorporated, 2017; pp 188–232.
51. Davidson, E. R.; Feller, D. Basis Set Selection for Molecular Calculations. *Chem. Rev.* **1986**, *86* (4), 681–696.
52. Feller, D.; Davidson, E. R. Basis Sets for Ab Initio Molecular Orbital Calculations and Intermolecular Interactions. In *Reviews in Computational Chemistry*; John Wiley & Sons, Inc., 1990; pp 1–43.
53. Jensen, F. Atomic Orbital Basis Sets. *Wiley Interdiscip. Rev. Comput. Mol. Sci.* **2013**, *3* (3), 273–295.
54. Binkley, J. S.; Pople, J. A.; Hehre, W. J. Self-Consistent Molecular-Orbital Methods. 21. Small Split-Valence Basis Sets for First-Row Elements. *J. Am. Chem. Soc.* **1980**, *102* (3), 939–947.
55. Francl, M. M.; Pietro, W. J.; Hehre, W. J.; Binkley, J. S.; Gordon, M. S.; DeFrees, D. J.; Pople, J. A. Self-Consistent Molecular Orbital Methods. XXIII. A Polarization-Type Basis Set for Second-Row Elements. *J. Chem. Phys.* **1982**, *77* (7), 3654–3665.

Chapter 3 – A Vibrational Spectroscopic and Computational Study of the Structures of Protonated Imidacloprid and its Fragmentation Products in the Gas Phase

3.1. Introduction

Imidacloprid belongs to a class of compounds called neonicotinoids which are used extensively in agricultural practice to control insect pests.[1–3] Neonicotinoids are structurally similar to nicotine[4–6] and like nicotine, they are neurotoxins that act as agonists at the nicotinic acetylcholine receptors (nAChRs) in the central nervous system of insects.[3,6–11] Neonicotinoids show selective toxicity toward insects over mammals, due to the stronger binding capability of insect nAChRs.[2,12–14] Neonicotinoid insecticides are systemic as they are absorbed by the roots or leaves of plants and distributed to all tissues in a plant's vascular system.[10,11,15–17] As a result, both pollen and nectar collected by forager bees often contain neonicotinoids, which may be transported back to the beehive.[2,9,16,18]

Colony collapse disorder (CCD), characterized by the decline of honey bee colonies, is widely attributed to the global overuse of neonicotinoids.[3,5,6,14,17] This concern led the European Union (EU) to introduce a two-year ban on the use of imidacloprid, clothianidin, and thiamethoxam for seed treatment, soil application, and foliar treatment in crops that are visited by bees.[10,16,19–21] Exposure to sublethal doses of neonicotinoids will not directly cause the mortality of honey bees and bumblebees; nonetheless this can

cause learning and memory dysfunctions, negatively affecting their ability to navigate.[6,16,20]

In honeybees, imidacloprid typically metabolizes to form olefin-imidacloprid, 5-hydroxyimidalcoprid, 4,5-dihydroxyimidacloprid, desnitro-imidacloprid, imidacloprid urea, and 6-chloronicotinic acid.[22,23] Acute oral toxicity tests conducted on honey bees showed that when forager bees were treated with high doses (10-10,000 µg/kg) of imidacloprid and its plant metabolites for short term periods (48 h), the 5-hydroxy- and olefin- metabolites exhibited toxicities close to that of imidacloprid.[24,25] Neonicotinoids that possess the nitroguanidine moiety are harmful to bees at concentrations lower than 1 µg/kg, thus, parent compounds and metabolites that are acutely toxic have been the focus of many studies for quantifying insecticides.[26] Chronic oral tests revealed that when honeybees ingested 0.1, 1.0, and 10.0 µg/kg of compound, imidacloprid and the six studied metabolites induced substantial mortality.[24] Chronic dietary toxicity tests toward honeybees for a 10 day exposure period to imidacloprid and two metabolites, imidacloprid urea and 6-chloronicotinic acid, were inspected on younger hive bees and older forager bees.[27] The experimental findings of this study showed no lethal effect when bees ingested 0.1, 1.0, and 10.0 µg/L metabolite solutions.

Methods for identification and confirmation of neonicotinoid insecticides in agricultural products by liquid chromatography-tandem mass spectrometry (LC-MS/MS), in food by ultraperformance liquid chromatography combined with electrospray ionization tandem mass spectrometry (UPLC-MS/MS), and in vegetable matrices using liquid chromatography in combination with time of flight mass spectrometry (LC/TOF-MS) have been used to investigate the fragmentation mechanisms of imidacloprid.[28–30]

Maximum residue limits (MRLs) for pesticides are specified by Government agencies to assess whether the concentrations of pesticides found in agricultural foods pose a significant threat to human health. Monitoring the degradation and residues of insecticides is essential for safe consumption of food. The quantitative analysis revealed that the measured concentrations of neonicotinoid insecticides are lower than the MRLs, therefore, the concentration levels are not a concern for humans exposed to foods contaminated with neonicotinoids.[28–30] Xie *et al.*[28] reported that protonated imidacloprid (*m/z* 256) produces fragment ions at *m/z* 209 and 175 corresponding to the loss of HNO_2 and the simultaneous loss of NO_2 and Cl, respectively. Liu *et al.*[29] proposed chemical structures for the product ions of imidacloprid at *m/z* 209 and 175 consistent with the fragmentation pattern suggested by Xie *et al.*[28] Ferrer *et al.*[30] demonstrate that imidacloprid produces fragments at *m/z* 210, 209, and 175 which are formed from radical loss of NO_2, loss of HNO_2, and radical losses of NO_2 and Cl, respectively. The degradation of neonicotinoids has also been studied by electrospray ionization (ESI) and atmospheric pressure chemical ionization (APCI) mass spectrometry.[31] The full-scan mass spectrum and the tandem mass spectrum (MS/MS) of imidacloprid show that the most abundant ions in the mass spectra are *m/z* 256 and 212. Chai *et al.*[31] concluded that the product ion at *m/z* 212 is protonated imidacloprid urea, generated from an intramolecular nucleophilic reaction where the oxygen of the nitro group attacks the carbon of the guanidine group resulting in N_2O loss. Furthermore, Lopes *et al.*[32] explored the degradation of imidacloprid by ESI-MS in acidic aqueous solution induced by zero-valent metals (Fe, Sn, Zn) exposed to ultrasonic irradiation. The degradation pathway for imidacloprid involves the initial reduction of the NO_2 moiety to NH_2.[32]

Like nicotine, imidacloprid contains multiple protonation sites (Scheme 3.1). In nicotine, the pyridine nitrogen is computed to be only 9.7 kJ mol^{-1} more acidic than the pyrrole nitrogen; this made it difficult to assign a proton affinity to either of these nitrogens, which was determined by bracketing experiments in a Fourier transform ion cyclotron resonance (FT-ICR) spectrometer.[33] Vibrational spectroscopy (Infrared multiphoton dissociation, IRMPD, spectroscopy) experiments on gaseous protonated nicotine clearly showed that the protonated site was the pyridine nitrogen.[34]

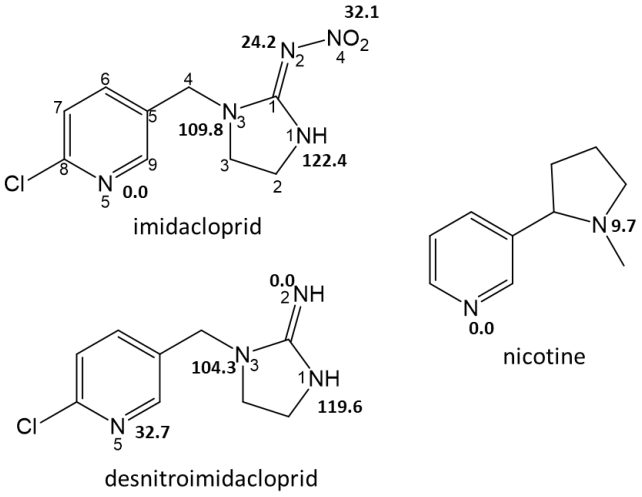

Scheme 3.1. Structures of imidacloprid, desnitroimidacloprid, and nicotine showing the computed differences in proton affinity (in kJ mol^{-1}) of their basic sites (imidacloprid and desnitroimidacloprid, reference 35; nicotine, reference 33). The scheme also shows the numbering for the nitrogen atoms and carbon atoms.

Imidacloprid contains five basic nitrogen atoms. The pyridine site is computed to be significantly more basic (24.2 kJ mol^{-1}) than the imine nitrogen[35] leaving little doubt as to the site of protonation, although there are no experimental determinations of the proton affinity of imidacloprid. More interesting, it has been determined that the two most basic sites in imidacloprid are reversed when imidacloprid loses $NO_2^{\bullet}$, the imine nitrogen being

32.7 kJ mol^{-1} more acidic than the pyridine nitrogen. This raises the obvious question as to the structure of protonated desnitroimidacloprid; does it retain the proton at the pyridine nitrogen, does it transfer to the imine nitrogen, or are there other lower energy tautomeric structures given the presence of the other N-H group. In a previous collision induced dissociation (CID) study, Donald *et al.*[35] observed that protonated imidacloprid loses $NO_2^{\bullet}$ and that a similar ion which has been methylated at the pyridine nitrogen does not lose $NO_2^{\bullet}$. Since in methylated imidacloprid, the charge is immobile, it was surmised that the position of the charge had a role in determining the fragmentation pattern, so proton transfer from the pyridine nitrogen to the imine nitrogen precedes $NO_2^{\bullet}$ loss in protonated imidacloprid. Indeed, their calculations provided a pathway that was slightly lower enthalpically, by 7 kJ mol^{-1}, for the proton transfer mechanism compared to simple loss of $NO_2^{\bullet}$ from the lowest energy protonated imidacloprid structure.

In this work, protonated imidacloprid and some of its fragmentation products are studied in the gas phase by IRMPD spectroscopy in the 600-2000 cm^{-1} region. The experimental IRMPD spectra are compared with the computed IR spectra from the electronic structure calculations to determine which structures contribute to the average population of sampled ions, and to provide more direct evidence of the protonation site of imidacloprid and its fragmentation products, including desnitroimidacloprid.

3.2. Methods

3.2.1. IRMPD Experimental Methods

All experiments were performed using a modified quadrupole ion trap mass spectrometer [Bruker, AmaZon Speed ETD] coupled to the Free Electron Laser for Infrared eXperiments (FELIX).[36,37] 1.0 mM imidacloprid solutions were prepared using 1.0 mL of 50/50 methanol and water to which 20 μL of 1% formic acid solution was added. Ions were generated by ESI using 20 μL of the 1.0 mM imidacloprid solution diluted to 1.0 mL of 50/50 acetonitrile and water. Precursor ions were isolated in the quadrupole ion trap and irradiated with two pulses of infrared radiation from the free electron laser (FEL). The isolated imidacloprid ions were irradiated for 0.5-1 s at a 10 Hz pulse repetition rate with each pulse having an energy of 40-100 mJ. The experimental IRMPD spectra were obtained by plotting the IRMPD efficiency, defined as the negative logarithm of the precursor intensity divided by the sum of the precursor and fragment ion intensities, versus the laser radiation wavenumber. All spectra were recorded in the 600-2000 cm^{-1} region. The bandwidth of the laser was 0.5% of the central frequency.

3.2.2. Computational Methods

Geometry optimizations and frequency calculations were conducted using the Gaussian 16 suite of programs.[38] Structures were optimized and their infrared spectra were computed using density functional theory (DFT) with the B3LYP functional and the 6-31+G(d,p) basis set. For all calculations, an empirical correction for dispersion was done using Grimme's D3 method with the original D3 damping function, B3LYP-D3.[39] Due to

errors associated with the harmonic approximation, the computed harmonic frequencies were scaled by 0.975 to better match with the experimental spectra.[40,41] The computed infrared spectra were convoluted with a Lorentzian profile with a width (FWHM) of 15 cm^{-1}. Reported thermochemistries, enthalpies and Gibbs energies, are 298 K values in kJ mol^{-1}.

3.3. Results and Discussion

3.3.1 IRMPD Mass Spectra

The mass spectra following isolation and IRMPD for protonated imidacloprid, *m/z* 256, and some of its dissociation products (loss of $NO^{\bullet}$, *m/z* 226; loss of N_2O, *m/z* 212; loss of $NO_2^{\bullet}$, *m/z* 210; and loss of 47 Da [N,O_2,H], *m/z* 209) are shown in Figure 3.1 labelled with the corresponding irradiation wavelength. Where comparisons exist, these IRMPD mass spectra are consistent with those observed for CID. For example, protonated imidacloprid shows fragment ions predominantly at *m/z* 226, 212, 210, 209, 175, and 128 corresponding to the losses of $NO^{\bullet}$, N_2O, $NO_2^{\bullet}$, HNO_2, NO_2Cl, and $C_3N_4O_2H_4$, respectively. The mass spectrum taken upon IRMPD of isolated *m/z* 226, protonated desnitrosoimidacloprid, shows that the *m/z* 209 ion is predominantly due to loss of $NO^{\bullet}$ followed by $^{\bullet}OH$ loss, entirely consistent with the conclusion of Donald *et al.*[32] The prominent fragment ion at *m/z* 173 in the IRMPD mass spectrum of *m/z* 226 corresponds to the loss of HCl, following the loss of $^{\bullet}OH$, which is also seen in the IRMPD mass spectrum of isolated *m/z* 209. The predominant loss upon IRMPD of isolated *m/z* 212, protonated imidacloprid urea, is a loss of 84 Da, with the molecular formula $C_3N_2OH_4$.

IRMPD of *m/z* 210, protonated desnitroimidacloprid, mostly shows the loss of $Cl^{\bullet}$ at *m/z* 175, but also some $H^{\bullet}$ loss at *m/z* 209. The *m/z* 174 peak could be due to loss of HCl from the *m/z* 210 ion or subsequent loss of $Cl^{\bullet}$ following $H^{\bullet}$ loss, however the absence of *m/z* 174 in the IRMPD mass spectrum of isolated *m/z* 209 rules out the latter.

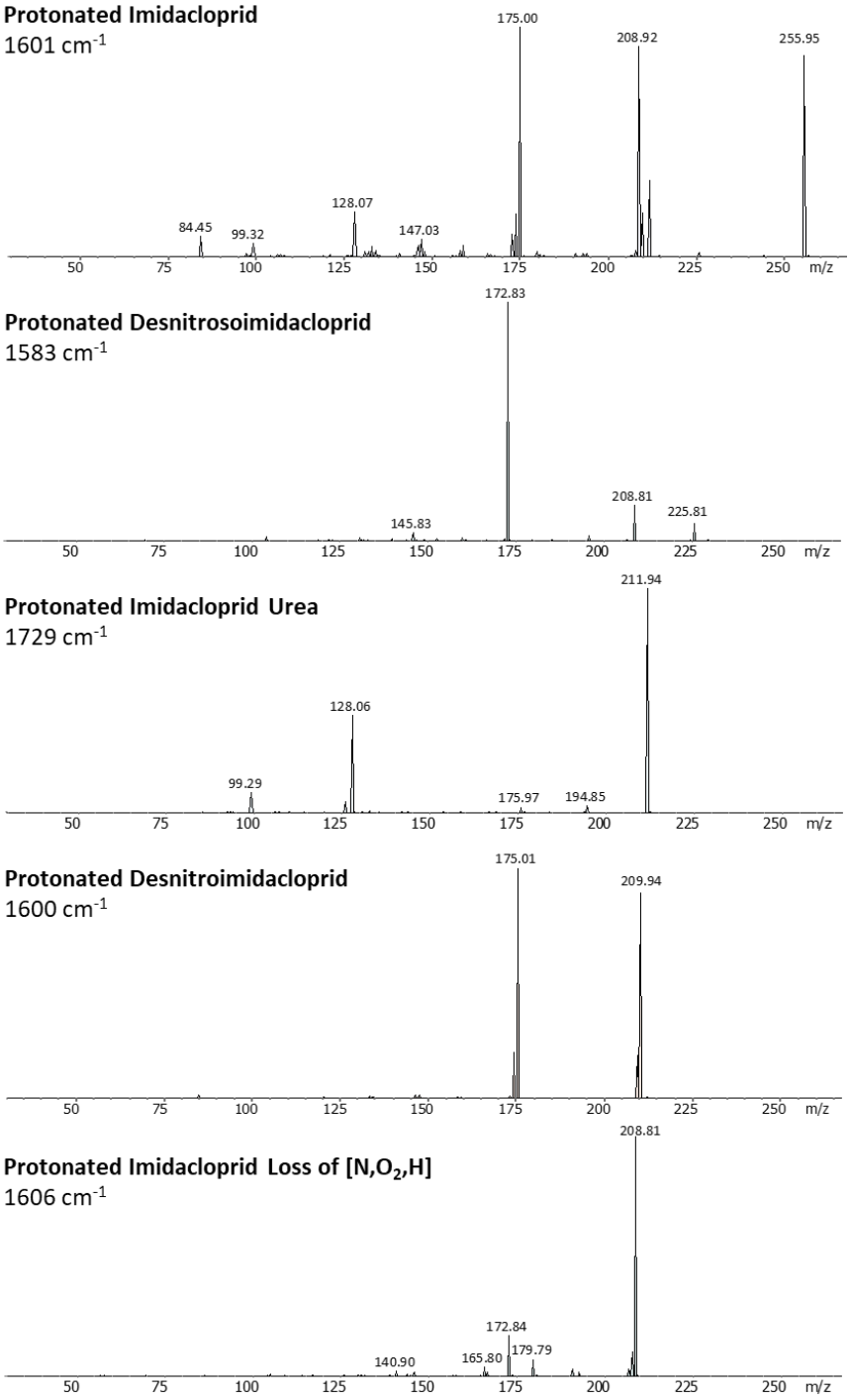

Figure 3.1. IRMPD mass spectra for protonated imidacloprid and its fragmentation products (*m/z* 256 → *m/z* 226, *m/z* 256 → *m/z* 212, *m/z* 256 → *m/z* 210, *m/z* 256 → *m/z* 209) at their maximum ion dissociation.

3.3.2. IRMPD Spectroscopy

3.3.2.1 Protonated Imidacloprid, *m/z* 256

The IRMPD spectrum for protonated imidacloprid in the 600-1800 cm^{-1} region is presented in Figure 3.2 (black trace) and compared to the computed spectra of various isomers (grey traces). Strong absorptions are observed between 1500 and 1600 cm^{-1} with maxima at 1560 and 1595 cm^{-1} and a strong broad band between 1200 and 1350 cm^{-1}. Weaker spectral features are also observed at 1450 and 1495 cm^{-1} as well as at 1135 and 780 cm^{-1}. The computed infrared spectrum for the lowest energy structure, protonated at N5 and a hydrogen on N1 (pIMI_N1-N5), is in excellent agreement with the observed spectrum. The absorption at 1595 cm^{-1} is assigned predominantly to C=C stretching and N-H wagging in the chloropyridine ring, as well as C=N stretching in the imidazolidine ring. The 1560 cm^{-1} absorption is attributed to the O-N-O asymmetric stretch of the nitro group and C=N stretching in the imidazolidine ring. The broad feature that is observed between 1200 and 1350 cm^{-1} is assigned to mainly motions of the C-H and CH_2 groups and C=C-H bending of the chloropyridine ring. The weak bands at 1450 and 1495 cm^{-1} correspond to CH_2 scissoring modes.

Three other N1-N5 minima were found within 14.1 kJ mol^{-1} in Gibbs energy, and their spectra are compared to the observed spectrum in Figure S3.1 in the supplementary material. Structures pIMI_N1-N5 and pIMI_N1-N5b differ by a rotation of the two rings with the C-H bond ortho to the pyridine nitrogen being closer to N2 and O2. pIMI_N1-N5c and pIMI_N1-N5d have a rotation of the two rings such that the C-H para to the pyridine nitrogen is in proximity to the NNO_2 substituent of the imidazolidine ring. All

four of these structures produce virtually the same predicted infrared spectrum and none could be ruled out based on the agreement with the observed vibrational spectrum, but based on the computed relative Gibbs energies, structure pIMI_N1-N5 and pIMI_N1-N5b might be expected to be present in the greatest abundance and the breadth and lack of features in the 1200-1350 cm^{-1} feature supports this.

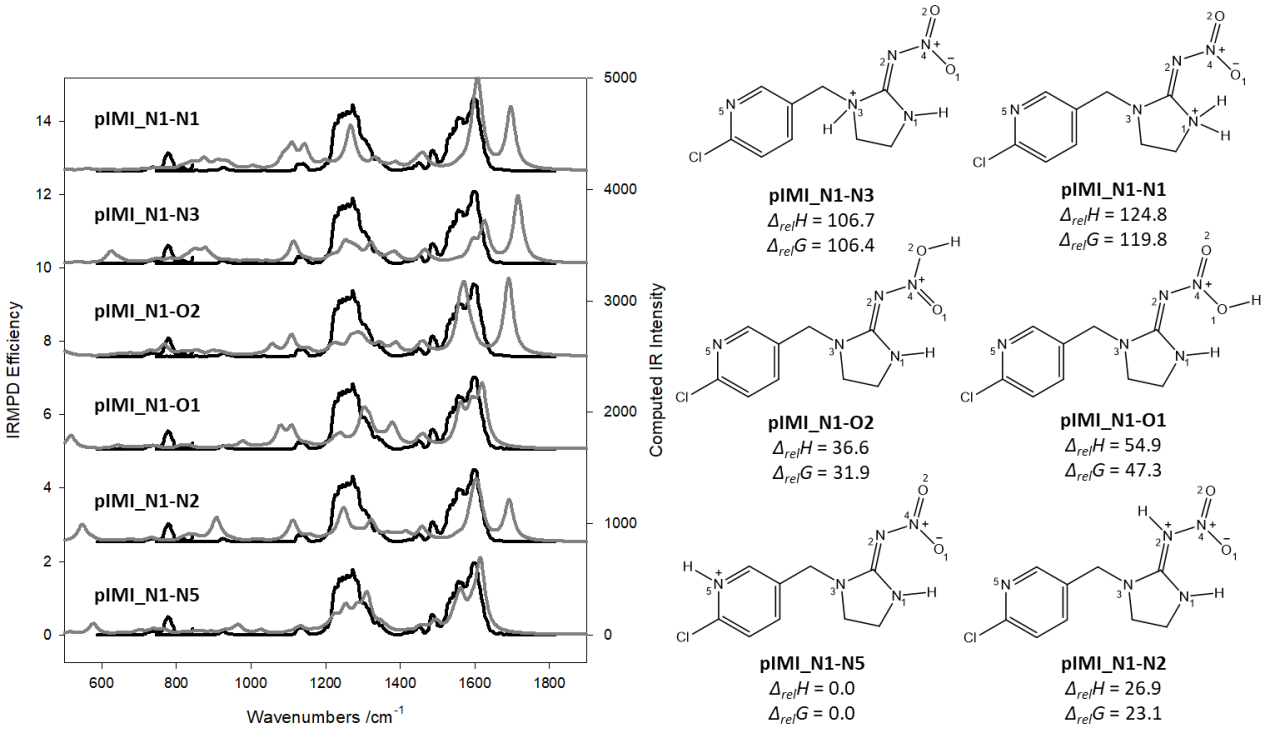

Figure 3.2. Comparison of the experimental IRMPD spectra (black trace) and the computed IR spectra (grey trace) for the lowest energy structures of protonated imidacloprid. Protonation at the nitrogen atom of the pyridine ring (N5 position) is calculated to be favoured over the other basic sites. All relative thermochemistries are 298 K values and are in kJ mol^{-1}.

The computed IR spectra for some higher energy N1 tautomer structures are also compared in Figure 3.2. The next lowest energy tautomeric structure, pIMI_N1-N2, protonated at N2, is 23.1 kJ mol^{-1} higher in Gibbs energy, and can be ruled out spectroscopically as there is an intense absorption predicted at 1692 cm^{-1} corresponding

to N-N-H bending in the nitroguanidine group which is not observed in the experimental spectrum. The O2 protonated structure, pIMI_N1-O2, is 31.9 kJ mol^{-1} higher in Gibbs energy and its computed infrared spectrum generally agrees with the observed spectrum, but it is not as good a match as the lowest energy structure, pIMI_N1-N5. Overall poor agreements are observed between the experimental spectrum and the calculated spectra for the pIMI_N1-O1, pIMI_N1-N3, and pIMI_N1-N1 structures which are 47.2, 106.4, and 119.8 kJ mol^{-1} higher in Gibbs energy, respectively. The intense bands predicted above 1690 cm^{-1} are due to N-O-H bending, N1-C-N2 asymmetric stretching, and N3-C-N2 asymmetric stretching for the pIMI_N1-O1, pIMI_N1-N3, and pIMI_N1-N1 structures, respectively. The poor agreement and featureless experimental spectrum between 1690 and 1800 cm^{-1}, rules out these higher energy structures as possible contributors to the experimental spectrum.

In Figures S3.2 and S3.3, the experimental vibrational spectrum of protonated imidacloprid is compared to other protonated tautomeric imidacloprid structures. None of the computed IR spectra closely resemble the experimental spectrum, and their computed energies are significantly higher than the N1-N5 tautomer. These higher energy tautomers can be ruled out as being significant contributors to the IRMPD spectrum.

Based on the spectroscopy as well as computed thermochemistries, the most likely structure of protonated imidacloprid is the N5 protonated N1 tautomer, pIMI_N1-N5.

3.3.2.2 Protonated Desnitrosoimidacloprid, *m/z* 226

Isolation and IRMPD activation of protonated imidacloprid resulted in the loss of NO$^{\bullet}$, *m/z* 226, corresponding to protonated desnitrosoimidacloprid. Scheme 3.2 shows two of

the possible protonation sites resulting from loss of NO•, one mechanism entails the direct dissociation of NO• without proton transfer and the other produces the lowest energy structure resulting from a proton transfer from N5 to N2, the former computed to be almost 22 kJ mol^{-1} higher in Gibbs energy. Donald *et al.*[32] also reported a proton affinity switch between the N5 and N2 position after NO• loss from protonated imidacloprid.

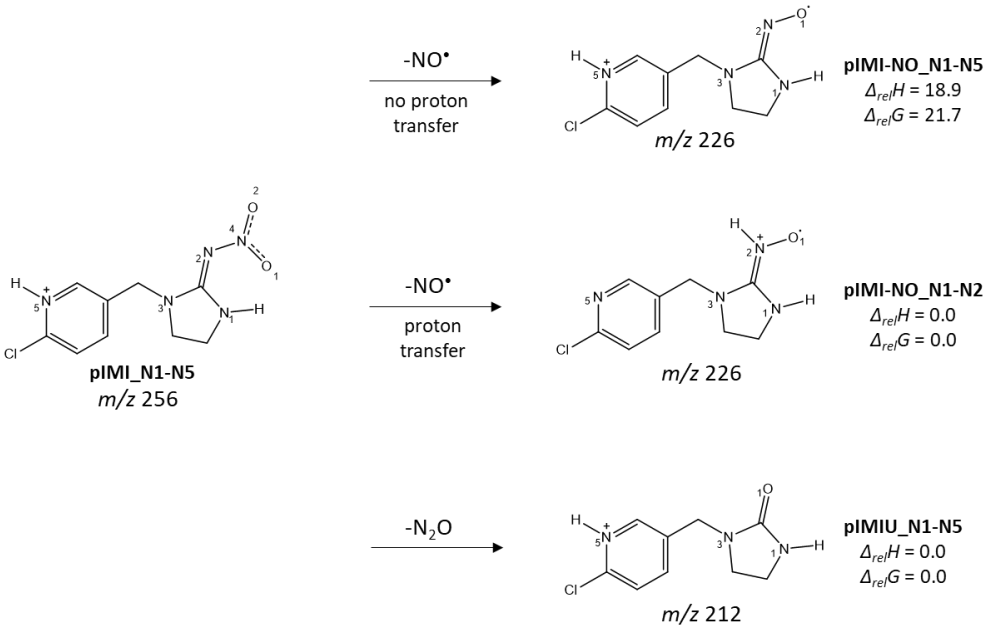

Scheme 3.2. Loss of NO• from protonated imidacloprid (without and with proton transfer) forming protonated desnitrosoimidacloprid and loss of N_2O from protonated imidacloprid forming protonated imidacloprid urea.

The IRMPD spectrum of protonated desnitrosoimidacloprid, pIMI-NO, in the 600-1800 cm^{-1} region is shown in Figure 3.3 and is compared to several possible isomers. The computed IR spectrum for the lowest energy isomer, protonated at N2 and a hydrogen at N1 (pIMI-NO_N1-N2), agrees very well with the experimental spectrum. Strong absorptions are observed between 1500 and 1650 cm^{-1} with maxima occurring at 1580 and 1630 cm^{-1}. The absorption at 1630 cm^{-1} corresponds to C=N2-H bending and N1-C-

N3 asymmetric stretching and the absorption at 1580 cm^{-1} is associated with C=C stretching in the chloropyridine ring and C-N1-H bending in the imidazolidine ring. The absorption band at 1485 cm^{-1} corresponds to C=C-H bending in the chloropyridine ring and N-H wagging in the imidazolidine ring. Features observed in the experimental spectrum between 1200 and 1400 cm^{-1} can be attributed to C-H and CH_2 bending modes. The absorptions centered at 1285 and 1110 cm^{-1} correspond to N-H wagging in the imidazolidine ring and C-Cl stretching in the chloropyridine ring, respectively.

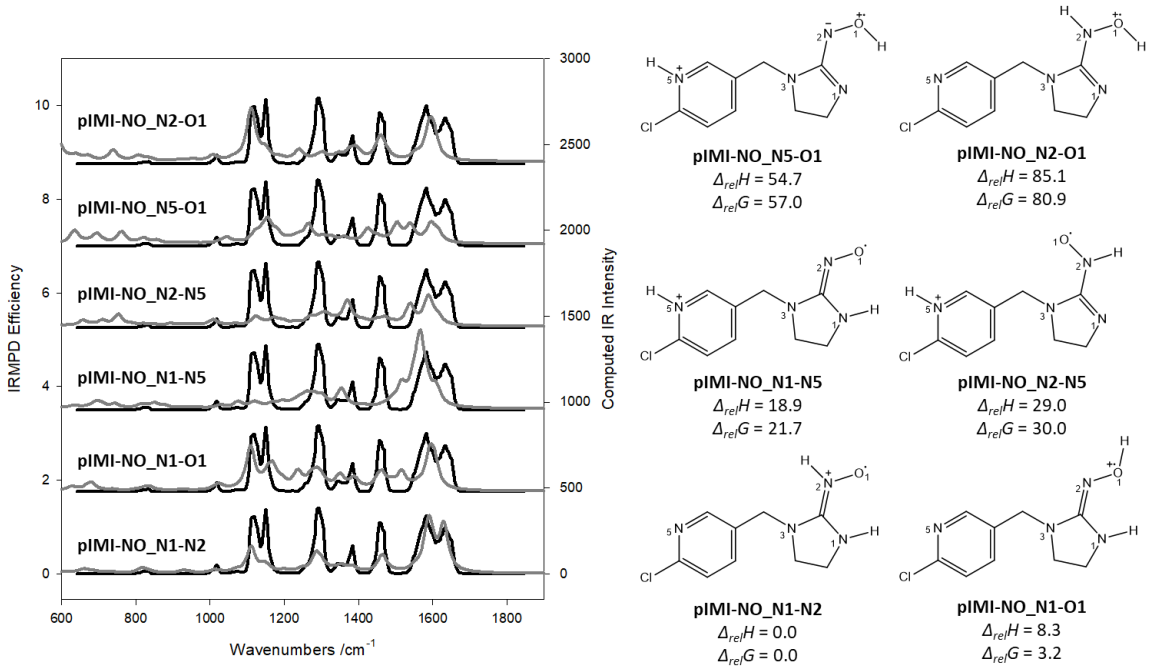

Figure 3.3. Comparison of the experimental IRMPD spectra (black trace) and the computed IR spectra (grey trace) for the lowest energy structures of protonated desnitrosoimidacloprid (loss of NO•). All relative thermochemistries are 298 K values and are in kJ mol^{-1}.

The computed IR spectra for higher energy pIMI-NO isomers are also compared to the experimental spectrum in Figure 3.3 and Figure S3.4. It is evident that these other isomers, including the N1-N5 isomer formed by simple NO• loss, can be ruled out

spectroscopically as both the C=N2-H bending mode and the N1-H wagging mode are not predicted by the electronic structure calculations. Furthermore, overall poor agreement is achieved between the experimental spectrum and the computed IR spectra of these higher energy isomers, thus these isomers can be ruled out as contributors.

Clearly, CID of protonated imidacloprid not only results in loss of $NO^{\bullet}$, but a N5 to N2 proton transfer to form the lowest energy isomer. The enthalpy and Gibbs energy barriers to proton transfer from N5 to N2 were computed to be about 150 and 160 kJ mol^{-1} (Figure S3.5).

3.3.2.3 Protonated Imidacloprid Urea, *m/z* 212

Protonated imidacloprid urea, *m/z* 212, is formed upon CID by loss of N_2O from protonated imidacloprid, Scheme 3.2. The IRMPD spectrum for protonated imidacloprid urea in the 600-1800 cm^{-1} region is depicted in Figure 3.4. Good agreement is obtained between the experimental spectrum and the computed spectrum for the lowest energy isomer, the N5 protonated N1 tautomer (pIMIU_N1-N5). An intense free C=O stretch is observed at 1730 cm^{-1}. Weaker bands are observed at 1580, 1530, 1485, 1410, and 1355 cm^{-1} in the experimental spectrum. These spectral features are due to C=C stretching and N-H wagging in the chloropyridine ring (1580 cm^{-1}), C=C-H bending and N-H bending (1530 cm^{-1}), CH_2 scissoring modes (1485 cm^{-1}), and CH_2 wagging and twisting modes (1410 and 1355 cm^{-1}). The intense absorption band centered at 1260 cm^{-1} in the experimental spectrum correlates well with the position of the predicted wagging and twisting motions of the three CH_2 groups. The two weaker low intensity absorptions at

1125 and 765 cm^{-1} can be attributed to the C-Cl stretching and N-H out-of-plane bending in the chloropyridine ring.

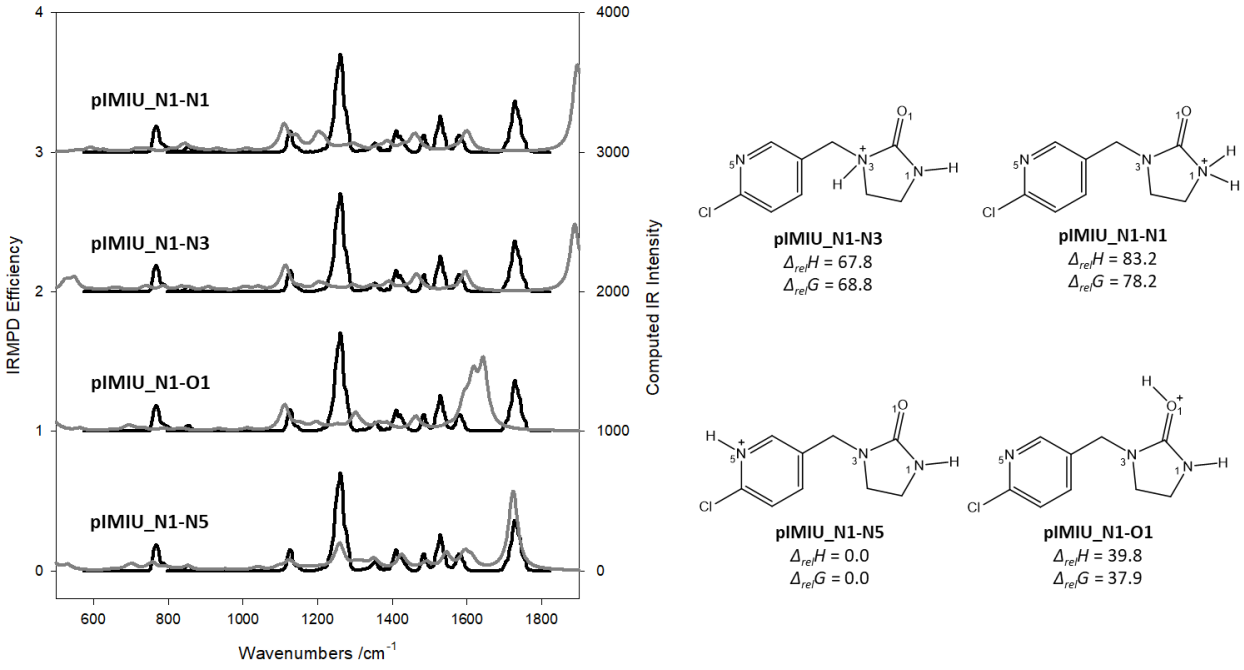

Figure 3.4. Comparison of the experimental IRMPD spectra (black trace) and the computed IR spectra (grey trace) for the lowest energy isomers of protonated imidacloprid urea (loss of N_2O). All relative thermochemistries are 298 K values and are in kJ mol^{-1}.

Three other computed spectra for higher energy N1-N5 conformers are compared to the computed spectra in Figure S3.6 and are within 8.4 kJ mol^{-1} in Gibbs energy. All four computed spectra are virtually indistinguishable in the fingerprint region and these conformers may certainly contribute to a minor extent to the experimental spectrum.

In Figure 3.4, the computed spectra for three higher energy N1 protomers – protonated at different positions – are compared to the experimental spectrum of protonated imidacloprid urea, and even higher energy isomers in Figure S3.7. The next lowest energy protomer is some 38 kJ mol^{-1} higher in energy than the lowest energy N1-

N5 structure. On inspection of Figures 3.4 and S3.7, it is clear that none of the computed IR spectra of the higher energy isomers account for the observed IRMPD spectrum. The spectroscopic results indicate that upon collisionally activated N_2O loss from protonated imidacloprid no hydrogen or proton transfer occurs. Based on the computational results, there is no thermodynamic drive for proton or hydrogen transfer since the lowest energy structure found is the N5 protonated N1 tautomer which is also the lowest energy protonated imidacloprid structure. Dissociation results of *m/z* 212 also support the charge being on N5 since loss of 84 Da is seen upon IRMPD of *m/z* 212 forming primarily *m/z* 128. This fragmentation is most likely loss of the imidazolidine-2-one moiety resulting in N-protonated 2-chloro-4 methylpyridine.

3.3.2.4 Protonated Desnitroimidacloprid, *m/z* 210

In section 3.3.2.1, it was shown that the structure which was entirely consistent with the observed vibrational spectrum of protonated imidacloprid was the lowest energy N1-N5 structure. Scheme 3.3 shows that simple cleavage of the N2-N4 bond to lose $NO_2^{\bullet}$ results in N5 protonated desnitroimidacloprid (pDIMI_N1-N5) which is not the lowest energy structure due to the switch in proton affinity from N5 to N2 upon loss of $NO_2^{\bullet}$. The pDIMI_N1_N2 structure was the lowest in energy found by Donald *et al.*[32] and is consistent with the present calculations which show it to be lower in Gibbs energy than the N1-N5 structure by about 33 kJ mol^{-1}. However, an even lower energy structure, pDIMI_N2-N2, is computed and involves both a proton shift from N5 to N2 and a hydrogen shift from N1 to N2.

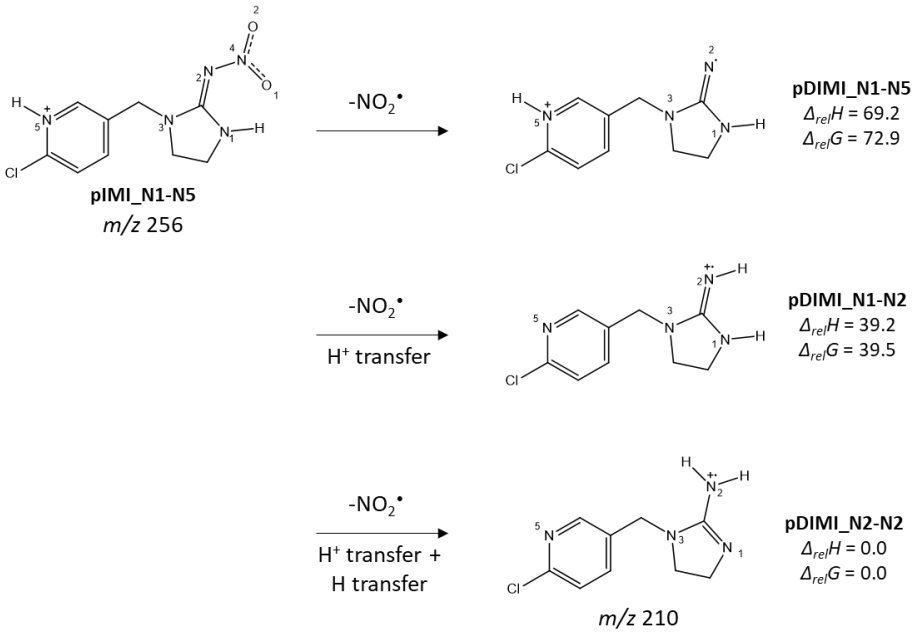

Scheme 3.3. Loss of $NO_2^{\bullet}$ from protonated imidacloprid forming protonated desnitroimidacloprid. Three mechanistic schemes consist of the direct dissociation of $NO_2^{\bullet}$, a proton transfer, and a proton transfer and hydrogen shift.

In Figure 3.5, the IRMPD spectrum of protonated desnitroimidacloprid, *m/z* 210, in the 600-1800 cm^{-1} region is presented and compared to the computed IR spectra of the six lowest energy computed isomers. The experimental IRMPD spectrum shows strong features at 1600, 1540, and 1460 cm^{-1}. Weak, but distinct shoulders are observed at 1485 and 1655 cm^{-1}. The absorption band observed at 1600 cm^{-1} can be attributed to C=C stretching, C=C-H bending and N-H wagging in the chloropyridine ring; the spectral feature at 1540 cm^{-1} corresponds to C=C-H bending and N-H wagging in the chloropyridine ring; and the band at 1460 cm^{-1} is assigned to CH_2 scissoring modes. Weaker absorptions are observed at 1345, 1300, 940, 810, and 625 cm^{-1} in the experimental spectrum.

Donald *et al.*[35] reasonably concluded that a proton transfer must occur prior to the loss of $NO_2^{\bullet}$ based on the fact that N5 methylated imidacloprid, where the charge is isolated at N5, does not lose $NO_2^{\bullet}$. A potential energy surface (UB3LYP)/6-311++G(d,p)) was constructed and showed that an indirect proton transfer from N5 to O2 and then O2 to N2 followed by the loss of $NO_2^{\bullet}$ producing pDIMI_N1-N2 was lower in energy than the direct dissociation route producing pDIMI_N1-N5. The indirect proton transfer enthalpy barrier was found to be 19 kJ mol^{-1} lower than the energy requirement for the direct loss of $NO_2^{\bullet}$. Similarly, a proton transfer directly from N5 to N2 followed by the loss of $NO_2^{\bullet}$ was also lower in energy than the direct dissociation pathway producing pDIMI_N1-N5 by 7 kJ mol^{-1}.[35] Our own UB3LYP/6-31+G(d,p) calculations (Figure S3.8) reproduce the energetics although the direct dissociation route is computed to be 35.9 kJ mol^{-1} higher in enthalpy than the indirect proton transfer barrier (a proton transfer from O2 to N2). However, when entropy is taken into account, the direct loss of $NO_2^{\bullet}$ is computed to be 24.4 kJ mol^{-1} lower in Gibbs energy than the direct proton transfer barrier (N5 to N2) and is 15.8 kJ mol^{-1} lower in Gibbs energy than the indirect proton transfer barrier (O2 to N2), making proton transfer prior to $NO_2^{\bullet}$ loss unlikely when entropy is taken into account.

More importantly, comparing the computed IR spectrum for pDIMI_N1-N2a (or the higher energy conformer, pDIMI_N1-N2b) in Figure 3.5, it is clear that these structures cannot be solely responsible for the observed vibrational spectrum. The general disagreement between the computed spectrum and the observed spectrum means that it is unlikely that proton transfer from N5 to N2 producing pDIMI_N1-N2 occurs to any great extent before or after loss of $NO_2^{\bullet}$.

It can be seen from Figure 3.5, by comparison of the computed IR spectrum for pDIMI_N2-N2 and the experimental spectrum that this lowest energy structure is also not entirely responsible for the experimental spectrum. The strongest absorption predicted for this isomer occurs at 1650 cm^{-1}, corresponding to NH_2 scissoring and C-N stretching in the guanidine moiety, but it is not predominant in the IRMPD spectrum, nor is the next strongest computed band, the C-Cl stretch, at about 1100 cm^{-1}. However, the weak shoulder observed at 1650 cm^{-1} is not predicted by any of the other computed isomers except the lowest energy pDIMI_N2-N2 structure. While pDIMI_N2-N2 cannot be completely ruled out, based on the weakness of the observed band, this isomer is not likely to be a major contributor.

The formation of pDIMI_N2-N2 would require an overall transfer of a proton from N5 to N2 and tautomerization from N1 to N2. In Figures S3.9 and S3.10, computed potential energy diagrams are shown that illustrate the proton transfer and tautomerization from pDIMI_N1-N5 to pDIMI_N2-N2 following $NO_2^{\bullet}$ loss, Figure S3.9 depicts a proton transfer preceding tautomerization, and S3.10 portrays a proton transfer succeeding tautomerization. The proton transfer, followed by tautomerization is the lowest energy route from pDIMI_N1-N5 to pDIMI_N2-N2, and the barriers are quite similar. They are, however, significantly higher (~50 kJ mol^{-1}) than for the proton transfer following $NO_2^{\bullet}$ loss which could be why proton transfer to the N1-N2 or N2-N2 structures are not observed to any great extent.

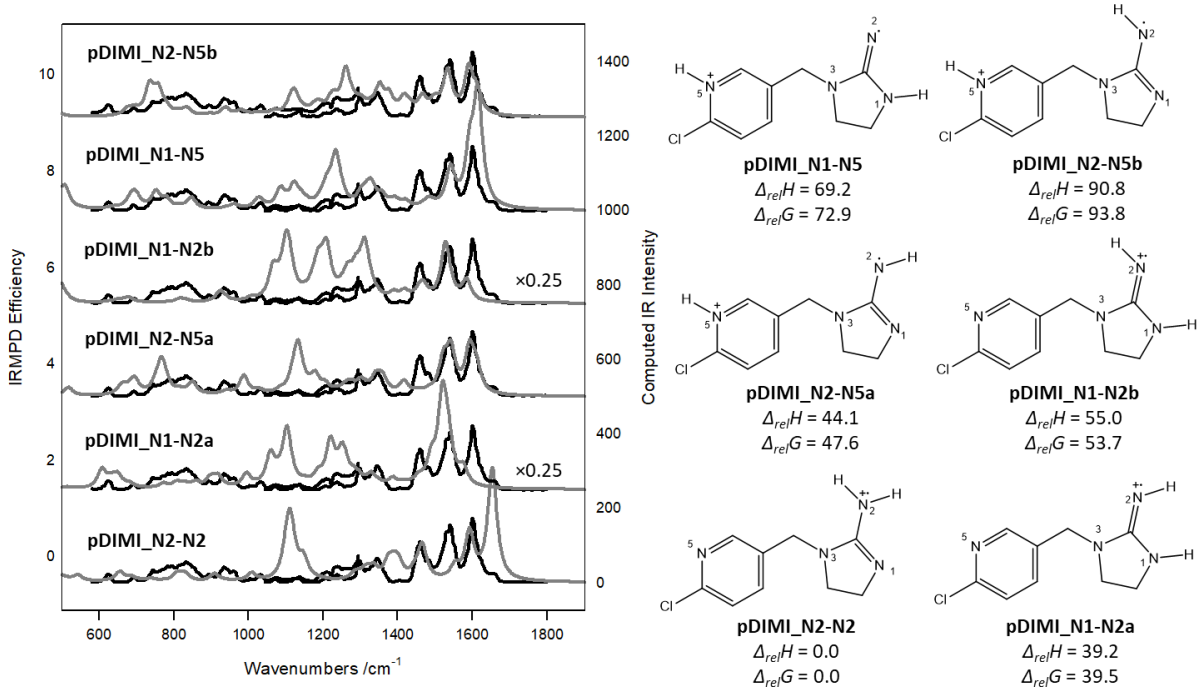

Figure 3.5. Comparison of the experimental IRMPD spectra (black trace) and the computed IR spectra (grey trace) for the lowest energy isomers of protonated desnitroimidacloprid (loss of $NO_2^{\bullet}$). All relative thermochemistries are 298 K values and are in kJ mol^{-1}.

The computed IR spectrum of the direct $NO_2^{\bullet}$ loss product, pDIMI_N1-N5, predicts many of the positions of the features observed in the experimental IRMPD spectrum and has a much better agreement than the two lower energy structures discussed so far. The tautomeric structures pDIMI_N2-N5a and pDIMI_N2-N5b are also decent matches to the experimental IRMPD spectrum, indicating that other higher energy tautomers may contribute to the vibrational spectrum of pDIMI. The N2-N5 structures do require a N1 to N2 tautomerization which is shown in the potential energy diagram in Figure S3.10. Figure S3.11 also compares the computed IR spectra of some much higher energy structures to the observed vibrational spectrum. Structures such as the pDIMI_N3-N5 structure, protonated at N3 cannot be completely ruled out based on the spectroscopy,

however, it is almost 100 kJ mol^{-1} higher in Gibbs energy than the global minimum and would require an endergonic proton and hydrogen transfer which are unlikely.

This example is clearly not as clean as those discussed above. This is due to there being a thermodynamic drive to tautomerize and undergo proton transfer to produce the lower energy isomers. If isomerization were required to occur before loss of $NO_2^{\bullet}$, then it would be expected that we would solely observe the N1-N2 structures which is not the case based on the spectroscopic results. The thermodynamic drive coupled with large energy barriers to proton and hydrogen transfer result in a complex mixture of protonated desnitroimidacloprid isomers.

3.3.2.5 Loss of [N,O_2,H] from protonated Imidacloprid, *m/z* 209

When protonated imidacloprid was isolated and subjected to IRMPD a prominent fragment ion at *m/z* 209 resulted from the loss of [N,O_2,H], see Figure 3.1. The *m/z* 209 ion is seen to result following isolation and fragmentation of both *m/z* 226 and *m/z* 210 indicating two sources; loss of $NO^{\bullet}$ followed by loss of $^{\bullet}OH$ and loss of $NO_2^{\bullet}$ followed by loss of $H^{\bullet}$, respectively. The prominent dissociation pathway for the dissociation of *m/z* 210 is loss of $Cl^{\bullet}$ (*m/z* 175), but the dissociation of *m/z* 226 produces predominantly *m/z* 209 and *m/z* 173. Further, *m/z* 173 is formed via loss of HCl following losses of $^{\bullet}OH$ and $NO^{\bullet}$. Based on this data, the *m/z* 209 ion isolated after CID of *m/z* 256, protonated imidacloprid, is predominantly formed by the loss of $NO^{\bullet}$ followed by the loss of $^{\bullet}OH$, with only a minor contribution from the losses of $NO_2^{\bullet}$ and then $H^{\bullet}$. In section 3.3.2.2 the structure of pIMI-NO, *m/z* 226, was concluded to be the lowest energy isomer, pIMI-

NO_N1-N2. First, we discuss the IRMPD spectra of *m/z* 209 in terms of loss of •OH from pIMI-NO_N1-N2.

The comparison between the computed IR spectra for four isomers and the experimental IRMPD spectrum in the 650-1850 cm^{-1} range for *m/z* 209 from protonated imidacloprid, pIMI-NO/OH, is presented in Figure 3.6 and there are comparisons with other higher energy isomers in Figures S3.12-S3.19 in the supplementary information. The lowest energy structure found is pIMI-NOOH_N2-N2a which can be formed via loss of NO• from protonated imidacloprid and then tautomerization from N1 to O1, followed by loss of •OH and then tautomerization from C2 to N2 (see Figure 3.7). The main disagreement between the experimental IRMPD spectrum and the computed spectrum for pIMI-NOOH_N2-N2a is the very strong N2=C stretching band predicted at 1700 cm^{-1}, but with no experimental band observed. Similarly, the comparison of the rest of the spectrum is generally poor.

The best matches to the experimental IRMPD spectrum are pIMI-NOOH_N1-N2b and pIMI-NOOH_N2-N2b which are 40 and 50 kJ mol^{-1} higher, respectively, in Gibbs energy than the lowest energy structure, pIMI-NOOH_N2-N2a. The weak experimental band observed at 1740 cm^{-1} is in good agreement with the predicted band positions for the N1-C=N2 and N1=C-N2 asymmetric stretches for the pIMI-NOOH_N1-N2b and pIMI-NOOH_N2-N2b isomers, respectively. Similarly, the most intense feature at about 1600 cm^{-1} in the experimental spectrum is well reproduced by the calculations for the pIMI-NOOH_N1-N2b and pIMI-NOOH_N2-N2b structures. The 1460 cm^{-1} band is better reproduced by the bend of the CH_2 group next to N3 in pIMI-NOOH_N1-N2b. In Figure S3.12 the computed spectra for some higher energy isomers are compared, but do not

agree as well with the experimental spectrum as does the pIMI-NOOH_N1-N2b computed spectrum.

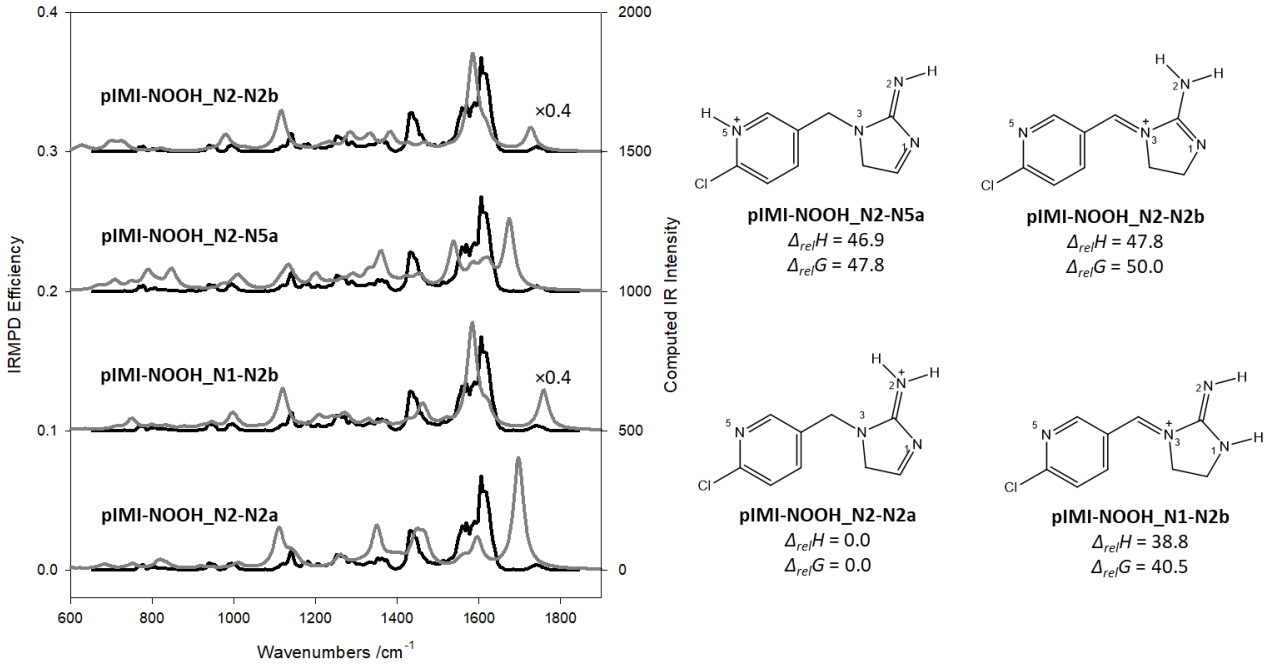

Figure 3.6. Comparison of the experimental IRMPD spectra (black trace) and the computed IR spectra (grey trace) for the loss of NO$^{\bullet}$ and $^{\bullet}$OH from protonated imidacloprid, singlet state isomers. All relative thermochemistries are 298 K values and are in kJ mol^{-1}.

In Figure 3.7 some possible pathways from protonated imidacloprid to pIMI-NO/OH are explored. As stated above, the first step is the loss of NO$^{\bullet}$ from protonated imidacloprid followed by a proton transfer from N5 to N2 producing pIMI-NO_N1-N2, the lowest energy *m/z* 226 structure. This is followed by isomerization transferring either the N1 or N2 hydrogen atom to the oxygen position, with Gibbs energy barriers (298 K) of 128.5 and 211.4 kJ mol^{-1}, respectively, forming pIMI-NO_N2-O1 and pIMI-NO_N1-O1, respectively. Note that while pIMI-NO_N2-O1 is higher in energy than pIMI-NO_N1-O1 by about 78 kJ mol^{-1}, the threshold for its formation is more than 80 kJ mol^{-1}

less. Both of the *m/z* 226 isomers can then lose •OH, forming high energy *m/z* 209 isomers (pDIMI-H_N1 and pDIMI-H_N2, both triplets) which are not expected to contribute to the experimental spectrum due to their poor agreement and the fact that they are so high in energy (see Figure S3.13). pDIMI-H_N1 can undergo a hydride transfer from C4 producing the singlet species pIMI-NOOH_N1-N2b. pDIMI-H_N2 can undergo tautomerization from either C4 or C2 to produce pIMI-NOOH_N2-N2b or pIMI-NOOH_N2-N2a, respectively. Despite pIMI-NOOH_N2-N2a being the thermodynamically favoured product, its formation is a multistep pathway (see Figure S3.20) with an energy requirement some 160 kJ mol^{-1} higher than for the formation of pIMI-NOOH_N2-N2b. The potential energy surface in Figure 3.7 is consistent with pIMI-NOOH_N2-N2b being the major *m/z* 209 product.

Other higher energy singlet structures can be seen in Figure S3.12 along with a comparison of their computed spectra with the experimental spectrum. Similarly, much higher energy triplet structures can be seen in Figure S3.13-S3.19. None of the structures agree very well with the experimental spectrum except for pDIMI-H_C2_N1-N5 (the triplet version of pIMI-NOOH_N2-N2a) which could be formed from pDIMI_N1-N5 following loss of a hydrogen atom from C2. While we cannot rule out this structure, it is probably a minor contributor since the NO•/•OH loss route is more likely than NO_2•/H• loss as described above.

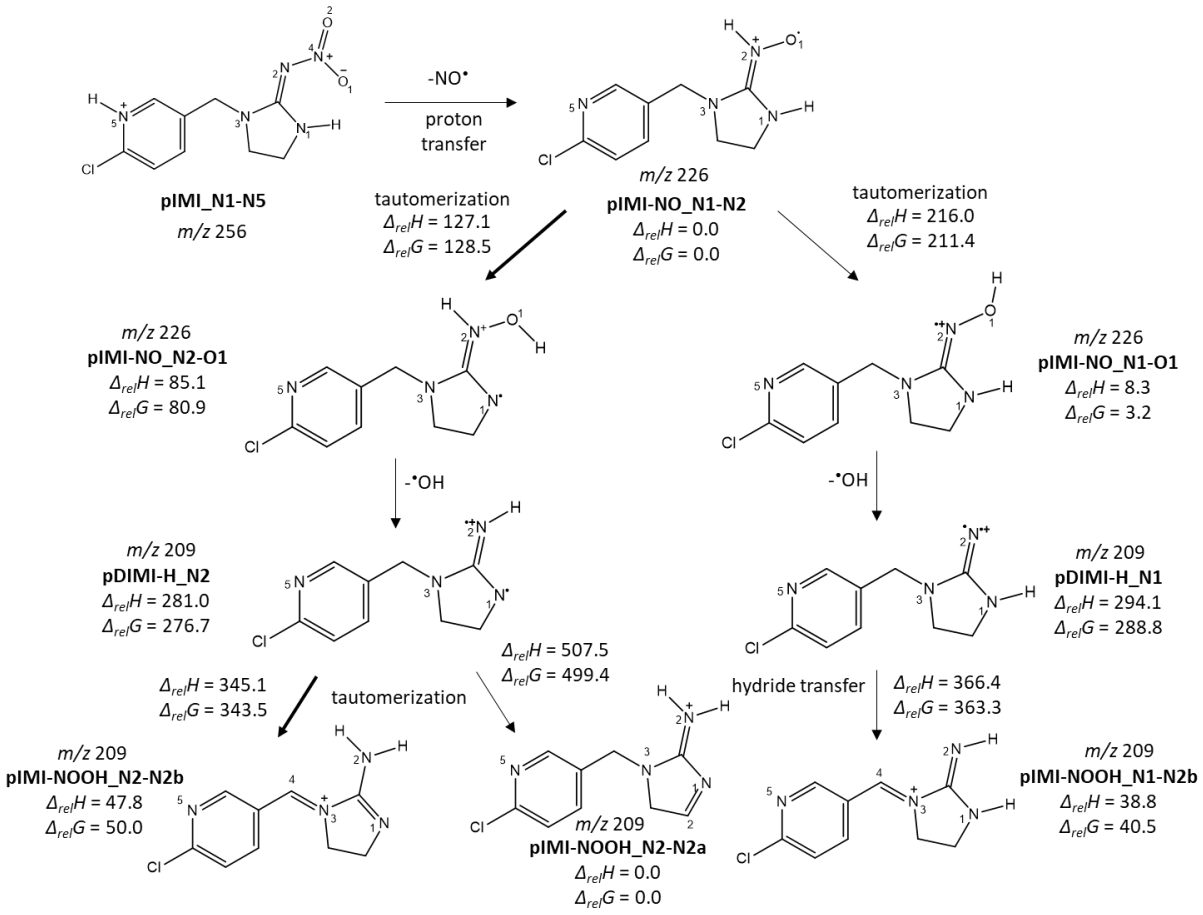

Figure 3.7. Potential mechanism for the formation of the *m/z* 209 ion resulting from the dissociation of NO• and •OH from protonated imidacloprid.

3.3.2.6. Protonated Dechlorinated Desnitroimidacloprid, *m/z* 175

The computed IR spectra for protonated dechlorinated desnitroimidacloprid, pDIMI-Cl, are compared to the experimental spectrum in the 600-2000 cm^{-1} region and are shown in Figures 3.8-3.9 and Supplementary Figures S3.21-S3.28. The IRMPD spectrum exhibits a broad absorption with two distinct maxima centered at 1640 and 1560 cm^{-1}. Weaker spectral features are observed in the range of 1200-1400 cm^{-1}, displaying a moderately intense peak at 1370 cm^{-1}.

Imidacloprid residues found in medicinal plants were identified by LC-MS/MS analysis using ESI operated in positive ion mode. A fragmentation pathway for imidacloprid residues was suggested by Besil *et al.*[42] where the structure for protonated dechlorinated desnitroimidacloprid is portrayed as a triple state diradical ion, protonated at the imidazolidine nitrogen. The calculated IR spectra for the diradical isomers with triplet spin multiplicities are compared to the experimental IRMPD spectrum in Figures 3.8 and S3.21. The computed IR spectrum for the pDIMI-Cl_N2-N2 isomer generates the best match with the IRMPD spectrum. The strong absorption calculated at 1655 cm^{-1} is assigned to NH_2 bending and C-N stretching in the guanidine group and the minor absorption calculated at 1545 cm^{-1} corresponds to C=C-H bending in the pyridine ring. The positions of these bands agree exceptionally well with the spectral features observed at 1640 and 1560 cm^{-1}, however, the intensity of the 1560 cm^{-1} absorption is not reproduced by the calculations. The calculated IR bands in the 1200-1400 cm^{-1} region are due to motions of the C-H and CH_2 groups, which are in good agreement with the experimental spectrum. It is clear from observation that none of the higher energy triplet diradical isomers contribute to the structure of pDIMI-Cl due to the overall poor agreement observed between the computed IR spectra and the experimental IRMPD spectrum, nevertheless the energetics of pDIMI-Cl_N2-N2 suggest that this isomer is not responsible for the structure of protonated dechlorinated desnitroimidacloprid.

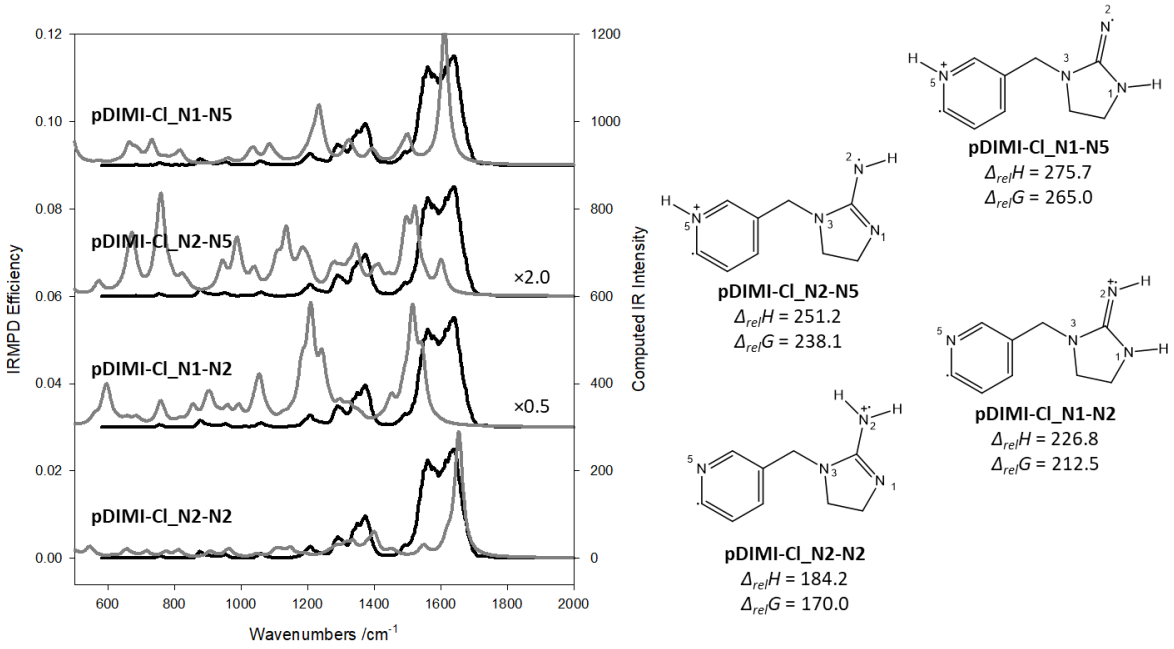

Figure 3.8. Comparison of the experimental IRMPD spectra (black trace) and the computed IR spectra (grey trace) for protonated dechlorinated desnitroimidacloprid (loss of $Cl^{\bullet}$), triplet state isomers. All relative thermochemistries are 298 K values and are in kJ mol^{-1}.

The fragmentation mechanism for the loss of $Cl^{\bullet}$ from protonated desnitroimidacloprid proposed by Donald *et al.*[35] involves intramolecular cyclization where the odd-electron radical generated in the pyridine ring reacts with the odd-electron radical of the guanidine moiety, forming a non-radical species with singlet spin multiplicity. A similar mechanism is reported by Chandran *et al.*[43] for the loss of $Cl^{\bullet}$ from the desnitro product ion of protonated nitenpyram, a nitromethylene neonicotinoid insecticide. For that reason, we inspected structures undergoing radical cyclization reactions. Firstly, we considered isomers where the guanidinyl radical attacks the C5=C6 bond or C5=C9 bond, generating a 5-membered ring encompassing the methylene bridge and the N2-C5 bond. The energetics and geometries of the pDIMI-Cl_N2C5A and

pDIMI-Cl_N2C5B isomers are depicted in the supplementary information (Figures S3.22 and S3.23); the pDIMI-Cl_N2C5 structural isomers differ by a rotation of the pyridine ring. It is noteworthy that the generated IR spectra for the N1-N2 isomers (pDIMI-Cl_N1-N2_N2C5A and pDIMI-Cl_N1-N2_N2C5B) and the N1-N5 isomers (pDIMI-Cl_N1-N5_N2C5A and pDIMI-Cl_N1-N5_N2C5B) are in reasonable agreement with the experimental IRMPD spectrum. The N1-N2 and N1-N5 computed isomers predict the absorption bands in the 1500-1700 cm^{-1} region, therefore, these calculated structures cannot be ruled out based on the spectroscopic agreement. Higher energy computed isomers protonated at various other basic sites shown in Figures S3.22 and S3.23 can be definitely ruled out energetically and spectroscopically.

The mechanism to form the second intramolecular cyclization reaction that we examined requires that the guanidinyl radical attacks the C6=C7 bond generating a 6-membered ring consisting of the N2-C6 bond; a radical-radical combination reaction occurs to form the C7=C8 bond. The singlet state pDIMI-Cl_N2C6 isomers are portrayed in Figure S3.24. The shape and positions of the calculated IR bands are in poor agreement with the measured bands, thus, the pDIMI-Cl_N2C6 computed structures can be excluded as possible contributors. The relative enthalpies and Gibbs energies suggest that these structures are not thermodynamically favoured. Moreover, the pDIMI-Cl_N2C6 isomers were subjected to a hydrogen shift from the C6 position to the N2 position. The singlet state pDIMI-Cl_N2C6H isomers are illustrated in Figure 3.9. It is evident from the comparison of the computed IR spectra and the IRMPD spectrum that the N1-N2-N5 isomer of the N2C6H structures demonstrates the best match with the experimental spectrum. The calculated IR band at 1652 cm^{-1} corresponds to C-N1-H and C-N2-H

bending in the imidazolidine ring, and the slight shoulder to the red of this calculated IR band corresponds to C=C-H bending in the pyridine ring and N3=C stretching (N3-C resonance form) in the imidazolidine ring. The minor calculated IR band predicted at 1546 cm^{-1} represents N5-H wagging, however, the intensity of the observed absorption is not reproduced by the calculations. The higher energy pDIMI-Cl_N2C6H computed structures can be eliminated as possible contributors with regard to the thermodynamic and spectroscopic results.

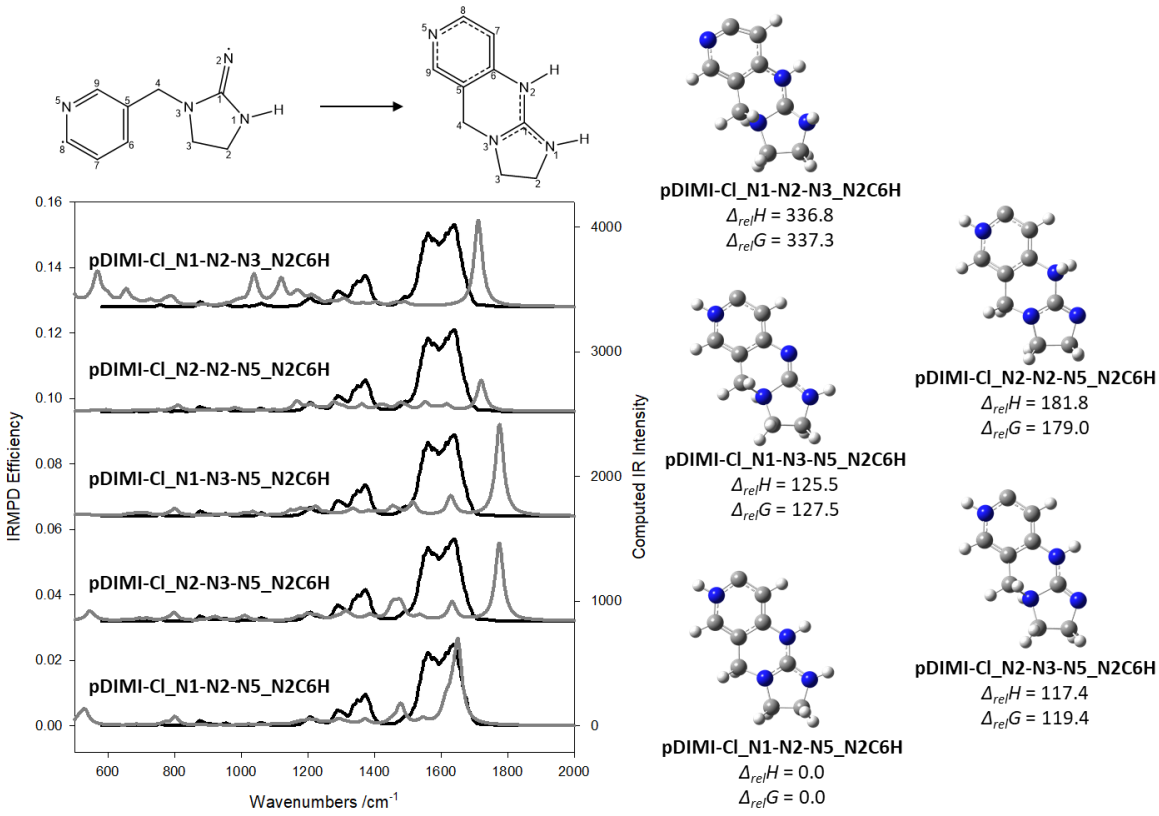

Figure 3.9. Comparison of the experimental IRMPD spectra (black trace) and the computed IR spectra (grey trace) for protonated dechlorinated desnitroimidacloprid (loss of $Cl^{\bullet}$), singlet state isomers involving N2-C6 bond formation and a hydrogen shift from C6 to N2. All relative thermochemistries are 298 K values and are in kJ mol^{-1}.

The mechanism to form the third intramolecular cyclization reaction we investigated involves guanidinyl radical attack on the C9=N5 bond generating a 6-membered ring that incorporates the N2-C9 bond; a radical-radical combination reaction occurs to produce the N5=C8 bond. The singlet state pDIMI-Cl_N2C9 isomers are displayed in Figure S3.25 and the computed IR spectra for the pDIMI-Cl_N2C6 and pDIMI-Cl_N2C9 isomers are virtually indistinguishable. None of the pDIMI-Cl_N2C9 computed structures generate a decent match with the IRMPD spectrum, thus, these isomers can be ruled out as probable contributors to the structure based on the spectroscopy and the energetics. The pDIMI-Cl_N2C9H isomers, shown in Figure S3.26, are closely related to the hydrogen shift isomers described above, however, in this case the isomers are derived from the pDIMI-Cl_N2C9 isomers, and the hydrogen is displaced from the C9 position to the N2 position. The computed IR spectrum of the N1-N2-N5 isomer of the N2C9H structures is the most consistent with the experimental IRMPD spectrum. The pDIMI-Cl_N1-N2-N5_N2C6H computed isomer generates a more fitting match with the experimental spectrum, and is lower in enthalpy and Gibbs energy than the pDIMI-Cl_N1-N2-N5_N2C9H isomer, however, neither isomer can be ruled out entirely. The higher energy pDIMI-Cl_N2C9H computed structures can be ignored as contributing to the observed vibrational spectrum due to the overall poor agreement between the experimental and computational results.

Lastly, we considered the intramolecular cyclization reaction reported by Donald *et al.*[35] for protonated dechlorinated desnitroimidacloprid. The pDIMI-Cl_N2C8A and pDIMI-Cl_N2C8B computed structures are generated from the radical-radical combination of the alkyl radical and the guanidinyl radical forming the N2-C8 bond. The

singlet state pDIMI-Cl_N2C8A and pDIMI-Cl_N2C8B isomers are presented in Figures S3.27 and S3.28, respectively. The comparison of the computed IR spectra and the experimental IRMPD spectrum reveals that none of the pDIMI-Cl_N2C8A and pDIMI-Cl_N2C8B computed structures can be eliminated as contributing to the IRMPD spectrum. The N1-N5 isomers predict the spectral feature observed at 1640 cm^{-1} corresponding to N2=C8 stretching, and the 1560 cm^{-1} spectral feature is also calculated but the intensity is not reproduced by the calculations. The N1-N2 isomers calculate the experimental IRMPD band at 1560 cm^{-1} which can be ascribed to C-N1-H and C-N2-H bending. The N1-N1 isomers predict a strong absorption for the 1640 cm^{-1} spectral feature which can be attributed to C=N2 stretching and NH_2 bending, and a minor absorption is calculated for the 1560 cm^{-1} spectral feature. The N2-N5 isomers predict the 1640 and 1560 cm^{-1} experimental bands which correlate to C=N1 stretching and N5-H wagging, respectively. The N2-N2 calculated isomers predict the 1640 cm^{-1} IRMPD absorption which is due C=N1 stretching, and a weakly intense IR band is calculated for the 1560 cm^{-1} IRMPD absorption. No individual pDIMI-Cl_N2C8A and pDIMI-Cl_N2C8B computed structure can be assigned as a primary contributor according to the spectroscopic comparison between the experimental spectrum and the computed spectra as well as the relatively high enthalpies and Gibbs energies computed.

The breadth of the 1500-1700 cm^{-1} absorption is not adequately reproduced by any of the investigated structures, therefore, additional geometry optimizations, energy calculations, and infrared spectroscopy data must be obtained to better describe the observed IRMPD spectrum.

3.4 Conclusions

A combination of IRMPD spectroscopy experiments in the 600-2000 cm^{-1} region and computational methods were conducted with the aim of elucidating the structures of protonated imidacloprid (pIMI) and its fragmentation products; protonated desnitrosoimidacloprid (pIMI-NO), protonated imidacloprid urea (pIMIU), protonated desnitroimidacloprid (pDIMI), the loss of N,O_2,H from protonated imidacloprid (pIMI-N,O_2,H), and protonated dechlorinated desnitroimidacloprid (pDIMI-Cl). The experimental IRMPD spectra were compared to the theoretical IR spectra and led to the definitive assignment of the lowest energy structures for pIMI, pIMI-NO, and pIMIU.

The decent agreement achieved between the calculated IR bands and the measured IRMPD bands for several isomers of protonated desnitroimidacloprid revealed a complex contribution, including isomers involving the simple loss of $NO_2^{\bullet}$ and some undergoing isomerization. Based on the comparison of the computed IR spectrum for the lowest energy structure of pDIMI and the IRMPD spectrum, it was concluded that the lowest energy structure did not contribute to the experimental spectrum. This observation is rationalized as being due to the energy requirement for proton transfer and hydrogen shift, being substantially higher than that for simple loss of $NO_2^{\bullet}$.

A comparison of the experimental IRMPD and computed IR spectra for the loss of $NO^{\bullet}$ and $^{\bullet}OH$ from protonated imidacloprid indicated that computed structures entailing a hydride shift from the methylene bridge to the guanidine moiety, succeeding $^{\bullet}OH$ elimination, generated the best match with the experimental spectrum. This was consistent with the computed potential energy surfaces showing this structure as having the lowest energy requirement.

3.5 References

1. Ding, T.; Jacobs, D.; Lavine, B. K. Liquid Chromatography-Mass Spectrometry Identification of Imidacloprid Photolysis Products. *Microchem. J.* **2011**, *99* (2), 535–541.
2. Yáñez, K. P.; Bernal, J. L.; Nozal, M. J.; Martín, M. T.; Bernal, J. Determination of Seven Neonicotinoid Insecticides in Beeswax by Liquid Chromatography Coupled to Electrospray-Mass Spectrometry Using a Fused-Core Column. *J. Chromatogr. A* **2013**, *1285*, 110–117.
3. Yamamoto, I.; Tomizawa, M.; Saito, T.; Miyamoto, T.; Walcott, E. C.; Sumikawa, K. Structural Factors Contributing to Insecticidal and Selective Actions of Neonicotinoids. *Arch. Insect Biochem. Physiol.* **1998**, *37* (1), 24–32.
4. Hao, C.; Noestheden, M. R.; Zhao, X.; Morse, D. Liquid Chromatography-Tandem Mass Spectrometry Analysis of Neonicotinoid Pesticides and 6-Chloronicotinic Acid in Environmental Water with Direct Aqueous Injection. *Anal. Chim. Acta* **2016**, *925*, 43–50.
5. Moreira, A. A. G.; De Lima-Neto, P.; Caetano, E. W. S.; Barroso-Neto, I. L.; Freire, V. N. Computational Electronic Structure of the Bee Killer Insecticide Imidacloprid. *New J. Chem.* **2016**, *40* (12), 10353–10362.
6. Cycoń, M.; Piotrowska-Seget, Z. Biochemical and Microbial Soil Functioning after Application of the Insecticide Imidacloprid. *J. Environ. Sci. (China)* **2015**, *27*, 147–158.
7. Fossen, M. Environmental Fate of Imidacloprid. *Regulation* **2006**, 1–16.

8. Seccia, S.; Fidente, P.; Barbini, D. A.; Morrica, P. Multiresidue Determination of Nicotinoid Insecticide Residues in Drinking Water by Liquid Chromatography with Electrospray Ionization Mass Spectrometry. *Anal. Chim. Acta* **2005**, *553* (1–2), 21–26.
9. Jovanov, P.; Guzsvány, V.; Franko, M.; Lazić, S.; Sakač, M.; Šarić, B.; Banjaca, V. Multi-Residue Method for Determination of Selected Neonicotinoid Insecticides in Honey Using Optimized Dispersive Liquid-Liquid Microextraction Combined with Liquid Chromatography-Tandem Mass Spectrometry. *Talanta* **2013**, *111*, 125–133.
10. Jiang, J.; Ma, D.; Zou, N.; Yu, X.; Zhang, Z.; Liu, F.; Mu, W. Concentrations of Imidacloprid and Thiamethoxam in Pollen, Nectar and Leaves from Seed-Dressed Cotton Crops and Their Potential Risk to Honeybees (Apis Mellifera L.). *Chemosphere* **2018**, *201*, 159–167.
11. Cresswell, J. E. A Meta-Analysis of Experiments Testing the Effects of a Neonicotinoid Insecticide (Imidacloprid) on Honey Bees. *Ecotoxicology* **2011**, *20* (1), 149–157.
12. Matsuda, K.; Buckingham, S. D.; Kleier, D.; Rauh, J. J.; Grauso, M.; Sattelle, D. B. Neonicotinoids: Insecticides Acting on Insect Nicotinic Acetylcholine Receptors. *Trends Pharmacol. Sci.* **2001**, *22* (11), 573–580.
13. Gbylik-Sikorska, M.; Sniegocki, T.; Posyniak, A. Determination of Neonicotinoid Insecticides and Their Metabolites in Honey Bee and Honey by Liquid Chromatography Tandem Mass Spectrometry. *J. Chromatogr. B Anal. Technol. Biomed. Life Sci.* **2015**, *990*, 132–140.

14. Fusetto, R.; White, J. M.; Hutton, C. A.; O'Hair, R. A. J. Structure of Olefin–imidacloprid and Gas-Phase Fragmentation Chemistry of Its Protonated Form. *Org. Biomol. Chem.* **2016**, *14* (5), 1715–1726.
15. Moreira, A. A. G.; De Lima-Neto, P.; Caetano, E. W. S.; Barroso-Neto, I. L.; Freire, V. N. The Vibrational Properties of the Bee-Killer Imidacloprid Insecticide: A Molecular Description. *Spectrochim. Acta - Part A Mol. Biomol. Spectrosc.* **2017**, *185*, 245–255.
16. Brandt, A.; Gorenflo, A.; Siede, R.; Meixner, M.; Büchler, R. The Neonicotinoids Thiacloprid, Imidacloprid, and Clothianidin Affect the Immunocompetence of Honey Bees (Apis Mellifera L.). *J. Insect Physiol.* **2016**, *86*, 40–47.
17. Jeria, Y.; Bazaes, A.; Báez, M. E.; Espinoza, J.; Martínez, J.; Fuentes, E. Photochemically Induced Fluorescence Coupled to Second-Order Multivariate Calibration as Analytical Tool for Determining Imidacloprid in Honeybees. *Chemom. Intell. Lab. Syst.* **2017**, *160* (July 2016), 1–7.
18. Kasiotis, K. M.; Anagnostopoulos, C.; Anastasiadou, P.; Machera, K. Pesticide Residues in Honeybees, Honey and Bee Pollen by LC-MS/MS Screening: Reported Death Incidents in Honeybees. *Sci. Total Environ.* **2014**, *485–486* (1), 633–642.
19. Lezi, N.; Economou, A. Voltammetric Determination of Neonicotinoid Pesticides at Disposable Screen-Printed Sensors Featuring a Sputtered Bismuth Electrode. *Electroanalysis* **2015**, *27* (10), 2313–2321.
20. Feltham, H.; Park, K.; Goulson, D. Field Realistic Doses of Pesticide Imidacloprid Reduce Bumblebee Pollen Foraging Efficiency. *Ecotoxicology* **2014**, *23* (3), 317–323.

21. Gross, M. EU Ban Puts Spotlight on Complex Effects of Neonicotinoids. *Curr. Biol.* **2013**, *23* (11), R462–R464.
22. Simon-Delso, N.; Amaral-Rogers, V.; Belzunces, L. P.; Bonmatin, J. M.; Chagnon, M.; Downs, C.; Furlan, L.; Gibbons, D. W.; Giorio, C.; Girolami, V.; et al. Systemic Insecticides (Neonicotinoids and Fipronil): Trends, Uses, Mode of Action and Metabolites. *Environ. Sci. Pollut. Res.* **2015**, *22* (1), 5–34.
23. Decourtye, A.; Devillers, J. Ecotoxicity of Neonicotinoid Insecticides to Bees. In *Insect Nicotinic Acetylcholine Receptors*; Thany, S. H., Ed.; Landes Bioscience and Springer Science+Business Media, 2010; Vol. 683, pp 85–95.
24. Suchail, S.; Guez, D.; Belzunces, L. P. Discrepancy Between Acute and Chronic Toxicity Induced By Imidacloprid and Its Metabolites in Apis Mellifera. *Environ. Toxicol. Chem.* **2001**, *20* (11), 2482.
25. Decourtye, A.; Lacassie, E.; Pham-Delégue, M. H. Learning Performances of Honeybees (Apis Mellifera L) Are Differentially Affected by Imidacloprid According to the Season. *Pest Manag Sci.* **2003**, *59* (3), 269–278.
26. Kamel, A. Refined Methodology for the Determination of Neonicotinoid Pesticides and Their Metabolites in Honey Bees and Bee Products by Liquid Chromatography-Tandem Mass Spectrometry (LC-MS/MS). *J. Agric. Food Chem.* **2010**, *58* (10), 5926–5931.
27. Schmuck, R. Effects of a Chronic Dietary Exposure of the Honeybee Apis Mellifera (Hymenoptera: Apidae) to Imidacloprid. *Arch. Environ. Contam. Toxicol.* **2004**, *47* (4), 471–478.

28. Xie, W.; Han, C.; Qian, Y.; Ding, H.; Chen, X.; Xi, J. Determination of Neonicotinoid Pesticides Residues in Agricultural Samples by Solid-Phase Extraction Combined with Liquid Chromatography-Tandem Mass Spectrometry. *J. Chromatogr. A* **2011**, *1218* (28), 4426–4433.
29. Liu, S.; Zheng, Z.; Wei, F.; Ren, Y.; Gui, W.; Wu, H.; Zhu, G. Simultaneous Determination of Seven Neonicotinoid Pesticide Residues in Food by Ultraperformance Liquid Chromatography Tandem Mass Spectrometry. *J. Agric. Food Chem.* **2010**, *58* (6), 3271–3278.
30. Ferrer, I.; Thurman, E. M.; Fernández-Alba, A. R. Quantitation and Accurate Mass Analysis of Pesticides in Vegetables by LC/TOF-MS. *Anal. Chem.* **2005**, *77* (9), 2818–2825.
31. Chai, Y.; Chen, H.; Liu, X.; Lu, C. Degradation of the Neonicotinoid Pesticides in the Atmospheric Pressure Ionization Source. *J. Am. Soc. Mass Spectrom.* **2018**, *29* (2), 373–381.
32. Lopes, R.; de Urzedo, A. P. F. M.; Nascentes, C. C.; Augusti, R. Degradation of the insecticides thiamethoxan and imidacloprid by zero-valent metals exposed to ultrasonic irradiation in water medium: electrospray ionization mass spectrometry monitoring. *Rapid Commun. Mass Spectrom.* **2008**, *22* (22), 3471–3480.
33. Graton, J.; Berthelot, M.; Gal, J. F.; Girard, S.; Laurence, C.; Lebreton, J.; Le Questel, J. Y.; Maria, P. C.; Nauš, P. Site of Protonation of Nicotine and Nornicotine in the Gas Phase: Pyridine or Pyrrolidine Nitrogen? *J. Am. Chem. Soc.* **2002**, *124* (35), 10552–10562.

34. Seydou, M.; Grégoire, G.; Liquier, J.; Lemaire, J.; Schermann, J. P.; Desfrançois, C. Experimental Observation of the Transition between Gas-Phase and Aqueous Solution Structures for Acetylcholine, Nicotine, and Muscarine Ions. *J. Am. Chem. Soc.* **2008**, *130* (12), 4187–4195.
35. Donald, W. A.; Leeming, M. G.; O'Hair, R. A. J. Gas-Phase Ion Chemistry of the Pesticide Imidacloprid: Proton Driven Radical Fragmentation of the Nitro-Guanidine Functional Group. *Int. J. Mass Spectrom.* **2012**, *316–318*, 91–99.
36. Martens, J.; Berden, G.; Gebhardt, C. R.; Oomens, J. Infrared Ion Spectroscopy in a Modified Quadrupole Ion Trap Mass Spectrometer at the FELIX Free Electron Laser Laboratory. *Rev. Sci. Instrum.* **2016**, *87* (10).
37. Martens, J.; van Outersterp, R. E.; Vreeken, R. J.; Cuyckens, F.; Coene, K. L. M.; Engelke, U. F.; Kluijtmans, L. A. J.; Wevers, R. A.; Buydens, L. M. C.; Redlich, B.; et al. Infrared Ion Spectroscopy: New Opportunities for Small-Molecule Identification in Mass Spectrometry - A Tutorial Perspective. *Anal. Chim. Acta* **2020**, *1093*, 1–15.
38. Frisch, M. J.; Trucks, G. W.; Schlegel, H. B.; Scuseria, G. E.; Robb, M. A.; Cheeseman, J. R.; Scalmani, G.; Barone, V.; Petersson, G. A.; Nakatsuji, H.; et al. Gaussian 16, Revision B.01. **2016**.
39. Grimme, S.; Antony, J.; Ehrlich, S.; Krieg, H. A Consistent and Accurate Ab Initio Parametrization of Density Functional Dispersion Correction (DFT-D) for the 94 Elements H-Pu. *J. Chem. Phys.* **2010**, *132*, 154104.
40. Linford, B. D.; Le Donne, A.; Scuderi, D.; Bodo, E.; Fridgen, T. D. Strong Intramolecular Hydrogen Bonding in Protonated β-Methylaminoalanine: A

Vibrational Spectroscopic and Computational Study. *Eur. J. Mass Spectrom.* **2019**, *25* (1), 133–141.

41. Cheng, R.; Loire, E.; Martens, J.; Fridgen, T. D. An IRMPD Spectroscopic and Computational Study of Protonated Guanine-Containing Mismatched Base Pairs in the Gas Phase. *Phys. Chem. Chem. Phys.* **2020**, 2999–3007.
42. Besil, N.; Pequeño, F.; Alonzo, N.; Hladki, R.; Cesio, M. V.; Heinzen, H. Evaluation of Different QuEChERS Procedures for Pesticide Residues Determination in Calendula Officinalis (L) Inflorescences. *J. Appl. Res. Med. Aromat. Plants* **2017**, *7* (September), 143–148.
43. Chandran, J.; Aravind, U. K.; Rajalakshmi, C.; Ipe, V.; Nguyen, P. T.; Aravindakumar, C. T. Solvent Dependent ESI-Collisionally Induced Dissociation of Protonated Nitenpyram. *Int. J. Mass Spectrom.* **2019**, *445*, 116207.

Chapter 4 – Investigation of the Structures and Unimolecular Fragmentations of Protonated Thiamethoxam in the Gas Phase by IRMPD Spectroscopy and Computational Methods

4.1 Introduction

Nicotine was once used as an insecticide to control sucking pests despite its relatively low potency toward insects.[1–3] Neonicotinoids are chemically similar to nicotine but contain unique structural features; possessing either a nitromethylene, nitroimine, or cyanoimine group that enhance their insecticidal efficacy in comparison to nicotine.[3–8] Neonicotinoids have a high target specificity to insects, acting at insect nicotinic acetylcholine receptors (nAChRs), making these insecticides particularly advantageous in the agricultural industry for crop protection against aphids, whiteflies, planthoppers, lepidopteran, dipteran, and coleopteran species.[4,9–12] Neonicotinoids persisting in the environment pose a significant threat to non-target organisms which include pollinators,[13–15] aquatic insects,[16,17] and birds[18,19] that are exposed to these insecticides.

Thiamethoxam is a second-generation insecticide belonging to the thianicotinyl subclass of the nitroguanidine class of neonicotinoids.[3,8,20] In plants and insects, the binding affinity of thiamethoxam on insect nAChRs is up to 10,000 times less active than other neonicotinoids, suggesting that the insecticidal activity of thiamethoxam is due to its open-chain metabolite clothianidin, which readily binds to the same receptor site as imidacloprid and other neonicotinoid compounds.[21] In mammalian systems, thiamethoxam metabolites are formed through cleavage of the nitroguanidine moiety,

producing the following metabolites: nitrosoguanidine (TMX-NNO), aminoguanidine (TMX-NNH_2), desnitroguanidine (TMX-NH), and the urea derivative (TMX-Urea).[22–25] Nitro reduction, demethylation (TMX-dm), and cleavage of the oxadiazine ring (formation of clothianidin) are the main metabolic reaction pathways of thiamethoxam in organisms.[22,25] Investigating the fragmentation pathways of thiamethoxam by applying mass spectrometric techniques is important for structural elucidation and understanding the unimolecular reactivities of thiamethoxam. In an electrospray ionization-collision induced dissociation (ESI-CID) study of nitenpyram, a nitromethylene neonicotinoid, it was found that the main fragmentation pathways of protonated nitenpyram are initiated by $NO_2^{\bullet}$ and $^{\bullet}OH$ losses.[26] The ESI-CID spectrum of protonated nitenpyram was contrasted with the CID spectrum of protonated imidacloprid previously investigated in the literature,[27] as well as thiamethoxam and ranitidine which are similar in structure to nitenpyram and consist of an NO_2 group.[26] In the ESI-CID spectrum of protonated thiamethoxam (*m/z* 292), minor $NO_2^{\bullet}$ and $NO^{\bullet}$ losses were observed (*m/z* 246 and *m/z* 262, respectively), however, the primary fragment ion results from the loss of $Cl^{\bullet}$ from protonated desnitro-thiamethoxam (*m/z* 246 → *m/z* 211). In addition, no $^{\bullet}OH$ elimination from the precursor ion is observed indicating that oxygen protonation does not occur.[26] Analogously, isotope labelling mass spectrometry experiments were conducted in order to assign fragment ions in the tandem mass spectrum (MS/MS) of thiamethoxam.[28] The MS/MS spectrum of protonated thiamethoxam (*m/z* 292) reveals fragment ions at *m/z* 211 and 181, which correspond to the loss of $NO_2^{\bullet}$ and $Cl^{\bullet}$ for the *m/z* 211 fragment ion, and the loss of N_2O_2, $Cl^{\bullet}$, and $CH_3^{\bullet}$ for the *m/z* 181 fragment ion, according to previously proposed fragmentation pathways.[29,30] Thiamethoxam isotope analogues, thiamethoxam-

d_3 and thiamethoxam-*d_4*, were used to assess the fragmentation pattern suggested in the literature. The MS/MS/MS analysis of thiamethoxam provides evidence that the fragment ion at *m/z* 181 is due to the loss of CH_2O from the fragment ion at *m/z* 211,[28] invalidating the proposed pathway. In the MS/MS spectrum of thiamethoxam, the fragment ion at *m/z* 246 originates from the loss of $NO_2^{\bullet}$, and the fragment ion at *m/z* 211 arises from the simultaneous loss of $NO_2^{\bullet}$ and $Cl^{\bullet}$,[28] consistent with the previously reported dissociation products.[29–33] It is interesting to note that in a study conducted using atmospheric pressure chemical ionization (APCI) and electrospray ionization (ESI) interfaces in mass spectrometry, protonated thiamethoxam urea is reported as a degradation product of protonated thiamethoxam, which is observed at *m/z* 248 in the mass spectrum.[34]

In this work, structures of protonated thiamethoxam and its fragment ions are investigated in the gas phase by infrared multiphoton dissociation (IRMPD) spectroscopy in the 600-1800 cm^{-1} region. Electronic structure calculations were carried out to compare the energies of isomeric structures and to compare the computed infrared (IR) spectra to the experimental IRMPD spectra.

4.2 Methods

4.2.1 Computational Methods

All calculations were performed using the Gaussian 16 program.[35] Optimized geometries and harmonic frequencies were carried out using the B3LYP density functional theory with the 6-31+G(d,p) basis set for all atoms. 298 K enthalpies and Gibbs energies, relative to the lowest energy structure, are reported in kJ mol^{-1}. Empirical dispersion

corrections were done using Grimme's D3 version with the original damping function, B3LYP-D3.[36] Due to errors associated with the computational method and the harmonic approximation, a scaling factor is applied. The vibrational frequencies were scaled by 0.975 when comparing the computed IR spectra to the experimental spectra,[37,38] and convoluted with a Lorentzian profile with a width (FWHM) of 15 cm^{-1}. Single point energy calculations using the B3LYP/6-311+G(3df,2pd) level of theory were performed on the lowest energy isomers of protonated thiamethoxam in order to compare electronic energies. When calculating thermodynamic properties for systems containing non-covalent interactions the M06-2X functional exhibits accurate results.[39] Optimization and frequency calculations were then repeated for the lowest energy isomers of protonated thiamethoxam using the M06-2X functional with the 6-31+G(d,p) basis set. The vibrational frequencies were scaled by 0.95 in the 600-1800 cm^{-1} region using the M06-2X/6-31+G(d,p) level of theory.[40]

4.2.2 Experimental Methods

IRMPD experiments were performed at the Free Electron Laser for Infrared eXperiments (FELIX) facility at Radboud University (Nijmegen, the Netherlands). Experiments were accomplished through the use of a 3D modified quadrupole ion trap (QIT) mass spectrometer [Bruker AmaZon Speed ETD] coupled to the IR beam line of the free electron laser.[41,42] FELIX provides tunable infrared radiation in the 600-1950 cm^{-1} region. The mass-isolated ions that are trapped in the QIT are irradiated with 5-10 μs macropulses (energies of 40-100 mJ/pulse) followed by a train of 6 ps long micropulses spaced by 1 ns. Thiamethoxam was obtained from Toronto Research Chemicals.

Protonated thiamethoxam ions were generated by electrospray ionization (ESI) using 20 µL of 1.0 mM thiamethoxam solution diluted in 1.0 mL of 50/50 acetonitrile and water. The 1.0 mM solution of thiamethoxam was prepared in 1.0 mL of 50/50 methanol and water to which 20 µL of 1% formic acid was added.

4.3 Results and Discussion

4.3.1 IRMPD Mass Spectra

Figure 4.1 depicts the IRMPD mass spectra for protonated thiamethoxam. The precursor ion at *m/z* 292 was isolated and subjected to IRMPD activation, producing fragment ions at *m/z* 246, 211, and 181, agreeing with the tandem mass spectrometry fragmentation pathways reported previously using CID as the activation technique.[28] The MS/MS spectrum for the *m/z* 246 product ion reveals fragmentations at *m/z* 211 and 181. In the MS^3 spectrum, the *m/z* 211 product ion dissociates into *m/z* 199, 181, 152, 139, and 122; where the most abundant fragment ion is the *m/z* 181 peak. The MS^4 spectrum for *m/z* 181 shows similar dissociation products at *m/z* 152, 139, and 122 so their appearance in the mass spectrum of *m/z* 211 is likely due to secondary fragmentation of *m/z* 181.

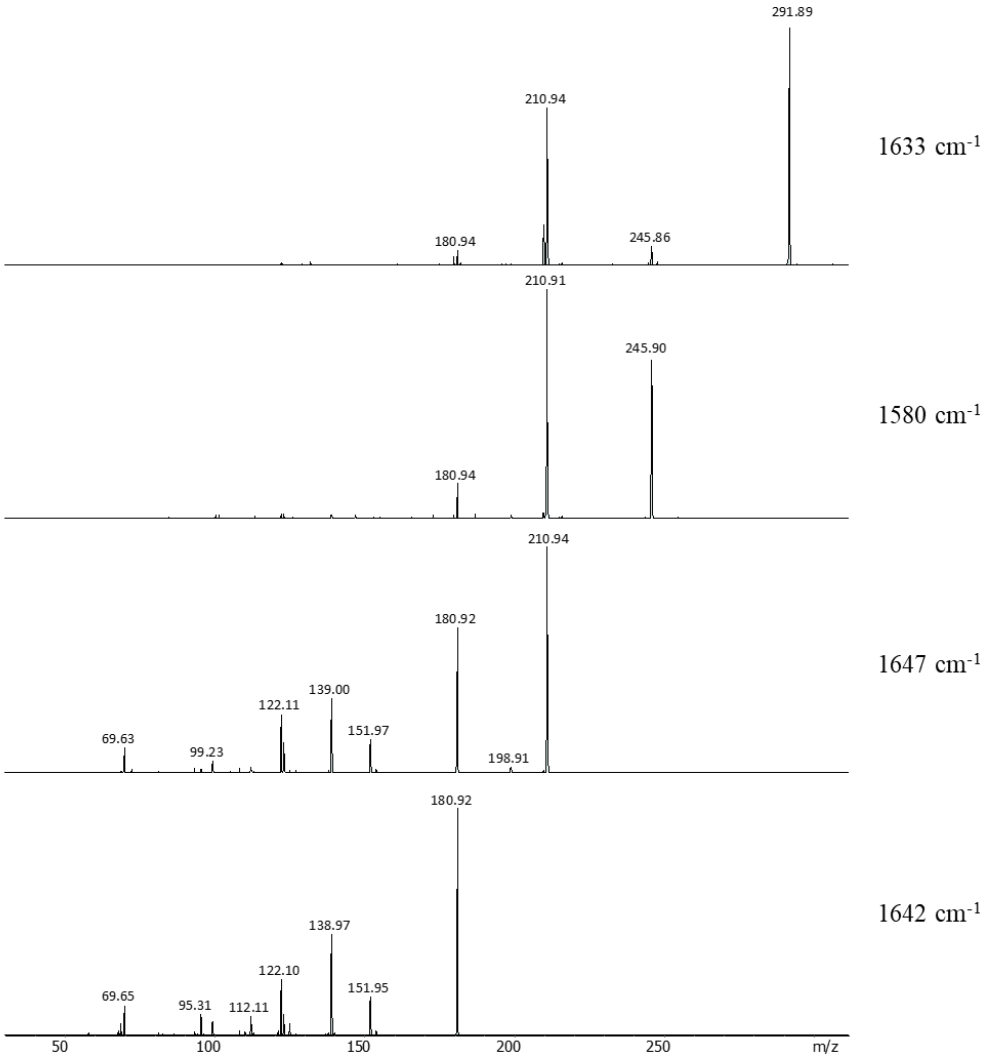

Figure 4.1. IRMPD mass spectra for protonated thiamethoxam and its fragmentation products (*m/z* 292 → *m/z* 246 → *m/z* 211 → *m/z* 181) at their maximum ion dissociation.

4.3.2 Computed Structures for Protonated Thiamethoxam

Structural optimization and frequency calculations were performed to determine the lowest energy isomers of protonated thiamethoxam (pTMX) and to investigate which isomer best represents the IRMPD vibrational spectrum. The thiamethoxam numbering scheme used throughout this study is presented in Scheme 4.1.

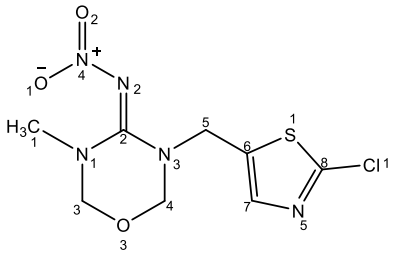

Scheme 4.1. Numbering scheme for thiamethoxam.

The structural isomers explored in the present study involve protonation at different basic sites. The schematics, geometries, and energetics of protonated thiamethoxam isomers using the B3LYP/6-31G+(d,p) level of theory are displayed in Figures 4.2 and 4.3. Protonation at the nitrogen atom in the nitroguanidine moiety (the N2 position) is the thermodynamically favoured site of protonation, followed by protonation at one of the oxygen atoms in the nitro group (the O2 position), differing by only 6.1 kJ mol^{-1} in Gibbs energy. Structures calculated using the M06-2X/6-31G+(d,p) level of theory are shown in Figures 4.4 and 4.5. In this case, protonation at the O2 position, the lowest energy isomer calculated using this level of theory, is computed to be 4.1 kJ mol^{-1} lower in Gibbs energy than protonation at the N2 position. The optimized geometries where protonation occurs at the O3 position results in cleavage of the C3−O3 or O3−C4 bond. The calculated IR spectrum of the lowest energy conformer of pTMX_O3 is compared to the experimental spectrum regardless of the O3 bond cleavage. Input calculations protonated at the N4 position resulted in optimized structures that converged to other protonation sites.

In order to conduct a complete investigation of the conformers of protonated thiamethoxam we adapted a computational method presented in the literature for calculating conformers of imidacloprid.[43] The conformational isomer with the lowest

Gibbs energy was selected for comparison with the vibrational spectrum. In the current work, the input structures were obtained by rotating the dihedral angle φ1-C2-N3-C5-C6 90° in a series of 3 steps while also rotating the dihedral angle φ2-N3-C5-C6-S1 180° in each step. Moreover, the dihedral angle φ3-N3-C2-N1-C1 was rotated by 60° and -60° from the initial position of 180°, generating a total of 24 conformers for each isomer. The half-chair enantiomers of the oxadiazinane ring structures for all conformers were calculated to determine if the calculated IR bands better explain the spectral features observed in the IRMPD spectrum. The comparison between the experimental IRMPD spectrum and the computed IR spectra for the half-chair enantiomers are shown in Supplementary Figures S4.1 and S4.2. Upon inspection, it is clear that the computed IR spectra for the half-chair enantiomers are identical to the computed IR spectra of the isomers presented in Figures 4.2 and 4.3, and the relative enthalpies and Gibbs energies are unchanged.

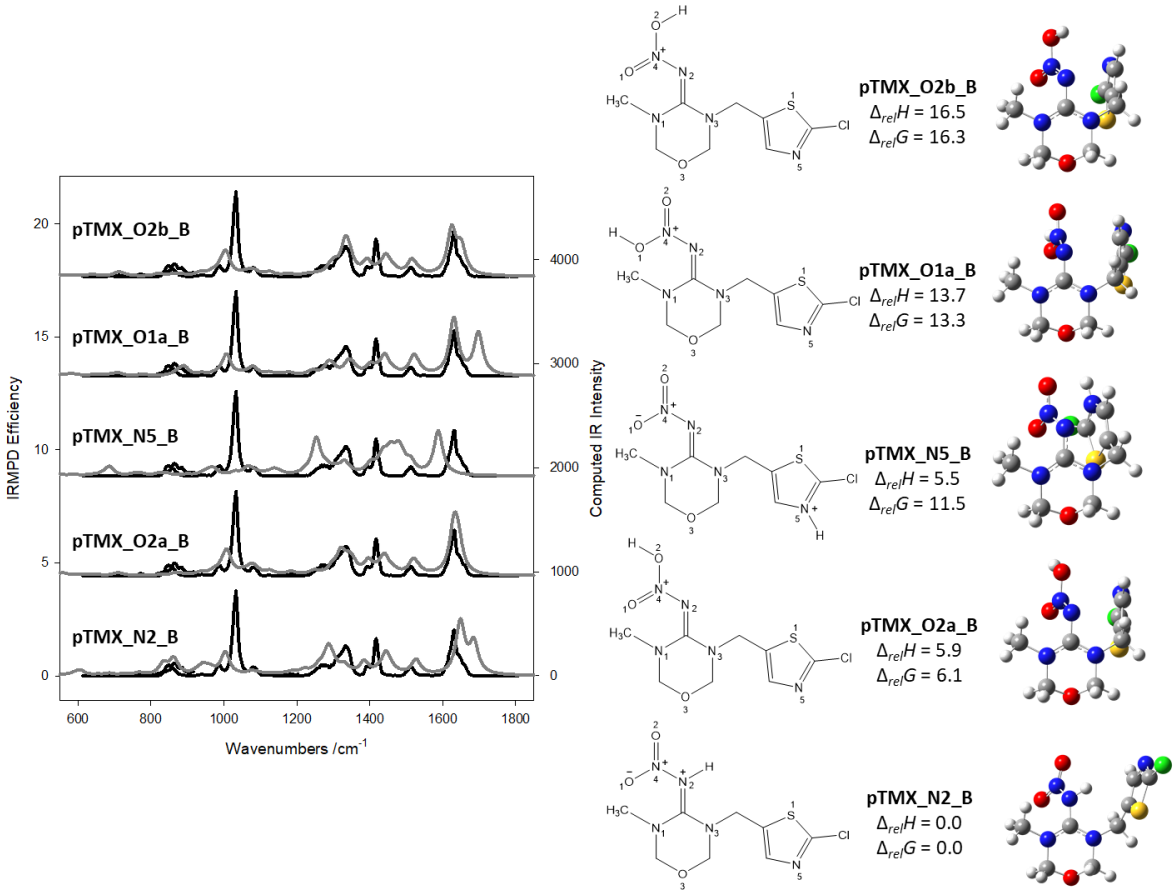

Figure 4.2. The experimental IRMPD spectrum (black trace) compared with the B3LYP computed IR spectra (grey trace) for the lower energy isomers of protonated thiamethoxam (pTMX_B).

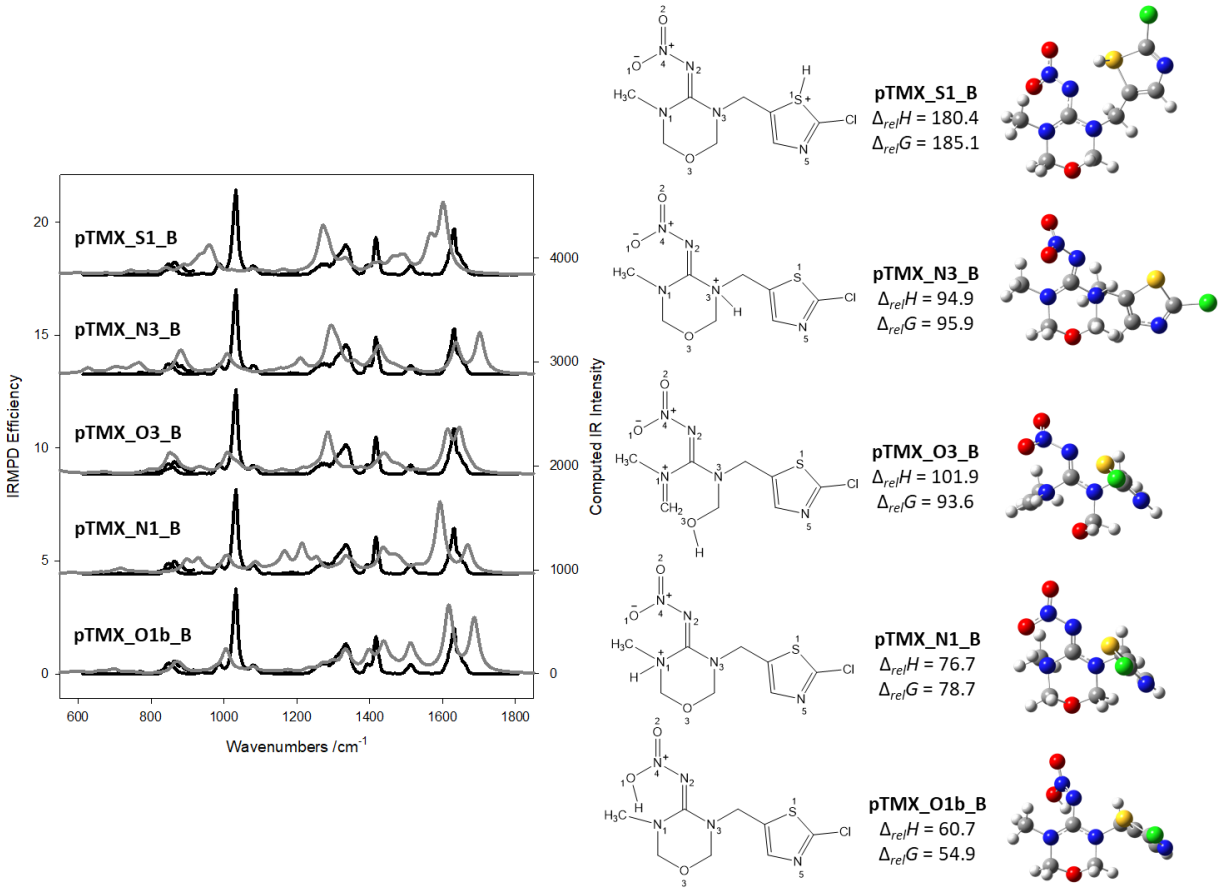

Figure 4.3. The experimental IRMPD spectrum (black trace) compared with the B3LYP computed IR spectra (grey trace) for the higher energy isomers of protonated thiamethoxam (pTMX_B).

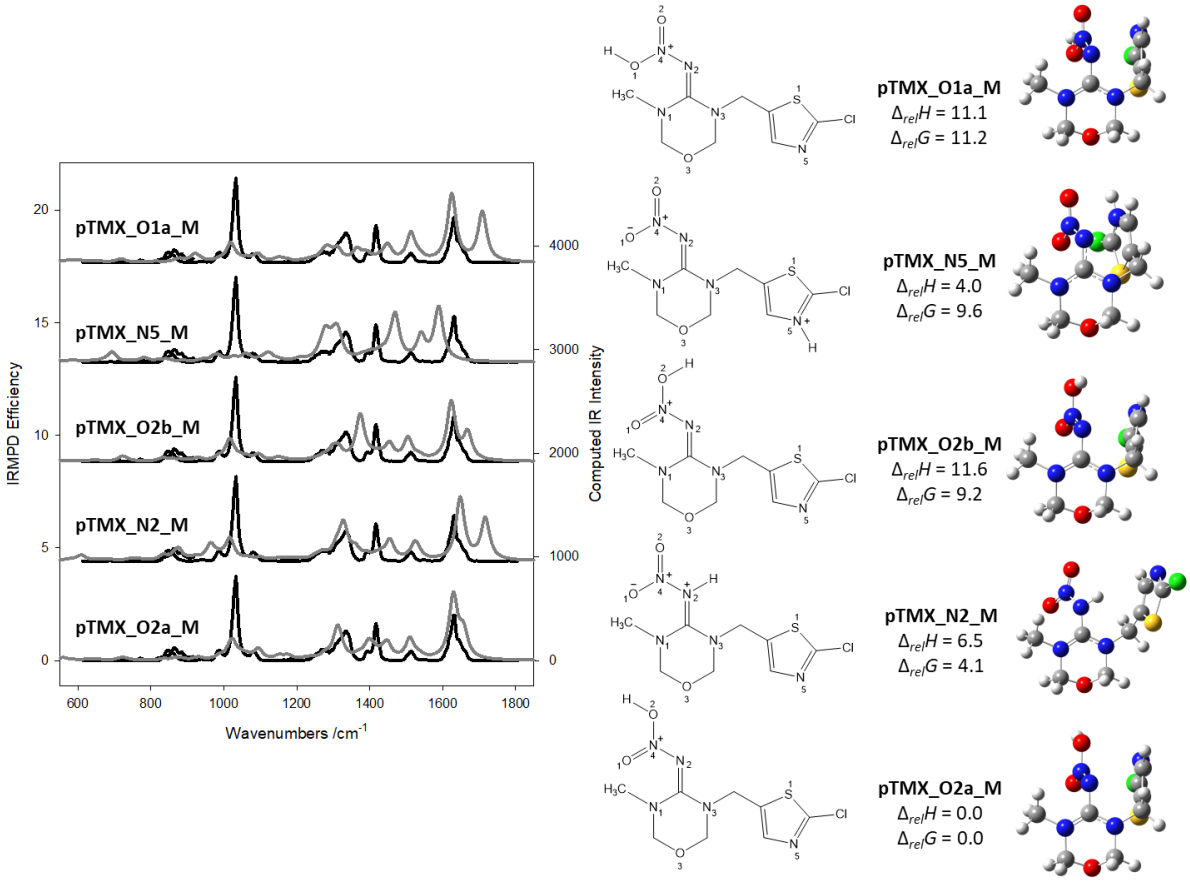

Figure 4.4. The experimental IRMPD spectrum (black trace) compared with the M06-2X computed IR spectra (grey trace) for the lower energy isomers of protonated thiamethoxam (pTMX_M).

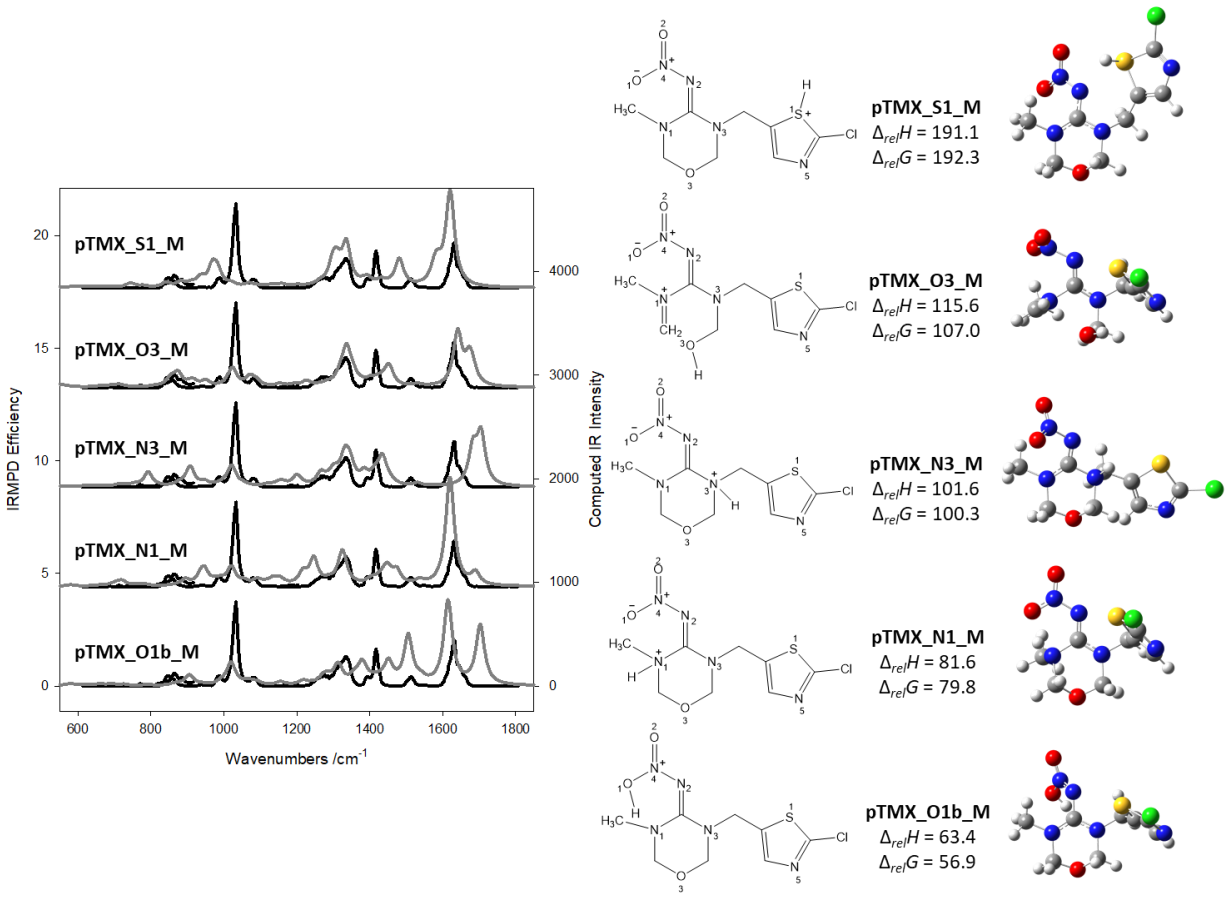

Figure 4.5. The experimental IRMPD spectrum (black trace) compared with the M06-2X computed IR spectra (grey trace) for the higher energy isomers of protonated thiamethoxam (pTMX_M).

4.3.3 Vibrational Spectroscopy for Protonated Thiamethoxam

The IRMPD spectra of protonated thiamethoxam and the computed IR spectra are compared in Figures 4.2-4.5 and Supplementary Figures S4.1-S4.2 in the 600-1800 cm^{-1} region. Evidently, the IRMPD spectrum is best reproduced by the calculated spectra where the proton is found on the O2 atom in the nitro group, pTMX_O2a_B (B3LYP method) and pTMX_O2a_M (M06-2X method). The experimental spectrum displays an

intense absorption band centered at 1633 cm^{-1}, with a slight shoulder to the blue side of the main absorption. From the calculated IR spectra of pTMX_O2a_B and pTMX_O2a_M, this absorption is predicted to occur at 1630 and 1629 cm^{-1}, respectively, corresponding to N=C−N asymmetric stretching in the oxadiazinane ring. The experimental, blue-shifted shoulder is better predicted by pTMX_O2a_M and correlates to O−H wagging and N−N=O asymmetric stretching in the nitro group. There is a minor spectral feature observed at 1510 cm^{-1} in the IRMPD spectrum which corresponds to N=C−N symmetric stretching. The strong absorption centered at 1417 cm^{-1} with a shoulder to the red of this band is predicted at 1440 and 1447 cm^{-1} by pTMX_O2a_B and pTMX_O2a_M, respectively, and can be assigned to N=C stretching in the chlorothiazole ring. Broad spectral features are observed in the range of 1250-1360 cm^{-1}, corresponding to CH_2 bending vibrations. There is a distinct maximum observed at 1033 cm^{-1} in the IRMPD spectrum which is predicted by the B3LYP and M06-2X calculations to occur at 1009 and 1023 cm^{-1}, respectively, and can be assigned to C−Cl stretching. The position of this calculated IR band matches well with the experimental band, although, the intensity does not agree strongly. The experimental absorption bands are in excellent agreement with the positions of the calculated IR bands, therefore, pTMX_O2a (and the higher energy conformer, pTMX_O2b) can be confidently assigned as major contributors to the structure of protonated thiamethoxam based on spectroscopic results. The thermodynamic results of the M06-2X calculations show that pTMX_O2a_M is the lowest Gibbs energy isomer, further supporting that pTMX_O2a_M is a plausible

structure, however, the B3LYP calculations show that pTMX_O2a_B is calculated to be 6.1 kJ mol^{-1} higher in Gibbs energy than the pTMX_N2_B isomer.

The comparison between the experimental IRMPD spectrum and the computed IR spectra involving protonation at the imine nitrogen of the nitroguanidine group, pTMX_N2_B and pTMX_N2_M, reveals a decent match between the experimental absorption at 1633 cm^{-1} and the computed absorption at 1648 cm^{-1}. An additional IR band is calculated at 1685 cm^{-1} for pTMX_N2_B and at 1717 cm^{-1} for pTMX_N2_M; nevertheless, this calculated IR band is absent in the experimental spectrum. The positions of the IR bands in the region of 1200-1600 cm^{-1} in the calculated spectra of pTMX_N2_B and pTMX_N2_M do not agree as well as the pTMX_O2a_B and pTMX_O2a_M calculations. The computed spectrum of the isomer protonated at the O2 position is more consistent with the vibrational spectrum, as a result the isomer protonated at the N2 position can ruled out spectroscopically. Overall poor agreement between the experimental and computed spectra is achieved for the other basic sites, consequently, the higher energy isomers (N5, O1, N1, O3, N3, and S1) can be eliminated as major contributors.

The computed 298 K relative enthalpies and Gibbs energies, in kJ mol^{-1}, are shown in Table 4.1. The M06-2X calculations show that the O2 position is the preferential site of protonation and the B3LYP calculations show that the N2 position is the favoured site of protonation. The split-valance basis set, 6-31+G(d,p), and the triple zeta basis set, 6-311+G(3df, 2pd), demonstrate the same general trend for the calculated thermochemistries when the B3LYP functional was employed. In the IRMPD mass spectrum displayed in the current study and in the CID spectrum of thiamethoxam shown

in the literature,[26] it is unmistakeable that no •OH dissociation is observed. Chandran *et al*.[26] rationalize that oxygen protonation in the nitro moiety is not likely to occur based on the observed fragmentation of protonated thiamethoxam. Notwithstanding, the IRMPD spectroscopy experiments and DFT calculations conducted in the present work reveal that oxygen protonation is in fact the most probable structure.

Table 4.1. A comparison of the 298 K relative enthalpies and Gibbs energies, in kJ mol^{-1}, of isomeric structures using three levels of theory.

	B3LYP/ 6-31+G(d,p)		**B3LYP/ 6-311+G(3df,2pd)**		**M06-2X/ 6-31+G(d,p)**	
Isomer	$\Delta_{rel}H$	$\Delta_{rel}G$	$\Delta_{rel}H$	$\Delta_{rel}G$	$\Delta_{rel}H$	$\Delta_{rel}G$
pTMX_N2	0.0	0.0	0.0	0.0	6.5	4.1
pTMX_O2a	5.9	6.2	7.2	7.3	0.0	0.0
pTMX_N5	5.5	11.5	7.1	13.1	4.0	9.6
pTMX_O1a	13.7	13.3	15.4	15.0	11.1	11.2
pTMX_O2b	16.5	16.3	16.3	16.0	11.6	9.2
pTMX_O1b	60.7	54.9	60.1	54.3	63.4	56.9
pTMX_N1	76.7	78.7	80.4	82.3	81.6	79.8
pTMX_O3	101.9	93.6	101.7	93.4	115.6	107.0
pTMX_N3	94.9	95.9	97.3	98.2	101.6	100.3
pTMX_S1	180.4	185.1	175.8	180.5	191.1	192.3

4.3.4 Computed Structures for Protonated Desnitro-Thiamethoxam

We first considered isomers of protonated desnitro-thiamethoxam (pDTMX) where the radical is localized on the N2 position of the guanidine group. All possible protonation sites were examined by placing the proton on various heteroatoms (N, O, and S). The energetics and geometries of the pDTMX isomers involving direct radical decomposition of NO_2 are presented in Figure 4.6. Next, we considered isomers where the radical is localized on the C7 position of the chlorothiazole ring. This mechanism requires the formation of a bond between N2 and C6 generating a 5-membered heterocyclic ring. Supplementary Figure S4.3 depicts the energetics and geometries of the pDTMX_N2-C6-S1 isomers where the radical is transferred to the C7 position, and the chlorothiazole ring is bonded directly to N2. The pDTMX_N2-C6-C7 isomers displayed in Supplementary Figure S4.4 differ from the aforementioned structures by a rotation of the chlorothiazole ring. Cleavage of the C6−S1 bond occurred in an effort to optimize structures where the proton was confined on the N5 and S1 basic sites. Consequently, we investigated isomers where the radical is transferred to the S1 position. The energies and optimized geometries of the pDTMX_S1d-C5 isomers entailing cleavage of the C6−S1 bond are presented in Supplementary Figure S4.5. The pDTMX_S1d-N2 isomers displayed in Supplementary Figure S4.6 differ from the pDTMX_S1d-C5 isomers in the orientation of the chlorothiazole chain, such that S1 is in proximity to N2. Supplementary Figure S4.7 shows pDTMX_S1d-C5H isomers which resemble the C6−S1 bond breakage structures, however, the S1d-C5H structures consist of a hydrogen shift from the C5 position of the methylene bridge to the S1 position of the chlorothiazole ring, the radical residing on the

C5 position. Moreover, we investigated isomers where the radical is localized on the C6 position. This is accomplished through bond formation between N2 and C7 producing a 6-membered heterocyclic ring. The energetics and geometries of the pDTMX_N2-C7 isomers are depicted in Figure 4.7. Lastly, an attempt was made to optimize geometries involving bond formation between N2 and S1, however, the structures reverted back to isomers where the radical is localized on the N2 position.

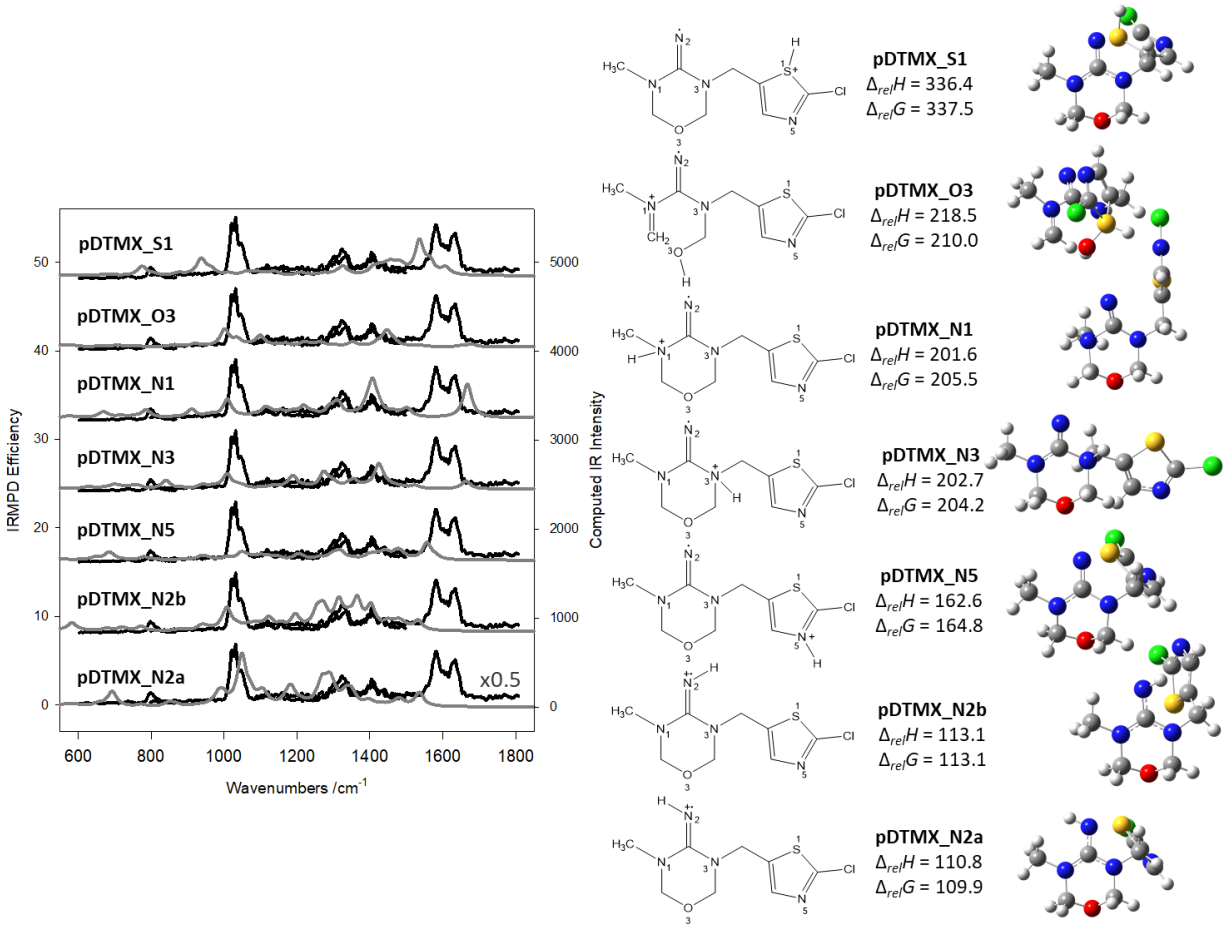

Figure 4.6. The experimental IRMPD spectrum (black trace) and the computed IR spectra (grey trace) for the isomers of protonated desnitro-thiamethoxam where the radical is localized on N2 (pDTMX).

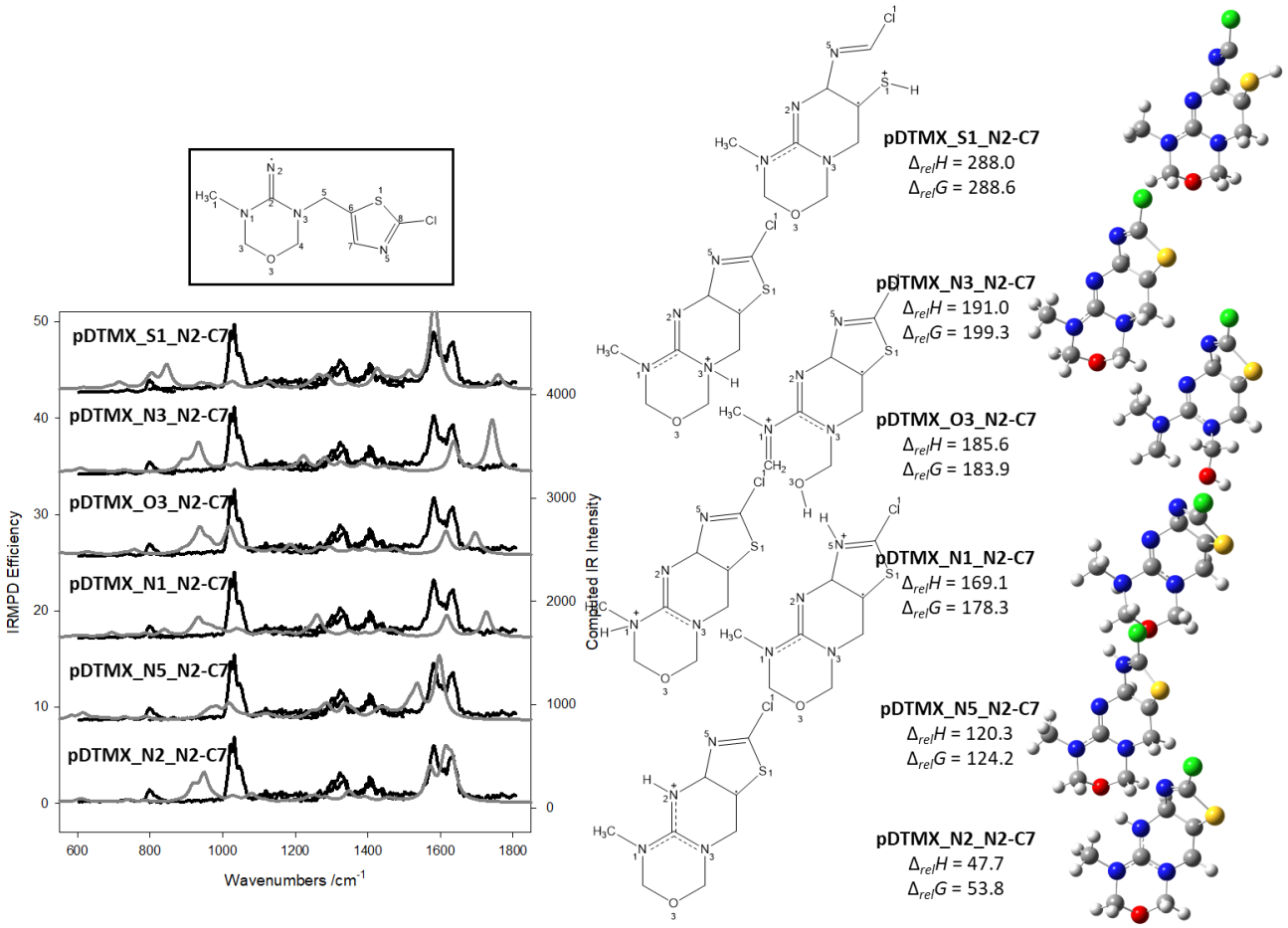

Figure 4.7. The experimental IRMPD spectrum (black trace) and the computed IR spectra (grey trace) for the isomers of protonated desnitro-thiamethoxam where the radical is localized on C6 (pDTMX_N2-C7).

4.3.5 Vibrational Spectroscopy for Protonated Desnitro-Thiamethoxam

The experimental IRMPD spectra compared to the computed IR spectra for protonated desnitro-thiamethoxam in the 600-1800 cm^{-1} region are presented in Figures 4.6-4.7 and Supplementary Figures S4.3-S4.7. The IRMPD spectrum displays an intense absorption with two distinct maxima – a band centered at 1635 cm^{-1} and another band at 1580 cm^{-1}.

Weaker absorptions are exhibited in the 1250-1450 cm^{-1} region. The most predominant spectral feature is observed at 1032 cm^{-1} which encompasses a shoulder to the blue.

The most prominent feature in the experimental spectrum at 1032 cm^{-1} is predicted by the pDTMX_N2a isomer, portrayed in Figure 4.6. The calculated IR band at 1049 cm^{-1} presents a good match with the experimental band revealing that the N2a isomer cannot be excluded as a possible contributor to the structure of protonated desnitro-thiamethoxam. The general disagreement obtained between the computed IR spectrum and the experimental spectrum in the 1540-1660 cm^{-1} and 1250-1450 cm^{-1} regions indicates that the N2a isomer is unlikely to be present in great abundance.

The intense spectral features observed at 1635 and 1580 cm^{-1} in the experimental spectrum are predicted at 1632 and 1571 cm^{-1} in the computed IR spectrum of pDTMX_N2_N2-C7, shown in Figure 4.7. The pDTMX_N2_N2-C7 structure is the only isomer investigated which is responsible for the absorptions observed in the 1540-1660 cm^{-1} region. The calculated IR band at 1632 cm^{-1} can be attributed to C=N2−H bending in the guanidine group and N1=C stretching (N1−C resonance form) in the oxadiazinane ring. The calculated IR band expected at 1613 cm^{-1} corresponds to N5=C stretching in the chlorothiazole ring and N3=C stretching (N3−C resonance form) in the oxadiazinane ring. The calculated IR band at 1571 cm^{-1} is assigned to N2=C stretching (N2−C resonance form) in the guanidine moiety. While the computed IR spectrum of pDTMX_N2_N2-C7 produces an excellent match with the IRMPD spectrum in the 1540-1660 cm^{-1} region, the spectroscopic agreement is very poor in the 1250-1450 cm^{-1} and 1000-1070 cm^{-1} regions. Also, the calculated IR band at 950 cm^{-1} is not observed in the

experimental spectrum. The N2 protonated N2-C7 isomer is not sufficient to explain the entire fingerprint region of the IRMPD spectrum for protonated desnitro-thiamethoxam, nonetheless, the N2-C7 structure cannot be eliminated as a possible contributor. The computed IR spectra of the pDTMX_N5_S1d-N2 and pDTMX_N5_S1d-C5H isomers, presented in Supplementary Figures S4.6 and S4.7, exhibit a reasonably good match with the experimental spectrum in the 1250-1450 cm^{-1} region. The weakly intense absorptions observed in this region correspond to CH_2 in-plane and out-of-plane bending, as well as C−H wagging.

4.3.6 Computed Structures for Protonated Dechlorinated Desnitro-Thiamethoxam

Isomers of protonated dechlorinated desnitro-thiamethoxam (pDTMX-Cl) were thoroughly explored in terms of bond connectivity and the location of the radical site. Triplet state pDTMX-Cl isomers resulting from the homolytic cleavage of $NO_2^{\bullet}$ and $Cl^{\bullet}$ without undergoing a skeletal rearrangement reaction are illustrated in Supplementary Figure S4.8. The radicals of the pDTMX-Cl isomers are situated on the N2 and C8 positions. The pDTMX-Cl structures are significantly higher (more than 385 kJ mol^{-1}) in enthalpy and Gibbs energy than the lowest energy structure, suggesting that contribution to any extent from the pDTMX-Cl isomers is improbable based on the computed energies. In Supplementary Figures S4.9 and S4.10, triplet state isomers of protonated dechlorinated desnitro-thiamethoxam involving radical migration are displayed. The mechanism to form the pDTMX-Cl_N2-C6-S1_T and pDTMX-Cl_N2-C6-C7_T isomers entails intramolecular radical cyclization. The N2 guanidinyl radical attacks the C6=C7 double bond, generating a 5-membered ring incorporating the methylene bridge and the

N2−C6 bond. An electron-transfer reaction occurs where the alkyl radical is transferred from the C6 position to the C7 position, forming the exo cyclized structure. These triplet state isomers differ from each other by a rotation of the thiazole ring. The N2-C6-S1_T and N2-C6-C7_T structures are notably higher (more than 293 kJ mol^{-1}) in enthalpy and Gibbs energy relative to the lowest energy structure calculated. In Supplementary Figures S4.11 and S4.12, singlet state isomers of protonated dechlorinated desnitro-thiamethoxam undergoing the same intramolecular radical cyclization reaction as the triplet state isomers are shown. The singlet state structures, pDTMX-Cl_N2-C6-S1_S and pDTMX-Cl_N2-C6-C7_S, require that the C7 methine radical combines with the C8 dechlorinated radical, giving rise to an electron pair on the C8 position. The computed energies of the N2-C6-S1_S and N2-C6-C7_S structures are remarkably higher in energy (more than 296 kJ mol^{-1}) than the lowest energy structure calculated, indicating that the N2-C6-S1 and N2-C6-C7 triplet and singlet state structures are not abundantly present.

In addition, isomers consisting of bond formation between N2 and C6 and cleavage of the C6-S1 bond are examined in Figure 4.8 and Supplementary Figure S4.13. Stabilization of the singlet state pDTMX-Cl_S1d-N2 and pDTMX-Cl_S1d-C5 isomers is obtained through a radical-radical combination reaction where the free radicals on adjacent atoms, C8 and S1, combine to form C8=S1. The acyclic thiazole is oriented toward the N2 position in the pDTMX-Cl_S1d-N2 isomers and is aligned with the C5 position in the pDTMX-Cl_S1d-C5 isomers. The N2 isomers of the S1d-N2 and S1d-C5 structures are calculated to be 16.3 kJ mol^{-1} and 21.9 kJ mol^{-1} in enthalpy, and 9.4 kJ mol^{-1} and 13.8 kJ mol^{-1} in Gibbs energy, respectively, relative to the lowest energy structure found, therefore, these isomers cannot be entirely ignored as contributors. The structures

presented in Supplementary Figure S4.14 are derived from the above-mentioned structures comprising cleavage of the C6−S1 bond. We investigated isomers wherein a hydrogen shift takes place, occurring between a carbon atom and a more basic site. For the triplet state pDTMX-Cl_S1d-C5H isomers depicted, a hydrogen is transferred from the C5 position to the S1 position, causing the radicals to reside on the C5 and C8 positions. The S1d-C5H structures are computed to be much higher (more than 258 kJ mol^{-1}) in enthalpy and Gibbs energy than the lowest energy structure, thus, it is implausible that contribution of the S1d-C5H structures will occur.

Furthermore, we considered structures undergoing intramolecular radical cyclization involving bond formation between the guanidinyl N2 and atoms besides the thiazole C6. The triplet state pDTMX-Cl_N2-C7 isomers encompass bond formation between the N2 and C7 positions, hence, the radicals are localized on the C6 and C8 positions of the thiazole ring. The N2-C7 structures are portrayed in Supplementary Figure S4.15. The enthalpies and Gibbs energies of the N2-C7 structures are computed to be considerably high in energy (more than 314 kJ mol^{-1}) in comparison to the lowest energy structure calculated. The singlet state pDTMX-Cl_N2-S1 isomers involve bond formation between the N2 and S1 positions leading to cleavage of the C8−S1 bond. The N2-S1 structures are depicted in Supplementary Figure S4.16. The enthalpies and Gibbs energies of the N2-S1 structures are quite high in energy (more than 201 kJ mol^{-1}) relative to the lowest energy structure found. The electronic energies suggest that the N2-C7 and N2-S1 structures are not contributors to the structure of protonated dechlorinated desnitro-thiamethoxam.

Moreover, in an attempt to optimize structures subjected to radical-radical combination between the N2 guanidinyl radical and the C8 dechlorinated radical, structural optimizations resulted in cleavage of the N3−C5 bond. The singlet state pDTMX-Cl_N2-C8-N5 isomers illustrated in Figure 4.9 demonstrate that the thiazole ring is oriented in such a way that the thiazole nitrogen, N5, is in close proximity to the oxadiazinane nitrogen, N3, while the singlet state pDTMX-Cl_N2-C8-S1 isomers shown in Supplementary Figure S4.17 reveal that the thiazole sulfur, S1, is in close proximity to N3. The N3 protonated N2-C8-N5 isomer is calculated to be the lowest enthalpy and Gibbs energy structure of protonated dechlorinated desnitro-thiamethoxam and the N3 protonated N2-C8-S1 isomer is calculated to be 24.7 kJ mol^{-1} in enthalpy and 21.1 kJ mol^{-1} in Gibbs energy relative to the N2-C8-N5 structure, therefore, these isomers cannot be ruled out energetically.

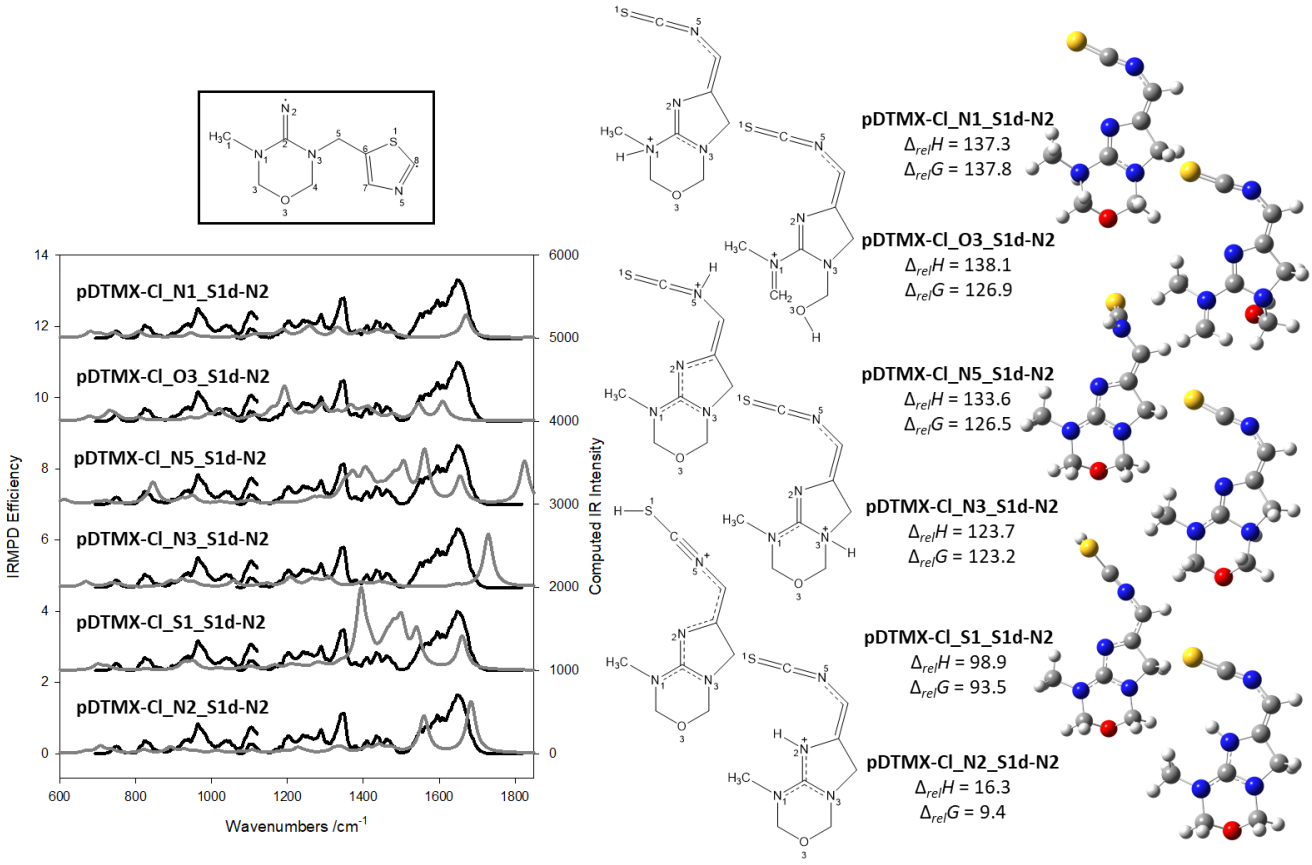

Figure 4.8. The experimental IRMPD spectrum (black trace) and the computed IR spectra (grey trace) for isomers of protonated dechlorinated desnitro-thiamethoxam where the N2-C6 bond is formed and the C6-S1 bond is cleaved (pDTMX-Cl_S1d-N2).

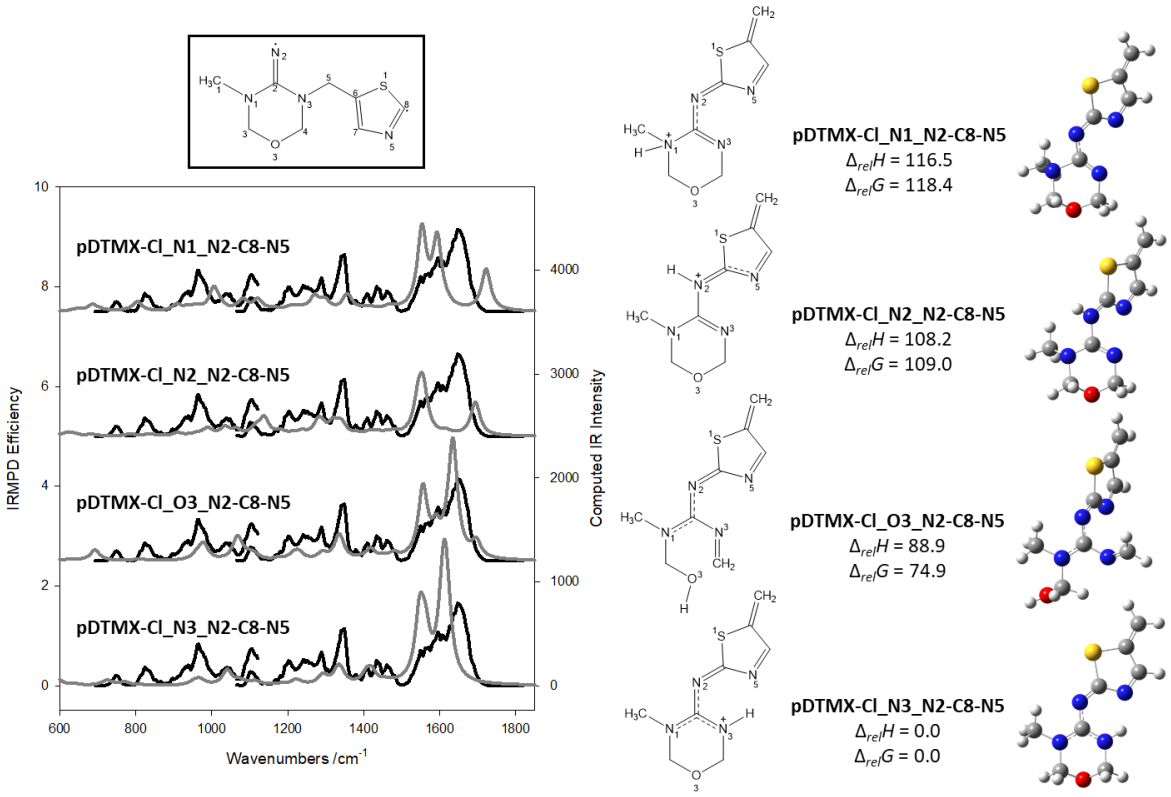

Figure 4.9. The experimental IRMPD spectrum (black trace) and the computed IR spectra (grey trace) for isomers of protonated dechlorinated desnitro-thiamethoxam where formation of the N2-C8 bond results in cleavage of the N3-C5 bond (pDTMX-Cl_N2-C8-N5).

4.3.7 Vibrational Spectroscopy for Protonated Dechlorinated Desnitro-Thiamethoxam

A comparison of the IRMPD spectra for protonated dechlorinated desnitro-thiamethoxam complexes in the 600-1800 cm^{-1} region are portrayed in Figures 4.8-4.9 and Supplementary Figures S4.8-S4.17. The experimental spectrum displays a broad absorption spanning the range of 1520-1720 cm^{-1}, exhibiting an intense absorption centered at 1650 cm^{-1} and a shoulder is experimentally observed on the red side of this absorption. The pDTMX-Cl_N3_N2-C8-N5 (Figure 4.9) computed isomer predicts an

intense IR band at 1614 cm^{-1} which can be attributed to N2=C8 stretching and N1−C–N3 asymmetric stretching. The pDTMX-Cl_N3_N2-C8-S1 (Figure S4.17) computed isomer predicts an intense absorption at 1642 cm^{-1} and a slight shoulder at 1616 cm^{-1} which can be ascribed to N2=C8 and N5=C7 stretching, and N1−C–N3 asymmetric stretching, respectively. The less intense maximum of this broad spectral feature corresponds to N5=C7 stretching and C–H wagging in the thiazole ring, as well as C–N3–H bending in the oxadiazinane ring which is calculated at around 1560 cm^{-1}.

The broad absorption observed in the IRMPD spectrum is projected by the pDTMX-Cl_N2_S1d-N2 (Figure 4.8) and pDTMX-Cl_N2_S1d-C5 (Figure S4.13) calculations. The absorption calculated at around 1680 cm^{-1} correlates to C−N2−H bending and N1−C–N3 asymmetric stretching, and the absorption calculated at around 1560 cm^{-1} corresponds to C=N3 stretching (C–N3 resonance form). In the experimental spectra, much less intense absorptions are observed below 1500 cm^{-1} which can be assigned to CH_2 bending vibrations and C−H wagging.

The positions of the calculated IR bands for all investigated complexes are not in agreement with the positions of the CH_2 and C–H vibrational frequencies observed in the experimental spectrum, therefore, no definitive structure can be assigned as a major contributor. The positions of the calculated IR bands are in reasonable agreement with the measured bands in the 1520-1720 cm^{-1} region for the lowest energy isomers described above, nonetheless, we are unable to distinguish which isomer is a better match spectroscopically. The calculated IR absorptions in this region do not reproduce the breadth of the IRMPD absorption, and as a result, further examination of structural

rearrangements and possible radical-radical combinations needs to be computed to find contributing structures which produce better agreement between the computed IR spectra and the experimental IRMPD spectrum.

4.3.8 Future Considerations

Additional computational work needs to be executed in order to gain a more accurate representation of the protonated desnitro-thiamethoxam system, necessarily, more skeletal rearrangements need to be explored. Intramolecular radical cyclization reactions involving guanidinyl radical bond formation have been investigated extensively, especially association with the C6, C7, and S1 positions. It is possible that bond formation between N2 and N5 may result in isomers with computed IR spectra that produce a more fitting match with the experimental IRMPD spectrum, also, these isomers may be more thermodynamically stable than the isomers analyzed in this current study. Furthermore, additional hydrogen shift reactions from carbon positions to various heteroatoms needs to be considered. It is probable that the Cl atom may migrate to other carbon positions or heteroatoms before it dissociates from the product ion in the subsequent MS stage. It is imperative that a more suitable contributing structure for protonated desnitro-thiamethoxam, the $NO_2^{\bullet}$ loss fragment ion, needs to be determined to further our knowledge about the structure and thermochemistry of protonated dechlorinated desnitro-thiamethoxam, the $Cl^{\bullet}$ loss fragment ion.

IRMPD spectroscopy is used to elucidate the unimolecular chemistry of protonated dechlorinated desnitro-thiamethoxam. The experimental spectrum for the *m/z* 181 fragment ion, originating from the *m/z* 211 fragment ion, is presented in Figure 4.10.

Contrasting fragmentation patterns are discussed in the literature; dissociation of CH_2O from protonated dechlorinated desnitro-thiamethoxam producing the triplet state structure[28] and the radical-radical combination reaction producing the singlet state structure[31]. Conversely, dissociation of $CH_3^{\bullet}$ and $NH^{2\bullet}$ from protonated dechlorinated desnitro-thiamethoxam is reported.[30] Theoretical studies need to be conducted in order to discover which dissociative isomer is better reproduced by the IRMPD spectrum.

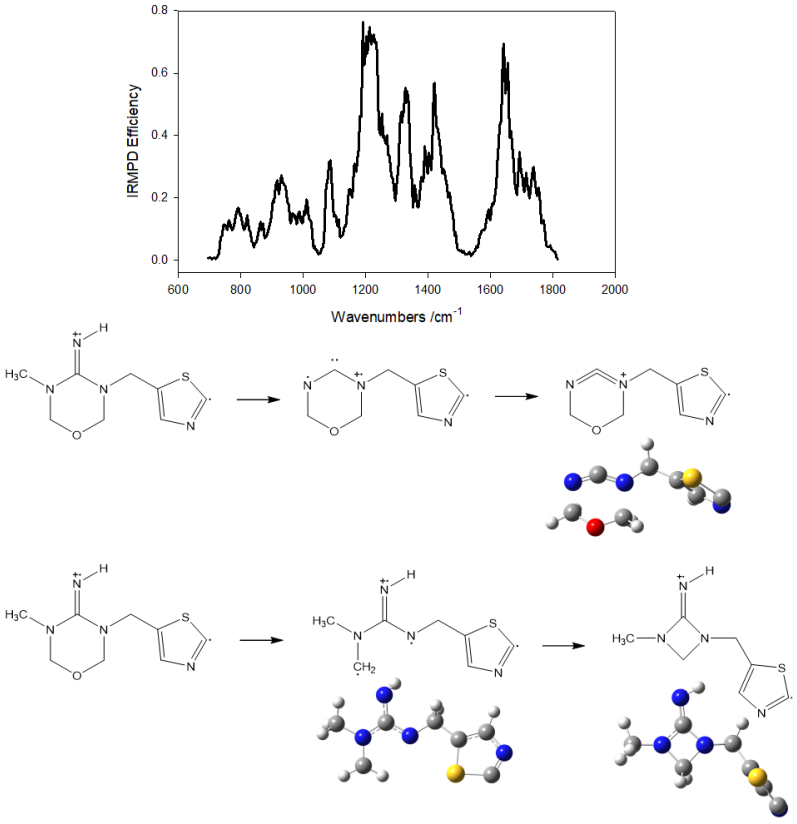

Figure 4.10. The IRMPD spectrum for the *m/z* 181 fragment ion depicting the reaction mechanism for the loss of $NH^{2\bullet}$ and $CH_3^{\bullet}$ and the reaction mechanism for the loss of CH_2O from protonated dechlorinated desnitro-thiamethoxam.

4.4 Conclusions

We have probed the gas phase structures of protonated thiamethoxam, protonated desnitro-thiamethoxam, and protonated dechlorinated desnitro-thiamethoxam using IRMPD spectroscopy in the 600-1800 cm^{-1}. Electronic structure calculations of protonated thiamethoxam were performed to compare the computed IR spectra to the experimental IRMPD spectra, and for energy comparison among isomers. Two different DFT methods were employed for protonated thiamethoxam; the B3LYP level of theory shows that the lowest energy isomer prefers protonation at the N2 position while the M06-2X level of theory reveals that the O2 position is the preferential protonation site. The calculated IR bands generated from the O2 protonated complexes reproduce the positions of the spectral features, thus, it can be concluded that the pTMX_O2a isomer (and the pTMX_O2b conformer) are major contributors to the structure of protonated thiamethoxam. For protonated desnitro-thiamethoxam, the computed IR spectrum generated from the DFT calculations of pDTMX_N2_N2-C7 exhibits reasonable agreement with the experimental spectrum in the 1540-1660 cm^{-1} region and the computed IR spectrum of pDTMX_N2a demonstrates a decent match with the experimental spectrum in the 1000-1070 cm^{-1} region. Despite the good agreement of these particular IRMPD absorptions, the pDTMX_N2_N2-C7 and pDTMX_N2a isomers cannot be concluded to be primary contributors to the structure of protonated desnitro-thiamethoxam based on the overall poor agreement obtained between the calculated IR and experimental IRMPD spectra. The N2_N2-C7 and N2a structures are not the lowest energy isomers explored in this present work, thus, it is possible that lower energy

isomers exist and better explain the features observed in the IRMPD spectrum. For protonated dechlorinated desnitro-thiamethoxam, none of the investigated isomers produced computed IR spectra that were consistent with the broad absorption in the 1520-1720 cm^{-1} region. Therefore, further computational work is required to rule out types of structures which do not match the breadth of this absorption.

4.5 References

1. Tomizawa, M.; Lee, D. L.; Casida, J. E. Neonicotinoid Insecticides: Molecular Features Conferring Selectivity for Insect versus Mammalian Nicotinic Receptors. *J. Agric. Food Chem.* **2000**, *48* (12), 6016–6024.
2. Millar, N. S.; Denholm, I. Nicotinic Acetylcholine Receptors: Targets for Commercially Important Insecticides. *Invertebr. Neurosci.* **2007**, *7* (1), 53–66.
3. Jeschke, P.; Nauen, R.; Schindler, M.; Elbert, A. Overview of the Status and Global Strategy for Neonicotinoids. *J. Agric. Food Chem.* **2011**, *59* (7), 2897–2908.
4. Sheets, L. P.; Li, A. A.; Minnema, D. J.; Collier, R. H.; Creek, M. R.; Peffer, R. C. A Critical Review of Neonicotinoid Insecticides for Developmental Neurotoxicity. *Crit. Rev. Toxicol.* **2016**, *46* (2), 153–190.
5. Yamamoto, I.; Tomizawa, M.; Saito, T.; Miyamoto, T.; Walcott, E. C.; Sumikawa, K. Structural Factors Contributing to Insecticidal and Selective Actions of Neonicotinoids. *Arch. Insect Biochem. Physiol.* **1998**, *37* (1), 24–32.
6. Matsuda, K.; Buckingham, S. D.; Kleier, D.; Rauh, J. J.; Grauso, M.; Sattelle, D. B. Neonicotinoids: Insecticides Acting on Insect Nicotinic Acetylcholine Receptors. *Trends Pharmacol. Sci.* **2001**, *22* (11), 573–580.

7. Hao, C.; Noestheden, M. R.; Zhao, X.; Morse, D. Liquid Chromatography-Tandem Mass Spectrometry Analysis of Neonicotinoid Pesticides and 6-Chloronicotinic Acid in Environmental Water with Direct Aqueous Injection. *Anal. Chim. Acta* **2016**, *925*, 43–50.
8. Hladik, M. L.; Main, A. R.; Goulson, D. Environmental Risks and Challenges Associated with Neonicotinoid Insecticides. *Environ. Sci. Technol.* **2018**, *52* (6), 3329–3335.
9. Elbert, A.; Haas, M.; Springer, B.; Thielert, W.; Nauen, R. Applied Aspects of Neonicotinoid Uses in Crop Protection. *Pest Manag. Sci.* **2008**, *64* (11), 1099–1105.
10. Tomizawa, M.; Casida, J. E. NEONICOTINOID INSECTICIDE TOXICOLOGY: Mechanisms of Selective Action. *Annu. Rev. Pharmacol. Toxicol.* **2005**, *45* (1), 247–268.
11. Bass, C.; Denholm, I.; Williamson, M. S.; Nauen, R. The Global Status of Insect Resistance to Neonicotinoid Insecticides. *Pestic. Biochem. Physiol.* **2015**, *121*, 78–87.
12. Gbylik-Sikorska, M.; Sniegocki, T.; Posyniak, A. Determination of Neonicotinoid Insecticides and Their Metabolites in Honey Bee and Honey by Liquid Chromatography Tandem Mass Spectrometry. *J. Chromatogr. B Anal. Technol. Biomed. Life Sci.* **2015**, *990*, 132–140.
13. Alkassab, A. T.; Kirchner, W. H. Sublethal Exposure to Neonicotinoids and Related Side Effects on Insect Pollinators: Honeybees, Bumblebees, and Solitary Bees. *J. Plant Dis. Prot.* **2017**, *124* (1), 1–30.

14. Brandt, A.; Gorenflo, A.; Siede, R.; Meixner, M.; Büchler, R. The Neonicotinoids Thiacloprid, Imidacloprid, and Clothianidin Affect the Immunocompetence of Honey Bees (Apis Mellifera L.). *J. Insect Physiol.* **2016**, *86*, 40–47.
15. Lundin, O.; Rundlöf, M.; Smith, H. G.; Fries, I.; Bommarco, R. Neonicotinoid Insecticides and Their Impacts on Bees: A Systematic Review of Research Approaches and Identification of Knowledge Gaps. *PLoS One* **2015**, *10* (8), 1–20.
16. Morrissey, C. A.; Mineau, P.; Devries, J. H.; Sanchez-Bayo, F.; Liess, M.; Cavallaro, M. C.; Liber, K. Neonicotinoid Contamination of Global Surface Waters and Associated Risk to Aquatic Invertebrates: A Review. *Environ. Int.* **2015**, *74*, 291–303.
17. Sánchez-Bayo, F.; Goka, K.; Hayasaka, D. Contamination of the Aquatic Environment with Neonicotinoids and Its Implication for Ecosystems. *Front. Environ. Sci.* **2016**, *4* (NOV), 1–14.
18. Hallmann, C. A.; Foppen, R. P. B.; Van Turnhout, C. A. M.; De Kroon, H.; Jongejans, E. Declines in Insectivorous Birds Are Associated with High Neonicotinoid Concentrations. *Nature* **2014**, *511* (7509), 341–343.
19. Gibbons, D.; Morrissey, C.; Mineau, P. A Review of the Direct and Indirect Effects of Neonicotinoids and Fipronil on Vertebrate Wildlife. *Environ. Sci. Pollut. Res.* **2015**, *22* (1), 103–118.
20. Maienfisch, P.; Angst, M.; Brandl, F.; Fischer, W.; Hofer, D.; Kayser, H.; Kobel, W.; Rindlisbacher, A.; Senn, R.; Steinemann, A.; Widmer, H. Chemistry and Biology of Thiamethoxam: A Second Generation Neonicotinoid. *Pest Manag. Sci.* **2001**, *57* (10), 906–913.

21. Nauen, R.; Ebbinghaus-Kintscher, U.; Salgado, V. L.; Kaussmann, M. Thiamethoxam is a Neonicotinoid Precursor Converted to Clothianidin in Insects and Plants. *Pestic. Biochem. Physiol.* **2003**, *76*, 55–69.
22. Casida, J. E. Neonicotinoid Metabolism: Compounds, Substituents, Pathways, Enzymes, Organisms, and Relevance. *J. Agric. Food Chem.* **2011**, *59* (7), 2923–2931.
23. Pandey, G.; Dorrian, S. J.; Russell, R. J.; Oakeshott, J. G. Biotransformation of the Neonicotinoid Insecticides Imidacloprid and Thiamethoxam by Pseudomonas Sp. 1G. *Biochem. Biophys. Res. Commun.* **2009**, *380* (3), 710–714.
24. Ford, K. A.; Casida, J. E. Unique and Common Metabolites of Thiamethoxam, Clothianidin, and Dinotefuran in Mice. *Chem. Res. Toxicol.* **2006**, *19* (11), 1549–1556.
25. Wang, Y.; Zhang, Y.; Xu, P.; Guo, B.; Li, W. Metabolism Distribution and Effect of Thiamethoxam after Oral Exposure in Mongolian Racerunner (Eremias Argus). *J. Agric. Food Chem.* **2018**, *66* (28), 7376–7383.
26. Chandran, J.; Aravind, U. K.; Rajalakshmi, C.; Thomas, V. I.; Nguyen, P. T.; Aravindakumar, C. T. Solvent Dependent ESI-Collisionally Induced Dissociation of Protonated Nitenpyram. *Int. J. Mass Spectrom.* **2019**, *445*, 116207.
27. Donald, W. A.; Leeming, M. G.; O'Hair, R. A. J. Gas-Phase Ion Chemistry of the Pesticide Imidacloprid: Proton Driven Radical Fragmentation of the Nitro-Guanidine Functional Group. *Int. J. Mass Spectrom.* **2012**, *316–318*, 91–99.
28. Son, S.; Kim, B.; Ahn, S. Inspection of the Fragmentation Pathway for Thiamethoxam. *Mass Spectrom. Lett.* **2017**, *8* (3), 65–68.

29. Xie, W.; Han, C.; Qian, Y.; Ding, H.; Chen, X.; Xi, J. Determination of Neonicotinoid Pesticides Residues in Agricultural Samples by Solid-Phase Extraction Combined with Liquid Chromatography-Tandem Mass Spectrometry. *J. Chromatogr. A* **2011**, *1218* (28), 4426–4433.
30. Rahman, M. M.; Farha, W.; Abd El-Aty, A. M.; Kabir, M. H.; Im, S. J.; Jung, D. I.; Choi, J. H.; Kim, S. W.; Son, Y. W.; Kwon, C. H.; Shin, H. C.; Shim, J. H. Dynamic Behaviour and Residual Pattern of Thiamethoxam and Its Metabolite Clothianidin in Swiss Chard Using Liquid Chromatography-Tandem Mass Spectrometry. *Food Chem.* **2015**, *174*, 248–255.
31. de Urzedo, A. P. F. M.; Diniz, M. E. R.; Nascentes, C. C.; Catharino, R. R.; Eberlin, M. N.; Augusti, R. Photolytic Degradation of the Insecticide Thiamethoxam in Aqueous Medium Monitored by Direct Infusion Electrospray Ionization Mass Spectrometry. *J. Mass Spectrom.* **2007**, *42* (10), 1319–1325.
32. Lopes, R. P.; de Urzedo, A. P. F. M.; Nascentes, C. C.; Augusti, R. Degradation of the Insecticides Thiamethoxam and Imidacloprid by Zero-Valent Metals Exposed to Ultrasonic Irradiation in Water Medium: Electrospray Ionization Mass Spectrometry Monitoring. *Rapid Commun. Mass Spectrom.* **2008**, *22*, 3472–3480.
33. Liu, S.; Zheng, Z.; Wei, F.; Ren, Y.; Gui, W.; Wu, H.; Zhu, G. Simultaneous Determination of Seven Neonicotinoid Pesticide Residues in Food by Ultraperformance Liquid Chromatography Tandem Mass Spectrometry. *J. Agric. Food Chem.* **2010**, *58* (6), 3271–3278.

34. Chai, Y.; Chen, H.; Liu, X.; Lu, C. Degradation of the Neonicotinoid Pesticides in the Atmospheric Pressure Ionization Source. *J. Am. Soc. Mass Spectrom.* **2018**, *29* (2), 373–381.
35. Frisch, M. J.; Trucks, G. W.; Schlegel, H. B.; Scuseria, G. E.; Robb, M. A.; Cheeseman, J. R.; Scalmani, G.; Barone, V.; Petersson, G. A.; Nakatsuji, H.; et al. Gaussian 16, Revision B.01. **2016**.
36. Grimme, S.; Antony, J.; Ehrlich, S.; Krieg, H. A Consistent and Accurate Ab Initio Parametrization of Density Functional Dispersion Correction (DFT-D) for the 94 Elements H-Pu. *J. Chem. Phys.* **2010**, *132* (15), 154104.
37. Linford, B. D.; Le Donne, A.; Scuderi, D.; Bodo, E.; Fridgen, T. D. Strong Intramolecular Hydrogen Bonding in Protonated β-Methylaminoalanine: A Vibrational Spectroscopic and Computational Study. *Eur. J. Mass Spectrom.* **2019**, *25* (1), 133–141.
38. Cheng, R.; Loire, E.; Martens, J.; Fridgen, T. D. An IRMPD Spectroscopic and Computational Study of Protonated Guanine-Containing Mismatched Base Pairs in the Gas Phase. *Phys. Chem. Chem. Phys.* **2020**, 2999–3007.
39. Zhao, Y.; Truhlar, D. G. The M06 Suite of Density Functionals for Main Group Thermochemistry, Thermochemical Kinetics, Noncovalent Interactions, Excited States, and Transition Elements: Two New Functionals and Systematic Testing of Four M06-Class Functionals and 12 Other Functionals. *Theor. Chem. Acc.* **2008**, *120* (1–3), 215–241.

40. Jami-Alahmadi, Y.; Linford, B. D.; Fridgen, T. D. Distinguishing Isomeric Peptides: The Unimolecular Reactivity and Structures of (LeuPro)M+ and (ProLeu)M+ (M = Alkali Metal). *J. Phys. Chem. B* **2016**, *120* (51), 13039–13046.
41. Martens, J.; Berden, G.; Gebhardt, C. R.; Oomens, J. Infrared Ion Spectroscopy in a Modified Quadrupole Ion Trap Mass Spectrometer at the FELIX Free Electron Laser Laboratory. *Rev. Sci. Instrum.* **2016**, *87* (10).
42. Martens, J.; van Outersterp, R. E.; Vreeken, R. J.; Cuyckens, F.; Coene, K. L. M.; Engelke, U. F.; Kluijtmans, L. A. J.; Wevers, R. A.; Buydens, L. M. C.; Redlich, B.; et al. Infrared Ion Spectroscopy: New Opportunities for Small-Molecule Identification in Mass Spectrometry - A Tutorial Perspective. *Anal. Chim. Acta* **2020**, *1093*, 1–15.
43. Moreira, A. A. G.; De Lima-Neto, P.; Caetano, E. W. S.; Barroso-Neto, I. L.; Freire, V. N. Computational Electronic Structure of the Bee Killer Insecticide Imidacloprid. *New J. Chem.* **2016**, *40* (12), 10353–10362.

Chapter 5 – Summary and Outlook

Infrared multiphoton dissociation (IRMPD) spectroscopic analysis combined with theoretical calculations of infrared (IR) spectra proves to be a valuable tool for structural elucidation. The mechanism of IRMPD involves the resonant absorption of several infrared photons. The energy absorbed by the ions is distributed to and stored in a bath of vibrational modes. Sequential absorption of photons followed by the redistribution of energy raises the total internal energy of the ions until the dissociation threshold is exceeded, leading to fragmentation of the molecule.[1] IRMPD spectra of molecular ions can be obtained by inducing dissociation using high-intensity, widely tunable IR radiation supplied by a free electron laser (FEL). Interpretation of the IRMPD spectra provides structural information about the location of charge and the presence of certain chemical moieties. In this thesis, the structures and energetics of protonated neonicotinoid insecticides have been explored using IRMPD spectroscopy and density functional theory (DFT) calculations.

Chapter 3 examined the tautomerization of protonated imidacloprid and its fragmentation products in the gas phase through experimental and theoretical methods. Theoretical methods have been used to determine the molecular geometries, calculate the enthalpies and Gibbs energies, and compute vibrational IR spectra for comparison with the experimental IRMPD spectra for the purpose of characterizing imidacloprid and its fragmentation products. The lowest energy isomer of protonated imidacloprid, the N1-N5 isomer, generated an IR spectrum that was the most consistent with the experimental spectrum, therefore, the N1-N5 isomer was concluded to be a primary contributor to the

structure. Likewise, the computed IR spectrum of the lowest energy isomer of protonated imidacloprid urea, the direct N_2O dissociation product, was in excellent agreement with the experimental spectrum, thus, the N1-N5 isomer could be assigned as a major contributor to the structure.

A potential energy diagram has been modelled formerly by Donald *et al*.[2] to show the enthalpy barriers to proton transfer between the two most basic sites of imidacloprid, the pyridine nitrogen, N5, and the imine nitrogen, N2. The effect of entropy was not considered when calculating the proton affinities of the ground state minima or the transition state structures; accordingly, the relative enthalpies and Gibbs energies were included in the potential energy diagram in the current work. The transition state enthalpy barriers for the direct proton transfer from the N5 to the N2 position and the indirect proton transfer from the N5 to O2 and then O2 to N2 positions were computed to be lower in enthalpy than the simple loss of $NO_2^{\bullet}$, suggesting that the N1-N2 isomer was the structure of protonated desnitroimidacloprid. However, when entropy was taken into account, the straightforward loss of $NO_2^{\bullet}$ from protonated imidacloprid was computed to be lower in Gibbs energy than the direct and indirect proton transfer mechanisms making proton transfer prior to $NO_2^{\bullet}$ loss unlikely, suggesting that the N1-N5 isomer was the structure of protonated desnitroimidacloprid.

The spectroscopic comparison between the experimental IRMPD spectrum and the computed IR spectra for protonated desnitroimidacloprid exhibited better agreement with the experimental spectrum for the N1-N5 isomer than the computed IR spectra for the N2-N2 and N1-N2 isomers, indicating that the N1-N5 isomer contributes to the structure to a greater extent than the lower energy isomers. Tautomerization of the imidazolidine

ring and a proton transfer from the pyridine nitrogen to the imine nitrogen resulted in the formation of the lowest energy isomer, the N2-N2 isomer. The N1-N2a and N1-N2b isomers were derived from a proton transfer from the N5 to the N2 position and the N2-N5a and N2-N5b isomers stem from a hydrogen shift from the N1 to the N2 position. Nonetheless, the N2-N2, N1-N2, and N2-N5 isomers could only be assigned as minor contributors to the structure based on the vibrational spectroscopy of protonated desnitroimidacloprid. The enthalpy and Gibbs energy barriers for the mechanistic routes involving a hydrogen shift and proton transfer, following the loss of $NO_2^{\bullet}$, were calculated to explain the minor contribution from the N2-N2 isomer, as well as the slight presence of the N1-N2 and N2-N5 isomers.

A comparison of the calculated IR bands and the IRMPD absorptions for protonated desnitrosoimidacloprid revealed that the N1-N5 isomer, formed by the simple loss of $NO^{\bullet}$, could be ruled out spectroscopically and energetically. The computed IR spectrum of the lowest energy isomer of protonated desnitrosoimidacloprid, the N1-N2 isomer, presented the best match with the experimental spectrum providing evidence that a proton transfer occurred between the pyridine nitrogen and the imine nitrogen following the loss of $NO^{\bullet}$. The N1-N2 isomer of protonated desnitrosoimidacloprid isomerizes such that the hydrogen is localized on the oxygen of the nitro group ensuring that $^{\bullet}OH$ dissociation could occur. The calculated energy barrier to isomerization for the N2-O1 isomer of protonated desnitrosoimidacloprid was computed to be more than 80 kJ mol^{-1} lower in enthalpy and Gibbs energy in comparison to the energy barrier for the N1-O1 isomer, hence, it is probable that isomerization proceeded via the N2-O1 isomer mechanistic route. Tautomerization succeeding $^{\bullet}OH$ dissociation gave rise to the formation of the N2-

N2a, N2-N2b, and N2-N2c isomers. The calculated IR bands of the N2-N2b isomer were in good agreement with the measured IRMPD bands, therefore, it could be deduced that the N2-N2b isomer contributes to the IRMPD spectrum. The general disagreement obtained between the computed IR spectra of the N2-Na and N2-N2c isomers and the experimental spectrum indicated that these isomers could be excluded as possible contributors.

Chapter 4 investigated the structures and thermochemistries of protonated thiamethoxam and its fragmentation products in the gas phase. The calculated relative enthalpies and Gibbs energies provided insight into the proton affinity and gas basicity of thiamethoxam. Geometry optimizations and theoretical infrared spectra were computed using the B3LYP and M06-2X methods. The B3LYP calculations showed that the N2 position was the preferred site of protonation for thiamethoxam, while M06-2X predicted that the O2 position was the favoured site of protonation. The computed IR spectrum of the O2a isomer (and the O2b conformer) was more consistent with the experimental IRMPD spectrum than the N2 isomer, demonstrating that the M06-2X functional outperforms the B3LYP functional in interpreting the spectroscopic results.

A comparison of the computed IR spectra and the experimental IRMPD spectrum for protonated desnitro-thiamethoxam, loss of $NO_2^{\bullet}$, was conducted to determine the preferred protonation site and identify functional groups. The IRMPD absorptions were not adequately reproduced by the calculated IR bands of the desnitro-thiamethoxam isomers protonated at any of the basic sites, therefore, the isomers that underwent radical ion rearrangements due to the decomposition of $NO_2^{\bullet}$ were inspected. The pDTMX_N2a and pDTMX_N2_N2C7 isomers were not concluded to be the main contributors to the

structure even though the computed IR spectrum for the pDTMX_N2a isomer displayed a decent match with the experimental band at 1030 cm^{-1} and the computed IR spectrum for the pDTMX_N2_N2C7 isomer was in relatively good agreement with the experimental spectrum in the 1540-1660 cm^{-1} region. Aside from the 1030 cm^{-1} spectral feature and the broad absorption spanning the 1540-1660 cm^{-1} region, the calculated IR bands in the mid-infrared were in poor agreement with the IRMPD absorptions, consequently, the pDTMX_N2a and pDTMX_N2_N2C7 isomers were not solely responsible for the observed IRMPD spectrum.

Further theoretical studies of protonated dechlorinated desnitro-thiamethoxam, loss of $NO_2^{\bullet}$ and $Cl^{\bullet}$, are crucial to obtain a more fitting match between the computed IR spectrum and the experimental IRMPD spectrum. The positions of the IRMPD absorptions in the 1520-1720 cm^{-1} region were predicted by the lower energy structures: pDTMX-C1_N3_N2-C8-N5, pDTMX-C1_N3_N2-C8-S1, pDTMX-C1_N2_S1d-N2, and pDTMX-C1_N2_S1d-C5, however, more rearrangements need to be explored to find isomers which better explain the breadth of the 1520-1720 cm^{-1} spectral feature.

Neonicotinoid insecticides possess a negatively charged nitro or cyano substituent at the tip of the molecule which can form interactions with positively charged amino acid residues: lysine, arginine, and histidine, in the binding site of insect nicotinic acetylcholine receptors (nAChRs).[3,4] The selective toxicity of neonicotinoid insecticides is attributed to the binding specificity of neonicotinoids at insect nAChRs. Therefore, it would be interesting to study the structures, thermochemistries, binding energies, and reactivities of amino acid – neonicotinoid complexes to gain an understanding of the

hydrogen bonding and electrostatic interactions involved in the binding of nitroguanidines, nitromethylenes, and cyanoamidines with cationic amino acid residues.

5.1 References

1. Polfer, N. C.; Oomens, J. Vibrational Spectroscopy of Bare and Solvated Ionic Complexes of Biological Relevance. *Mass Spectrom. Rev.* **2009**, *28* (3), 468–494.
2. Donald, W. A.; Leeming, M. G.; O'Hair, R. A. J. Gas-Phase Ion Chemistry of the Pesticide Imidacloprid: Proton Driven Radical Fragmentation of the Nitro-Guanidine Functional Group. *Int. J. Mass Spectrom.* **2012**, *316–318*, 91–99.
3. Tomizawa, M.; Casida, J. E. Selective Toxicity of Neonicotinoids Attributable To Specificity of Insect and Mammalian Nicotinic Receptors. *Annu. Rev. Entomol.* **2003**, *48* (1), 339–364.
4. Moreira, A. A. G.; De Lima-Neto, P.; Caetano, E. W. S.; Barroso-Neto, I. L.; Freire, V. N. Computational Electronic Structure of the Bee Killer Insecticide Imidacloprid. *New J. Chem.* **2016**, *40* (12), 10353–10362.

Appendix A – Supplemental Information for Chapter 3

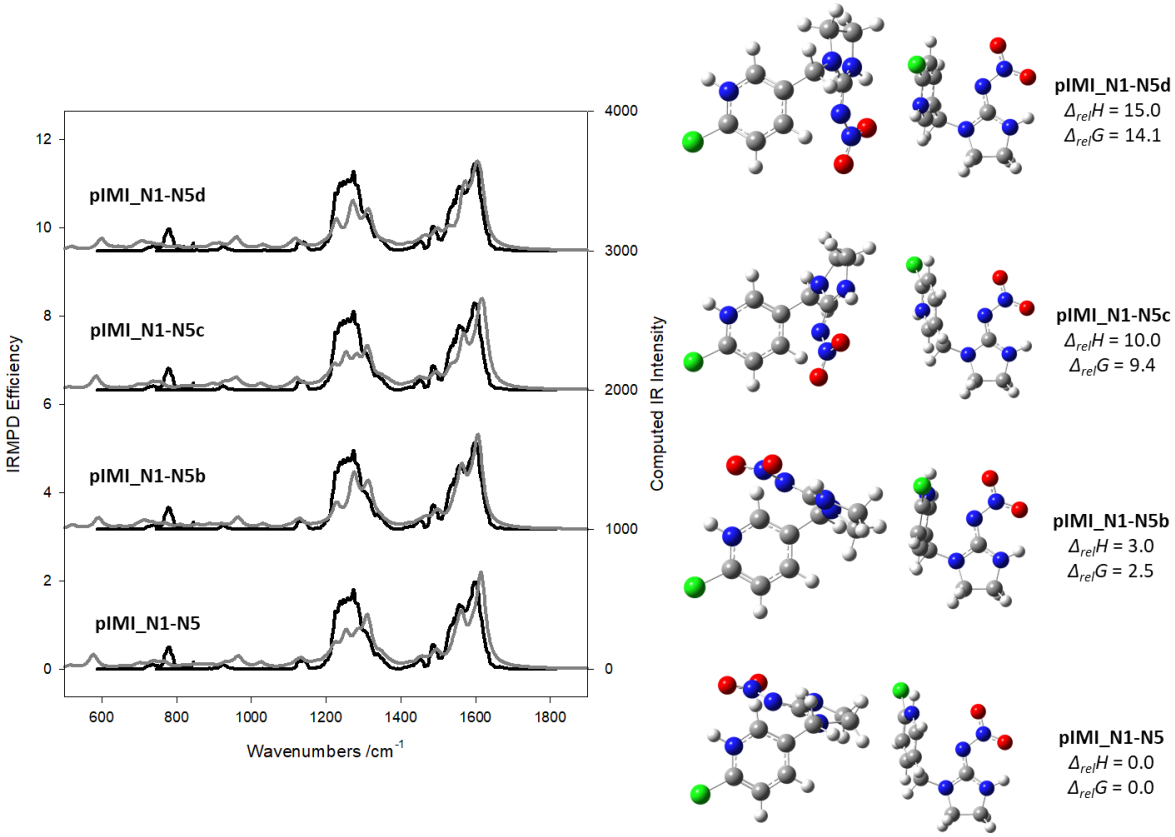

Figure S3.1. Comparison of the experimental IRMPD spectra (black trace) and the computed IR spectra (grey trace) for the lowest energy isomer of protonated imidacloprid, the N1-N5 conformers. All relative thermochemistries are 298 K values and are in kJ mol^{-1}.

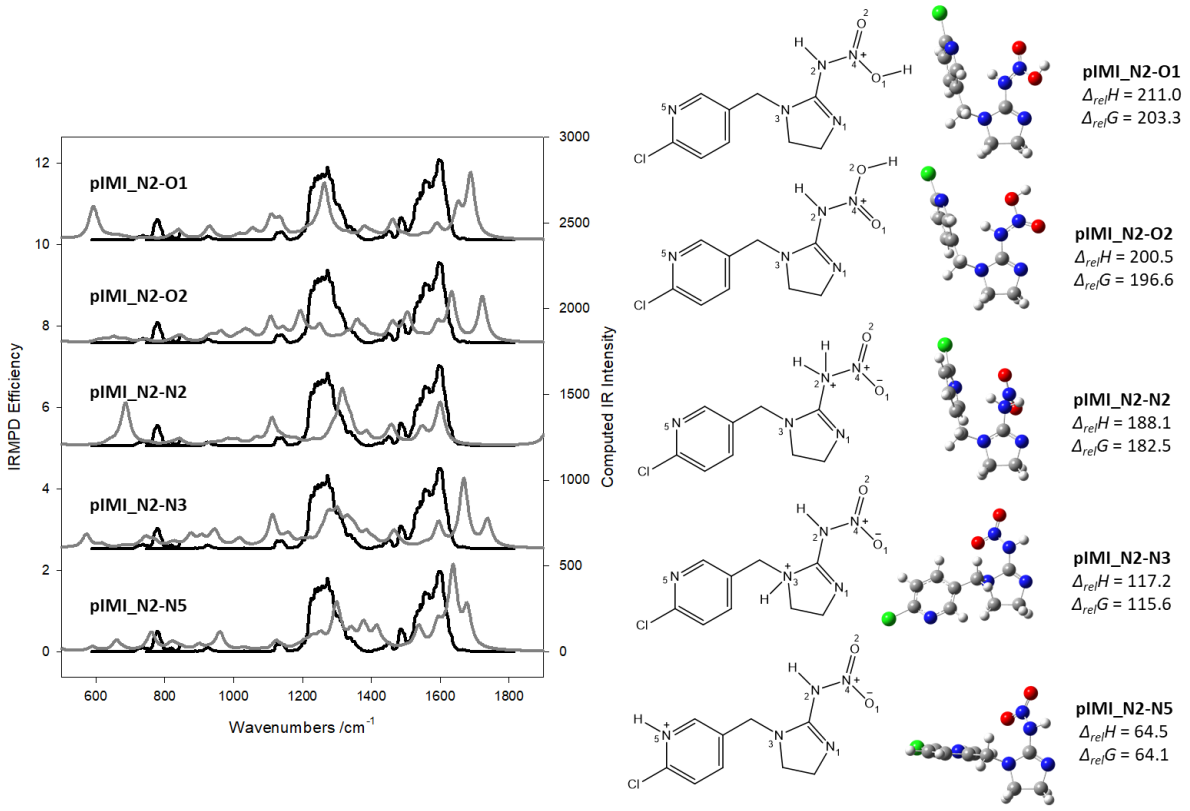

Figure S3.2. Comparison of the experimental IRMPD spectra (black trace) and the computed IR spectra (grey trace) for higher energy tautomers of protonated imidacloprid. All relative thermochemistries are 298 K values and are in kJ mol^{-1}.

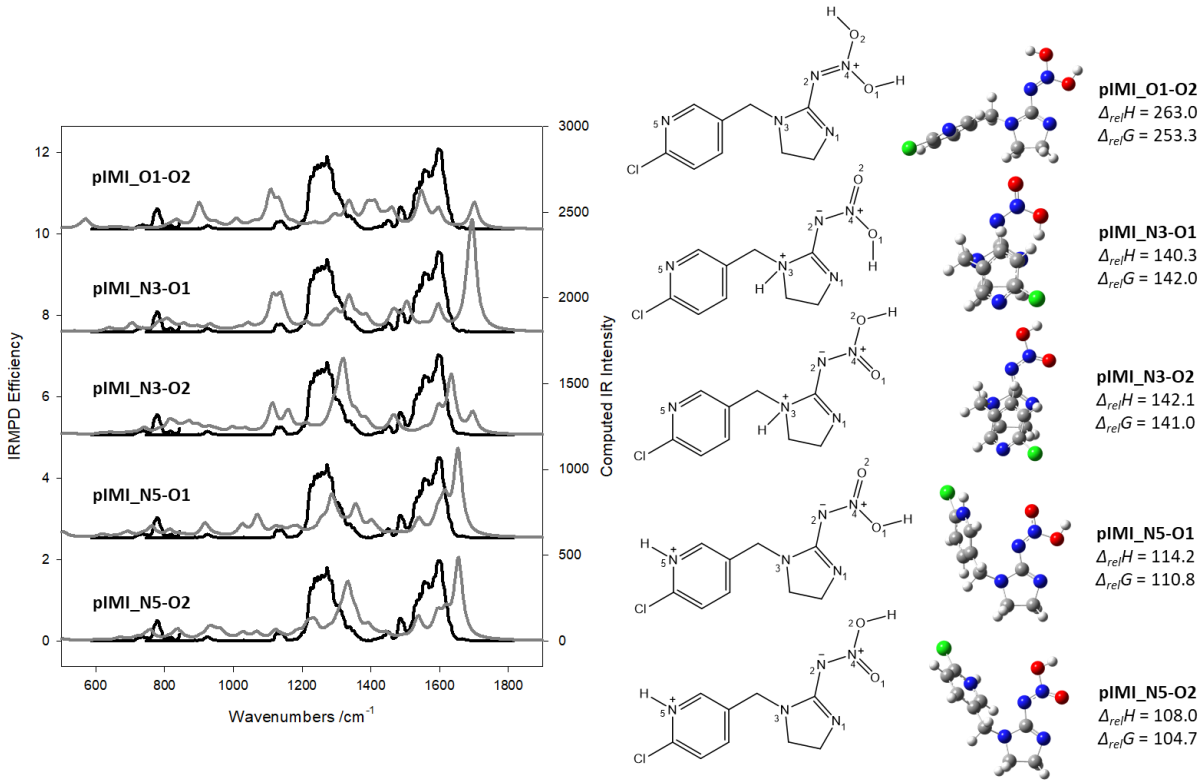

Figure S3.3. Comparison of the experimental IRMPD spectra (black trace) and the computed IR spectra (grey trace) for higher energy tautomers of protonated imidacloprid. All relative thermochemistries are 298 K values and are in kJ mol^{-1}.

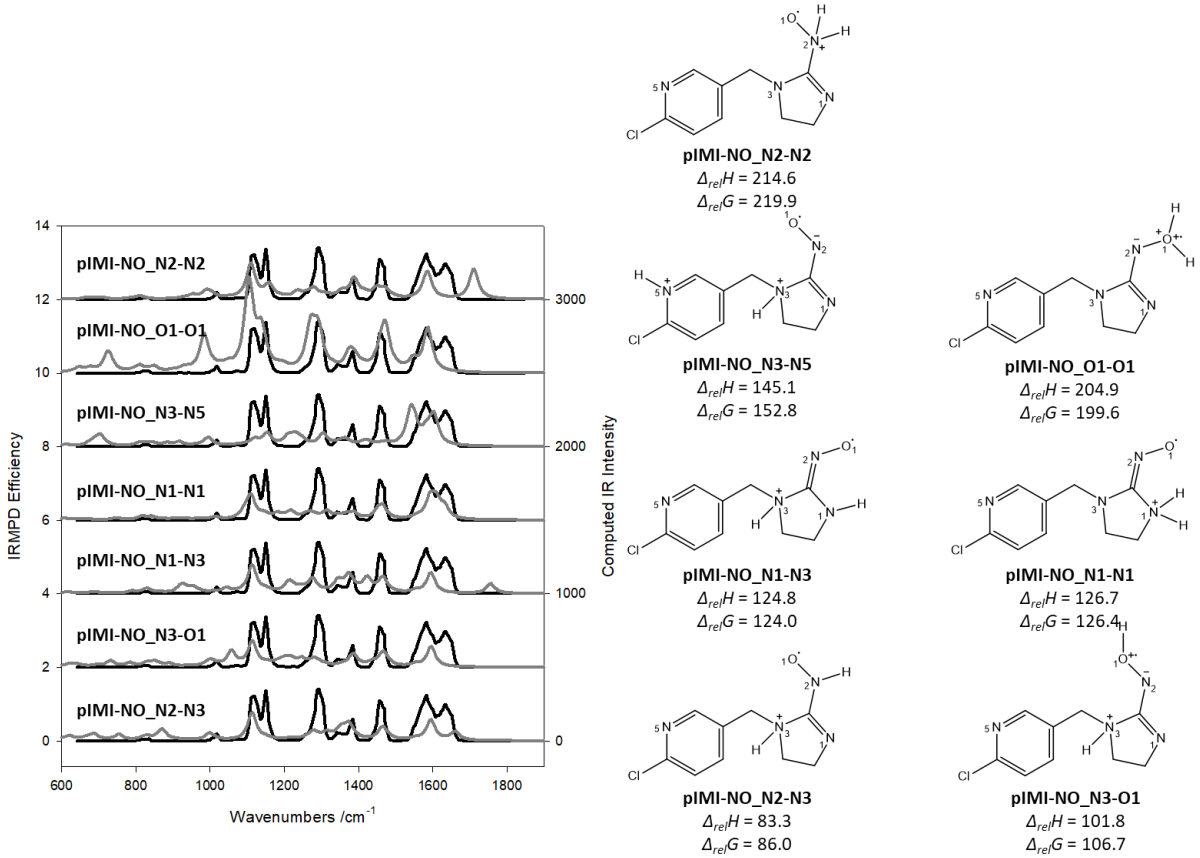

Figure S3.4. Comparison of the experimental IRMPD spectra (black trace) and the computed IR spectra (grey trace) for higher energy tautomers of protonated desnitrosoimidacloprid (loss of NO•). All relative thermochemistries are 298 K values and are in kJ mol^{-1}.

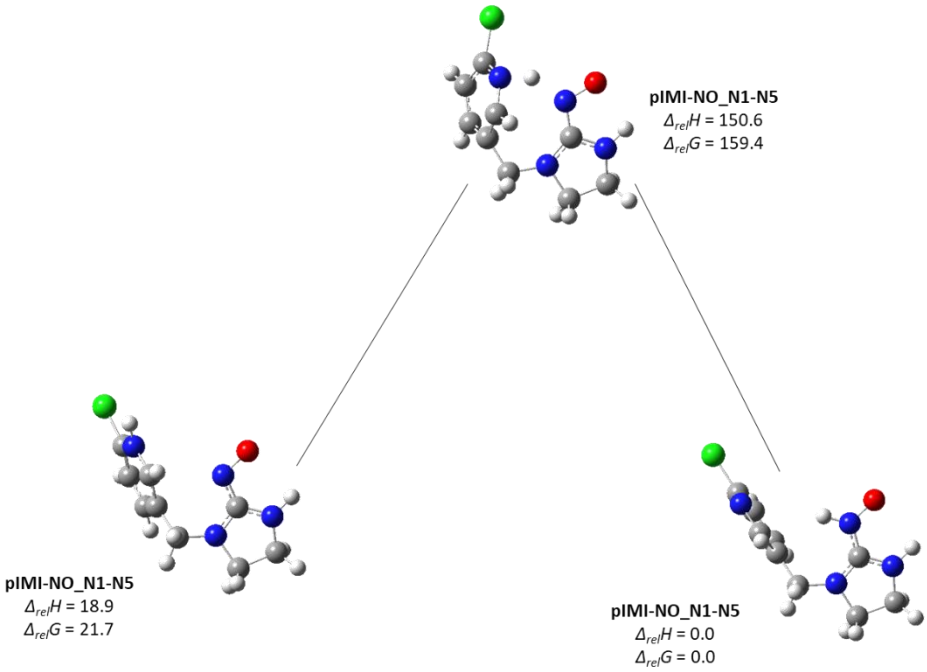

Figure S3.5. Potential energy diagram for protonated desnitrosoimidacloprid to show the enthalpy and Gibbs energy barrier for proton transfer following the loss of NO$^{\bullet}$.

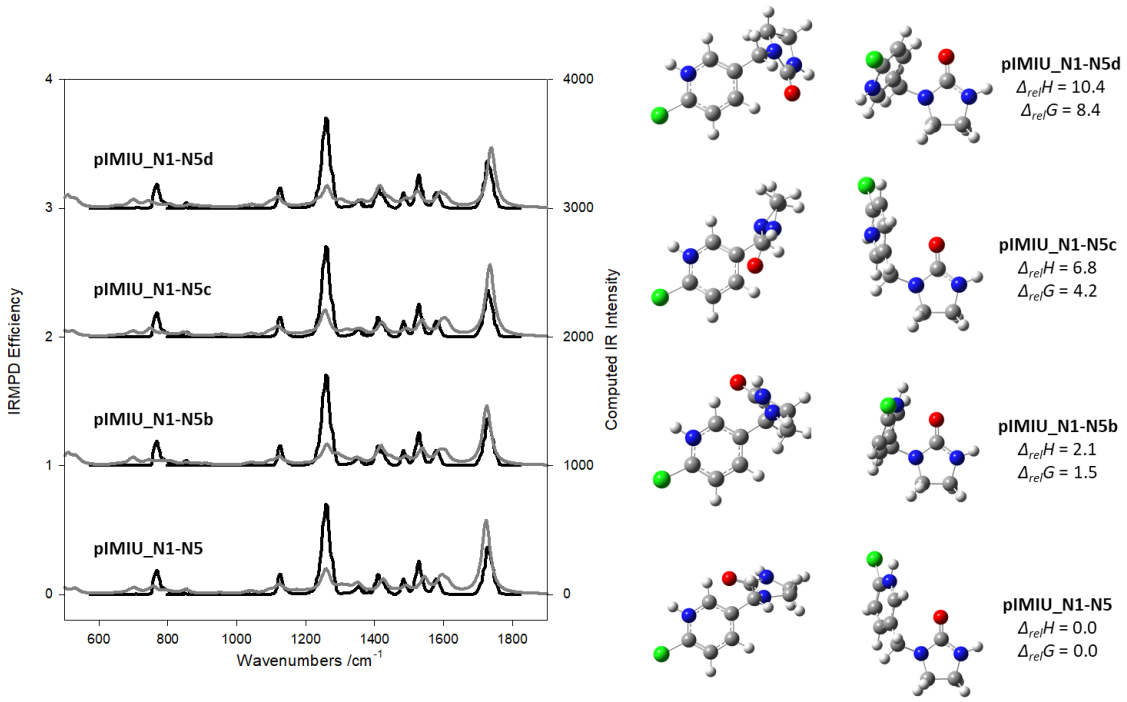

Figure S3.6. Comparison of the experimental IRMPD spectra (black trace) and the computed IR spectra (grey trace) for the lowest energy isomer of protonated imidacloprid urea (loss of N_2O), the N1-N5 conformers. All relative thermochemistries are 298 K values and are in kJ mol^{-1}.

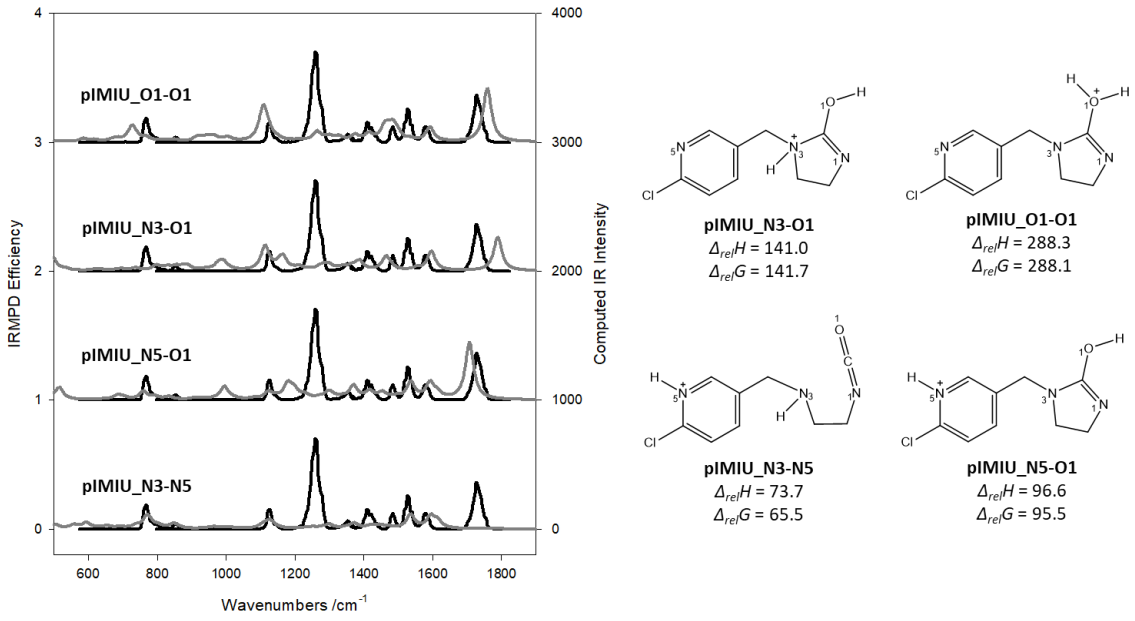

Figure S3.7. Comparison of the experimental IRMPD spectra (black trace) and the computed IR spectra (grey trace) for higher energy tautomers of protonated imidacloprid urea (loss of N_2O). All relative thermochemistries are 298 K values and are in kJ mol^{-1}.

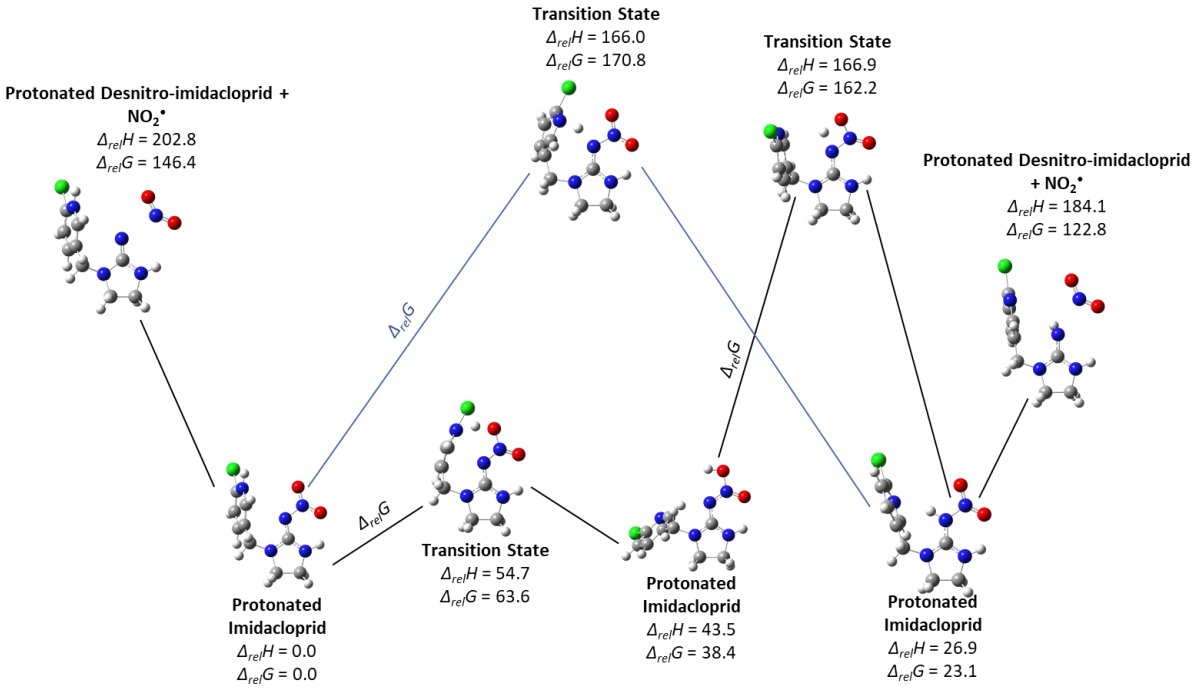

Figure S3.8. Potential energy diagram for protonated desnitroimidacloprid to show the enthalpy and Gibbs energy barriers for proton transfer preceding the loss of $NO_2^{\bullet}$.

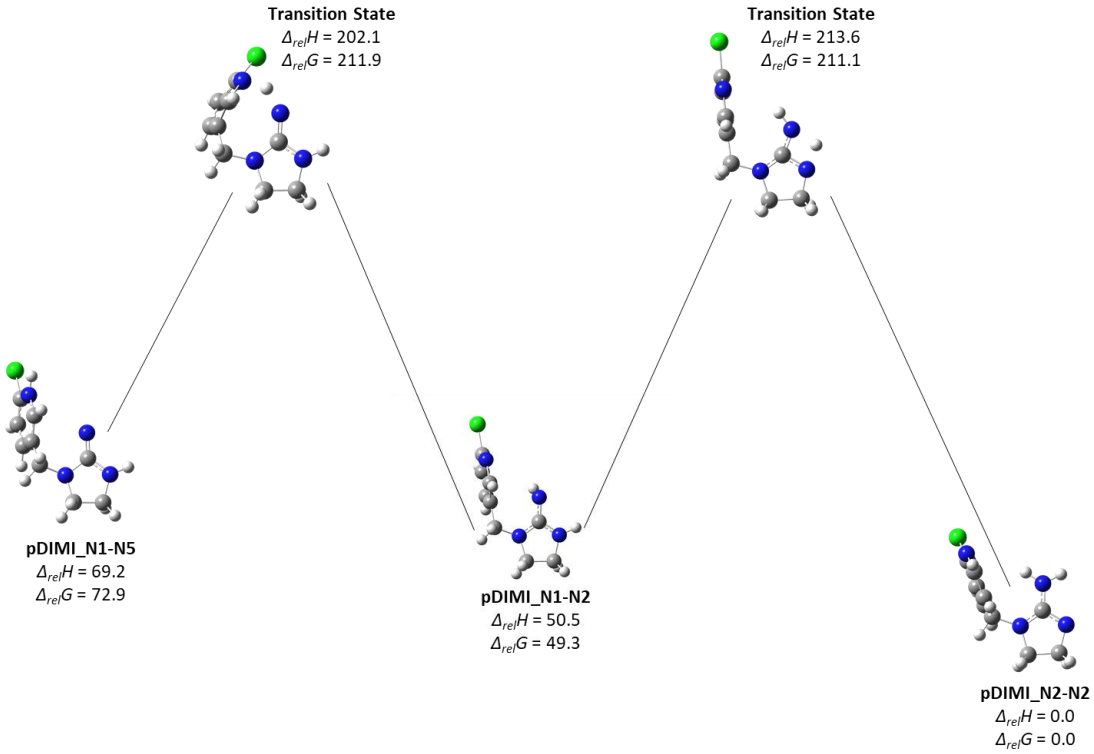

Figure S3.9. Potential energy diagram for protonated desnitroimidacloprid to show the enthalpy and Gibbs energy barriers for proton transfer following the loss of $NO_2^{\bullet}$.

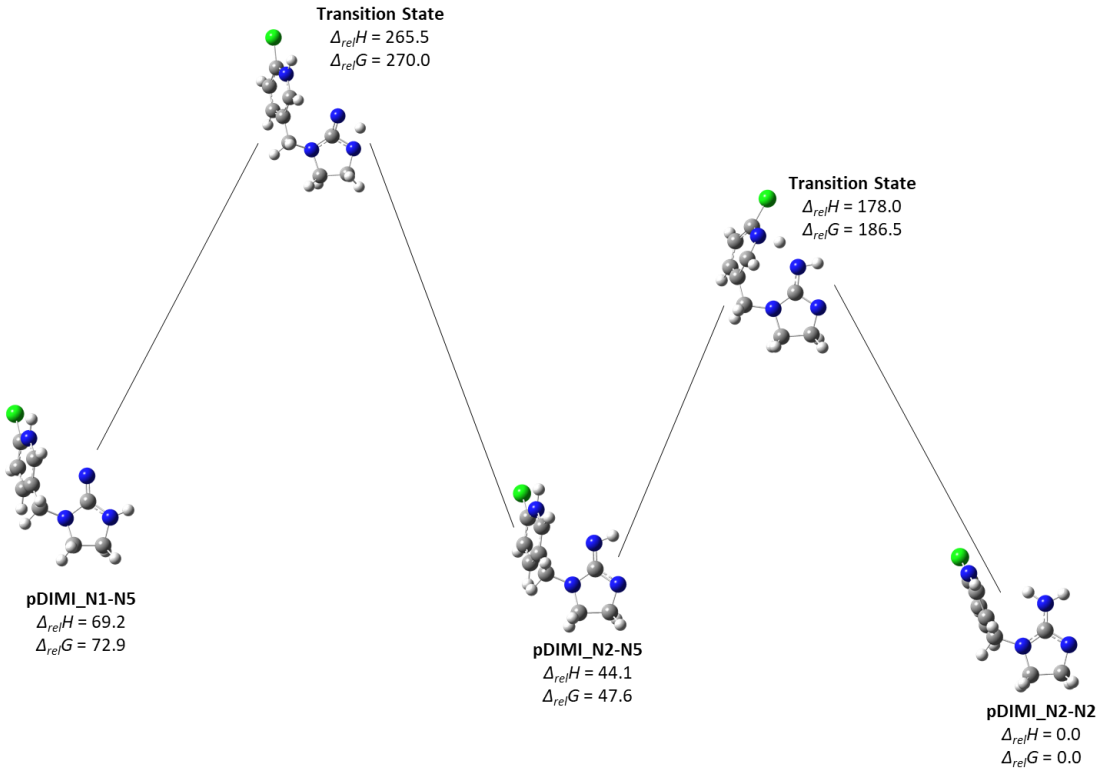

Figure S3.10. Potential energy diagram for protonated desnitroimidacloprid to show the enthalpy and Gibbs energy barriers for tautomerization following the loss of $NO_2^{\bullet}$.

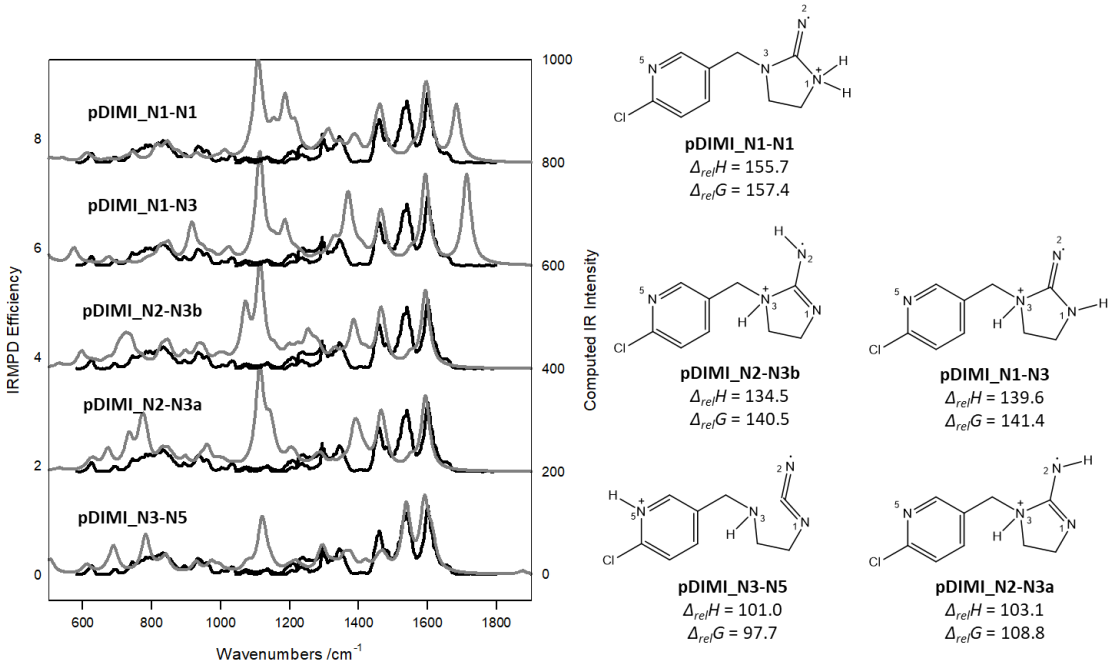

Figure S3.11. Comparison of the experimental IRMPD spectra (black trace) and the computed IR spectra (grey trace) for higher energy tautomers of protonated desnitroimidacloprid (loss of $NO_2^{\bullet}$). All relative thermochemistries are 298 K values and are in kJ mol^{-1}.

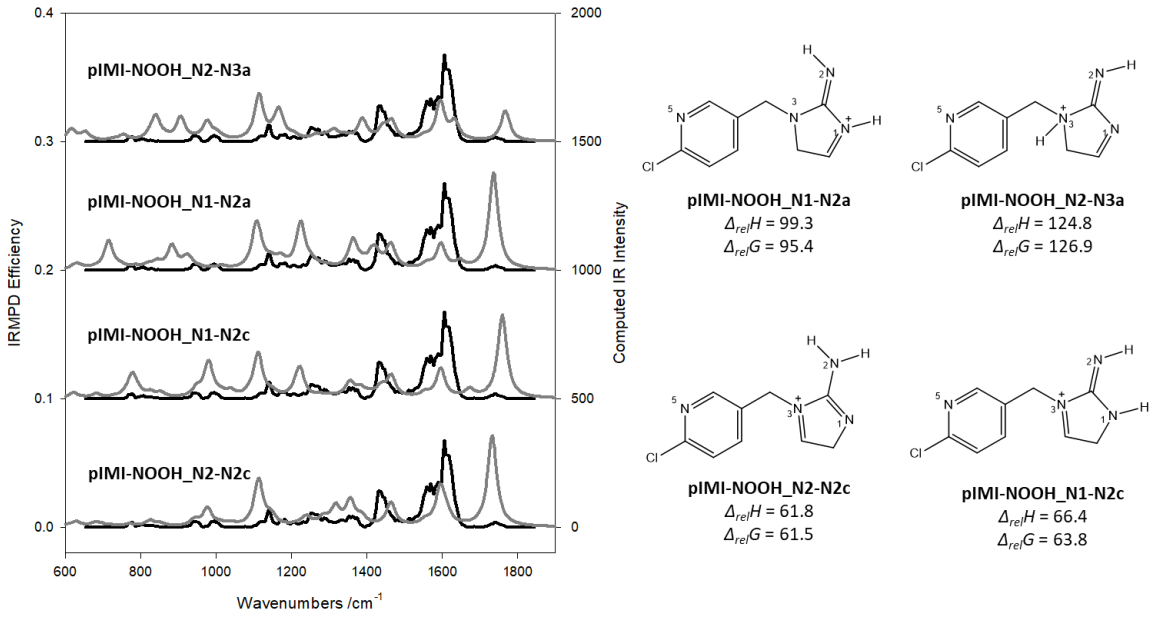

Figure S3.12. Comparison of the experimental IRMPD spectra (black trace) and the computed IR spectra (grey trace) for the loss of NO$^{\bullet}$ and $^{\bullet}$OH from protonated imidacloprid, singlet state isomers. All relative thermochemistries are 298 K values and are in kJ mol^{-1}.

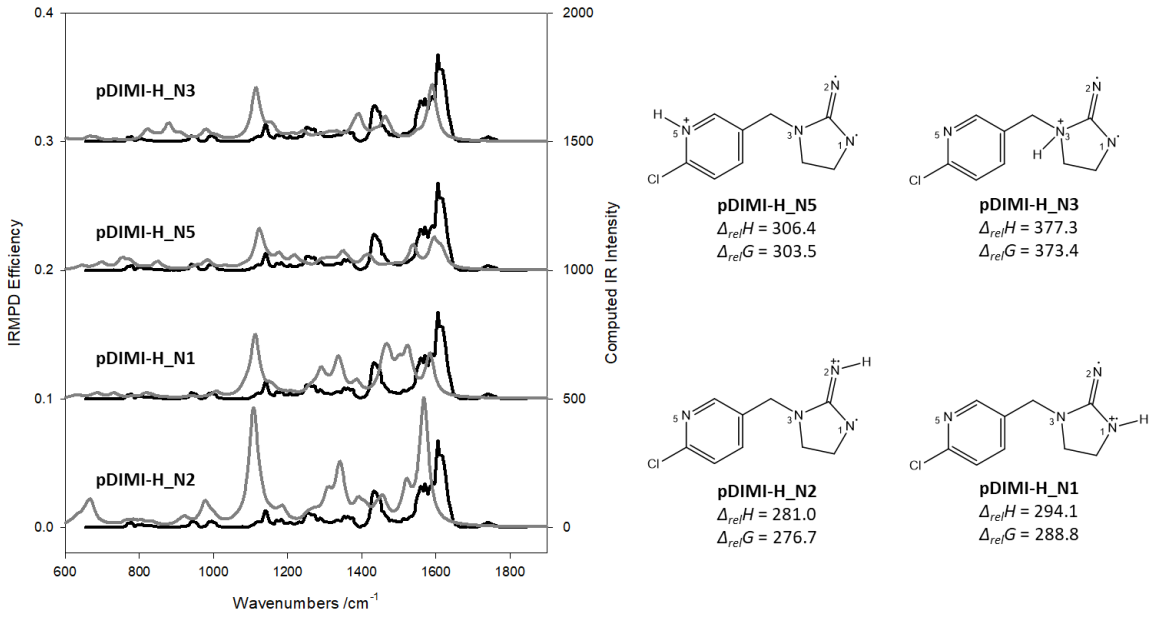

Figure S3.13. Comparison of the experimental IRMPD spectra (black trace) and the computed IR spectra (grey trace) for the loss of NO$^{\bullet}$ and $^{\bullet}$OH from protonated imidacloprid, triplet state isomers. All relative thermochemistries are 298 K values and are in kJ mol^{-1}.

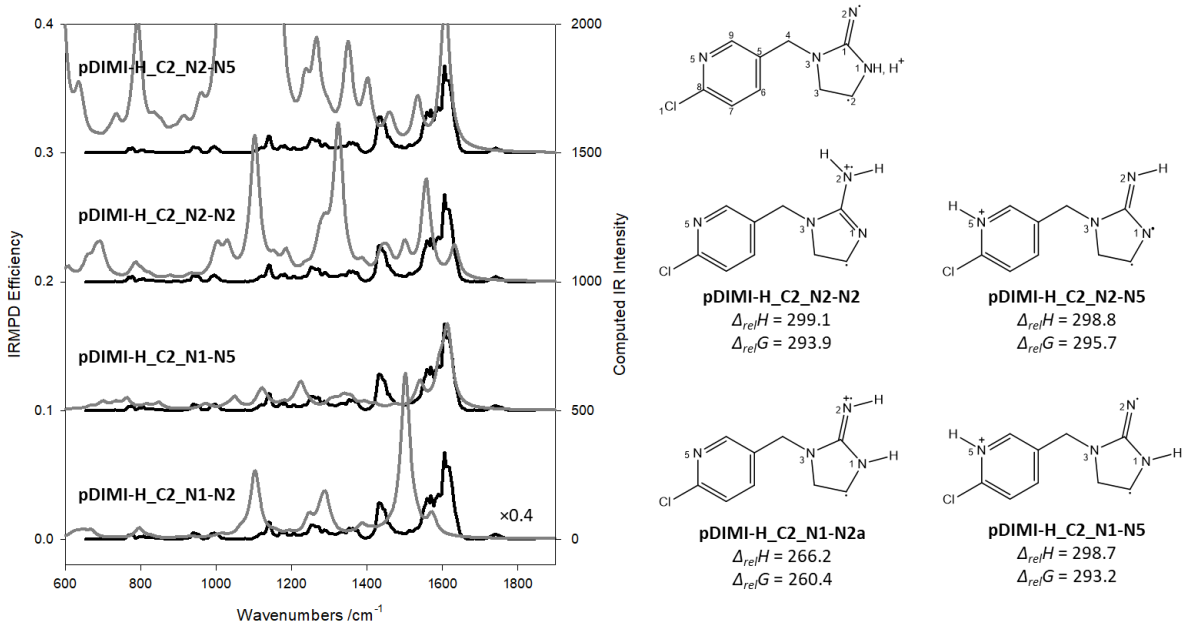

Figure S3.14. Comparison of the experimental IRMPD spectra (black trace) and the computed IR spectra (grey trace) for the loss of $NO_2^{\bullet}$ and $H^{\bullet}$ from the C2 position of protonated imidacloprid, triplet state isomers. All relative thermochemistries are 298 K values and are in kJ mol^{-1}.

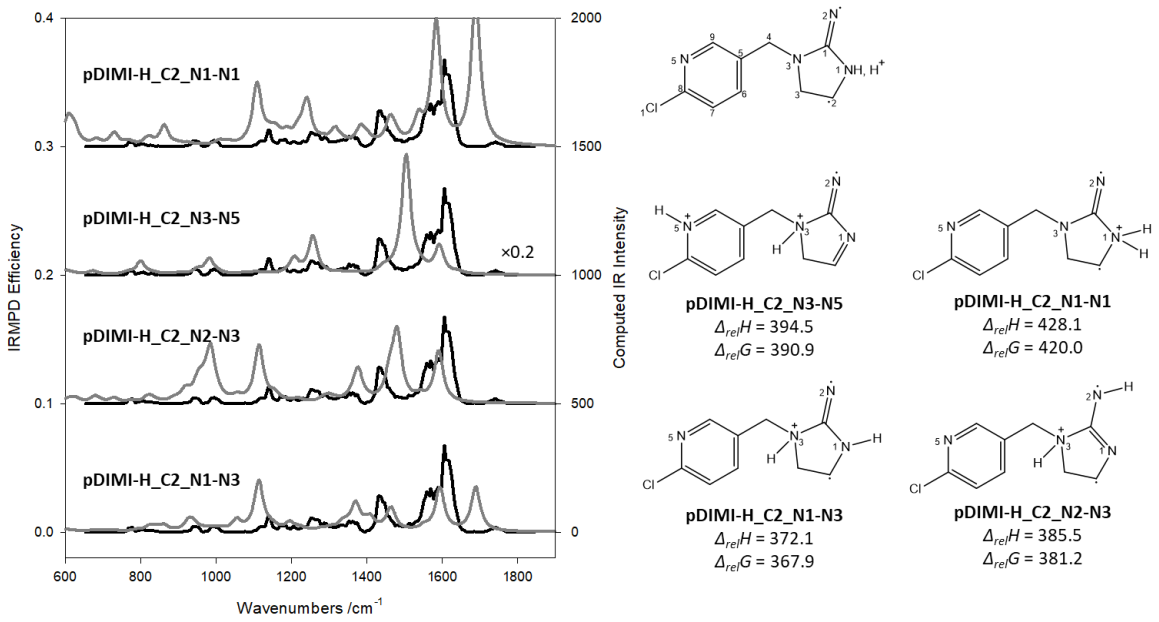

Figure S3.15. Comparison of the experimental IRMPD spectra (black trace) and the computed IR spectra (grey trace) for the loss of $NO_2^{\bullet}$ and $H^{\bullet}$ from the C2 position of protonated imidacloprid, triplet state isomers. All relative thermochemistries are 298 K values and are in kJ mol^{-1}.

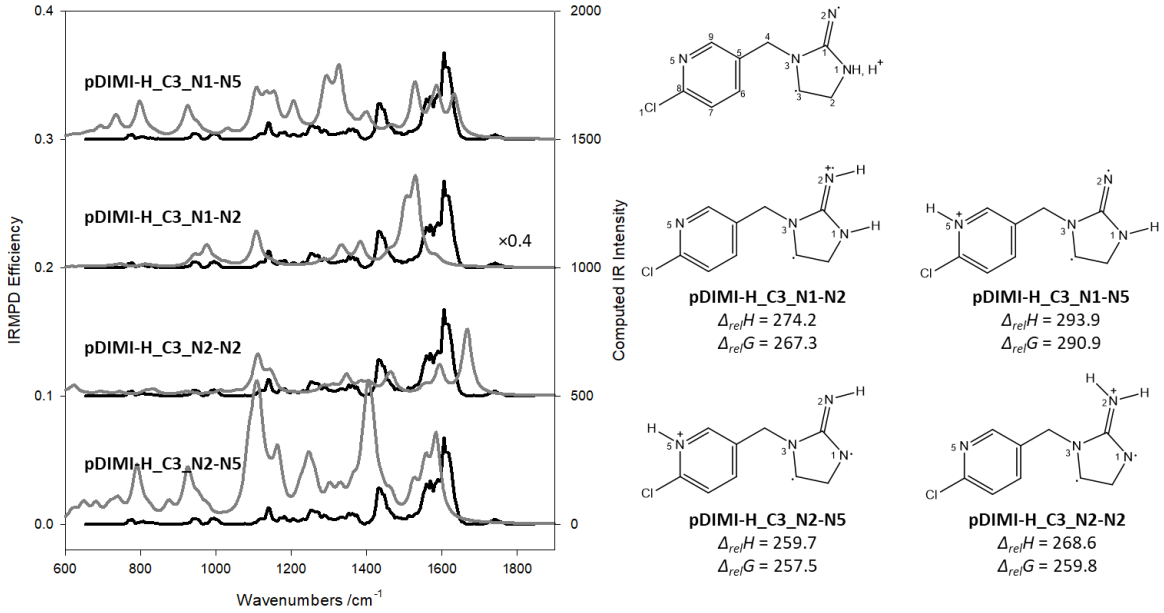

Figure S3.16. Comparison of the experimental IRMPD spectra (black trace) and the computed IR spectra (grey trace) for the loss of $NO_2^{\bullet}$ and $H^{\bullet}$ from the C3 position of protonated imidacloprid, triplet state isomers. All relative thermochemistries are 298 K values and are in kJ mol^{-1}.

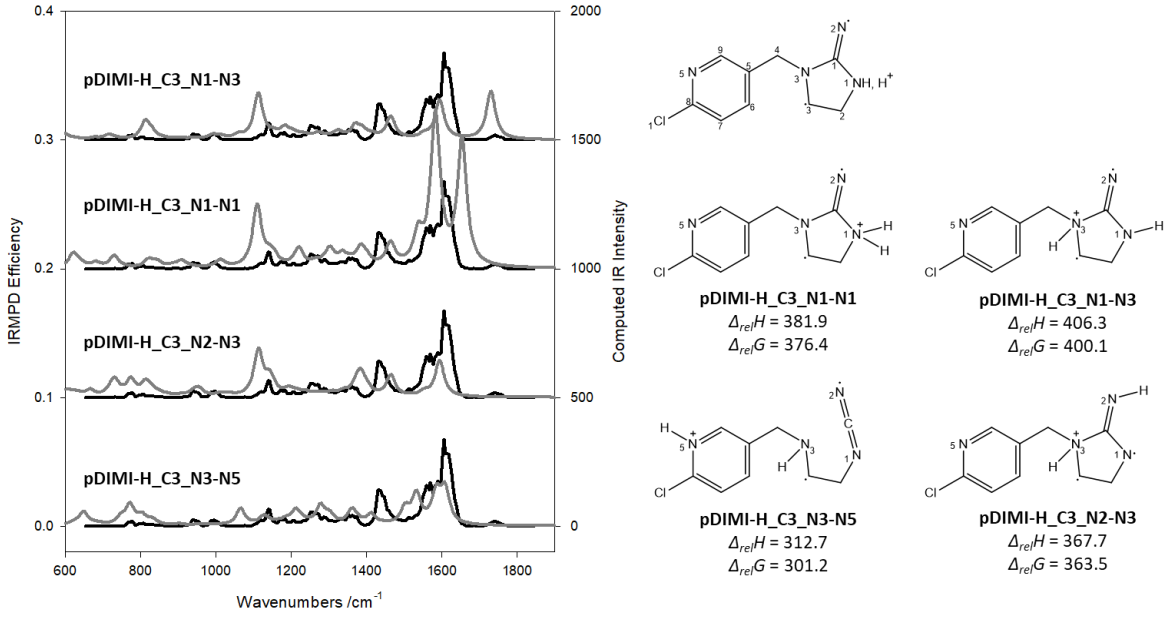

Figure S3.17. Comparison of the experimental IRMPD spectra (black trace) and the computed IR spectra (grey trace) for the loss of $NO_2^{\bullet}$ and $H^{\bullet}$ from the C3 position of protonated imidacloprid, triplet state isomers. All relative thermochemistries are 298 K values and are in kJ mol^{-1}.

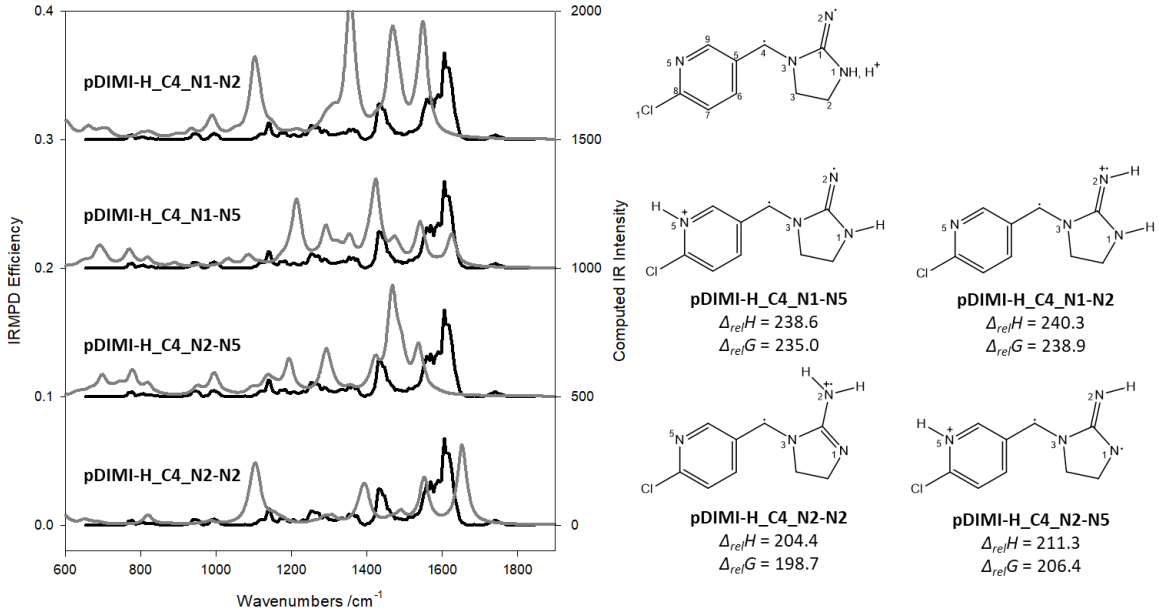

Figure S3.18. Comparison of the experimental IRMPD spectra (black trace) and the computed IR spectra (grey trace) for the loss of $NO_2^{\bullet}$ and $H^{\bullet}$ from the C4 position of protonated imidacloprid, triplet state isomers. All relative thermochemistries are 298 K values and are in kJ mol^{-1}.

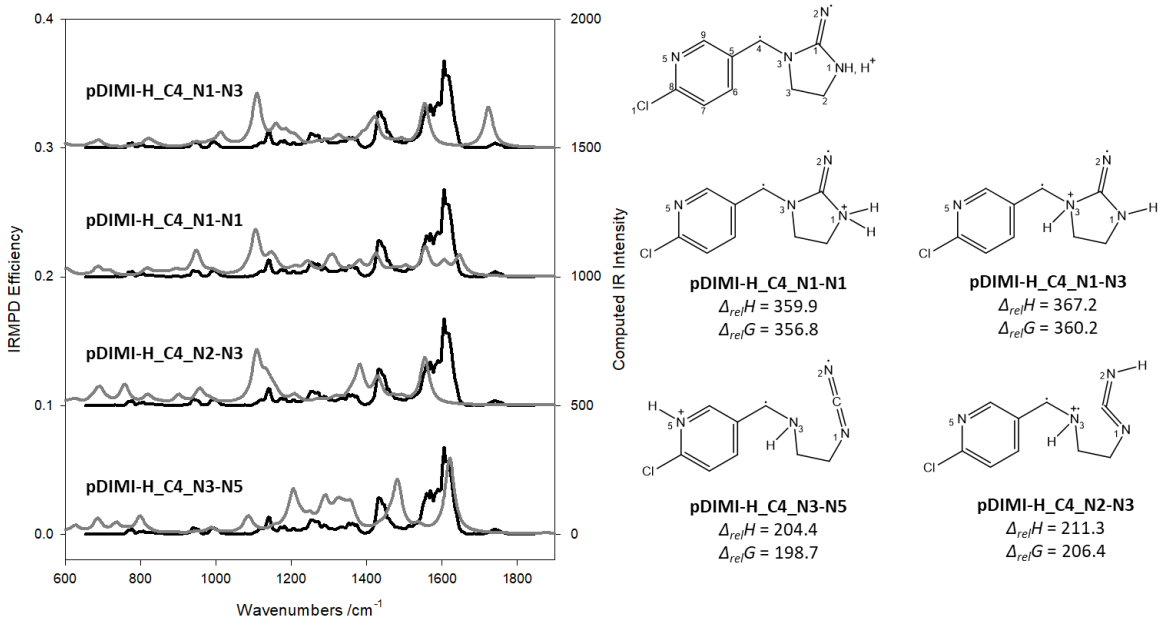

Figure S3.19. Comparison of the experimental IRMPD spectra (black trace) and the computed IR spectra (grey trace) for the loss of $NO_2^{\bullet}$ and $H^{\bullet}$ from the C4 position of protonated imidacloprid, triplet state isomers. All relative thermochemistries are 298 K values and are in kJ mol^{-1}.

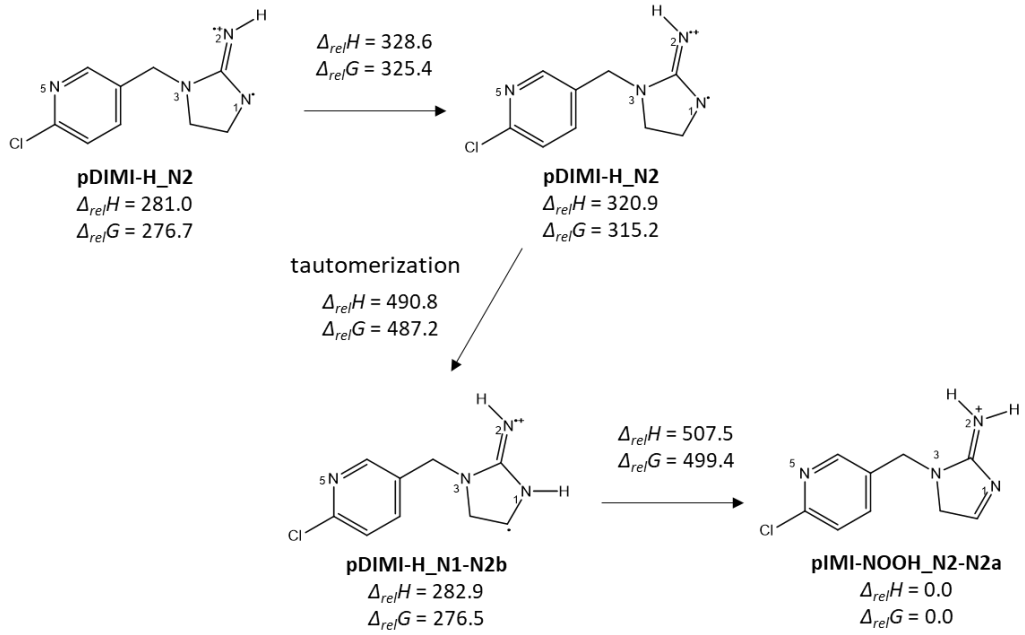

Figure S3.20. Energetics for the formation of pIMI-NOOH_N2-N2a from pDIMI-H_N2.

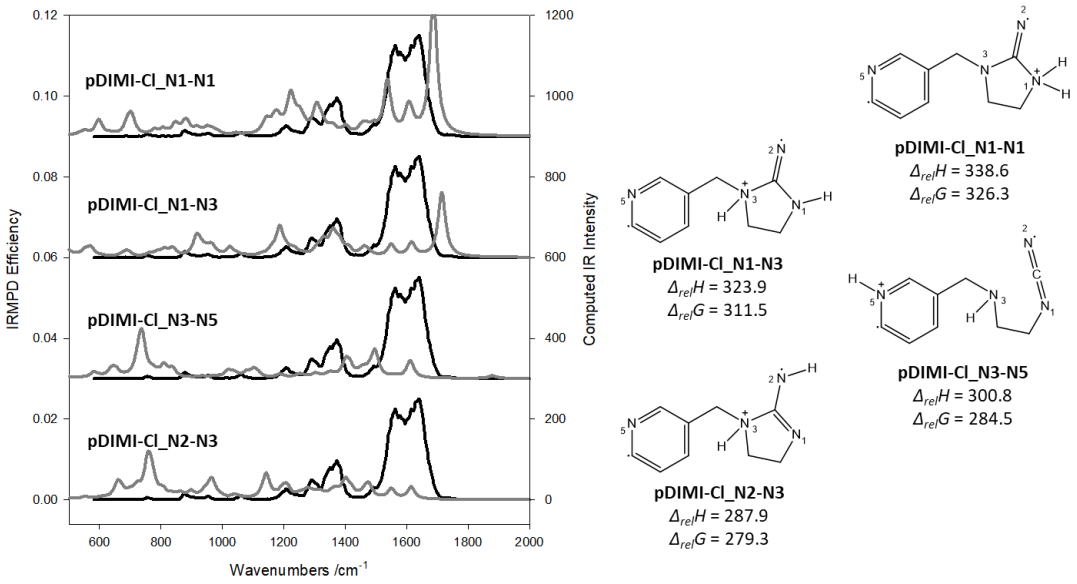

Figure S3.21. Comparison of the experimental IRMPD spectra (black trace) and the computed IR spectra (grey trace) for protonated dechlorinated desnitroimidacloprid (loss of $Cl^{\bullet}$), triplet state isomers. All relative thermochemistries are 298 K values and are in kJ mol^{-1}.

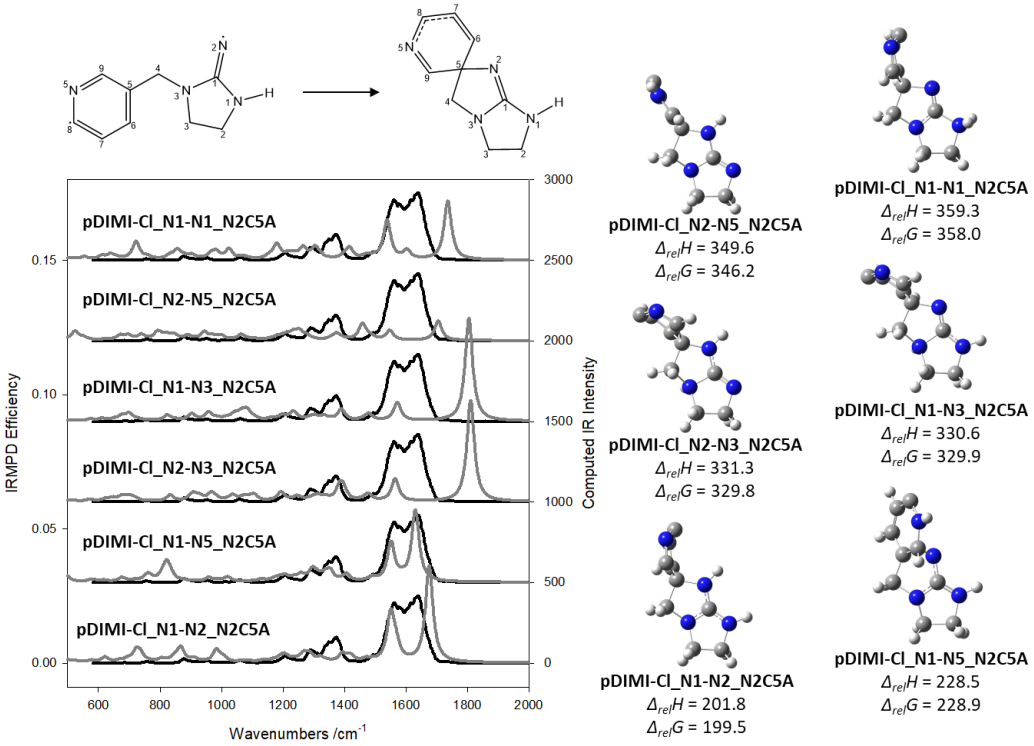

Figure S3.22. Comparison of the experimental IRMPD spectra (black trace) and the computed IR spectra (grey trace) for protonated dechlorinated desnitroimidacloprid (loss of Cl˙), singlet state isomers involving N2-C5 bond formation. All relative thermochemistries are 298 K values and are in kJ mol^{-1}.

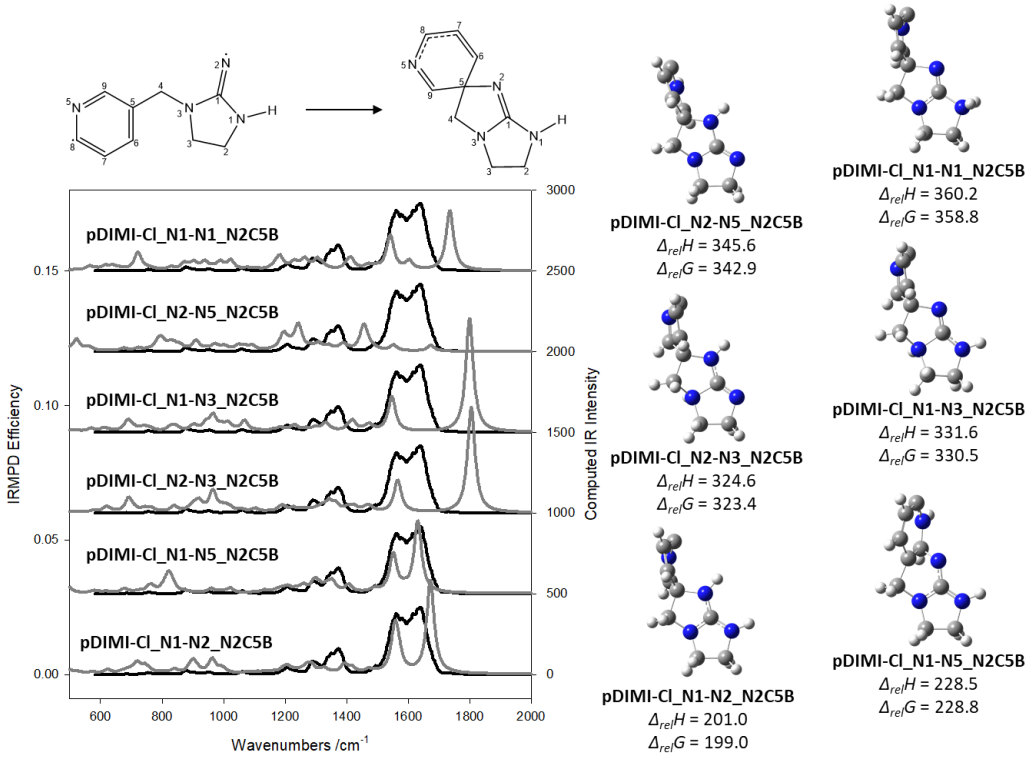

Figure S3.23. Comparison of the experimental IRMPD spectra (black trace) and the computed IR spectra (grey trace) for protonated dechlorinated desnitroimidacloprid (loss of Cl$^{\bullet}$), singlet state isomers involving N2-C5 bond formation. All relative thermochemistries are 298 K values and are in kJ mol^{-1}.

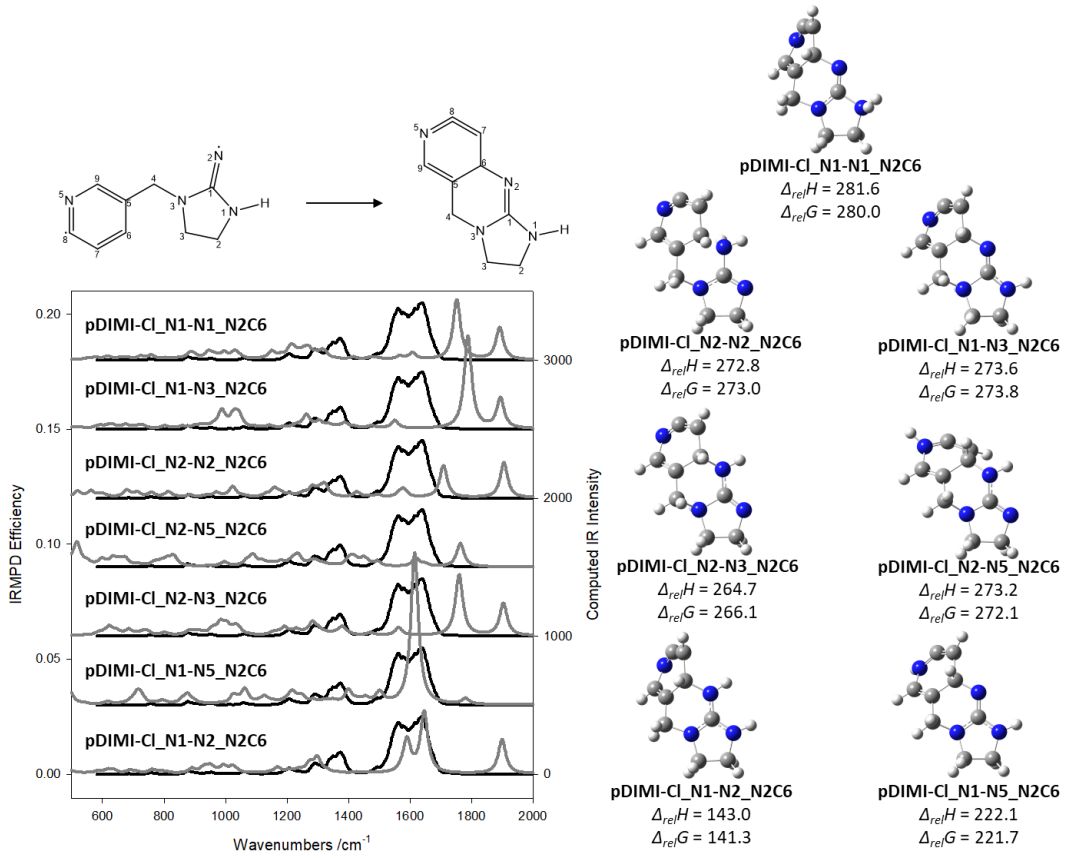

Figure S3.24. Comparison of the experimental IRMPD spectra (black trace) and the computed IR spectra (grey trace) for protonated dechlorinated desnitroimidacloprid (loss of Cl•), singlet state isomers involving N2-C6 bond formation. All relative thermochemistries are 298 K values and are in kJ mol^{-1}.

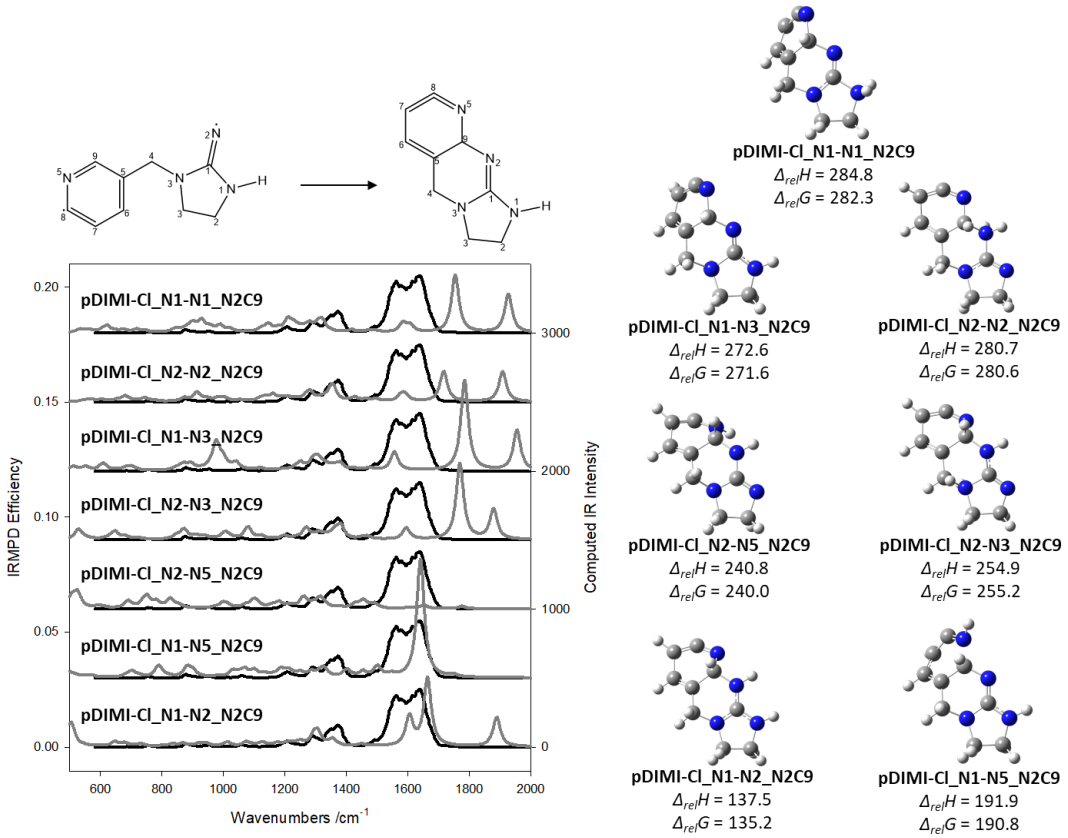

Figure S3.25. Comparison of the experimental IRMPD spectra (black trace) and the computed IR spectra (grey trace) for protonated dechlorinated desnitroimidacloprid (loss of Cl•), singlet state isomers involving N2-C9 bond formation. All relative thermochemistries are 298 K values and are in kJ mol^{-1}.

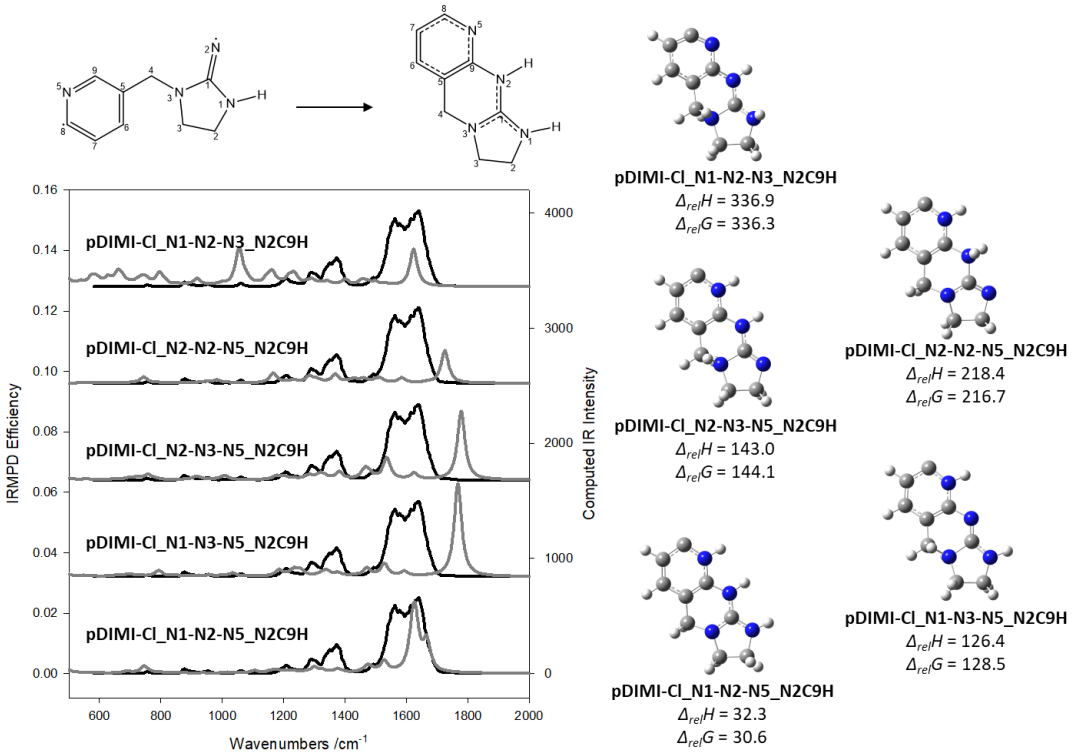

Figure S3.26. Comparison of the experimental IRMPD spectra (black trace) and the computed IR spectra (grey trace) for protonated dechlorinated desnitroimidacloprid (loss of $Cl^{\bullet}$), singlet state isomers involving N2-C9 bond formation and a hydrogen shift from C9 to N2. All relative thermochemistries are 298 K values and are in kJ mol^{-1}.

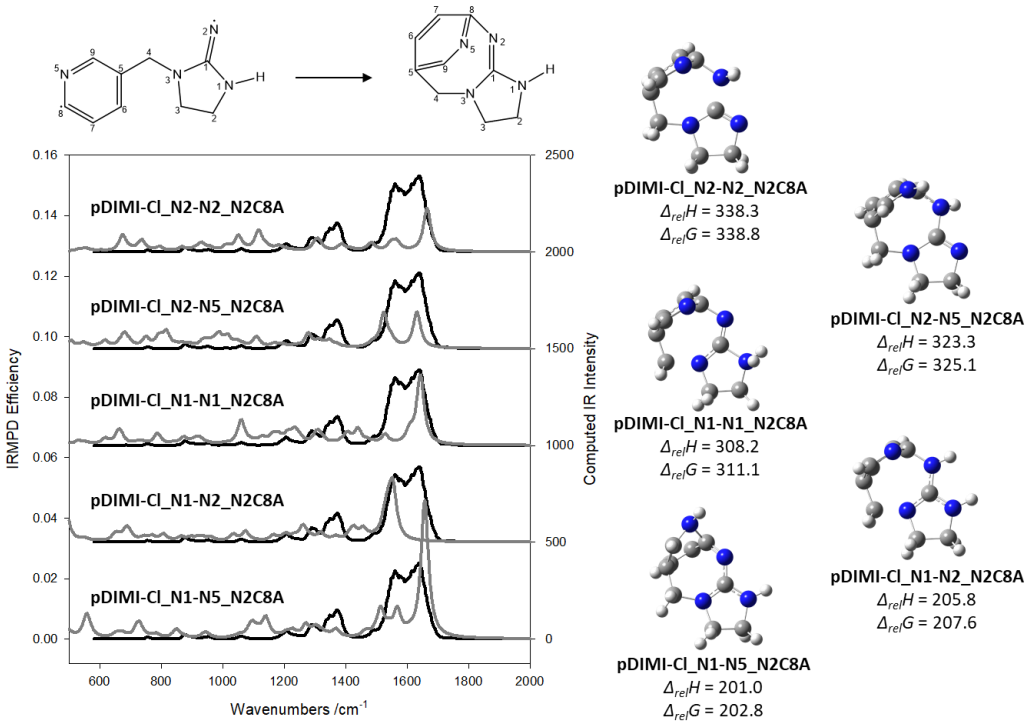

Figure S3.27. Comparison of the experimental IRMPD spectra (black trace) and the computed IR spectra (grey trace) for protonated dechlorinated desnitroimidacloprid (loss of $Cl^{\bullet}$), singlet state isomers involving N2-C8 bond formation. All relative thermochemistries are 298 K values and are in kJ mol^{-1}.

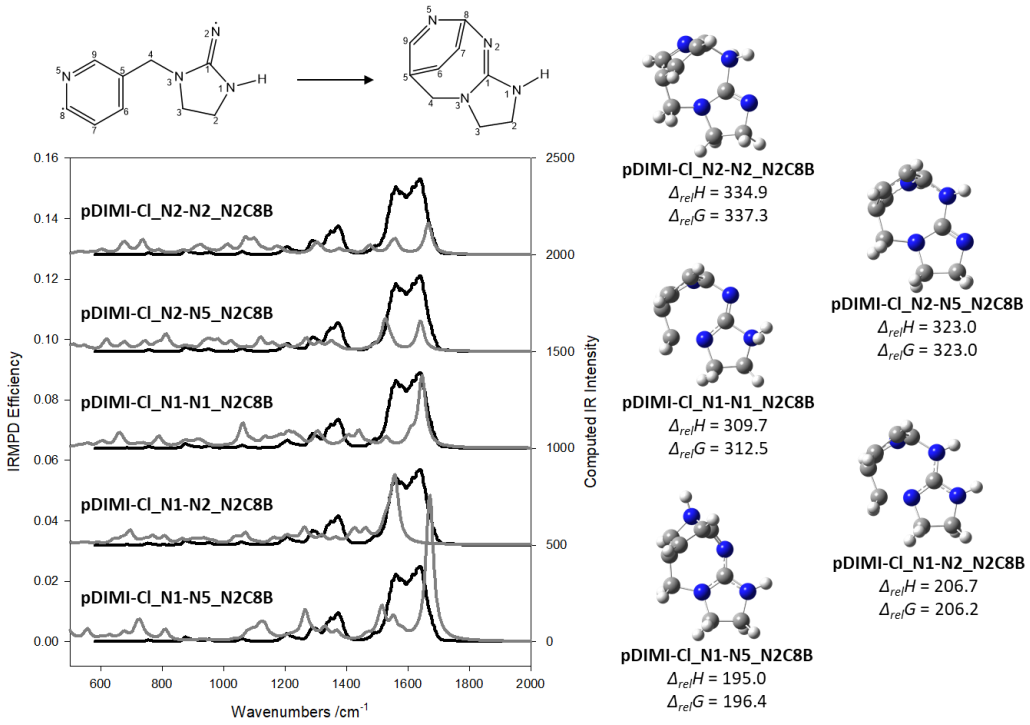

Figure S3.28. Comparison of the experimental IRMPD spectra (black trace) and the computed IR spectra (grey trace) for protonated dechlorinated desnitroimidacloprid (loss of Cl•), singlet state isomers involving N2-C8 bond formation. All relative thermochemistries are 298 K values and are in kJ mol^{-1}.

Appendix B – Supplemental Information for Chapter 4

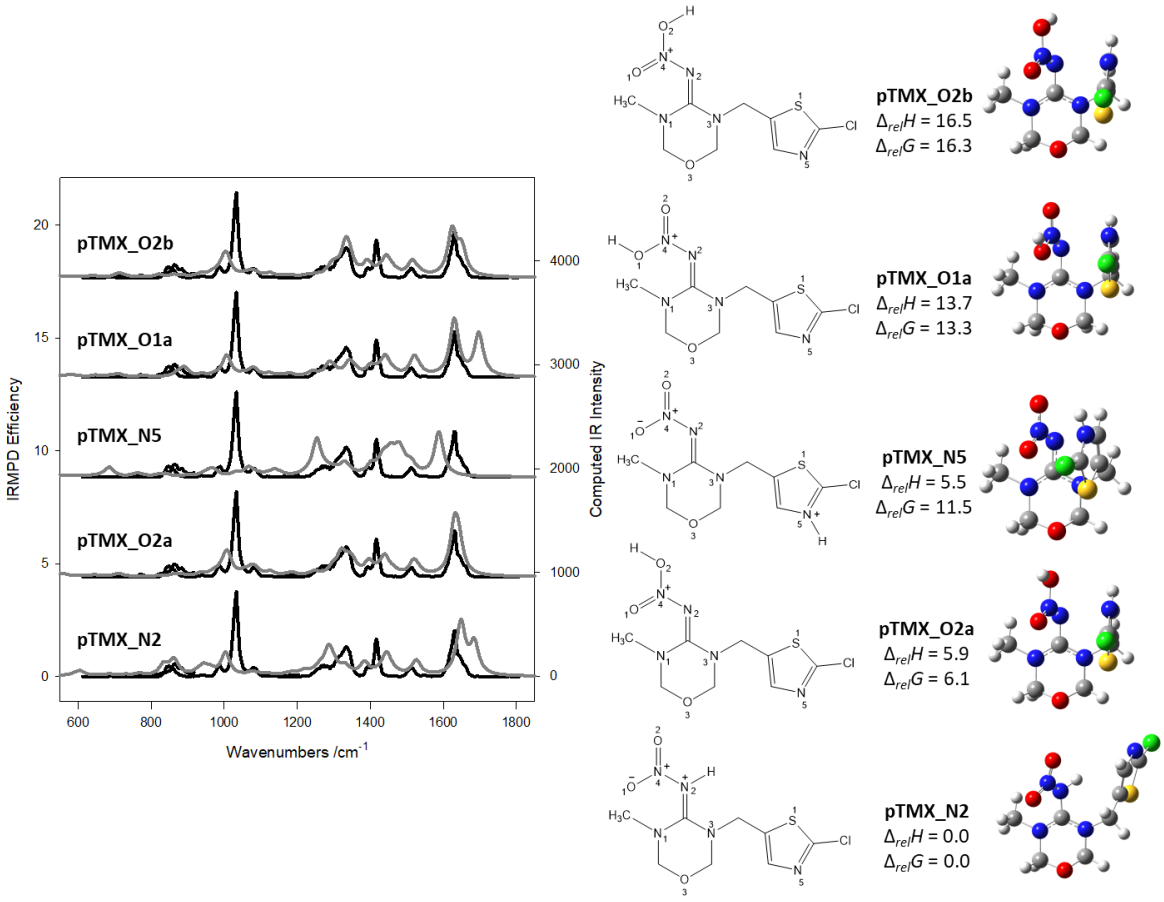

Figure S4.1. Half chair enantiomer of the oxadiazinane ring for the lower energy isomers of protonated thiamethoxam.

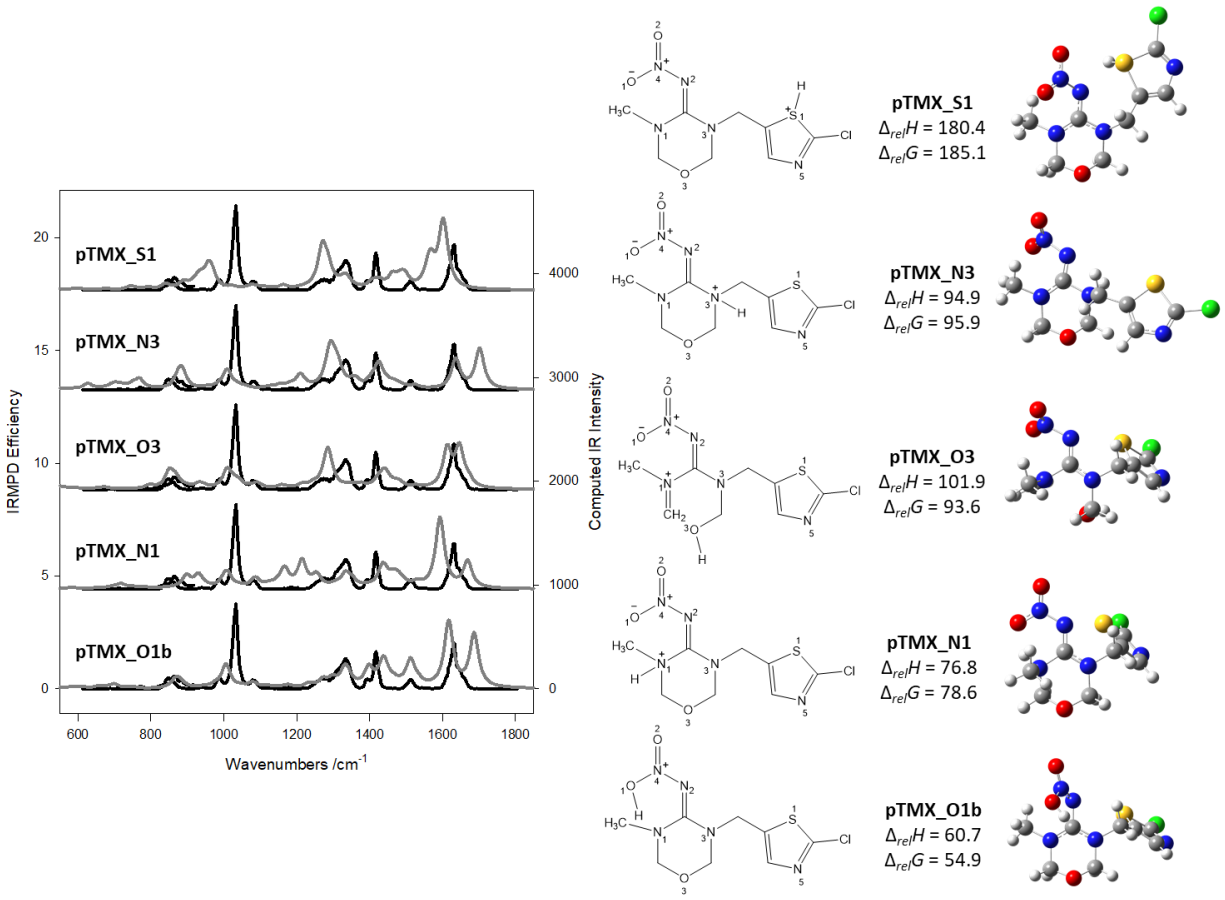

Figure S4.2. Half chair enantiomer of the oxadiazinane ring for the higher energy isomers of protonated thiamethoxam.

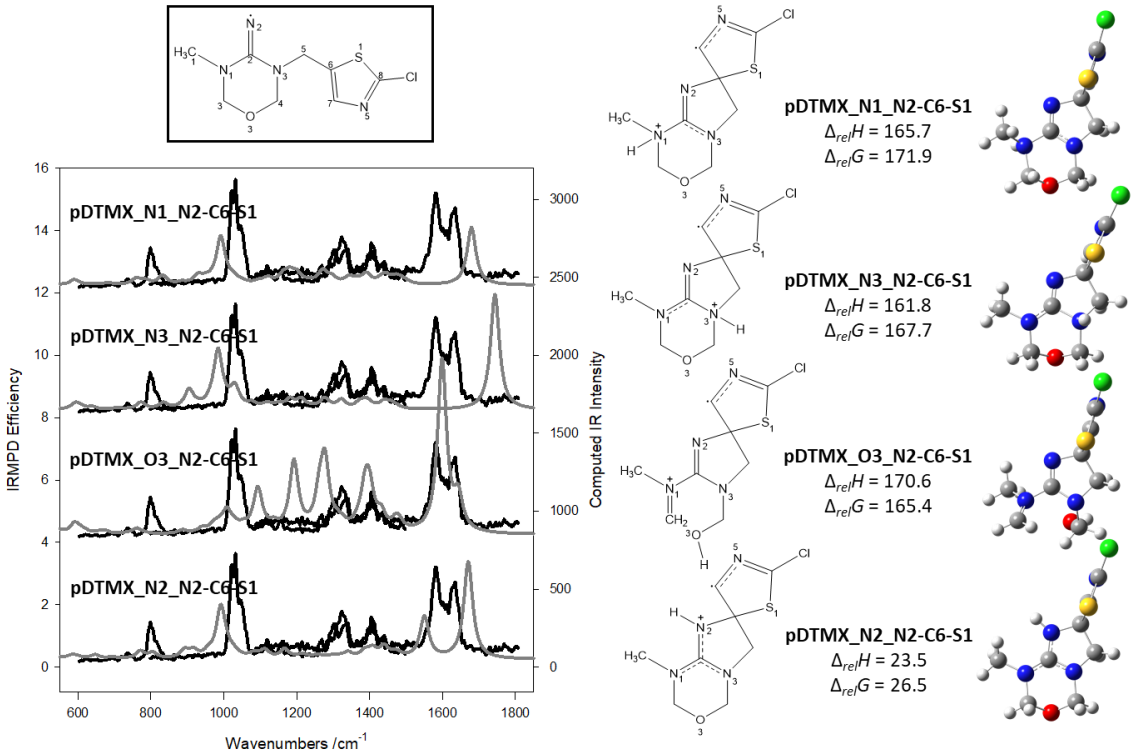

Figure S4.3. The experimental IRMPD spectrum (black trace) and the computed IR spectra (grey trace) for the isomers of protonated desnitro-thiamethoxam where the radical is localized on C7 (pDTMX_N2-C6-S1).

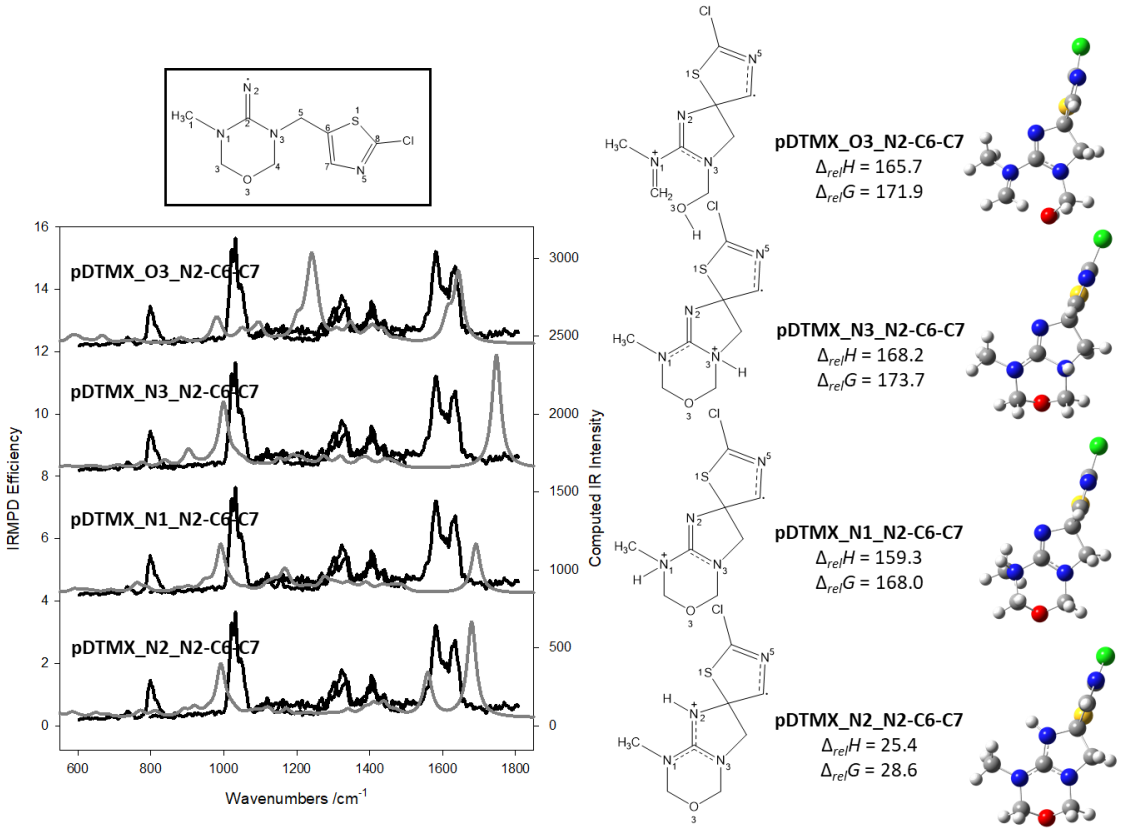

Figure S4.4. The experimental IRMPD spectrum (black trace) and the computed IR spectra (grey trace) for the isomers of protonated desnitro-thiamethoxam where the radical is localized on C7 (pDTMX_N2-C6-C7).

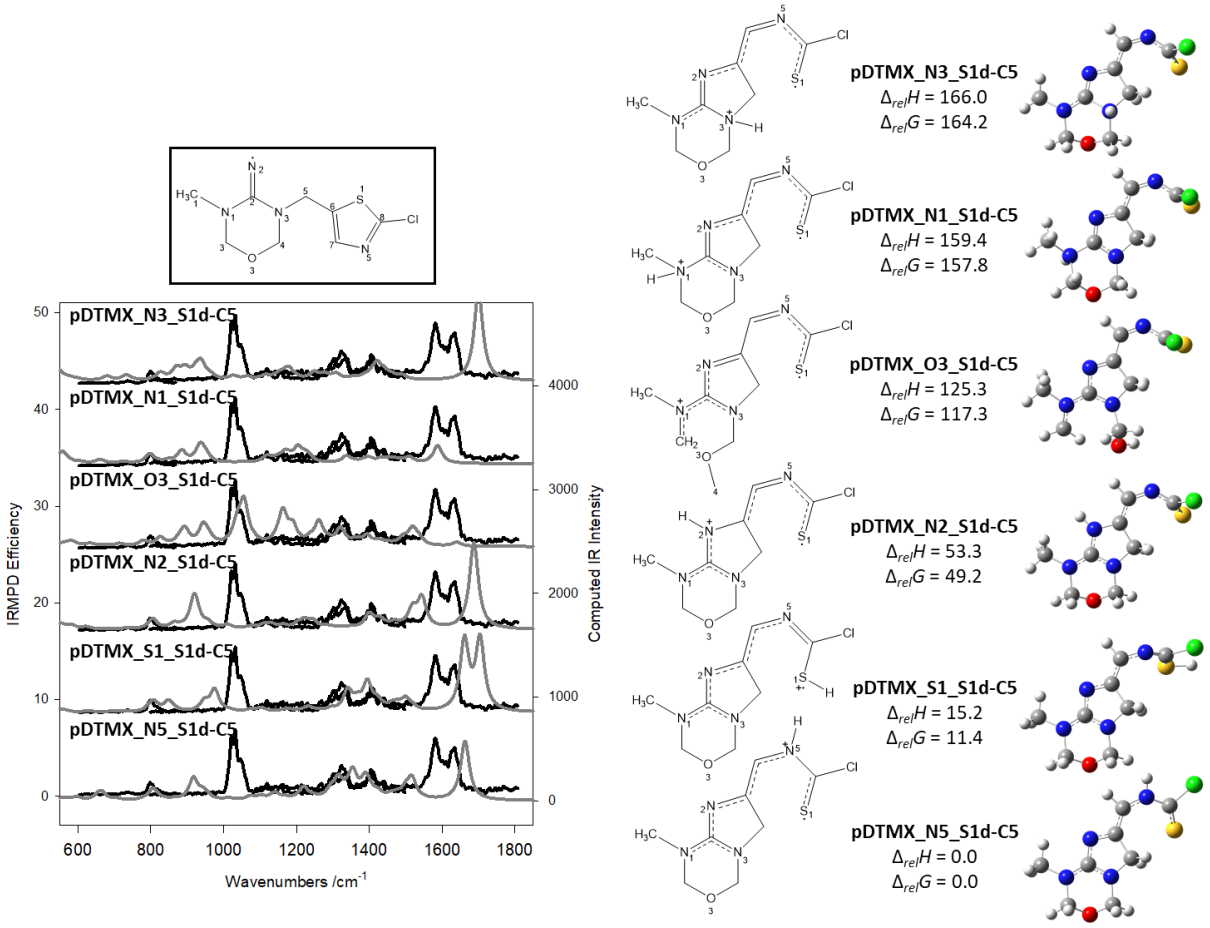

Figure S4.5. The experimental IRMPD spectrum (black trace) and the computed IR spectra (grey trace) for the isomers of protonated desnitro-thiamethoxam where the radical is localized on S1 (pDTMX_S1d-C5).

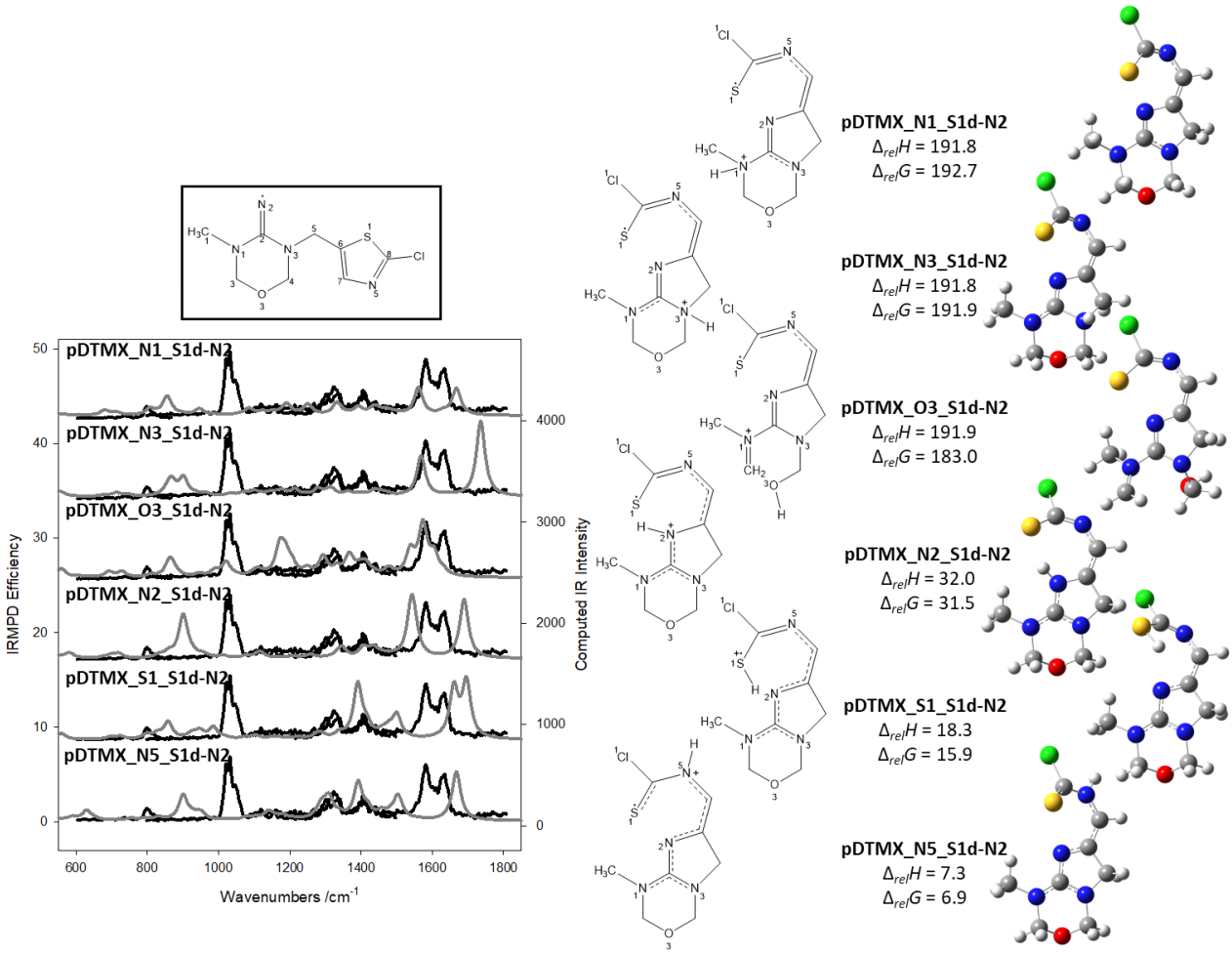

Figure S4.6. The experimental IRMPD spectrum (black trace) and the computed IR spectra (grey trace) for the isomers of protonated desnitro-thiamethoxam where the radical is localized on S1 (pDTMX_S1d-N2).

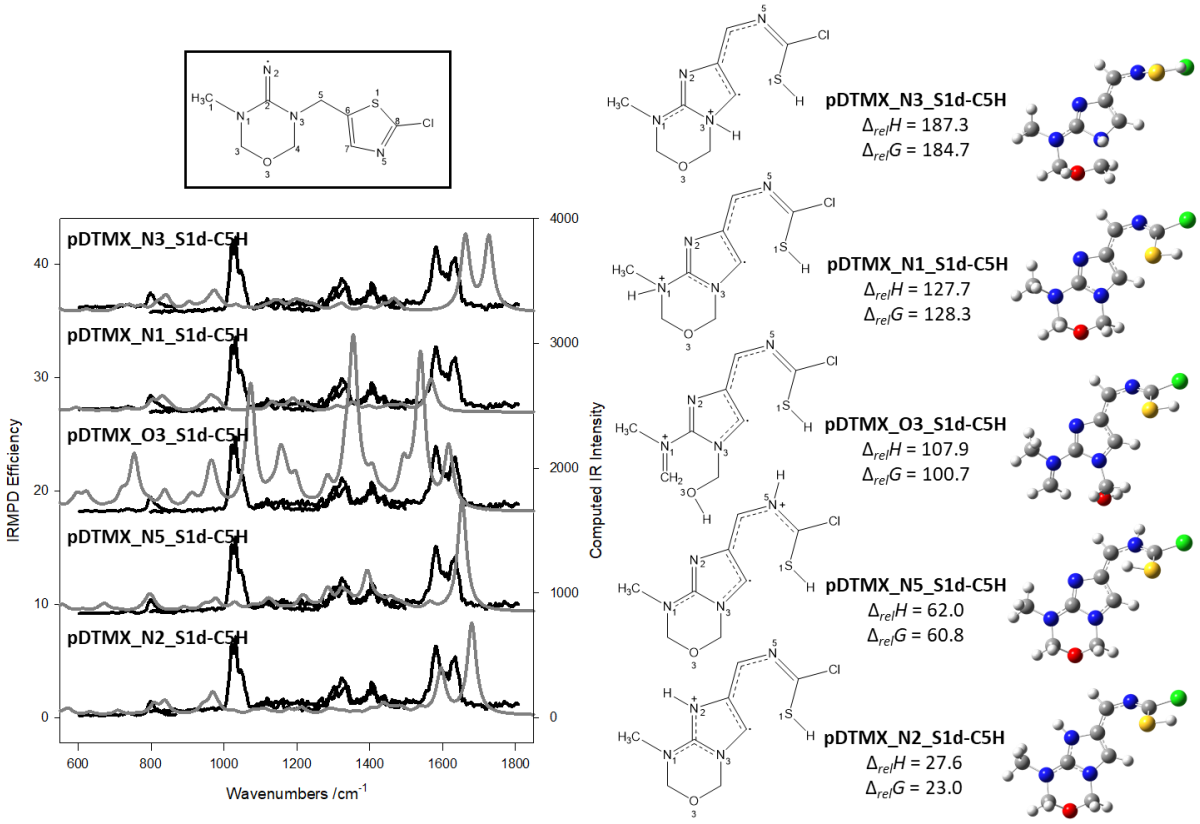

Figure S4.7. The experimental IRMPD spectrum (black trace) and the computed IR spectra (grey trace) for the isomers of protonated desnitro-thiamethoxam where the radical is localized on C5 (pDTMX_S1d-C5H).

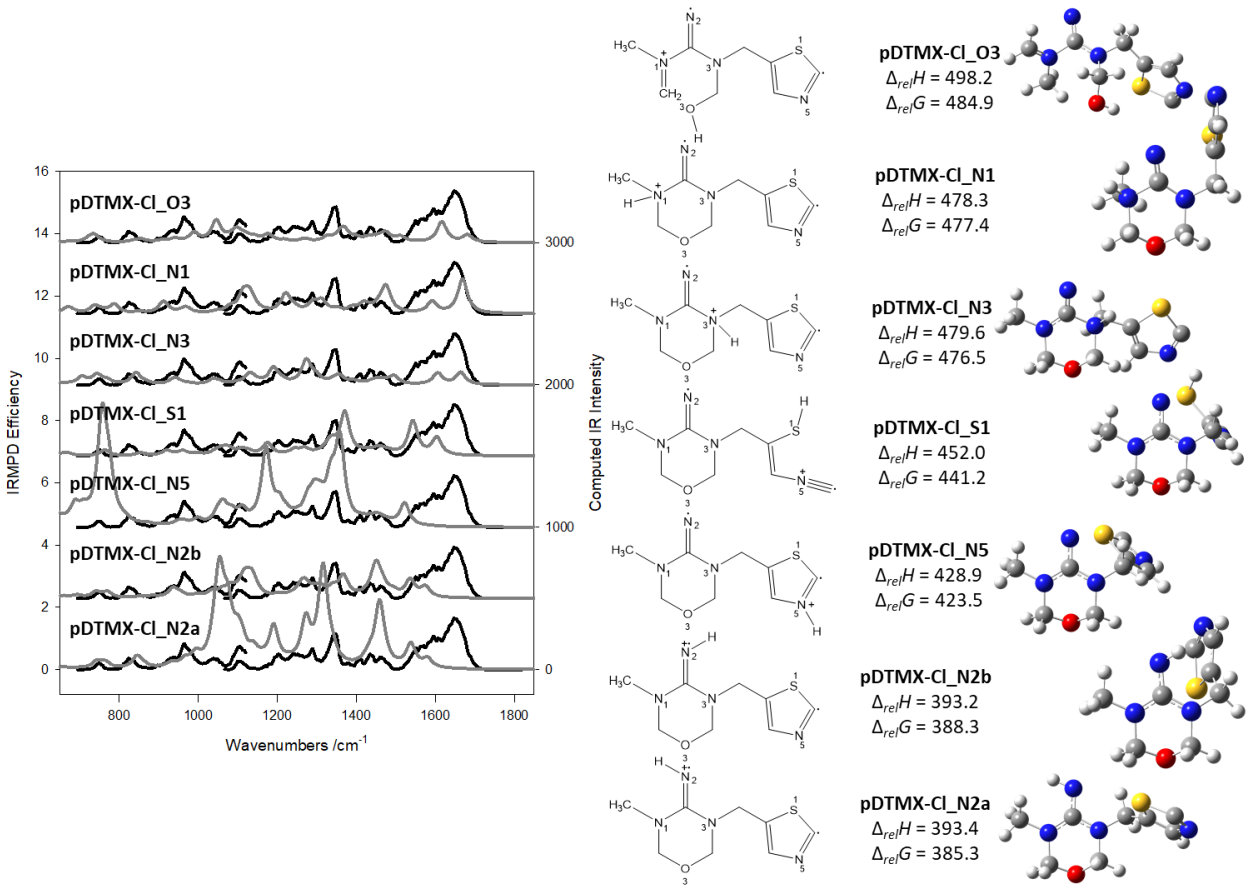

Figure S4.8. The experimental IRMPD spectrum (black trace) and the computed IR spectra (grey trace) for isomers of protonated dechlorinated desnitro-thiamethoxam where the radicals reside on N2 and C8 (pDTMX-Cl).

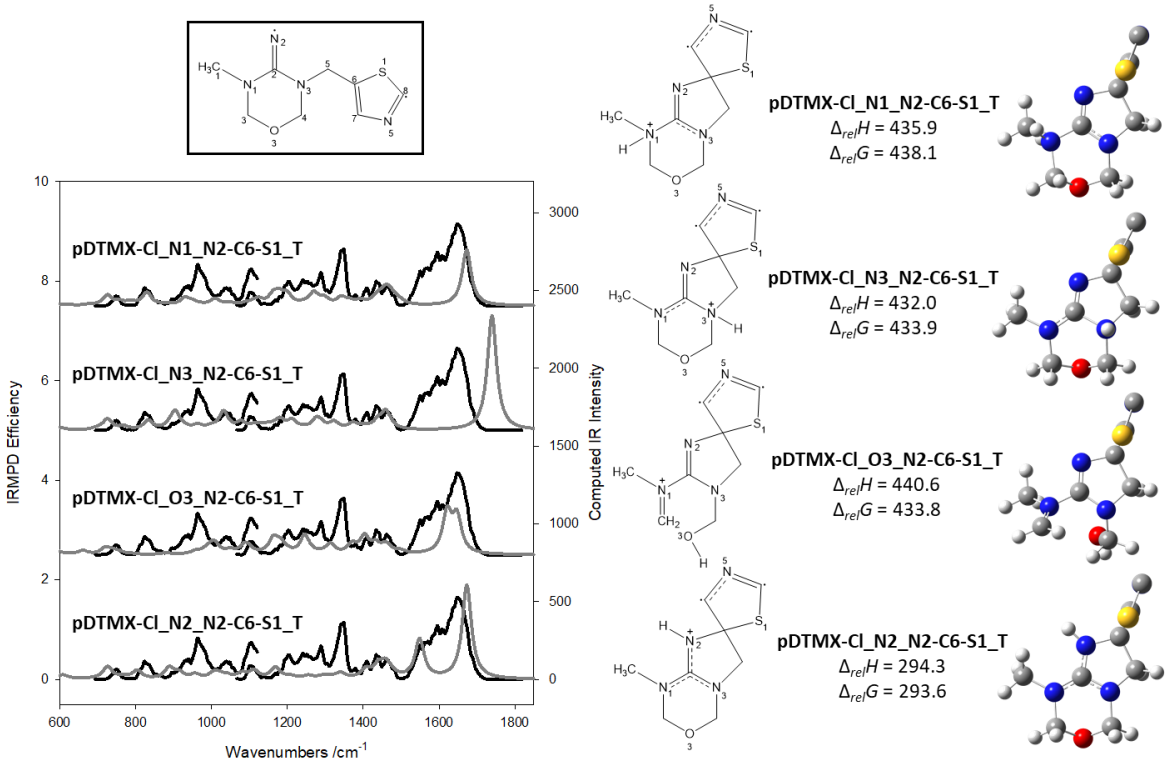

Figure S4.9. The experimental IRMPD spectrum (black trace) and the computed IR spectra (grey trace) for isomers of protonated dechlorinated desnitro-thiamethoxam where the N2-C6 bond is formed and the radicals reside on C7 and C8 (pDTMX-Cl_N2-C6-S1_T).

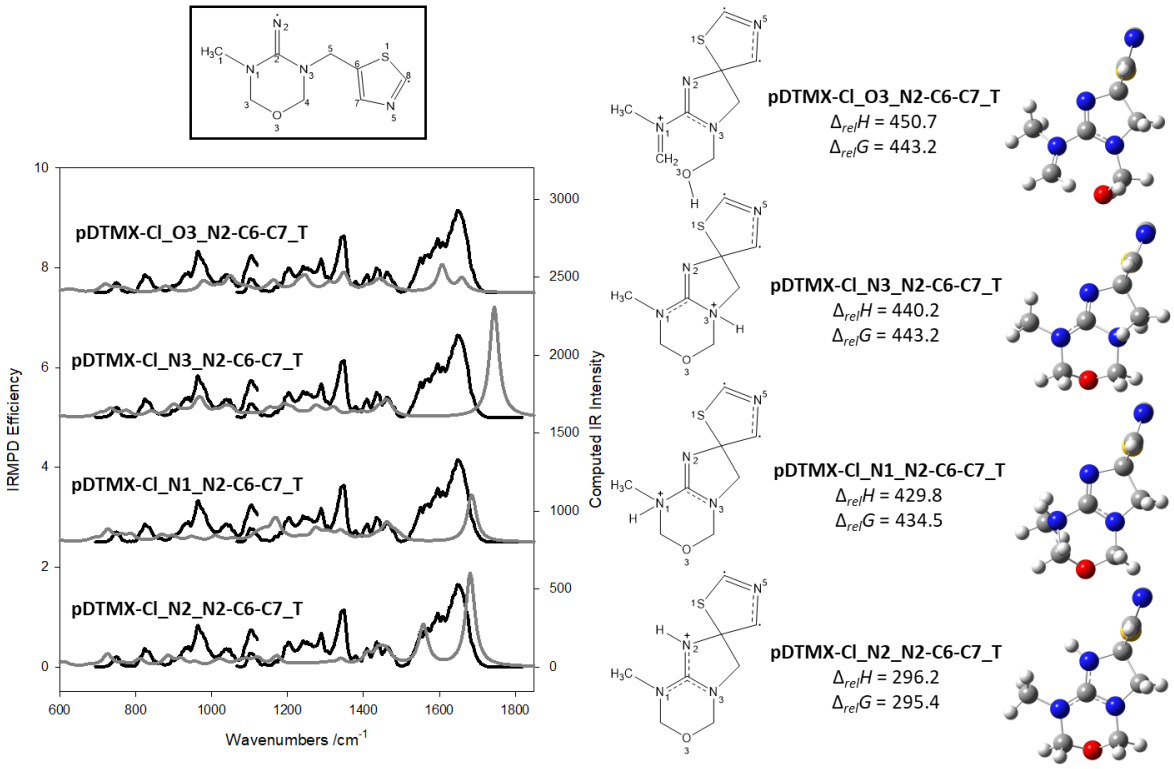

Figure S4.10. The experimental IRMPD spectrum (black trace) and the computed IR spectra (grey trace) for isomers of protonated dechlorinated desnitro-thiamethoxam where the N2-C6 bond is formed and the radicals reside on C7 and C8 (pDTMX-Cl_N2-C6-C7_T).

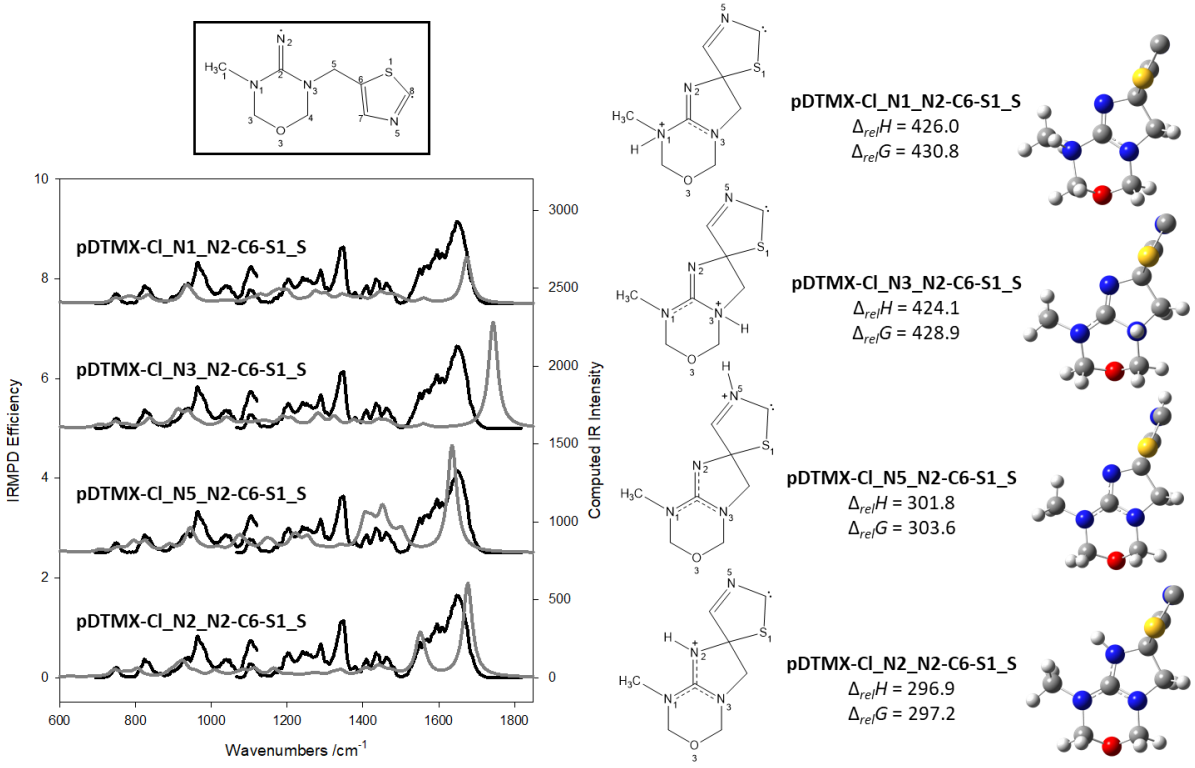

Figure S4.11. The experimental IRMPD spectrum (black trace) and the computed IR spectra (grey trace) for isomers of protonated dechlorinated desnitro-thiamethoxam where the N2-C6 bond is formed and the radicals reside on C8 (pDTMX-Cl_N2-C6-S1_S).

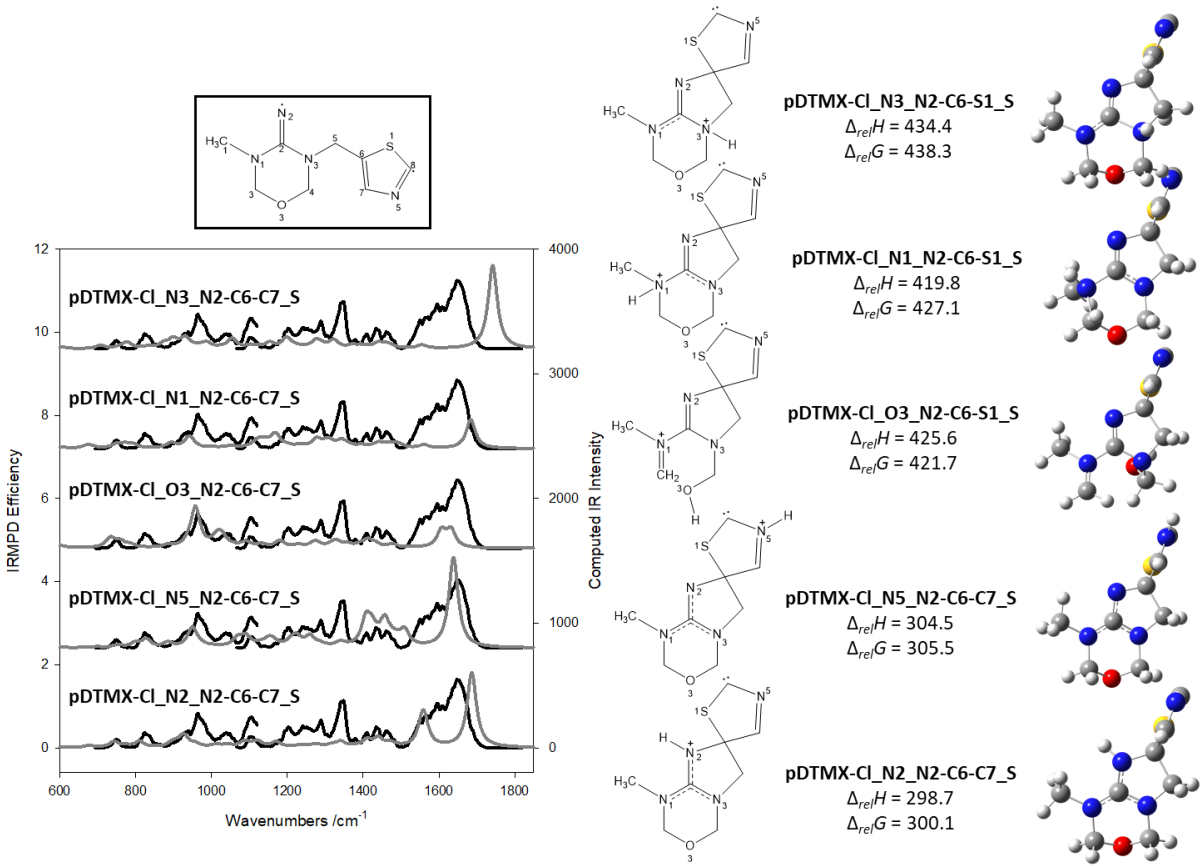

Figure S4.12. The experimental IRMPD spectrum (black trace) and the computed IR spectra (grey trace) for isomers of protonated dechlorinated desnitro-thiamethoxam where the N2-C6 bond is formed and the radicals reside on C8 (pDTMX-Cl_N2-C6-C7_S).

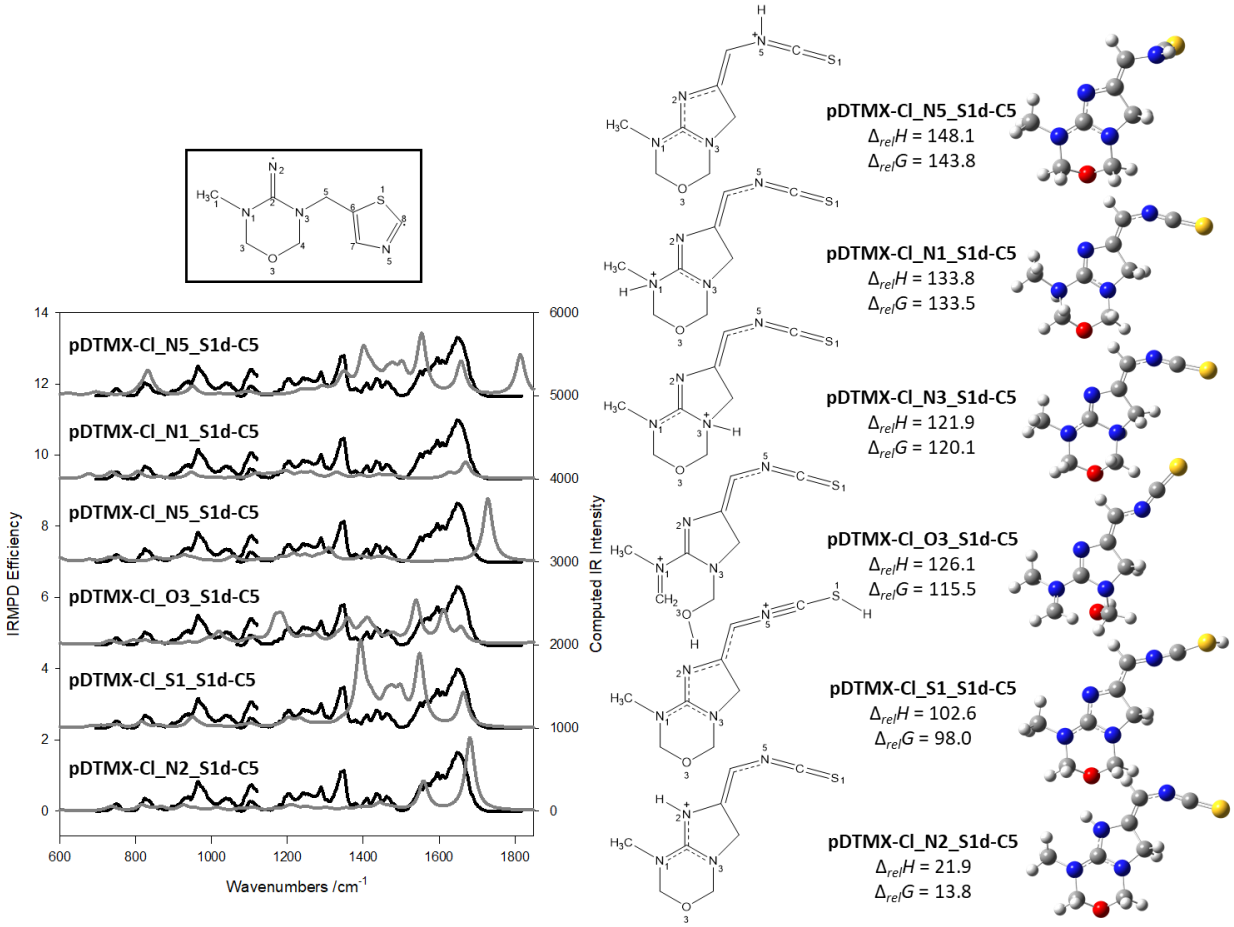

Figure S4.13. The experimental IRMPD spectrum (black trace) and the computed IR spectra (grey trace) for isomers of protonated dechlorinated desnitro-thiamethoxam where the N2-C6 bond is formed and the C6-S1 bond is cleaved (pDTMX-Cl_S1d-C5).

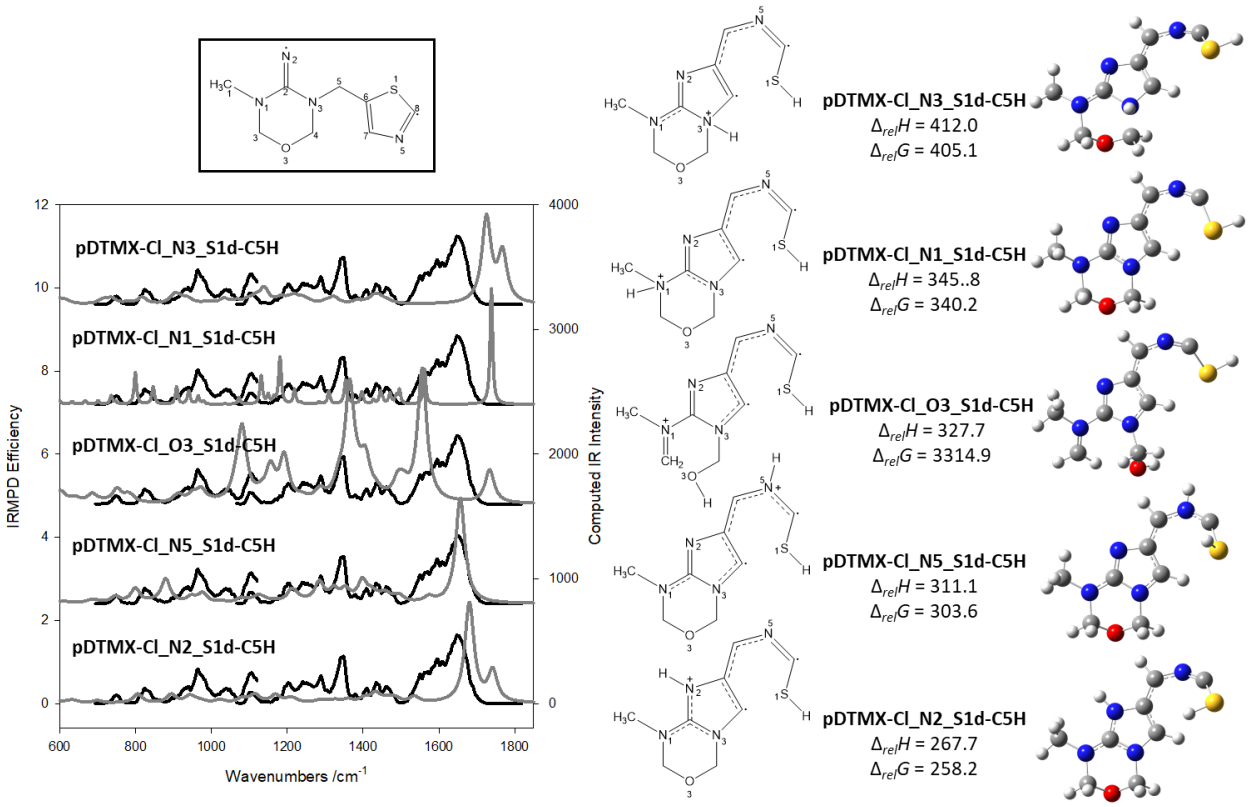

Figure S4.14. The experimental IRMPD spectrum (black trace) and the computed IR spectra (grey trace) for isomers of protonated dechlorinated desnitro-thiamethoxam where a hydrogen is transferred from C5 to S1 and the radicals reside on C5 and C8 (pDTMX-Cl_S1d-C5H).

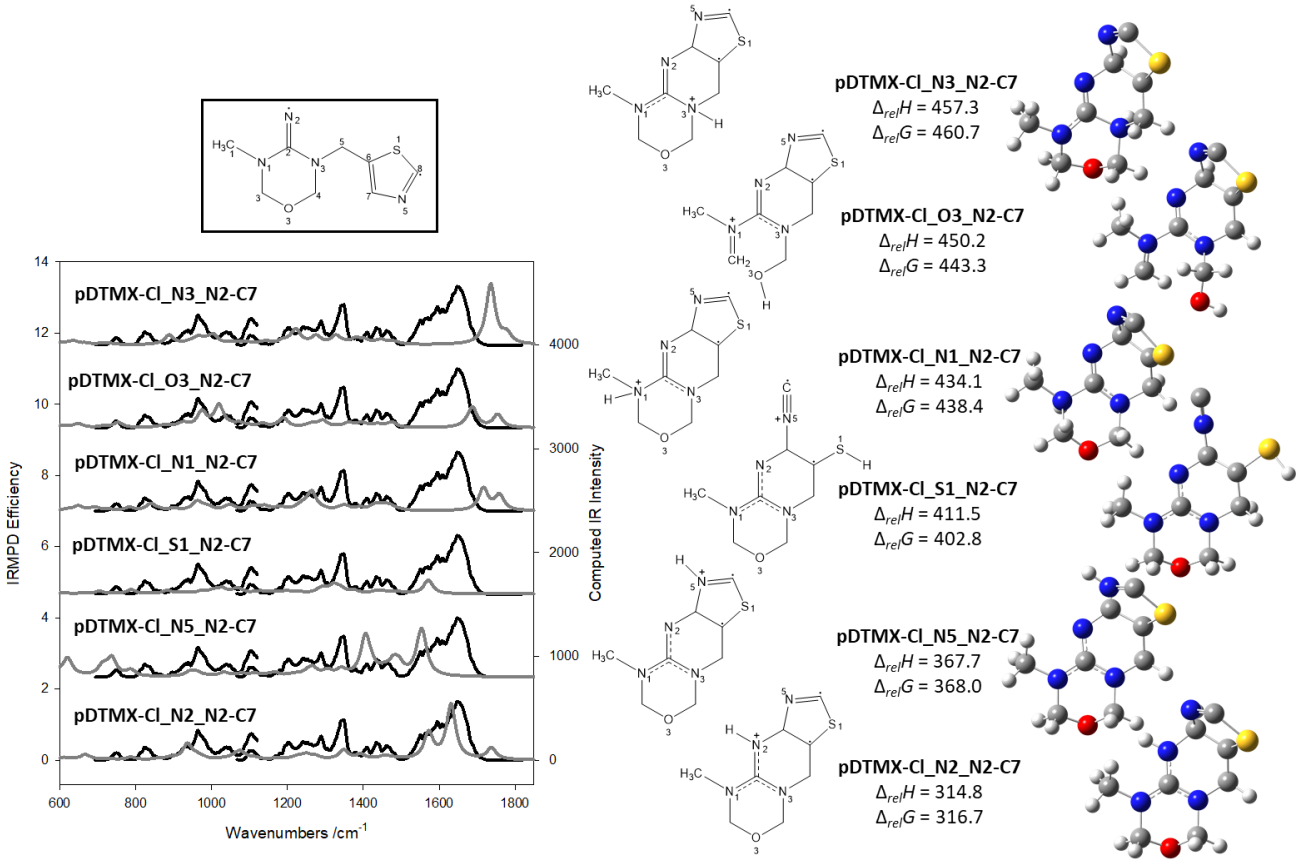

Figure S4.15. The experimental IRMPD spectrum (black trace) and the computed IR spectra (grey trace) for isomers of protonated dechlorinated desnitro-thiamethoxam where the N2-C7 bond is formed and the radicals reside on C6 and C8 (pDTMX-Cl_N2-C7).

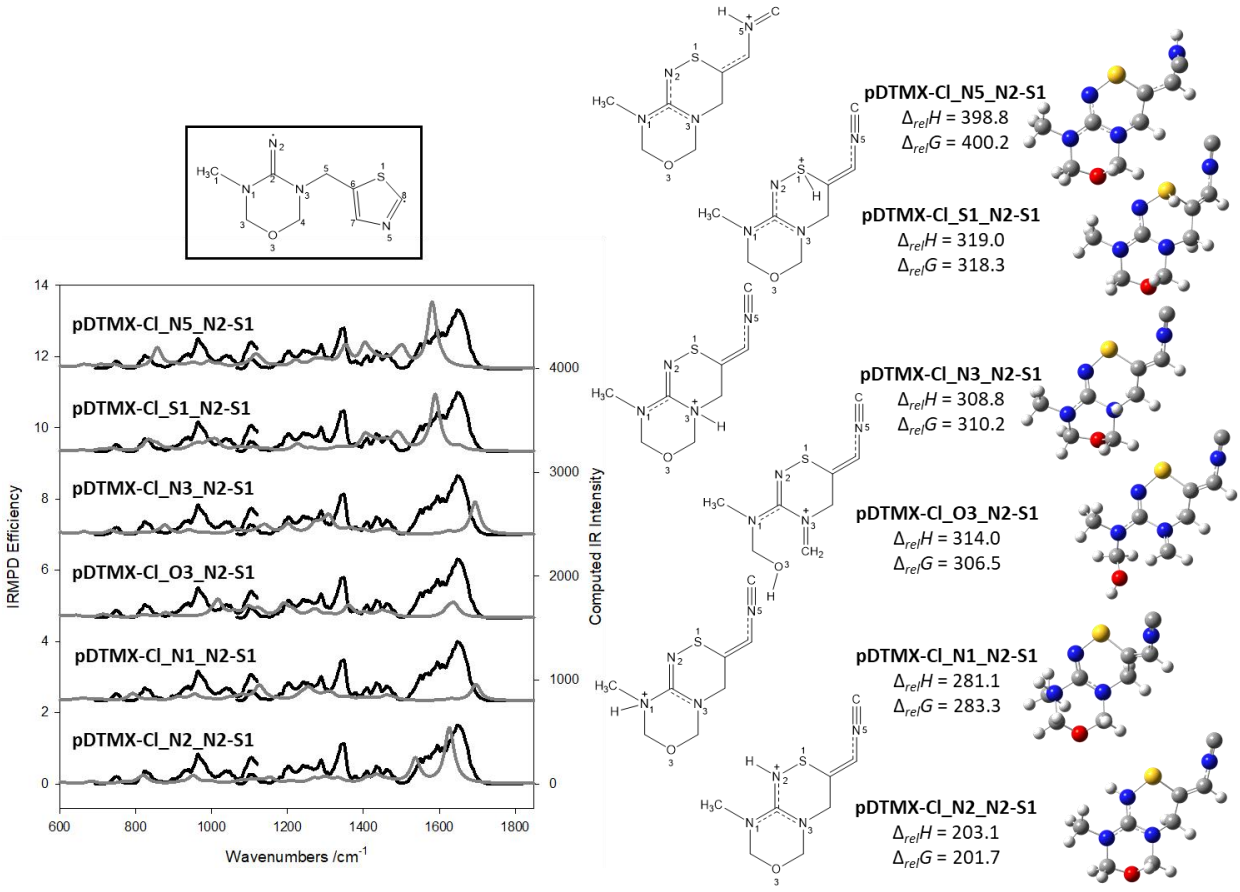

Figure S4.16. The experimental IRMPD spectrum (black trace) and the computed IR spectra (grey trace) for isomers of protonated dechlorinated desnitro-thiamethoxam where the N2-S1 bond is formed and the C8-S1 bond is cleaved (pDTMX-Cl_N2-S1).

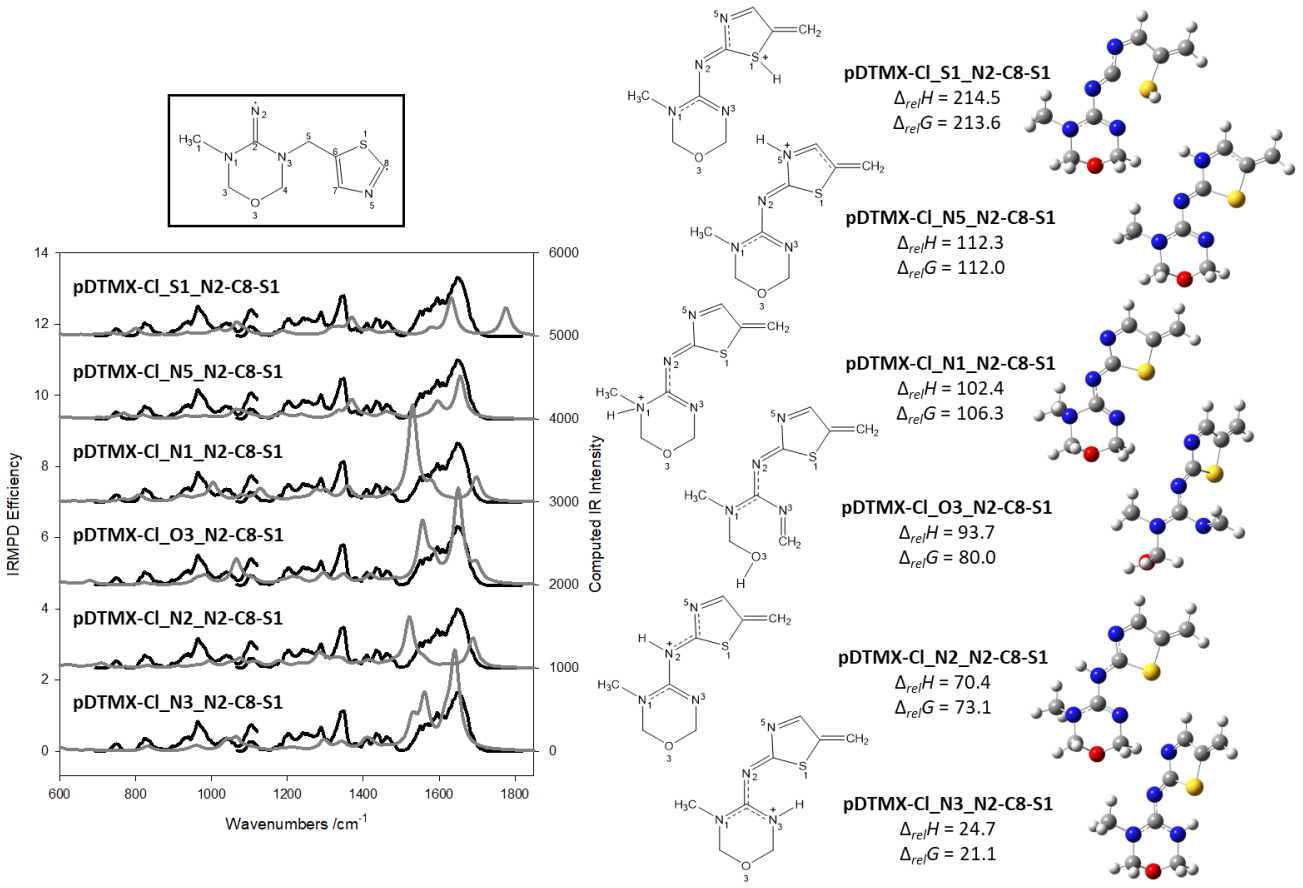

Figure S4.17. The experimental IRMPD spectrum (black trace) and the computed IR spectra (grey trace) for isomers of protonated dechlorinated desnitro-thiamethoxam where formation of the N2-C8 bond results in cleavage of the N3-C5 bond (pDTMX-Cl_N2-C8-N5).